



University of Southampton Research Repository

Copyright © and Moral Rights for this thesis and, where applicable, any accompanying data are retained by the author and/or other copyright owners. A copy can be downloaded for personal non-commercial research or study, without prior permission or charge. This thesis and the accompanying data cannot be reproduced or quoted extensively from without first obtaining permission in writing from the copyright holder/s. The content of the thesis and accompanying research data (where applicable) must not be changed in any way or sold commercially in any format or medium without the formal permission of the copyright holder/s.

When referring to this thesis and any accompanying data, full bibliographic details must be given, e.g.

Thesis: Author (Year of Submission) "Full thesis title", University of Southampton, name of the University Faculty or School or Department, PhD Thesis, pagination.

Data: Author (Year) Title. URI [dataset]

Declaration of Authorship

Print name:

Title of thesis:

I declare that this thesis and the work presented in it is my own and has been generated by me as the result of my own original research. I confirm that:

1. This work was done wholly or mainly while in candidature for a research degree at this University
2. Where any part of this thesis has previously been submitted for a degree or any other qualification at this University or any other institution, this has been clearly stated
3. Where I have consulted the published work of others, this is always clearly attributed
4. Where I have quoted from the work of others, the source is always given. With the exception of such quotations, this thesis is entirely my own work
5. I have acknowledged all main sources of help
6. Where the thesis is based on work done by myself jointly with others, I have made clear exactly what was done by others and what I have contributed myself
7. Parts of this work have been published and are listed in the List of Publications section (section)

Signature:

Date:

Computational Modelling of Modern Battery Material Interfaces

Julian Holland

A Ph.D. Thesis
ORCID: 0000-0001-8959-0112

School of Chemistry
University of Southampton
United Kingdom
6th March 2024

*Life before Death
Strength before Weakness
Journey before Destination*

-BRANDON SANDERSON

When you are a Bear of Very Little Brain, and you Think of Things, you find sometimes that a Thing which seemed very Thingish inside you is quite different when it gets out into the open and has other people looking at it

-WINNIE THE POOH

Wisdom comes from experience. Experience is often a result of lack of wisdom.

-TERRY PRATCHETT

Contents

Preface	i
Acknowledgements	i
Motivation	ii
Abstract	ii
Thesis Structure	iii
List of Publications	iv
Papers and Reviews	iv
Conferences and Talks	iv
1 Theoretical Background	1
1.1 Quantum Mechanics	1
1.1.1 The Schrödinger Equation	1
1.1.2 The Time-independent Schrödinger Equation	1
1.1.3 The Born-Oppenheimer Approximation	2
1.1.4 Bra and Ket notation	2
1.1.5 The Variational Principle	3
1.1.6 Electron Correlation	4
1.2 Principles of Density Functional Theory	6
1.2.1 Hohenberg-Kohn Theorems	6
1.2.2 Kohn-Sham Theory	6
1.2.3 Exchange-Correlation Functionals	8
1.2.4 Basis Sets	8
1.2.5 Pseudopotentials	9
1.3 Linear-Scaling Density Functional Thoery	11
1.3.1 ONESTEP Underlying Principles	11
1.3.2 Psinc Basis Set	12
1.3.3 Non-gapped Systems in ONESTEP	13
1.4 Molecular Dynamics	18
1.5 Density Fuctional Tight-Binding Theory	19
1.6 Machine Learning	21

1.6.1 Linear Regression	21
1.6.2 Hierarchical Clustering	23
2 Battery Materials	26
2.1 Li-ion Batteries	27
2.1.1 General Chemistry	27
2.1.2 Solid Electrolyte Interphase	28
2.1.3 Graphite Anodes	28
2.2 Solid-state Batteries	31
2.2.1 Solid Electrolytes	31
2.2.2 $\text{Li}_7\text{La}_3\text{Zr}_2\text{O}_{12}$	31
2.2.3 Interfaces with Solid Electrolytes	32
3 A Study of Graphite Nanoparticles	34
3.1 Abstract	34
3.2 Introduction	35
3.3 Methodology	37
3.3.1 ONETEP for Graphite	37
3.3.2 Modelling Graphite Properties	37
3.3.3 Nanoparticle	40
3.3.4 Intercalation Process	41
3.3.5 Placement restriction	42
3.4 Results and Discussion	44
3.4.1 Structure	44
3.4.2 Mulliken Population Analysis	45
3.4.3 Density of States	50
3.4.4 Voltage Step Profiles	52
3.4.5 AB Pinning	56
3.5 Conclusions	57
3.6 Supplementary Results and Discussion	58
3.6.1 Bulk	58
3.6.2 Different Terminations of the Nanoparticle	59
3.6.3 A Posteriori Dispersion Correction	62
3.6.4 Confidence of Lithium Placement	64
4 A Study of Bulk c-LLZO	66
4.1 Abstract	66
4.2 Introduction	67
4.3 Reducing the Configuration Space	68

CONTENTS

4.4	Energetic Ordering of the Perfect Crystals	70
4.5	Energetic Ordering of the Optimised Crystals	74
4.6	Conclusion	76
4.7	Supplementary Results and Discussion	77
4.7.1	Data	77
4.7.2	Experimental Literature Summary Table	77
4.7.3	Theoretical Literature Summary Table	78
4.7.4	Dimer in Vacuum	80
4.7.5	Symmetry Against Energy	80
4.7.6	Configurational Entropy	81
5	A Study of LLZO Interfaces	83
5.1	Abstract	83
5.2	Introduction	84
5.3	Surfaces	85
5.3.1	Li Surfaces	85
5.3.2	t-LLZO Surfaces	87
5.3.3	Chemical Potentials	89
5.4	Interfaces	92
5.4.1	Interface Parameters	92
5.4.2	Commensurate Interfaces	92
5.4.3	Miller Planes	94
5.4.4	Surface Cuts	94
5.4.5	Inter-Slab Distance	95
5.4.6	Relative Inter-slab Translation	96
5.4.7	Configuration Space	98
5.5	DFTB parameterisation for LLZO	99
5.5.1	Library Development	99
5.5.2	Electronic term parameterisation	101
5.5.3	Repulsive term parameterisation for LLZO pair interactions	102
5.5.4	Pair-interaction Evaluation	104
5.5.5	Library Evaluation	105
5.6	Conclusion	109
6	Conclusions	110
6.1	Outlook and Future Work	112

Preface

Acknowledgements

I would like to thank my infinitely supportive and often wonderfully unhelpful family who I love to bits, particularly my Mum and Dad who did just the right amount of kicking up the arse to get me to this point, my sister for consistently putting me in my place, and my Auntie Amanda for proving to me what ever I can do she can do whilst raising twins. I also thank all my friends especially those of you for which figure 1 means anything to. It is safe to say without you this may well have been an unfinished project.

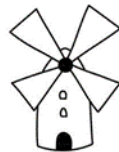


Figure 1: The Windmill

I have to thank my partner (now wife!), Sophie, for giving her extensive patience, providing necessary distractions, and generally being the best person I know. I also extend my eternal gratitude to my group (Davide, Brad, Gabriel, Tom D., Lennart, Rebecca, Nabeel, Tom E., Cat, Jacek, Arianth, Apostolos, Dimitrios, and Loukas) as well as my supervisors and mentors (Chris, Felix, and Victor) who between you all made these four years both more and less challenging by just the right amount. I thank my academic collaborators for helping me get this work finished (Johan, Martin, Elizabeth, Hamid, Bora, Sener, Ben, Nehzat, and Denis). I would like to show my appreciation to my former lecturers at the University of Sussex for inspiring me down this path, Hazel and John in particular. Finally, I would like to thank my cats Pebbles and Benzene, and Bailey the dog (they know what they did).¹

¹I should also thank Ryan Letourneau (Northernlion) for providing upwards of 1000 hours of inane entertainment that I consumed over the course of my Ph.D.

Motivation

The United Nations' Intergovernmental Panel on Climate Change (IPCC)'s 2023 Synthesis Report stated that, in order to keep in line with the Paris Climate Agreement's goal of limiting the average global temperature increase to under 1.5 °C, we need to reduce global carbon emissions by 48% before 2030 and by 99% before 2050.[52] Of the total global CO₂ emissions, in 2021, transportation accounted for 22.7%. [135] Section C.3.3 of the IPCC report stated "Electric vehicles powered by low-GHG emissions electricity have large potential to reduce land-based transport GHG emissions"². The International Transport Forum's 2023 report[137] echoed this sentiment, strongly recommending all vehicle sales, globally, after 2040 should be electric vehicles (EVs). It is clearly vital that every effort is made to facilitate the transition away from fossil fuel-dependent transport infrastructure to lower carbon-emitting technologies such as EVs.

One of the main ways research can accelerate the uptake of EVs is through finding improvements to the battery systems used by these vehicles. Towards this goal, the field of chemistry has often been concerned with innovations of battery materials with a focus on increased safety and capacity, as well as reduced manufacturing costs. Many of the most important chemical processes inside batteries occur at the interface. Unfortunately, they are also some of the most difficult to probe experimentally. Computational investigations have often been the method of choice when providing insights into the mechanisms occurring at these interfaces.[198]

Abstract

Material interface simulations often require electronic-level accuracy to deliver meaningful results.[284]. However, interfaces for the complex systems observed in batteries often require larger simulation sizes than can be simulated to this level of accuracy. This work aims to provide electron-level chemical information, through leveraging the recent innovations of linear-scaling density functional theory over the last decade with the ever-increasing scale of computational resources available to us, about previously inaccessibly large battery interfaces.

Li intercalation is one of the most fundamental mechanisms that occur in a Li-ion battery. Providing an electronic-level resolution of this process could significantly enhance the rational design of electrodes. We present an electrostatically-driven workflow that seeks to emulate the charging process for an anode. This workflow proceeds by selecting intercalation sites within a material using the global electrostatic minimum calculated using density functional theory (DFT). This methodology is applied to a high surface area to volume ratio structure in order to better investigate the anodic interface. The structure we select is a 592-atom graphite nanoparticle. We are able to simulate the charging of this large structure with electronic-level accuracy by using linear-scaling DFT methods which allow for the calculation of far larger systems than conventional DFT. The results of our application showed how several experimentally observed features of graphitic intercalation are retained in an unparameterised manner, lending to the quality of our selected methodologies. We observe Li staging, Li to C charge transfer, and the formation of an OCV-like voltage step profile using a convex-hull formalism. We also demonstrate the importance of the role of the interface in large structural shifts. Specifically, how Li accumulation at the edges can hamper the typical graphite transition from the AB to AA polymorphs with increasing Li content.

Moving towards the other side of this interface, we present work on the solid electrolyte material Li₇La₃Zr₂O₁₂ (LLZO). cubic LLZO's (c-LLZO) exact structure has not been able to be established through experiment or simulation. This problem is essential to resolve as the ground state structure of c-LLZO is required before performing more complex atomistic investigations. By implementing a three-stage methodology of generation, symmetry checking, and energetic ordering we have been able to reduce the vast configuration space of c-LLZO (7.4×10^{34} structures) to just four crystallographically predicted structures. This is achieved by implementing a restriction that no Li atom may be within 1.7 Å of each other. By considering this geometrical constraint we also determine that a large portion of previously reported structures may not be feasible or stable. We further reduce our configuration space by developing a symmetry checking technique capable of handling over 1×10^8 structures. Finally, we conclude by energetically ordering our symmetrically unique structure with a machine learning-based energetic calculator that was able to reproduce DFT energetic ordering with 99.96% accuracy. The data set of our produced structures is freely accessible to all with the aim of improving the accuracy and reproducibility of future LLZO research.

To expand the utility of our efforts made in our c-LLZO research we move towards simulation of the entire Li|LLZO interface, featuring a tetragonal LLZO (t-LLZO) interphase. One of the major obstacles in including the solid-state electrolyte LLZO in modern battery packs is the formation of dendrites at the Li|LLZO interface. Experimentally, such interfaces are challenging to probe. This provides a niche in which theory can deliver insights. In this work, we present the progress we have made towards simulating the Li|t-LLZO interface using linear-scaling DFT and high-accuracy surface energies. We also present a methodology to compute the configuration space structures necessary for thoroughly sampling solid-state interfaces which we apply to the system in question and find a minimum, well-sampled, configuration space of 1.04×10^7 structures. To get to this number we find all possible Miller plane combinations, find all possible t-LLZO cuts, create a scheme for sampling inter-slab translations, provide a methodology for finding low-strain commensurate interfaces, and present the results of large-scale DFT calculations on the Li|t-LLZO interface that find a reasonable

²GHG = greenhouse gasses

inter-slab distance value. Finally, having established our configuration space, we present our efforts towards the creation of density functional tight-binding Slater-Koster libraries specific to LLZO. During the process, we demonstrate a general workflow for solid-state systems. We find that our Slater-Koster libraries are able to reproduce DFT values for the total electronic density of states at the Fermi level of bulk t-LLZO. However, further parameterisation is required in order to apply these libraries to Li|LLZO interfaces, particularly the Li-O element-pair interaction.

Thesis Structure

In chapter 1 we will discuss the theoretical underpinning of the methods and theories that we use in the later chapters. This includes a general discussion of quantum mechanics focusing on the derivation of the Schrödinger equation (section 1.1) and the approximations typically used for solid state physics (sections 1.1.3 to 1.1.5). We then discuss the construction of Density Functional Theory (section 1.2) and how this is reformatted into a linear-scaling approach (section 1.3). After discussing the base theories underpinning the research in this work we discuss the underlying theories of how DFT is applied. We discuss ab-initio molecular dynamics in section 1.4, density functional tight-binding theory in section 1.5, and finally outline some machine learning methods we use in section 1.6.

Having established the theoretical background we summarise the primary chemistry and materials we intend to study in chapter 2. Specifically, we look at the specific internal elements of a Li-ion battery (section 2.1) and contrast them with a thorough literature investigation on solid state batteries with a focus on the electrolyte and the anode|electrolyte interface (section 2.2).

We then move to our first major research project in chapter 3. Here, we discuss the simulated intercalation of a graphite nanoparticle (section 3.3.3) using an electrostatically motivated methodology (section 3.3.4). In section 3.4 we find good replication of experimentally observed phenomena as well as the emergence of a new graphite chemistry in the form of graphite AB pinning (section 3.4.5).

The next major project presented in chapter 4 involves construction of a reasonable bulk crystal of cubic LLZO. In this study, we found that literature was unable to agree on what the ground state structure should look like (section 4.2) so we sought to do a thorough sampling of all 7.4×10^{34} structures. We were able to eliminate candidates through chemical intuition, high-throughput symmetry checking, and machine learned energetic ordering (section 4.4). Through applying this methodology we were able to reduce the number of structures down to five potential candidates for the crystallographically predicted structures.

The final research project undertaken in this work is presented in chapter 5. Here, we discuss the difficulties of finding accurate surface energies for Li and tetragonal LLZO (section 5.3) and how we overcome them. Then, we move on to how we could construct a realistic Li|t-LLZO interface (section 5.4) and get an estimate on how large a sample of configuration space we would realistically need to sample. Having found that this configuration space is too large to sample with DFT alone, we end with our efforts we made towards parameterising a LLZO Slater-Koster library for DFTB (section 5.5).

A summary of the findings of all projects we outline here as well as future steps we recommend to advance them can be found in chapter 6. Happy reading!

List of Publications

Papers and Reviews

Pushing the Boundaries of Lithium Battery Research with Atomistic Modelling on Different Scales

Lucy M Morgan, Michael P Mercer, Arijant Bhandari, Chao Peng, Mazharul M Islam, Hui Yang, Julian Holland, Samuel W Coles, Ryan Sharpe, Aron Walsh, Benjamin J Morgan, Denis Kramer, M Saiful Islam, Harry E Hostler, Jacqueline Sophie Edge, and Chris-Kriton Skylaris

Progress in Energy, 2022, Volume 4, Issue 1, Page 012002

10.1088/2516-1083/AC3894

Ab Initio Study of Lithium Intercalation into a Graphite Nanoparticle

Julian Holland, Arijant Bhandari, Denis Kramer, Felix Hanke, Victor Milman, Chris-Kriton Skylaris

Materials Advances, 2022, Volume 3, Issue 23, Pages 8469-8484

10.1039/D2MA00857B

A Workflow for Identifying Viable Crystal Structures with Partially Occupied Sites Applied to Solid Electrolyte: Cubic $\text{Li}_7\text{La}_3\text{Zr}_2\text{O}_{12}$

Julian Holland, Tom Demeyere, Arijant Bhandari, Felix Hanke, Victor Milman, Chris-Kriton Skylaris

The Journal of Physical Chemistry Letters, 2023, Pages 10257-10262

10.1021/ACS.JPCLETT.3C02064

Conference Contributions

(1) Holland, J.; Demeyere, T.; Bhandari, A.; Hanke, F.; Milman, V.; Skylaris, C.-K. A Workflow for Identifying Viable Crystal Structures with Partially Occupied Sites Applied to the Solid Electrolyte Cubic $\text{Li}_7\text{La}_3\text{Zr}_2\text{O}_{12}$. *J. Phys. Chem. Lett.* 2023, 10257–10262. <https://doi.org/10.1021/acs.jpclett.3c02064>.

Conference Talks

- Modelling LLZO: Limiting Structures in a Near-unlimited Configuration Space
 - STFC Early Career Researchers Conference (Abingdon UK, 2023)
 - EuChemS European Conference on Computational and Theoretical Chemistry (Thessaloniki Greece, 2023)
 - 74th Annual Meeting of the International Society of Electrochemistry (Lyon France, 2023)
- Building more realistic models of battery materials: Quantum mechanical simulations of an entire graphite nanoparticle and its lithium intercalation
 - Royce Student Summit (online, 2021)
 - The Faraday Institution Conference (online, 2021)
 - Multi-Scale Modelling Project Consortium (London UK, 2020)

Conference Posters

- 6th General Psi-K Conference (Lausanne Switzerland, 2022)
- 31st Topical Meeting of the International Society of Electrochemistry (Aachen Germany, 2022)
- ICTP Workshop on Electrochemical Energy Storage: Theory, Experiments, and Applications (online, 2022)
- RSC Twitter Conference (online, 2021)
- The BIOVIA Conference (online, 2021)
- The Faraday Institution Conference (online, 2021)
- Southampton PhD poster conference (Southampton UK 2019)

Chapter 1

Theoretical Background

1.1 Quantum Mechanics

1.1.1 The Schrödinger Equation

Computational chemistry is the study of chemical systems by using approximate solutions to the Schrödinger equation.[122] The time-dependent Schrödinger equation (equation 1.1) describes how a system's wavefunction will change over time. An intuitive and contextual derivation of this equation is highlighted in Atkins' *Molecular Quantum Mechanics: An Introduction to Quantum Chemistry*[15], but will not be provided in this thesis. The wavefunction is a description of the state of the system upon which operators can act to extract information about the system.[189] By taking the square modulus of the wavefunction we can find the probability of all particles (electrons and nuclei) in the system adopting a certain set of positions.

$$i\hbar \frac{\partial \Phi(\vec{r}, t)}{\partial t} = \hat{H}\Phi(\vec{r}, t), \quad (1.1)$$

The operator acting upon the wavefunction, Φ , on the right-hand side is the Hamiltonian operator, \hat{H} . It retrieves the energy from the wavefunction. The Hamiltonian can be split up in to potential, \hat{V} , and kinetic, \hat{T} , operators. The Hamiltonian for a hydrogen atom is written below

$$\hat{H} = \hat{T} + \hat{V} = -\frac{\hbar^2}{2\mu} \nabla^2 - \frac{e^2}{4\pi\epsilon_0 \vec{r}}, \quad (1.2)$$

$$\nabla^2 = \left(\frac{\partial^2}{\partial x^2} + \frac{\partial^2}{\partial y^2} + \frac{\partial^2}{\partial z^2} \right), \quad (1.3)$$

where \hat{V} is a purely attractive coulombic system and μ is the reduced mass.

1.1.2 The Time-independent Schrödinger Equation

By assuming that the wavefunction can be represented as a stationary state[163] and that potential is independent of time, we can factorise out positional and time-dependent components

$$\Phi(\vec{r}, t) = \psi(\vec{r})\theta(t), \quad (1.4)$$

substituting in equations 1.2 and 1.4 into equation 1.1 gives

$$\left(-\frac{\hbar^2}{2m\psi(\vec{r})} \nabla^2 \psi(\vec{r}) - \frac{e^2}{4\pi\epsilon_0 \vec{r}} \psi(\vec{r}) \right) - \frac{i\hbar}{\theta(t)} \frac{\partial \Phi(\vec{r}, t)}{\partial t} = 0, \quad (1.5)$$

the first and second terms in this equation are independent of time and position respectively

$$\left(-\frac{\hbar^2}{2m\psi(\vec{r})} \nabla^2 \psi(\vec{r}) - \frac{e^2}{4\pi\varepsilon_0 \vec{r}} \psi(\vec{r}) \right) = E\psi(\vec{r}), \quad (1.6)$$

$$\frac{i\hbar}{\theta(t)} \frac{\partial\Phi(\vec{r}, t)}{\partial t} = E\theta(t). \quad (1.7)$$

The time dependent part of this equation has a solution

$$\theta(t) = Ce^{\frac{-iEt}{\hbar}}, \quad (1.8)$$

which allows for equation 1.4 to be rewritten as

$$\Phi(\vec{r}, t) = C\psi(\vec{r})e^{\frac{-iEt}{\hbar}}, \quad (1.9)$$

C is a constant and can be absorbed into the wavefunction. E has energy units (J), t has time units (s), and the reduced Plank's constant has units of energy times time ($J.s$). This means that $e^{\frac{-iEt}{\hbar}}$ is dimensionless and that $\Phi(\vec{r}, t)\Phi^*(\vec{r}, t) = \psi(\vec{r})\psi^*(\vec{r})$ over all space. This allows us to write the time independent Schrödinger equation in the format it is best known for.

$$\hat{H}\Psi(\vec{r}) = E\Psi(\vec{r}). \quad (1.10)$$

For a system of M nuclei and N electrons, as well as assuming atomic units where $\hbar = m_e = e = \frac{4\pi}{\varepsilon_0} = 1$ we can write the Hamiltonian as

$$\hat{H} = -\frac{1}{2} \sum_{i=1}^N \nabla_i^2 - \frac{1}{2} \sum_{A=1}^M \frac{1}{M_A} \nabla_A^2 - \sum_{i=1}^N \sum_{A=1}^M \frac{Z_A}{\vec{r}_{iA}} + \sum_{i=1}^N \sum_{j>i}^N \frac{1}{\vec{r}_{ij}} + \sum_{A=1}^M \sum_{B>A}^M \frac{Z_A Z_B}{\vec{R}_{AB}}. \quad (1.11)$$

1.1.3 The Born-Oppenheimer Approximation

A further approximation is also typically applied when working with the Schrödinger equation. We assume the electronic and nucleic Schrödinger equations can be separated. Given that they both are dependent on the positions of the electrons and the nuclei respectively, and that the mass of electrons are several orders of magnitude smaller than that of the nuclei. We can therefore conclude the relative time-scales of their motion are equally disparate, this is a reasonable assumption to make in nearly all cases. This is known as the Born-Oppenheimer approximation. Most modern quantum chemical calculations are performed with this approximation with a few exceptions (see Ref. 65 and the references therein).

Applying this approximation allows us to remove the kinetic energy and potential energy of nuclei interaction present in equation 1.11. This gives the following form of the Hamiltonian operator known as the electronic Hamiltonian

$$\hat{H}_{\text{elec}} = -\frac{1}{2} \sum_{i=1}^N \nabla_i^2 - \sum_{i=1}^N \sum_{A=1}^M \frac{Z_A}{\vec{r}_{iA}} + \sum_{i=1}^N \sum_{j>i}^N \frac{1}{\vec{r}_{ij}}, \quad (1.12)$$

Retrieving energy values from equation 1.10 would involve using the Hamiltonian to find the rate of change of the wavefunction. We can then apply this change over a small time step $\Phi(r, t + \delta t)$ and repeat for as long as desired. This, however, is computationally intractable and not how the Schrödinger equation is used in nearly all quantum chemistry.

1.1.4 Bra and Ket notation

We will take a quick detour before defining the variational principle to define Bra and Ket notation. For this section we will use the definition provided by Szabo and Ostlund's *Modern quantum chemistry*[286].

A 3-dimensional vector can be defined as

$$\mathbf{a} = \mathbf{e}_1 a_1 + \mathbf{e}_2 a_2 + \mathbf{e}_3 a_3, \quad (1.13)$$

where a_i are the components of \mathbf{a} and \mathbf{e}_i are perpendicular unit vectors, also known as its basis.

Likewise, for an N -dimensional complex vector we can define its basis as $|i\rangle$ where $i = 1, 2, \dots, N$ known as ket vectors. By assuming this basis is complete we can write any ket vector as

$$|a\rangle = \sum_{i=1}^N |i\rangle a_i, \quad (1.14)$$

by taking the adjoint of a ket vector we find a bra vector, denoted as $\langle a|$. so if our ket vector can be written as

$$|a\rangle = \mathbf{a} = \begin{pmatrix} a_1 \\ a_2 \\ \vdots \\ a_N \end{pmatrix}, \quad (1.15)$$

then our equivalent bra vector is written as

$$\langle a| = \mathbf{a}^\dagger = (a_1^*, a_2^*, \dots, a_N^*), \quad (1.16)$$

Having defined both ket and bra vectors we can combine equation 1.15 with an arbitrary bra vector them to form a bracket. we can find the scalar product by taking the dot product of these vectors over N dimensions

$$\langle b|a\rangle = (b_1^*, b_2^*, \dots, b_N^*) \begin{pmatrix} a_1 \\ a_2 \\ \vdots \\ a_N \end{pmatrix} = \sum_i^N b_i^* a_i, \quad (1.17)$$

when $N = \infty$ we convert equation 1.17 to an integral of the form

$$\langle b|a\rangle = \int b^*(x) a(x) dx, \quad (1.18)$$

this is known as the inner product.

1.1.5 The Variational Principle

Even with the simplifications previously discussed in sections 1.1.2 and 1.1.3, any system with more than one electron proves impossible to solve analytically due to their correlated motion. However, numerical methods can be employed in order to get very close to the true wavefunction. These numerical methods utilise the variational principle, which states that the lower the total energy expectation value of your trial system, the closer you are to the true value (i.e. your trial wavefunctions will not produce a lower energy value).[286] We shall now consider the proof of this statement.

If equation 1.19 is true then so is equation 1.20

$$\langle \tilde{\psi}|\tilde{\psi}\rangle = 1, \quad (1.19)$$

$$\langle \tilde{\psi}|\hat{H}|\tilde{\psi}\rangle \geq E_0, \quad (1.20)$$

where $\tilde{\psi}$ is any trial wavefunction that can be represented as a linear combination of normalised and orthogonal actual eigenfunctions of the Hamiltonian, (ψ_α), with a corresponding expansion coefficient that describes the degree of overlap between the trial and actual solution.

$$|\tilde{\psi}\rangle = \sum_{\alpha} |\psi_{\alpha}\rangle c_{\alpha} = \sum_{\alpha} |\psi_{\alpha}\rangle \langle \psi_{\alpha}|\tilde{\psi}\rangle, \quad (1.21)$$

$$\langle \tilde{\psi}| = \sum_{\alpha} c_{\alpha}^* \langle \psi_{\alpha}| = \sum_{\alpha} \langle \psi_{\alpha}|\tilde{\psi}\rangle \langle \psi_{\alpha}|, \quad (1.22)$$

equation 1.19 can now be rewritten

$$\langle \tilde{\psi} | \tilde{\psi} \rangle = \sum_{\alpha\beta} \langle \tilde{\psi} | \psi_\alpha \rangle \langle \psi_\alpha | \psi_\beta \rangle \langle \psi_\beta | \tilde{\psi} \rangle, \quad (1.23)$$

given that

$$\langle \psi_\alpha | \psi_\beta \rangle = \delta_{\alpha\beta} \quad (1.24)$$

$$\delta_{\alpha\beta} = \begin{cases} 1, & \text{if } \alpha = \beta \\ 0, & \text{if } \alpha \neq \beta \end{cases}, \quad (1.25)$$

then equation 1.23 can be simplified

$$\sum_{\alpha\beta} \langle \tilde{\psi} | \psi_\alpha \rangle \langle \psi_\alpha | \psi_\beta \rangle \langle \psi_\beta | \tilde{\psi} \rangle = \sum_{\alpha\beta} \langle \tilde{\psi} | \psi_\alpha \rangle \delta_{\alpha\beta} \langle \psi_\beta | \tilde{\psi} \rangle = \sum_{\alpha} \langle \tilde{\psi} | \psi_\alpha \rangle \langle \psi_\alpha | \tilde{\psi} \rangle = \sum_{\alpha} |\langle \psi_\alpha | \tilde{\psi} \rangle|^2, \quad (1.26)$$

this allows us to rewrite equation 1.20 in the following form

$$\langle \tilde{\psi} | \hat{H} | \tilde{\psi} \rangle = \sum_{\alpha\beta} \langle \tilde{\psi} | \psi_\alpha \rangle \langle \psi_\alpha | \hat{H} | \psi_\beta \rangle \langle \psi_\beta | \tilde{\psi} \rangle = \sum_{\alpha} E_\alpha |\langle \psi_\alpha | \tilde{\psi} \rangle|^2, \quad (1.27)$$

Given that we know the ground state energy is the lowest energy possible ($E_\alpha \geq E_0$) a trial wavefunction, that is normalised, gives the following expression

$$\langle \tilde{\psi} | \hat{H} | \tilde{\psi} \rangle \geq \sum_{\alpha} E_0 |\langle \psi_\alpha | \tilde{\psi} \rangle|^2 = E_0 \sum_{\alpha} |\langle \psi_\alpha | \tilde{\psi} \rangle|^2 = E_0, \quad (1.28)$$

thereby showing that any trial wavefunction that is not the true ground state, will give a higher energy than the actual ground state energy.

1.1.6 Electron Correlation

One of the earliest and most influential of the methods that utilises the variational principle is Hartree-Fock theory (HF)[84, 120], which was dubbed the self-consistent field method by Hartree in 1928. To summarise this theory it works on the principle that the ground state wavefunction of a many-electron system can be represented by a normalized Slater determinant of one-electron wavefunctions[155]

$$\Psi_0 \approx \frac{1}{\sqrt{N!}} \begin{vmatrix} \chi_1(\vec{x}_1) & \chi_2(\vec{x}_1) & \dots & \chi_N(\vec{x}_1) \\ \chi_1(\vec{x}_2) & \chi_2(\vec{x}_2) & \dots & \chi_N(\vec{x}_2) \\ \vdots & \vdots & \ddots & \vdots \\ \chi_1(\vec{x}_N) & \chi_2(\vec{x}_N) & \dots & \chi_N(\vec{x}_N) \end{vmatrix}, \quad (1.29)$$

Where N is the number of electrons and $\chi_i(\vec{x}_i)$ are the one electron spin-orbitals. Which, as their name suggests contain both spatial and spin components.

$$\chi(\vec{x}) = \begin{cases} \psi(\vec{r})\alpha(\omega) \\ \text{or} \\ \psi(\vec{r})\beta(\omega) \end{cases}, \quad (1.30)$$

where $\alpha(\omega)$ is the up spin function acting on the spin and $\beta(\omega)$ is the down spin function acting on the spin. By applying the variational principle we can find the best Slater determinant and therefore the energy of our system. For further details about the mathematical machinery underpinning this theory please refer to Lin and Lu's *A mathematical introduction to electronic structure theory*[176]. It is important to understand that this method makes two primary assumptions

1. Electrons do not interact with each other and instead travel through a mean-field of electrostatic potential
2. The ground state wave function can be represented by a single Slater determinant

These two assumptions lead to the main source of error in Hartree-Fock theory. This error was coined as "electron correlation" by Löwdin and is given below.[181]

$$E_{\text{corr}} = E - E_{HF}, \quad (1.31)$$

where E is the exact energy and E_{HF} is the total Hartree-Fock energy. E_{corr} can be further divided based on the two assumptions with assumption 1 giving dynamic correlation as the mean field is insufficient to properly model electron interaction and allows electrons to get too close to one another and assumption 2 giving static correlation as some systems, such as the stretching of a H₂ dimer, are unable to be properly represented with a single Slater determinant.

Many post-Hartree-Fock methods like configuration-interaction (CI) and Möller-Plesset theory (MP) allow excitations of orbitals in order to account for the electron correlation. These methods, however, have huge computational costs even for relatively small systems.

1.2 Principles of Density Functional Theory

To avoid the use of costly methods a new theory was developed that uses the electron density instead of the many-electron wavefunction.

1.2.1 Hohenberg-Kohn Theorems

In 1964, Hohenberg and Kohn[129] sought to develop an exact theory of many body systems, i.e. a general system of interacting particles in an external potential, where the Hamiltonian can be written as

$$\hat{H} = -\frac{1}{2} \sum_i \nabla_i^2 + \sum_i V_{ext}(\vec{r}_i) + \frac{1}{2} \sum_{i \neq j} \frac{1}{|\vec{r}_i - \vec{r}_j|}, \quad (1.32)$$

where V_{ext} is the external potential. This led them to develop their theorems, which stated

- All the properties of a molecule in a ground electronic state are determined by the ground state electron density function
- Any trial electron density function will give an energy higher than the true ground state energy (c.f. section 1.1.5)

the proofs of these theorems are explained neatly in Martin's *Electronic Structure*[186] and from these, we can construct an equation that represents the total energy of the system[174]

$$E_{HK}[n] = T[n] + E_{int} + \int d^3\vec{r} V_{ext}(\vec{r}) n(\vec{r}) + E_{II}, \quad (1.33)$$

where $T[n]$ is the kinetic energy functional, E_{int} is the internal potential energy of the system, V_{ext} is the external potential and E_{II} is the interaction energy of the nuclei. This did not provide a way to calculate the ground state energy from electron density as $T[n]$ and parts of $E_{int}(n)$ are unknown. We can group all the internal kinetic and potential energy functionals into one functional which must be the same for all electron systems as they are only dependent on the electron density and independent of the external potential into a functional known as the Hohenberg-Kohn Functional (F_{HK})

$$E_{HK}[n] = F_{HK} + \int d^3\vec{r} V_{ext}(\vec{r}) n(\vec{r}) + E_{II}. \quad (1.34)$$

1.2.2 Kohn-Sham Theory

Kohn and Sham[157] later rephrased the problem laid out in equation 1.32 in terms of an independent particle equation. This meant that the density of the system could be written as the sum of densities that form a set of molecular orbitals[122].

$$n(\vec{r}) = \sum_i^{n_{elec}} |\psi_i(\vec{r})|^2, \quad (1.35)$$

These are known as Kohn-Sham (KS) orbitals. An auxiliary Hamiltonian also needs to be constructed. This uses the same kinetic operator but replaces the external potential with an effective local potential $V_{loc}^\sigma(\vec{r})$. The local potentials depend on the spin, σ , in order to give the correct spin density. We can express the new auxiliary Hamiltonian as below

$$\hat{H}_{aux}^\sigma = -\frac{1}{2} \sum_i^N \nabla^2 + \sum_\sigma \sum_i^{N^\sigma} V_{loc}^\sigma(\vec{r}), \quad (1.36)$$

as no components here contain electron-electron interaction we can write our orbitals as a Slater determinant (c.f. equation 1.29) where the solutions to each orbital can be found with the one-electron Kohn-Sham operator, \hat{f}^{KS}

$$\hat{f}^{KS} \psi_i = \varepsilon_i \psi_i, \quad (1.37)$$

where

$$\hat{f}^{KS} = -\frac{1}{2} \nabla^2 + V_{loc}^\sigma(\vec{r}), \quad (1.38)$$

By enforcing that the density of the real system is the same as that of the imagined one we have just created we provide a route to obtain equation 1.35.

the independent-particle kinetic energy T_s can be written as

$$T_s = -\frac{1}{2} \sum_{\sigma} \sum_{i=1}^{N^{\sigma}} \langle \psi_i^{\sigma} | \nabla^2 | \psi_i^{\sigma} \rangle, \quad (1.39)$$

where N^{σ} is the total electrons with a specific spin. The Coulomb energy of the electron density interacting with itself, also known as the Hartree self-interaction energy, can be written as

$$E_{Hartree}[n] = \frac{1}{2} \int d^3 \vec{r} d^3 \vec{r}' \frac{n(\vec{r}) n(\vec{r}')}{|\vec{r} - \vec{r}'|}, \quad (1.40)$$

these definitions allow us to rewrite equation 1.33 in terms of a Kohn-Sham approach to the full interacting many-body problem.

$$E_{KS} = T_s[n] + \int d\vec{r} V_{ext}(\vec{r}) n(\vec{r}) + E_{Hartree}[n] + E_{II} + E_{XC}, \quad (1.41)$$

Which after further derivation (please refer to Parr and Yang's *Density-functional theory of atoms and molecules*[214]) gives the KS equation with a grouped effective potential V_{eff}

$$\left(-\frac{1}{2} \nabla^2 + \left[\int \frac{n(\vec{r}')}{|\vec{r} - \vec{r}'|} d\vec{r}' + V_{XC}(\vec{r}') - \sum_A^M \frac{Z_A}{|\vec{r} - \vec{r}_A|} \right] \right) \psi_i = \varepsilon_i \psi_i, \quad (1.42)$$

$$V_{\text{eff}} \psi_i = \varepsilon_i \psi_i, \quad (1.43)$$

The equation is now of the form of equation 1.37 therefore allowing us to equate V_{eff} and V_{loc} . Where the potential due to exchange-correlation energy, V_{XC} , is the only unknown term.

$$V_{XC} = \frac{\delta E_{XC}}{\delta n}, \quad (1.44)$$

by grouping the internal potential and kinetic energies as we did in equation 1.34 and comparing this equation to that of equation 1.41, we can show that all exchange and correlation effects can be written as

$$E_{XC}[n] = F_{HK}[n] - (T_s[n] + E_{Hartree}[n]), \quad (1.45)$$

or alternatively

$$E_{XC}[n] = \langle \hat{T} \rangle - T_s[n] + \langle \hat{V}_{int} \rangle - E_{Hartree}[n], \quad (1.46)$$

i.e. the difference in kinetic and potential energies between the true interacting many-body system compared to the non-interacting many-body system. If the exchange-correlation functional were known then we could predict the exact ground state density as all other terms present can be calculated exactly. Finding a good approximation to E_{XC} is an active and ongoing area of research.

The central point of Kohn-Sham orbitals is that they give us a means to finding attainable solutions to the Hohenberg-Kohn Theorems. Practically this is done by constructing a non-interacting Slater determinant (c.f. equation 1.29) with a density the same as that of a real system and expressing them in terms of an effective potential where the vast majority of the energy contributors are known. The remaining contributors (E_{XC}) are what we will discuss next.

1.2.3 Exchange-Correlation Functionals

There have been many attempts to approximate E_{XC} in equation 1.46. The earliest approach, known as the local density approximation (LDA), assumes the exchange-correlation part of the energy can be calculated as if your system were made up of a uniform electron gas at a given point. This approximation is made because the exchange and correlation energies can be calculated exactly or to an arbitrary accuracy.[57, 312] The Exchange-correlation energy can be written simply as

$$E_{XC}^{\text{LDA}}(n(\vec{r})) = \int n(\vec{r})\varepsilon_{XC}(n(\vec{r})) d\vec{r}, \quad (1.47)$$

where ε_{XC} is the exchange-correlation per electron of a uniform electron gas. This method, while simple, has some deficiencies. Specifically, LDA is notorious for overbinding and too close atomic distances among other issues.[110]

This model can be improved by taking into account the gradient of the density at a given point.

$$E_{XC}^{\text{GGA}}(n(\vec{r})) = \int n(\vec{r})\varepsilon_{XC}(n(\vec{r}) |\nabla n(\vec{r})|) d\vec{r}, \quad (1.48)$$

This is known as the generalised gradient approximation (GGA). This is the primary approximation we will use in the work for this thesis. More specifically, we will be using the PBE (Perdew, Burke, and Ecker)[223] GGA functional unless otherwise stated.

1.2.4 Basis Sets

To use the systems we have just defined in a practical manner basis sets are employed. Methods that are similar to the linear combination of atomic orbitals (LCAO) are the simplest approach. Here we construct each of our orbitals ψ_i defined in equation 1.37 as a linear combination of L basis functions $\eta_q = \eta_q(\vec{r})$

$$\psi_i = \sum_{q=1}^L c_{iq}\eta_q \quad (1.49)$$

Expressing ψ_i exactly would require $L = \infty$ basis functions but in reality, a finite number is used. Inserting this into equation 1.37

$$\hat{f}^{KS} \sum_{q=1}^L c_{iq}\eta_q = \varepsilon_i \sum_{q=1}^L c_{iq}\eta_q, \quad (1.50)$$

Multiplying from the left with basis function $\eta_s = \eta_s(\vec{r})$ and integrating over space we generate

$$\sum_{q=1}^L c_{iq} \int \eta_s \hat{f}^{KS} \eta_q d\vec{r} = \sum_{q=1}^L c_{iq} \varepsilon_i \int \eta_s \eta_q d\vec{r}, \quad (1.51)$$

both integrals can be represented by a $L \times L$ hermitian matrix and are given the conventional names of the Khon-Sham matrix, \mathbf{F}^{KS} , and the overlap matrix, \mathbf{S} . The coefficients are written as a $L \times L$ matrix \mathbf{C} and the orbital energies are a $L \times L$ diagonal matrix $\boldsymbol{\varepsilon}$. Condensing equation 1.51

$$\mathbf{F}^{\text{KS}} \mathbf{C} = \mathbf{S} \mathbf{C} \boldsymbol{\varepsilon}, \quad (1.52)$$

It is common practice to split \mathbf{F}^{KS} into four matrices: h_{qs} containing all components that are dependent on a single electron coordinate, P_{qs} known as the density matrix, J_{qs} for the Coulomb contribution and V_{qs}^{XC} the exchange-correlation part.

For molecular systems, a popular choice of basis set are Gaussian-type-orbitals (GTOs) of the form

$$\eta^{\text{GTO}} = N x^l y^m z^n e^{-\alpha r^2}, \quad (1.53)$$

where N is a normalization factor, $L = l + m + n$, and corresponds to the angular momentum of the chosen function.

Slater-type-orbitals (STOs) are a more natural choice for the basis as they exhibit a number of desirable properties that GTOs do not. However, they are hard to compute efficiently and GTOs' shortcomings can be made up for by performing a linear combination of GTOs to give a contracted Gaussian function (CGF)

$$\eta_t^{\text{CGF}} = \sum_a^A d_{at} \eta_a^{\text{GTO}}, \quad (1.54)$$

These basis' have been the most popular choice of function for an LCAO-based code[86]. For further discussion on different types and extensions of LCAO-based basis sets please consult Koch and Holthausen's *A chemist's guide to density functional theory*[155]. Another popular basis set uses plane waves and is used by codes such as CASTEP[62] and VASP[158]. These basis' are more suited to solid state systems that have periodic lattices (c.f. Martin's *Electronic Structure*[186] for more details).

1.2.5 Pseudopotentials

Practically, even with basis sets implemented, simulating systems, particularly modern battery solid electrolyte systems discussed in section 2.2.2, is computationally prohibitive. To alleviate a good proportion of the work required, the core states can be approximated to be general as they remain relatively unchanged in different chemical environments. This is because the core states are bound close to the atomic centre and are, for the most part, shielded by the valence states. A consequence of the close-bound core states and that all electronic states are eigenstates of the Hamiltonian and are by definition orthogonal, is that there is a large variation of valence states close to the nucleus. The large variation requires a large number of basis functions to properly model and therefore increased computational cost. To mitigate this strong Coulomb potential, a potential is used to screen most of the nuclear attraction with a repulsive term localised on the nucleus. This term is known as a pseudopotential and mimics the effects of core electrons. If the highly oscillating valence states are replaced by smoother pseudo-states then the number of basis functions required will be reduced and therefore the computational effort will also be reduced.[228]

Phillips and Kleinman [227] showed that wavefunction of a valence state ψ_v can be split into non-orthogonal components of a smooth, easy to compute, valence pseudo-state $\tilde{\psi}_v$ and a linear combination of core states ψ_c .

$$|\psi_v\rangle = |\tilde{\psi}_v\rangle + \sum_c \alpha_c |\psi_c\rangle, \quad (1.55)$$

where α_c are coefficient. The core and valence states are orthogonal

$$\langle \psi_c | \psi_v \rangle = 0, \quad (1.56)$$

meaning that the coefficients can be written as

$$\begin{aligned} \langle \psi_c | \tilde{\psi}_v \rangle + \alpha_c &= 0, \\ \alpha_c &= -\langle \psi_c | \tilde{\psi}_v \rangle, \end{aligned} \quad (1.57)$$

placing this into equation 1.55

$$|\psi_v\rangle = |\tilde{\psi}_v\rangle - \sum_c |\psi_c\rangle \langle \psi_c | \tilde{\psi}_v \rangle, \quad (1.58)$$

rewriting this for $|\tilde{\psi}_v\rangle$

$$|\tilde{\psi}_v\rangle = |\psi_v\rangle + \sum_c |\psi_c\rangle \langle \psi_c | \tilde{\psi}_v \rangle, \quad (1.59)$$

and then applying the Hamiltonian to such a system gives

$$\hat{H} |\tilde{\psi}_v\rangle = \varepsilon_v |\psi_v\rangle + \sum_c \varepsilon_c |\psi_c\rangle \langle\psi_c|\tilde{\psi}_v\rangle, \quad (1.60)$$

where ε_v and ε_c are the energies for individual valence and core states respectively. Finally, we can define a Hamiltonian for our pseudopotential

$$\hat{H}_{\text{PS}} = \hat{H} + \sum_c (\varepsilon_v - \varepsilon_c) |\psi_c\rangle \langle\psi_c|, \quad (1.61)$$

where our pseudopotential V_{PS} of our pseudo-state is given by the true potential V plus an energy-dependent, atom-centered, repulsive term that cancels out a significant part of the Coulombic nuclear interaction[200]

$$V_{\text{PS}} = V + \sum_c (\varepsilon_v - \varepsilon_c) |\psi_c\rangle \langle\psi_c|. \quad (1.62)$$

This is the simplest pseudopotential to construct. However, it has little applicability in modern DFT. Throughout this work we use norm-conserving[156, 186, 200, 228], ultra-soft[156, 186], and plane augmented wave pseudopotentials.[186] Derivations for each of these are unnecessary in this work but can be further explored in Martin's *Electronic Structure*[186]

1.3 Linear-Scaling Density Functional Theory

DFT has proven to be the method of choice for several decades when calculating properties of chemical systems over a handful of atoms.[146] Despite its success, several issues with theory have emerged and have in turn forced innovation in their respective areas. One of the most pressing is the $\mathcal{O}(N^3)$ scaling with increasing system size. This puts an effective limit on the size of system you can model. KS-DFT scales cubically due to the need to orthogonalize molecular orbitals and diagonalize the Hamiltonian.

Linear-scaling DFT programs allow for $\mathcal{O}(N)$ scaling above a certain threshold of system size. This is conventionally achieved by exploiting the “*near-sightedness of electronic matter*” formulated by Walter Kohn[45, 231]. While many linear algebra operations, such as matrix multiplication, are not linear scaling, if the matrix can be made sparse enough, enough off-diagonal elements are zero, then these operations can be made scale linearly provided that the number of non-zero elements increases at the same rate as the matrix size. To achieve sparse matrices electronic interactions we expect to be small in their contribution can be set to zero. Returning to Kohn’s “*electronic near-sightedness*” it is safe to assume that interactions at a sufficiently large distance will be minimal and that they can be set to zero, thus achieving $\mathcal{O}(N)$ scaling. This general concept has been implemented in several codes[12, 99, 100], here we address how it is implemented in the *Order-N Electronic Total Energy Package* (ONETEP).[230]

1.3.1 ONETEP Underlying Principles

Rewriting equation 1.35 to include occupancies of the KS orbitals, (f_i), gives

$$\rho(\vec{r}, \vec{r}') = \sum_i f_i \psi_i(\vec{r}) \psi_i^*(\vec{r}'), \quad (1.63)$$

implementing Kohn’s “near-sightedness” truncation of the density matrix’s exponentially decreasing tail with increasing distance is trivial for the left-hand side of equation 1.63. However, it is not as obvious for the right-hand side. Specifically, we need to rewrite the molecular orbitals in order for them to be truncatable. This implementation means that we no longer need to work with pure KS orbitals and may instead use non-orthogonal, localised orbitals. The linear transformation ($M_{i\alpha}$) to get from KS to the new local orbitals (ϕ_α) is shown below

$$\phi_\alpha(\vec{r}) = \sum_i \psi_i(\vec{r}) M_{i\alpha} \text{ and } \psi_i(\vec{r}) = \phi_\alpha(\vec{r}) M_i^\alpha, \quad (1.64)$$

from now on we shall use Greek letters for non-orthogonal components and Latin indices for orthogonal components. We shall also use the Einstein implicit summation convention for repeated Greek indices.

The overlap matrix elements corresponding to the non-orthogonal local functionals are defined as

$$S_{\alpha\beta} = \langle \phi_\alpha | \phi_\beta \rangle = \int d\vec{r} \phi_\alpha^*(\vec{r}) \phi_\beta(\vec{r}), \quad (1.65)$$

or in terms of the linear transformation

$$M_i^\alpha = S^{\alpha\beta} \langle \phi_\beta | \psi_i \rangle, \quad (1.66)$$

Looking at the relationships in equation 1.64 we can change the representation of the Hamiltonian with only diagonal elements, to one of non-diagonal elements. This allows the rewriting of the typical Kohn-Sham equation below

$$\hat{H} |\psi_i\rangle = \epsilon_i |\psi_i\rangle, \quad (1.67)$$

to that of the form

$$H_{\alpha\beta} M_i^\beta = S_{\alpha\beta} M_i^\beta \epsilon_i, \quad (1.68)$$

where the Hamiltonian is defined as

$$H_{\alpha\beta} = \langle \phi_\alpha | \hat{H} | \phi_\beta \rangle = S_{\alpha\gamma} \sum_i^{N_b} [M^\gamma_i \epsilon_i M_i^{\dagger\delta}] S_{\delta\beta}, \quad (1.69)$$

for a set of N_b eigenvalue problems which are defined entirely if the Hamiltonian and the non-orthogonal localised orbitals are known. Where ϵ_i are the eigenvalues corresponding to energy.

A density matrix can also be constructed, known as the density kernel, from the KS occupation function

$$K^{\alpha\beta} = \sum_i M^\alpha_i f_i M_i^{\dagger\beta}, \quad (1.70)$$

by combining equation 1.64 and 1.70 we can rewrite equation 1.63 for the new localised orbitals.

$$\rho(\vec{r}, \vec{r}') = \phi_\alpha(\vec{r}) K^{\alpha\beta} \phi_\beta^*(\vec{r}'), \quad (1.71)$$

By optimising both the localised orbitals and the density kernel, near-complete basis set accuracy can be achieved, while retaining small localised matrix sizes of a minimal atomic orbital basis. The KS energy (as defined in equation 1.41) can now be written as

$$E[\phi_\alpha, K] = K^{\alpha\beta} \left[\langle \phi_\beta | -\frac{1}{2} \nabla^2 | \phi_\alpha \rangle + \langle \phi_\beta | \hat{V}_{loc} | \phi_\alpha \rangle + \langle \phi_\beta | \hat{V}_{nl} | \phi_\alpha \rangle \right] + E_{XC}[n], \quad (1.72)$$

1.3.2 Psinc Basis Set

Unlike the basis sets described in section 1.2.4 the orbitals used in ONETEP are non-orthogonal generalised Wannier functions (NGWFs) and are expanded with a set of periodic sinc (psinc) basis functions shown in figure 1.1. The NGWFs are atom-centered and can be modified to include as many orbitals as required (depending on the valence electrons pseudopotential selected, c.f. section 1.2.5) The sparsity requirement is enforced by ensuring that the density matrix is zero when the centres of these NGWFs are sufficiently far away

$$K^{\alpha\beta} = 0 \text{ when } |\mathbf{R}_\alpha - \mathbf{R}_\beta| > r_{cut}, \quad (1.73)$$

where \mathbf{R} are the centres of the NGWFs (atomic positions) and r_{cut} is an arbitrary distance defined by the user.

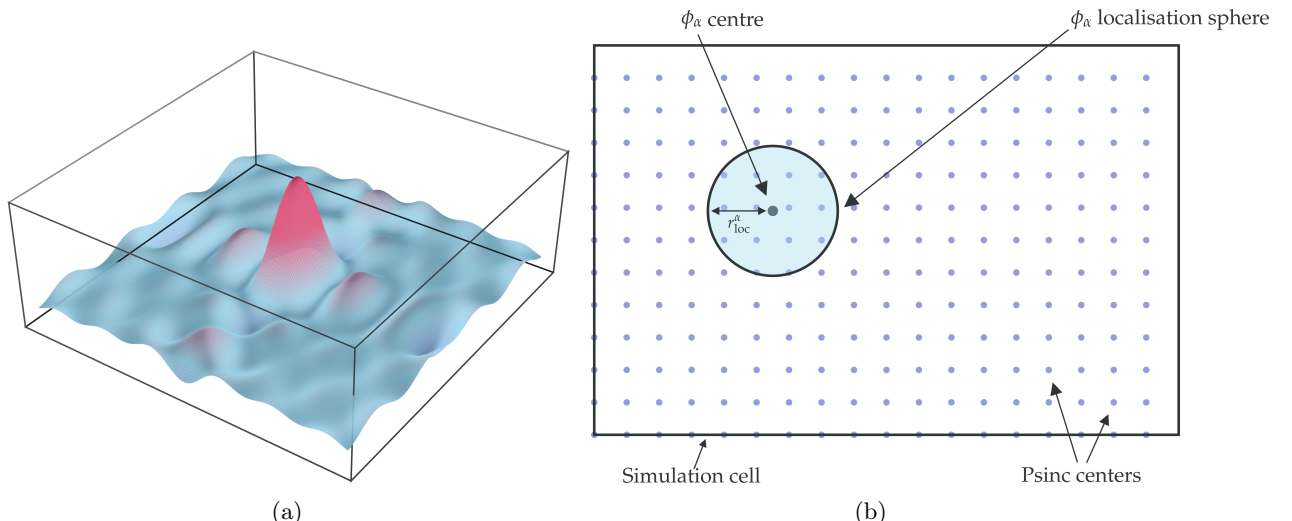


Figure 1.1: (a) Graphical representation of a psinc function in 3-dimensional space. (b) Imposed localisation of NGWFs using a regular grid of psinc functions where r_{loc}^α is the NGWF cutoff radii. Both figures are provided by Davide Sarpa with his permission for use in this work.

$$\phi_\alpha(\vec{r}) = \sum_k D_k(\vec{r}) C_{k,\alpha}, \quad (1.74)$$

where k is the index that defines the grid point in the simulation cell and $C_{k,\alpha}$ is the expansion coefficient.

1.3.3 Non-gapped Systems in ONETEP

Systems that do not have a well-defined band-gap, like metals, are notoriously difficult to converge using conventional Kohn-Sham DFT. This is because the effective degeneracy of states in the continuum makes it exceedingly hard to assign integer occupancy according to the *aufbau* principle.[158]

One approach to dealing with this is by using a finite temperature grand canonical ensemble as proposed by Mermin[195]. In a grand canonical ensemble, each system is said to be placed in a container with heat-conducting and permeable (with respect to molecules) walls.[190] This type of ensemble has non-zero probabilities for different particle numbers. A definition for the density operator for such an ensemble is given below

$$\hat{\rho} = \sum_N \sum_i f_{Ni} |\psi_{Ni}\rangle \langle \psi_{Ni}|, \quad (1.75)$$

The grand potential can then be written as

$$\Omega[\hat{\Gamma}] = Tr \hat{\rho} \left[\frac{1}{\beta} \ln \hat{\rho} + \hat{H} - \mu \hat{N} \right] = \sum_N \sum_i f_{Ni} \left[\frac{1}{\beta} \ln f_{Ni} + \langle \psi_{Ni} | \hat{H} | \psi_{Ni} \rangle - \mu N \right], \quad (1.76)$$

where p_{Ni} represents the probability of the system having a certain number of particles. N is the average number of particles and μ is the chemical potential. The variational principle outlined in equations 1.19 to 1.28 applies to the grand canonical ensemble and is outlined in Refs. 195 and 214.

We can then construct a density functional theory

$$\Omega^0 = \Omega[\hat{\rho}] = \min_{\rho} Tr \left[\hat{\rho} \left[\frac{1}{\beta} \ln \hat{\rho} + \hat{H} - \mu \hat{N} \right] \right] = \min_n \left[\min_{\rho \rightarrow n} Tr \left[\hat{\rho} \left[\hat{T} + \hat{V} + \frac{1}{\beta} \ln \hat{\rho} \right] \right] + \int [V_{ext}(\vec{r}) \mu] n(\vec{r}) d\vec{r} \right], \quad (1.77)$$

where \hat{T} is the kinetic operator and \hat{V} is the potential operator. We can then define the universal functional of density.

$$F[n(\vec{r})] = \min_{\rho \rightarrow n} Tr \left[\hat{\rho} \left[\hat{T} + \hat{V} + \frac{1}{\beta} \ln \hat{\rho} \right] \right], \quad (1.78)$$

making the grand potential functional

$$\Omega[\hat{n}(\vec{r})] = F[n(\vec{r})] + \int [V_{ext}(\vec{r}) - \mu] n(\vec{r}) d\vec{r}, \quad (1.79)$$

where we can split $F[n(\vec{r})]$ into its components.

$$F[n(\vec{r})] = T[n(\vec{r})] + V[n(\vec{r})] - \theta \mathcal{S}[n(\vec{r})], \quad (1.80)$$

where θ is the temperature. We have therefore shown how to construct a density functional theory for a finite-temperature grand canonical ensemble. This extension to Hohenberg-Kohn DFT can be brought forward into Kohn-Sham DFT.[143] From henceforth it is unnecessary to use the grand canonical ensemble and we shall stick to just the canonical ensemble as the number of particles in our calculations will remain constant. Using our definition of density in equation 1.63, we further define our occupation function in terms of Fermi-Dirac statistics as

$$f_i(\epsilon_i) = \left(1 + \exp\left[\frac{\epsilon_i - \mu}{k_B T}\right]\right)^{-1}, \quad (1.81)$$

where T is the finite electronic temperature, μ is the Fermi level and k_B is the Boltzmann constant. The entropy of the distribution is entirely dependent on the occupation function f_i

$$\mathcal{S}(f_i) = -k_B \sum_i [f_i \ln f_i + [1 - f_i] \ln [1 - f_i]], \quad (1.82)$$

as we are including entropy in the total energy we should use the Helmholtz free energy defined below

$$A[T; \epsilon_i, |\psi_i\rangle] = \sum_i f_i \langle \psi_i | \hat{T} + \hat{V}_{ext} | \psi_i \rangle + E_{Hartree}[n] + E_{XC}[n] - T\mathcal{S}[f_i], \quad (1.83)$$

for a non-orthogonal basis set like the one used in ONETEP, Ruiz-Serrano and Skylaris demonstrated how it could be implemented.[251] They showed equation 1.83 could be rewritten in terms of NGWFs and the elements of the Hamiltonian.

$$A[T; \hat{H}_{\alpha\beta}, |\phi_\alpha\rangle] = K^{\alpha\beta} \langle \phi_\beta | \hat{T} + \hat{V}_{ext} | \phi_\alpha \rangle + E_{Hartree}[n] + E_{XC}[n] - T\mathcal{S}[f_i], \quad (1.84)$$

The Hamiltonian is in the form defined in equation 1.69. The Helmholtz free energy is then minimized using an ensemble-DFT method (EDFT) developed by Marzari et al.[187] This method involves the natural splitting of the minimisation of the Helmholtz free energy into an inner and outer loop.

Marzari et al. achieve this by exploiting the Helmholtz free energy functional's covariance under a change of representation. They can then define a new functional that is dependent only on the orbitals and not on the occupation function.

Freysoldt et al.[87] used the Hamiltonian instead of the occupation function. This is used in ONETEP because this allows for the occupancies to be determined by the energy levels and not vice versa (i.e. the *aufbau* principle holds). It also allows for easier linear-scaling as only the Hamiltonian will need to be diagonalized at each step.[250] The eigenspectra is not compressed between a range of values, meaning degenerate states will not appear in many subgroups that are orthonormal to each other. Reorthonormalizing these small groups is not very computationally expensive.

Other methods require the diagonalizing of the density kernel for which the eigenvalues are compressed between the values 0 and 1. This means degeneracy is more frequent and in larger groups. The computational effort required to reorthonormalize these large groups is significant enough to make many calculations impossible, due to memory requirements from the diagonalizer.

$$A'[T; |\phi_\alpha\rangle] = \min_{\hat{H}_{\alpha\beta}} A[T, \hat{H}_{\alpha\beta}, |\phi_\alpha\rangle], \quad (1.85)$$

The inner loop seeks to minimise the Hamiltonian without changing orbitals. A cycle of the inner loop is given below.

First, the Hamiltonian of iteration m is diagonalized.

$$H_{\alpha\beta}^{(m)} M_i^{\beta(m)} = S_{\alpha\beta} M_i^{\beta(m)} \epsilon_i^{(m)}, \quad (1.86)$$

The occupancies are found using equation 1.81 and the entropy is found using equation 1.82. A new density kernel can be built using equation 1.70 and the density can then be updated using equation 1.71. The density-dependent parts of the Hamiltonian can then be calculated and used to create a new Hamiltonian.

$$\tilde{H}_{\alpha\beta}^{(m)} = \langle \phi_\alpha | \hat{T} + \hat{V}_{ext} + \hat{V}_{Hartree}[n]^{(m)} + \hat{V}_{XC}[n]^{(m)} | \phi_\beta \rangle, \quad (1.87)$$

this allows for the definition of the search direction

$$\Delta_{\alpha\beta}^{(m)} = \tilde{H}_{\alpha\beta}^{(m)} - H_{\alpha\beta}^{(m)}, \quad (1.88)$$

and the creation of the next iteration of the Hamiltonian.

$$H_{\alpha\beta}^{(m+1)} = H_{\alpha\beta}^{(m)} + \lambda \Delta_{\alpha\beta}^{(m)}, \quad (1.89)$$

where λ is an optimised damping function. The search direction is reminiscent of those presented by Marzari et al.[187] and Freysoldt et al.[87]

The outer loop works by keeping a fixed Hamiltonian and minimising for the orbitals. A cycle of the outer loop is described below.

The first step is to take the derivative of the newly defined partitioned Helmholtz free energy functional of iteration l . We shall define this derivative as $\Gamma^{\beta(l)}$

$$\frac{\delta A'^{(l)}}{\delta \langle \phi_\beta^{(l)} |} = |\Gamma^{\beta(l)}\rangle = \hat{H}^{(l)} |\phi_\gamma^{(l)}\rangle K^{\gamma\beta}. \quad (1.90)$$

By employing a technique discovered by Gan et al.[91] we can project out $|\tilde{\Gamma}^{\beta(l)}\rangle$'s components that are parallel to $|\phi_\gamma^{(l)}\rangle$ giving

$$|\tilde{\Gamma}^{\beta(l)}\rangle = \hat{H}^{(l)} |\phi_\gamma^{(l)}\rangle K^{\gamma\beta} - |\phi_\gamma^{(l)}\rangle S^{\gamma\delta(l)} \hat{H}_{\delta\nu}^{(l)} K^{\nu\delta}, \quad (1.91)$$

we do this in order to obtain a gradient with no overlap with $\langle \phi_\beta^{(l)} |$

To ensure the covariance of the NGWFs is accounted for, as it is currently contravariant, we right-multiply the previous equation with $S_{\alpha\beta}$.

$$|\tilde{\Gamma}_\alpha^{(l)}\rangle = \hat{H}^{(l)} |\phi_\gamma^{(l)}\rangle K^{\gamma\beta} S_{\beta\alpha}^{(l)} - |\phi_\gamma^{(l)}\rangle S^{\gamma\delta(l)} \hat{H}_{\delta\nu}^{(l)} K^{\nu\delta} S_{\delta\alpha}, \quad (1.92)$$

Kinetic energy[201] and occupancy[187] preconditioning can then be applied in order to find the steepest descent search direction efficiently.

Occupancy preconditioning works by replacing the density kernel with the inverse overlap. This is the equivalent of setting all occupancies to one. Proof of this is demonstrated below.

We start by expanding equation 1.70 with equation 1.66

$$K^{\alpha\beta} = \sum_i S^{\alpha\gamma} \langle \phi_\gamma | \psi_i \rangle f_i \langle \psi_i | \phi_\zeta \rangle S^{\zeta\beta}, \quad (1.93)$$

Setting all occupancies to 1, we update the density kernel, $K^{\alpha\beta}$, to an appropriate representation of a completely occupied system, $X^{\alpha\beta}$

$$X^{\alpha\beta} = S^{\alpha\gamma} \langle \phi_\gamma | \left(\sum_{i=1} |\psi_i\rangle \langle \psi_i| \right) |\phi_\zeta\rangle S^{\zeta\beta}, \quad (1.94)$$

The molecular orbitals are in a projection operator and will become a unit matrix. The NGWFs can be simplified to an overlap matrix using equation 1.65

$$X^{\alpha\beta} = S^{\alpha\gamma} S_{\gamma\zeta} S^{\zeta\beta} = S^{\alpha\beta}, \quad (1.95)$$

Thus, proving that replacing the density kernel with an inverse overlap matrix is the equivalent of setting all occupancies to 1. This means we can optimise our search direction faster as we converge to all states at the same rate. As opposed to fully occupied states converging faster than partially occupied ones, also known as occupancy ill-conditioning.

This allows us to write the steepest descent direction as

$$|\tilde{\Delta}_\alpha^{(l)}\rangle = \hat{H}^{(l)} |\phi_\gamma^{(l)}\rangle S^{\gamma\beta} S_{\beta\alpha}^{(l)} - |\phi_\gamma^{(l)}\rangle S^{\gamma\delta} \hat{H}_{\delta\alpha}^{(l)} = \hat{H}^{(l)} |\phi_\alpha^{(l)}\rangle - |\phi_\beta^{(l)}\rangle S^{\gamma\delta} \hat{H}_{\delta\alpha}^{(l)}, \quad (1.96)$$

We then need to account for the kinetic energy ill-conditioning with preconditioning. For a standard plane wave vector being acted upon by the kinetic operator, the following is given

$$\hat{T}e^{igx} = g^2 e^{igx}, \quad (1.97)$$

where g is the plane wave frequency. It is evident from this equation that a high frequency will yield a very large g^2 and a low frequency, a very small g^2 . This is an issue for minimisation as it means the large g^2 terms will be minimised with a much higher priority than that of the small ones. In order to have all plane waves converge at the same rate and thereby have the most efficient iterative steps to convergence, we apply a preconditioning operator[215]

$$\hat{P} = \frac{g^2}{\gamma^2} \xrightarrow[g \rightarrow \infty]{} 1. \quad (1.98)$$

The exact details of how this operator is constructed can be found in Ref. 200. Applying both of these preconditions gives the following steepest search direction

$$|\tilde{\Delta}_\alpha\rangle = -\hat{P}[\hat{H}^{(l)} |\phi_\alpha^{(l)}\rangle - |\phi_\beta^{(l)}\rangle S^{\beta\gamma} H_{\gamma\alpha}], \quad (1.99)$$

the negative sign is a consequence of the “downhill” update of the steepest descent method. Using the psinc representation we can define a spherically localised steepest descent search vector as

$$\tilde{\Delta}_\alpha^{(l)}(\vec{r}) = \sum_{k=1}^{N_k} D_k(\vec{r}) \tilde{d}_{k\alpha}^{(l)}, \quad (1.100)$$

$\tilde{d}_{k\alpha}^{(l)}$ are expansion coefficients. All elements outside the localisation sphere are set to zero.

$$d_{k\alpha}^{(l)} = \begin{cases} \tilde{d}_{k\alpha}^{(l)}, & \text{if } |\vec{r}_\alpha - \vec{r}_k| < r_{loc}, \\ 0, & \text{if } |\vec{r}_\alpha - \vec{r}_k| \geq r_{loc}, \end{cases}, \quad (1.101)$$

\vec{r}_α is the position vector of the nucleus where the NGWFs are centered and \vec{r}_k is the position vector of the specific psinc point. The resulting vectors are the steepest search directions.

$$\Delta_\alpha^{(l)}(\vec{r}) = \sum_{k=1}^{N_k} D_k(\vec{r}) d_{k\alpha}^{(l)}, \quad (1.102)$$

Conjugate gradients $|\chi_\alpha^{(l)}\rangle$ can be found by conjugating our steepest descent search direction $|\Delta_\alpha^{(l)}\rangle$ with $|\chi_\alpha^{(l-1)}\rangle$.

$$|\chi_\alpha^{(l)}\rangle = |\Delta_\alpha^{(l)}\rangle + \frac{\langle \tilde{\Gamma}^{\alpha(l)} | \tilde{\Delta}_\beta^{(l)} \rangle}{\langle \tilde{\Gamma}^{\gamma(l-1)} | \chi_\gamma^{(l-1)} \rangle} |\chi_\alpha^{(l-1)}\rangle, \quad (1.103)$$

By monitoring the slope along the search direction $\langle \tilde{\Gamma}^{\alpha(l)} | \chi_\alpha^{(l)} \rangle$ the convergence performance can be found as this term will be 0 at self-consistency. If self-consistency is not achieved then the NGWFs are iterated as below.

$$|\phi_\alpha^{(l+1)}\rangle = |\phi_\alpha^{(l)}\rangle + \eta |\chi_\alpha^{(l)}\rangle, \quad (1.104)$$

Where η is the optimal step length. This is found using a second order polynomial fitting of $A'[T; |\phi_\alpha\rangle]$ along search direction $|\chi_\alpha^{(l)}\rangle$. Each iteration updates the overlap and inverse overlap matrices. From this we can rebuild the linear transformation M_i^α as

$$\tilde{M}_i^\alpha = S^{\alpha\beta(l+1)} \langle \phi_\beta^{(l+1)} | \phi_\gamma^{(l)} \rangle M_i^\gamma, \quad (1.105)$$

The density kernel is then

$$\tilde{K}^{\alpha\beta} = \sum_i^{N_b} \tilde{M}_i^\alpha f_i \tilde{M}_i^{\dagger\alpha}, \quad (1.106)$$

and we can update the electron density as

$$n^{l+1}(\vec{r}) = \phi_\alpha^{(l+1)}(\vec{r}) \tilde{K}^{\alpha\beta} \phi_\beta^{*(l+1)}(\vec{r}), \quad (1.107)$$

This then feeds into the density-dependent components of the Hamiltonian. The process then restarts at the inner loop and is repeated until self-consistency is achieved across both loops.

1.4 Molecular Dynamics

Molecular dynamics (MD) is an approach that probes the dynamic evolution of a system over time. MD simulations rely on the calculation of a well-defined potential energy surface (PES), describing the interactions between atoms, to accurately predict system evolution. In *ab initio* MD (AIMD), this is described by solving the Schrödinger equation.

AIMD is able to capture events that potentials-based MD cannot, including bond breaking, and bond formation. AIMD assumes that the dynamics of particles can be treated classically and that the equation of motion for all nuclei can be written as:

$$M_I \ddot{\mathbf{R}}_I = -\nabla_I [\varepsilon_0(\vec{r}) + V_{NN}(\mathbf{R})], \quad (1.108)$$

where M_I is the mass of a given nucleus, \vec{r} denotes all nuclear coordinates, ∇_I is the Laplacian operator of a given nucleus, $\varepsilon_0(\vec{r})$ represents the ground state energy of the system at that given nuclear configuration, and $V_{NN}(\vec{r})$ represents the nuclear-nuclear coulomb repulsion at that given nuclear configuration.

Most modern techniques use KS-DFT (c.f. section 1.2) to solve the Schrödinger equation which finds the ground state energy. AIMD can be broadly split up into two main categories: Born-Oppenheimer dynamics and Car-Parrinello extended Lagrangean. The Born-Oppenheimer dynamics method uses a symplectic integrator to numerically integrate the equation of motion in equation 1.108 for each time step. The Car-Perrinello extended Lagrangean method gives the Kohn-Sham orbitals an artificial time-dependence. To attain a minimum energy with each new \vec{r} , the orbital dynamics are kept at a temperature much lower than that of the nuclei, but still high enough for the orbitals to quickly relax as the equation of motion proceeds. The new orbitals and their dynamics can then be defined by the Lagrangean equation:[54]

$$L = \mu \sum_i f_i \int d\vec{r} |\psi_i(\vec{r}, t)|^2 + \frac{1}{2} \sum_{I=1}^N M_I \dot{\vec{r}}_I^2(t) - E [\psi(t), \vec{r}(t)] + \sum_{i,j} \Lambda_{ij} \left[\int d\vec{r} \psi_i^*(\vec{r}, t) \psi_j(\vec{r}, t) - \delta_{ij} \right], \quad (1.109)$$

where μ is an artificial kinetic energy term (discussed further in Refs. 302 and 109), $\psi_x(\vec{r}, t)$ are the time-dependent Kohn-Sham orbitals, and Λ_{ij} contains a set of Lagrange multipliers to implement the orthonormality constraint on the orbitals.

1.5 Density Fuctional Tight-Binding Theory

Density functional tight-binding is based on a second-order expansion of equation 1.41.[77] This is a desirable approximation to make as it can speed up calculations by several orders of magnitude. By substituting the charge density with a superposition of a reference density n_0 with a small change δn we can rewrite equation 1.41 as

$$\begin{aligned} E = & \sum_i \langle \psi_i | -\frac{1}{2} \nabla + V_{\text{ext}} + \int \frac{n_0(\vec{r}')}{|\vec{r} - \vec{r}'|} d\vec{r}' + V_{\text{XC}}[n_0] |\psi_i\rangle \\ & - \frac{1}{2} \int \int \frac{n_0(\vec{r}')(n_0(\vec{r}) + \delta n(\vec{r}))}{|\vec{r} - \vec{r}'|} d\vec{r}' d\vec{r} \\ & - \int V_{\text{XC}}[n_0(\vec{r})](n_0(\vec{r}) + \delta n(\vec{r})) d\vec{r} \\ & + \frac{1}{2} \int \int \frac{\delta n(\vec{r}')(n_0(\vec{r}) + \delta n(\vec{r}))}{|\vec{r} - \vec{r}'|} d\vec{r}' d\vec{r} \\ & + E_{\text{XC}}[n_0 \vec{r} + \delta n \vec{r}] + E_{II}, \end{aligned} \quad (1.110)$$

where E is the energy for all occupied Kohn-Sham orbitals, the second term accounts for any double counting, the third term is the new exchange-correlation contribution, and the fourth term arises due to the division of the energy into parts related to n_0 and δn .

By expanding E_{XC} at the reference density we get

$$\begin{aligned} E = & \sum_i \langle \psi_i | \hat{H}_0 | \psi_i \rangle \\ & + \frac{1}{2} \int \int \frac{n_0(\vec{r}') n_0(\vec{r})}{|\vec{r} - \vec{r}'|} d\vec{r}' d\vec{r} + E_{\text{XC}}[n_0(\vec{r})] \\ & - \int V_{\text{XC}}[n_0(\vec{r})] n_0(\vec{r}) \\ & + \frac{1}{2} \int \int \left(\frac{1}{|\vec{r} - \vec{r}'|} + \frac{\delta^2 E_{\text{XC}}}{\delta n(\vec{r}) \delta n(\vec{r}')} \Big|_{n_0(\vec{r})} \right) \delta n(\vec{r}) \delta n(\vec{r}') d\vec{r} d\vec{r}' + E_{II}, \end{aligned} \quad (1.111)$$

From equation 1.111 a number of approximations can be made in order to obtain a standard modern DFTB model. Such as representing the molecular orbitals as a LCAO[77]. Here, the variational principle can be applied and we can obtain a reformulation of equation 1.52

$$\sum_{\nu} C_{\nu i} (H_{\mu\nu}^0 - \varepsilon_i S_{\mu\nu}) = 0, \forall \mu, i, \quad (1.112)$$

where μ and ν are basis functions, i is the index of a given electron, and $S_{\mu\nu}$ is the overlap matrix such that $S_{\mu\nu} = \langle \phi_{\mu} | \phi_{\nu} \rangle$. Another simplification is made by replacing the density with atomic electron populations, typically via Mulliken charges (c.f. section 3.4.2). Further to this, DFTB models typically only retain the two-center contributions in their matrix elements[180]

$$H_{\mu,\nu}^0 = \begin{cases} \varepsilon_{\mu}^{\text{free atom}}, & \mu = \nu \\ \langle \phi_{\mu}^{\alpha} | \hat{T} + V_0^{\alpha} + V_0^{\beta} | \phi_{\nu}^{\beta} \rangle, & \mu \in \{\alpha\}, \nu \in \{\beta\}, \alpha \neq \beta \\ 0, & \mu \neq \nu \in \{\alpha\} \text{ or } \nu \in \{\beta\}, \end{cases} \quad (1.113)$$

where μ and ν are the basis functions centered on atoms α and β . The repulsive term (E_{rep}) can be represented as a sum of pair potentials.[277] This finally gives us the general second-order DFTB equation for energy

$$E = \sum_i \langle \psi_i | \hat{H}_0 | \psi_i \rangle + \frac{1}{2} \sum_{\alpha,\beta}^N \gamma_{\alpha\beta} \Delta q_{\alpha} \Delta q_{\beta} + E_{\text{rep}}, \quad (1.114)$$

where $\gamma_{\alpha\beta}$ is the two electron integral and Δq is the point charge. The speed obtained from this method comes partially from the minimal basis set chosen with this method but primarily it comes from the ability to precalculate parameters for these equations. Specifically, the diagonal matrix components in equation 1.113 form some of the monoatomic parameters which are just the atomic eigenvalues. The other monoatomic parameters come from elemental atomic hardness, or

Hubbard parameters, and are used in the γ term in equation 1.114. The off-diagonal components of equation 1.113 form the first set of diatomic parameters. Conventionally they are calculated using

$$\left[\hat{T} + V_0^\alpha + \left(\frac{\vec{r}}{r_0} \right)^x \right] \phi_\nu = \varepsilon_\nu \phi_\nu, \quad (1.115)$$

where x and r_0 are variables to optimised to suit the desired outcomes of the model (i.e. to reproduce good band structures). The second set calculates the overlap off-diagonal matrix elements for $S_{\mu\nu}$ in equation 1.112. All of these electronic parameters can be found through DFT calculations where the atomic distances are varied to ensure good coverage of inter-atomic distances. Each type of orbital interaction is assigned to an appropriate level of angular moment for each type of atomic pair interaction. This allows the fitting of the first two terms of equation 1.114. The final term can be written simply as

$$E_{\text{rep}}(R_{\alpha\beta}) = E_{\text{DFT}}(R_{\alpha\beta}) - \left(\sum_i \langle \psi_i | \hat{H}_0 | \psi_i \rangle + \frac{1}{2} \sum_{\alpha,\beta}^N \gamma_{\alpha\beta} \Delta q_\alpha \Delta q_\beta \right), \quad (1.116)$$

The parameters for E_{rep} are often fit to a polynomial function. All of these parameters are often saved to a Slater-Koster file which stores the precalculated values for a parameterised system. In section 5.5 we show the process taken to develop a DFTB parameter set for solid electrolyte material LLZO and produce two of our own Slater-Koster files.

1.6 Machine Learning

Battery material interfaces are complex and have multi-scale effects that would be near-impossible to probe with sufficient accuracy using the methods discussed in previous sections. Even the bulk properties of some of the more complex systems remain elusive (c.f. section 4.2). Recent innovations in machine learning (ML) have allowed us to use the highly accurate *ab-initio* data we already have and extrapolate it to enable us to perform more complex and potentially larger systems. Broadly, ML methods can be split into supervised and unsupervised learning. Supervised learning entails training your data on known samples and enabling iterative improvements by adding more high-quality data to your model. An example of this is multiple linear regression which we discuss in section 1.6.1 Unsupervised ML techniques can help us make sense of and spot trends in large volumes of data here we discuss hierarchical clustering as an example (section 1.6.2).

1.6.1 Linear Regression

Linear regression forms the cornerstone of predictive supervised learning. The simplicity of this method allows easy analysis of variables' relationships and their ability to predict outcomes. The most simple of linear regression methods is ordinary linear regression (OLR). Which uses one input variable X to predict an output variable Y .

$$Y = \beta_0 + X\beta, \quad (1.117)$$

where β_0 and β are variables that should be optimised to minimise the error between the line drawn. The practicalities of how we do this we will come to later.

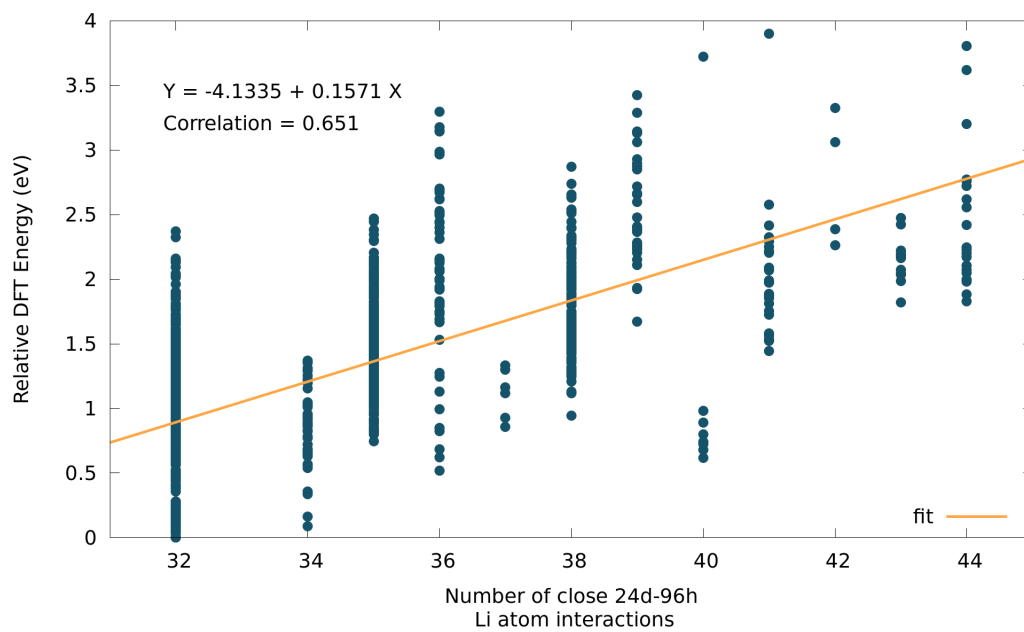


Figure 1.2: A demonstration of fitting an output value with a single input variable. In this case, we use the data for the number of a specific type of Li-Li interaction in solid electrolyte material c-LLZO occurring in a unit cell compared against the relative DFT energy of the full structure

In figure 1.2 we can see that β_0 and β are set to -4.1335 and 0.1571 respectively. should we wish to predict new data with our model all we would need is the single input value from the structure in question and we get a very rough estimate of our DFT energy.

Multiple linear regression (MLR) is generalisation of OLR and is a significantly more powerful predictive method. To predict a variable Y with a number of given variables X_i with MLR we construct the following formula

$$\hat{Y} = \beta_0 + \sum_{i=1}^p X_i \beta_i, \quad (1.118)$$

where β_0 is the intercept, or in the field of machine learning the bias, and β_i are the coefficients associated with each variable. It is common to include β_0 with β_i and an associated variable of 1 in X_i . This allows the reformulation of equation 1.118 as

$$\hat{Y} = X^T \hat{\beta}. \quad (1.119)$$

\hat{Y} can be a scalar or a vector depending on the number of dimensions we are working with.

The linear regression function can be written as the error of the output, Y , from the true value using input variables X , $E(Y|X)$. The coefficients β are optimised in order to reduce this error.

To quantify this error the most popular method is the least squares method. Whereby, β are chosen to find the minimum, within a tolerance, residual sum of squares. This is how the β_0 and β values were predicted in figure 1.2.

$$\text{RSS}(\beta) = (\mathbf{y} - \mathbf{X}\beta)^T(\mathbf{y} - \mathbf{X}\beta), \quad (1.120)$$

where \mathbf{y} represents a vector of N outputs and \mathbf{X} is a matrix of p parameters by N measurements. We can minimise our RSS by taking the derivative of the expanded equation 1.120

$$\text{RSS}(\beta) = (\mathbf{y}^T - \beta^T \mathbf{X}^T)(\mathbf{y} - \mathbf{X}\beta) \quad (1.121)$$

$$\text{RSS}(\beta) = \mathbf{y}^T \mathbf{y} - \mathbf{y}^T \mathbf{X}\beta - \beta^T \mathbf{X}^T \mathbf{y} + \beta^T \mathbf{X}^T \mathbf{X}\beta, \quad (1.122)$$

because the term $\mathbf{y}^T \mathbf{X}\beta$ is a scalar we can write the following

$$\mathbf{y}^T \mathbf{X}\beta = (\mathbf{y}^T \mathbf{X}\beta)^T = \beta^T \mathbf{X}^T \mathbf{y}, \quad (1.123)$$

Substituting in to equation 1.122

$$\text{RSS}(\beta) = \mathbf{y}^T \mathbf{y} - 2\beta^T \mathbf{X}^T \mathbf{y} + \beta^T \mathbf{X}^T \mathbf{X}\beta, \quad (1.124)$$

Using the denominator layout of the following identity

$$\frac{\partial(\mathbf{u} \cdot \mathbf{A}\mathbf{v})}{\partial \mathbf{x}} = \frac{\partial \mathbf{u}^T \mathbf{A}\mathbf{v}}{\partial \mathbf{x}} = \frac{\partial \mathbf{u}}{\partial \mathbf{x}} \mathbf{A}\mathbf{v} + \frac{\partial \mathbf{v}}{\partial \mathbf{x}} \mathbf{A}^T \mathbf{u}, \quad (1.125)$$

Where we set $\mathbf{A} = \mathbf{X}^T \mathbf{X}$ and $u = v = \beta$. Now we can differentiate

$$\frac{\partial \text{RSS}}{\partial \beta} = -2\mathbf{X}^T \mathbf{y} + \left(\frac{\beta^T \mathbf{X}^T \mathbf{X}\beta}{\partial \beta} \right) = -2\mathbf{X}^T \mathbf{y} + (\mathbf{X}^T \mathbf{X}\beta + (\mathbf{X}^T \mathbf{X})^T \beta) = -2\mathbf{X}^T \mathbf{y} + 2\mathbf{X}^T \mathbf{X}\beta = -2\mathbf{X}^T (\mathbf{y} - \mathbf{X}\beta), \quad (1.126)$$

and it is trivial to find the second derivative

$$\frac{\partial^2 \text{RSS}}{\partial \beta \partial \beta^T} = 2\mathbf{X}^T \mathbf{X}. \quad (1.127)$$

Assuming that \mathbf{X} is positive definite we can find a solution to 1.126

$$-2\mathbf{X}^T (\mathbf{y} - \mathbf{X}\beta) = 0, \quad (1.128)$$

which can be rearranged for β giving

$$\hat{\beta} = (\mathbf{X}^T \mathbf{X})^{-1} \mathbf{X}^T \mathbf{y}, \quad (1.129)$$

Thereby finding our β values assigned to each input variable turning our object β into our model $\hat{\beta}$.

By multiplying both sides by \mathbf{X} we find an expression that finds the orthogonal projection of \mathbf{y} on the subspace of the training data.

$$\hat{y} = \mathbf{X}\hat{\beta} = \mathbf{X}(\mathbf{X}^T \mathbf{X})^{-1} \mathbf{X}^T \mathbf{y}, \quad (1.130)$$

Hence finding our model or ‘fit’ when referring to our simplistic version in figure 1.2. This model can now be extended to an arbitrary number of dimensions which can significantly improve our predictive ability.[123] Figure 1.3 demonstrates this with a marked increase in correlation between the input variables and that of the DFT energy. Note that in this figure we now have 3 β values assigned via equation 1.129.

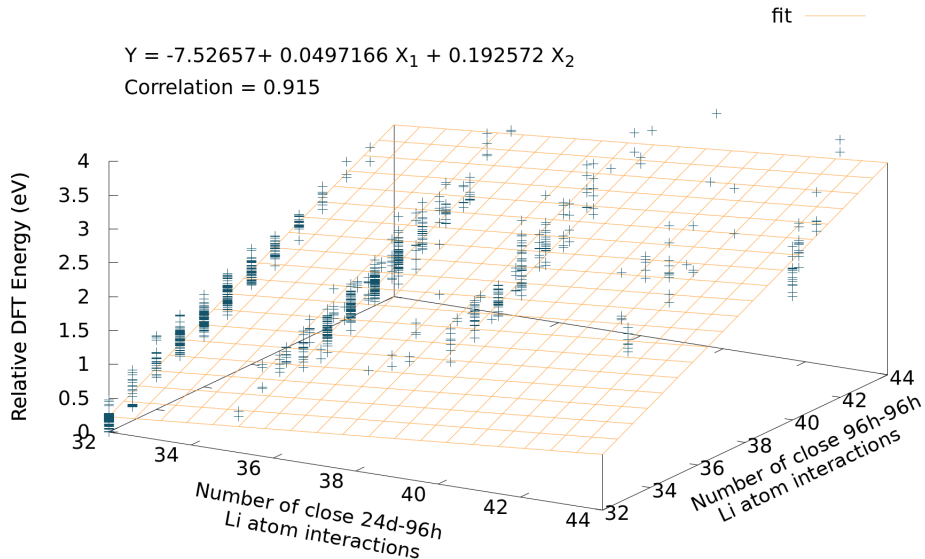


Figure 1.3: Demonstration of how adding just a single extra dimension can have a marked difference on the correlation. Here we include another input variable to the data displayed in figure 1.2: the number of nearest 96h-96h Li-Li interactions for a given cLLZO structure

We use MLR in chapter 4 where 86 different input variables are used.

1.6.2 Hierarchical Clustering

The purpose of HC is to organise a set of data based on its similarity. This data can be organised into groups and subgroups of other data displaying similar properties. These groups and sub-groups are called clusters. A cluster must have the following properties

1. Compact, the members of a cluster are similar to one another
2. Close, the members of a cluster are distinct from other clusters

For a set of data to be clustered means that the data within that cluster are more similar than it is to data in other clusters. One of the main things required to define is a measure of dissimilarity. The hierarchy element comes from the fact that at the lowest level, all data is its own cluster, at the highest all data is in a single cluster. The high-level clusters are created by progressively merging clusters together.

There are two main types of hierarchical clustering agglomerative (bottom-up) and divisive (top-down), we will focus purely on agglomerative. Agglomerative HC starts from all data and finds the two most similar data points which then forms a cluster. The next iteration finds the next most similar pair of data points or cluster and forms a new cluster. This step is repeated for all N data points. Agglomerative HC provides $N - 1$ levels in the hierarchy. Each level of the hierarchy represents a grouping of data into disjoint clusters. One of the major advantages of using HC is that from this style of clustering, we can draw a dendrogram (c.f. Figure 1.4).

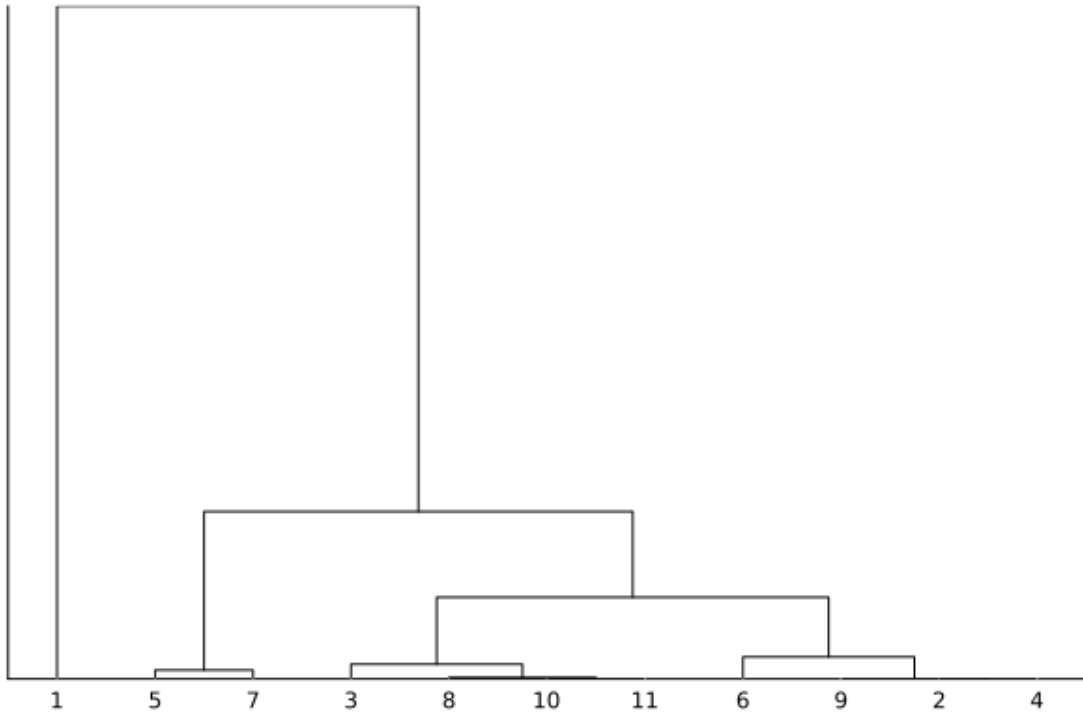


Figure 1.4: An example dendrogram showing the clustering of the 11 13:43 c-LLZO structures (c.f. chapter 4). The height of each node indicates the level of dissimilarity between individual data points and clusters.

In Figure 1.4 the N terminal nodes represent one of the individual data points. Each parent node has two daughter nodes. Most agglomerative methods have a monotonicity property, i.e. the dissimilarity between merged clusters increases with the level of the merger. This allows you to plot a dendrogram where the heights of the daughter nodes are proportional to their relative intergroup dissimilarity. This allows for you to be able to spot potential natural subgroups at a glance.

To perform any HC on data a measure of dissimilarity needs to be defined. Assuming two clusters G and H the dissimilarity between the two $d(G, H)$ can be computed from a set of pairwise dissimilarities $d_{ii'}$ where $i \in G$ and $i' \in H$. Once the process of clustering begins we must then define how the respective clusters' dissimilarity is computed. There are a number of ways of doing this. Each of these methods can produce very different results. Selecting the best method is dependent on the data being clustered.

- Single Linkage (SL)

$$d_{SL}(G, H) = \min_{i \in G, i' \in H} d_{ii'}, \quad (1.131)$$

SL has a comparatively low threshold for clustering which may be good for certain highly diffuse data but can lead to issues such as linking very different data points through a few intermediary points. This process is called chaining. Chaining can lead to a violation of the compactness property of clusters.

- Complete Linkage (CL)

$$d_{CL}(G, H) = \max_{i \in G, i' \in H} d_{ii'}, \quad (1.132)$$

CL has a high threshold for clustering and will often lead to tighter and more compact clusters than SL. However, this method has another issue whereby some clusters could have values that are closer to values in other clusters than in their own. This would be a violation of the closeness property of clusters.

- Group Average (GA)

$$d_{GA}(G, H) = \frac{1}{N_G N_H} \sum_{i \in G} \sum_{i' \in H} d_{ii'}, \quad (1.133)$$

where N_G and N_H are the number of terminal nodes (data points) in each cluster. GA is often seen as compromise between CL and SL. But, unlike SL and CL, GA is dependent on the numerical scale on which $d_{ii'}$ is measured. SL and CL are only dependent on their ordering whereas a monotone transformation (e.g. multiplying all values by a scalar) of $d_{ii'}$ for GA clustering could have entirely different results

- Ward's Linkage (WL)

$$d_{WL}(G, H) = \min \left\{ \frac{N_G N_H}{N_G + N_H} \left\| \frac{\sum_{i \in G} i}{N_G} - \frac{\sum_{i \in H} i'}{N_H} \right\|^2 \right\}, \quad (1.134)$$

Ward's linkage is based on the variance introduced when merging two clusters. When two clusters are merged there will be an increase in the error sum of squares. This method will seek to merge clusters that minimise that increase.

The complexity of this problem scales as $\mathcal{O}(N^2)$ with the number of data points present as a comparison of every data point needs to be carried out. This can make this process computationally intractable for large enough data sets.

Silhouette Score

It is often the case where the number of clusters required is unknown. One method that can be used to evaluate this is the silhouette score which we define as

$$s(i) = \frac{b(i) - a(i)}{\max\{a(i), b(i)\}}, \text{ if } |G| \geq 1, \quad (1.135)$$

where $a(i)$ is the mean distance from a given point to all other points within its own cluster and can be found as

$$a(i) = \frac{1}{|G| - 1} \sum_{i' \in G, i \neq i'} d_{ii'}, \quad (1.136)$$

and $b(i)$ is the smallest average distance of i to all points in each other cluster. The minimum value can be described as the neighbouring cluster of this particular data point.

$$b(i) = \min_{G \neq H} \frac{1}{|H|} \sum_{i' \in H} d_{ii'}, \quad (1.137)$$

The closer the silhouette score to 1 the better the clustering has been. With sufficient computing power the clustering techniques outlined in Section 1.6.2 can be run multiple times for multiple different desired cluster numbers. This would allow the attainment of ideal input parameters for hierarchical clustering.

Chapter 2

Battery Materials

2.1 Li-ion Batteries

Li-ion batteries are set to become a several-hundred billion-dollar industry in the coming decades. The advent of electric vehicles is predicted to vastly accelerate this process[276, 307]. A typical cell consists of a transition metal-oxide such as LiCoO_2 as the cathode. LiCoO_2 is one of the oldest cathodes developed for Li-ion batteries and yet still is the most popular cathode material today, being identified by Goodenough et al.[196, 229] in 1980. This cathode material went on to be developed into the first practical Li-ion battery by Yazami and Touzain[331]. They utilised graphite as the anode material and a solid electrolyte based on polyethylene oxide. This was later developed into a battery that used a non-aqueous electrolyte by Yoshino, Sanechika, and Nakajima[333].

2.1.1 General Chemistry

The typical Li-ion battery works by having an anode and cathode attached to current collectors (usually copper and aluminium plates). They allow for the transport of electrons from the cathode to the anode upon charging or vice versa for discharging. In the battery itself, the anode and cathode are separated using an electrolyte consisting of organic solvents such as a mixture of ethylene carbonate (EC) and dimethyl carbonate (DMC) with lithium complexes like LiPF_6 . The electrolyte allows for the transport of Li-ions but remains electrically insulating. On discharge, Li-ions will move from the anode to the cathode completing the circuit and generating a potential.[261, 305] This process is visualised in Fig. 2.1

The half-cell equations for the discharge process are given below



which reduces the cobalt from the +4 to +3 oxidation state

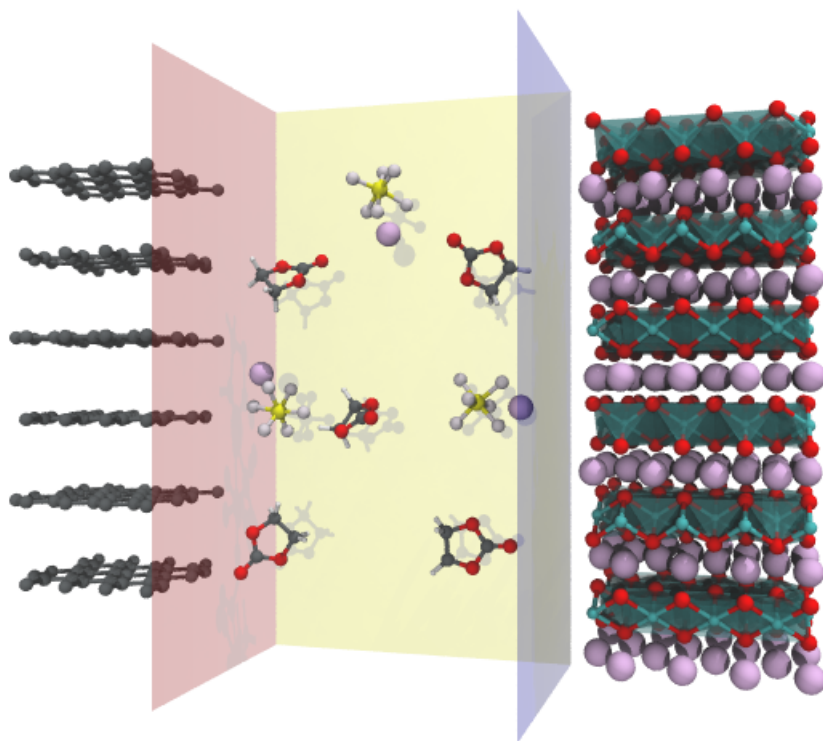


Figure 2.1: A typical Li-ion cell with a graphite anode on the left and a LiCoO_2 cathode on the right. The electrodes are separated by electrolyte which in this example is made up of ethylene carbonate and LiPF_6

The electrolyte becomes electronically insulated due to the formation of the solid electrolyte interface (SEI) (c.f. section 2.1.2).

The Li-ion battery is not limited to the materials we describe here. On the anode side recent innovations such as Si/C composite electrodes have shown promise[165] by significantly increasing the storage capacity of the anode. However,

issues such as large volume expansion upon charging[82] Have limited the volume of Si that can be added to these anodes. Other carbon analogues such as hard carbon (HC) have also been researched extensively as a potential replacement material to graphite. However, the relatively complexity of the intercalation mechanisms coupled with the large variance in reversible capacities has stifled the proliferation of this anode material commercially.[151] Electrolytes have undergone far more dramatic innovations than anodes with the typical LiPF₆ in EC and DMC, such as replacing them entirely with ionic liquids[184] allowing for higher battery energy densities and improved safety. Ionic liquids are a promising technology but commercialisation has been hampered by the prohibitively high cost of the electrolyte materials.[332] Another way to improve upon energy density and safety but has shown commercial promise is to replace the liquid electrolyte with an ionically conductive solid electrolyte. We will discuss this more in section 2.2.1. Finally, the cathode has undergone multiple iterations from its earliest form as LiCoO₂,[330] we will not discuss them further here as they are beyond the scope of the research conducted in later chapters.

2.1.2 Solid Electrolyte Interphase

The SEI was first observed by Dey and Sullivan [70] in 1970. They detailed how propylene carbonate decomposes on the graphite anode. The discovery of the SEI being electronically insulative and ionically passive was made by Peled[216]. This was supported by observations over the next 2 decades[16, 217]. The SEI has proven to be a double-edged sword. It prevents electron tunneling which would lead to further degradation of the electrolyte, vital for the stability of the battery. However, it also consumes active lithium and electrolyte materials leading to a reduction in battery performance[319] as well as proving to be the limiting factor in ion transport from anode to electrolyte.[306, 329]

Upon immersion into the liquid, the electrode forms the initial passivating layer. The thickness of this layer is determined by the electron tunneling range of the electrode.[216, 218]. The SEI size does not remain static and is affected by state of charge, temperature, and electrolyte composition.[47, 310, 318, 350]

An ideal SEI should be a few nanometers across and be able to accommodate the expansion and contraction of the anode as it is charged and discharged.[218] We demonstrate this expansion and contraction of the anode upon charging in section 3.3.2 and following sections. SEI thickness on graphite is also dependent on the orientation of the structure.[219] The basal plane will form an SEI 3-5 times smaller than one at a cross-sectional edge. This is expected given that electron tunnelling will be more prevalent in an inhomogeneously terminated edge-site rather than a stable aromatic ring. Most SEI currently employed continue to grow and/or fracture as the battery is cycled eventually leading to capacity fade and/or dendrite growth[8].

The reduction at the electrode within the electron-tunneling range can take on 4 major pathways:

1. Reduction of salt anions
2. Reduction to insoluble organic species
3. Polymerisation of the solvent
4. Reduction to soluble electrolyte species

Where 1-3 contribute to SEI growth and 4 is eventually redissolved into solution. Peled et al.[219] demonstrated that both paths 1 and 2 occur simultaneously forming a ‘mosaic’ pattern of organic and inorganic species on and close to the electrode-electrolyte interface. The polymerisation in 4 is thought to originally occur through electron-tunneling as previously mentioned. However, polymerisation continues to occur beyond the permitted electron tunneling range. Soto et al.[275] attributed this to the presence of radicals allowing for SEI growth beyond 20 Å of the solvent then occurs coating the internal mosaic. The SEI is believed to have an inorganic-rich inner layer consisting of LiF, Li₂CO₃, and Li₂O and an organic-rich outer layer.

Modelling the SEI has proven a particularly challenging feat given the size and complexity of the system. For example, multi-scale approaches have been necessary to approach this issue Abbott and Hanke[1] use a combination of Monte Carlo-molecular dynamics and DFT. Where DFT was used to find the reaction barriers to individual product formation which fed parameters into a higher-level simulation.

The electrolyte’s instability and capacity degradation as well as its flammability[249], has led to the development of solid electrolytes. Solid electrolytes have garnered particular attention from the automotive industry for the development of electronic vehicles (EVs). We discuss the topic more in-depth in chapter 2.2.1.

2.1.3 Graphite Anodes

The formation of an SEI enabled the use of the high-capacity, low de-intercalation potential anode material, graphite.[85, 289] Graphite’s structure takes the form of hexagonal carbon units with three strong covalent bonds to carbons within

the same sheet and a weaker van der Waals-based inter-sheet interaction (c.f. figures 2.2 and 2.3).[67, 226]

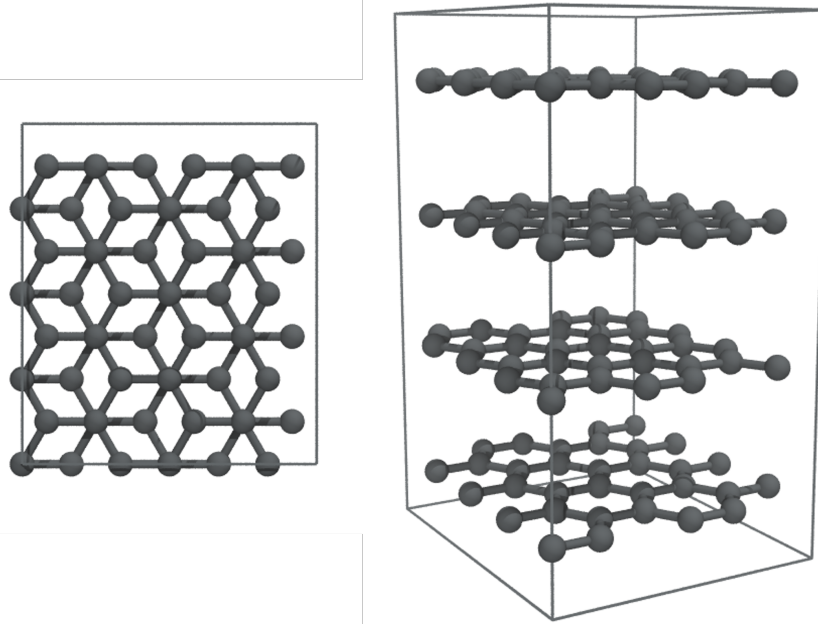


Figure 2.2: AB graphite from above (left) and from the side (right)

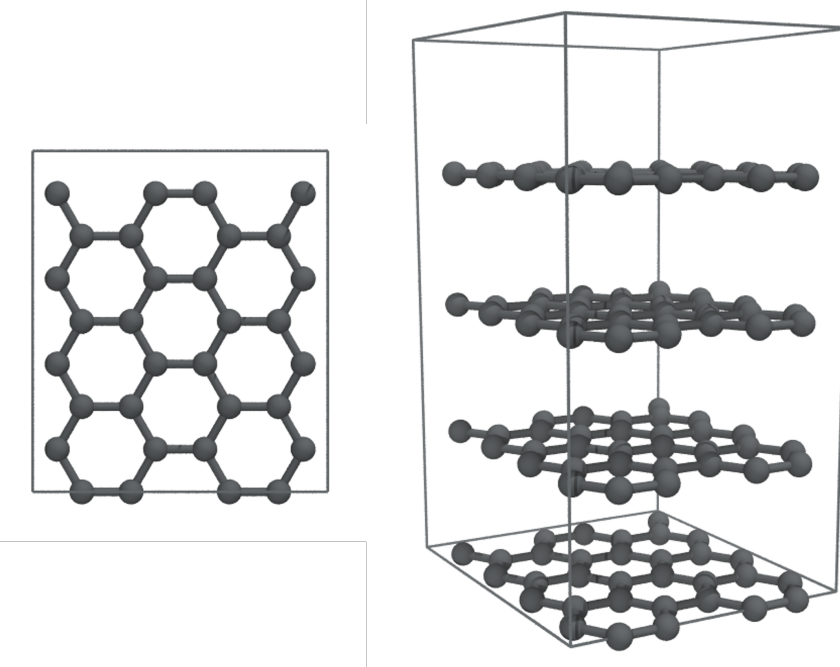


Figure 2.3: AA graphite from above (left) and from the side (right)

Bulk graphite's lowest energy state comes is the AB polymorph (c.f. figure 2.2) where carbon in the layers are offset so that a carbon in one layer is directly above and below the centre of a hexagon in the neighbouring layers. Bulk graphite also has a local minimum energy polymorph where the carbon layers align their carbons so that they are on top of each other (c.f. figures 2.3). While the AA polymorph is not stable in pure graphite, intercalants between the graphite layers can render this polymorph more stable than its AB counterpart.

Interfaces

Broadly, graphite can be said to have three major types of interfaces. Basal (001), which is the in-page face in figure 2.3(left), zig-zag (100) the up-down face in figure 2.3(left), and arm-chair (110) the left-right face in figure 2.3(left). The basal surface has been the one most computationally explored due to relative computational ease and lack of assumption need to be made of not having to terminate the dangling bonds with anything[198]. However, it has been

shown through experiment [177, 344] that SEI growth occurs primarily along zig-zag and armchair edges. It should also be noted that, unless there are significant defects, Li diffusion is unable to occur through the basal plane.[226, 292] For these reasons it is far more important when investigating graphite interfaces computationally that the zig-zag or armchair interfaces are the primary subject of focus. The dangling bonds of these surfaces are often terminated either with hydrogen[131] or a hydroxyl group.[220]

Li Staging

Lithium enters bulk crystalline graphite like this between the individual graphite sheets forming a graphite intercalated compound (GIC). The naming system attributed to the way this occurs is called staging.[322] We choose an intercalant (in this case Li) layer and count the number of graphite layers between the chosen layer and the next intercalant layer. The number of layers counted is equal to the stage number. In figures 2.4b and 2.4c this is clearly shown with two layers and one layer between each Li layer respectively corresponding to their assigned stage. As the graphite becomes more intercalated with Li the long-range C-C interactions are weakened and replaced with stronger C-Li interactions that prefer an AA arrangement.

Li staging has importance beyond being an interesting structural artifact. It provides a direct through-line from *ab-initio* calculations to that of experiments. Experimentalists can observe the formation of different stages through the use of open circuit voltage diagrams (c.f. figure 3.17b and references therein for details) which can be directly compared to a voltage step profile created with *ab-initio* calculations (c.f. section 3.4.4 and specifically figure 3.17a). In both these types of diagrams, the different plateaus correspond to different stages for a given Li occupancy[198].

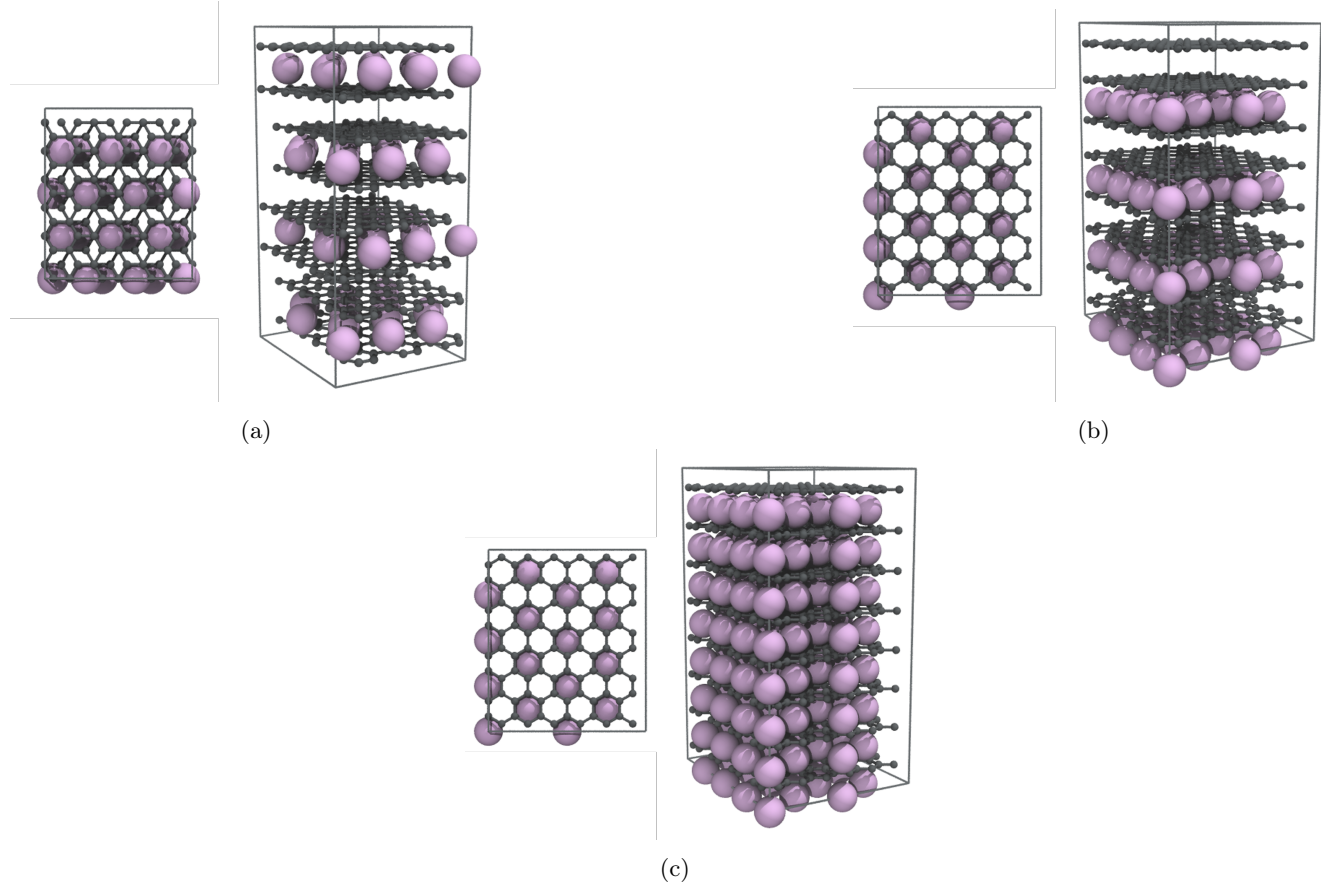


Figure 2.4: Different GICs where C and Li atoms are black and pink respectively. Shown here is (a) a stage II AB GIC, (b) a stage II AA GIC, and (c) a stage I GIC.

2.2 Solid-state Batteries

2.2.1 Solid Electrolytes

Solid Electrolytes (SEs) offer an array of advantages over their liquid counterparts. This includes safety improvements (vital for the automotive industry), increased energy density (with the ability to use lithium metal as the anode), higher stability, and better cycling.[281, 345]

Recent reviews on SEs include Sun et al. [281], providing a general review of solid-state batteries, and Zhang et al., [345] discussing the future directions of solid-state batteries. Famprikis et al. [80] have highlighted the advances in the fundamental understanding of SEs and solid-state batteries, with Gurung et al. [111] providing details of the challenges faced when using SEs in a battery. More specific reviews of the SE interfaces include Xu et al. [327] and Xiao et al. [325], exploring the challenges and stability, and Tateyama et al. [290], summarising the cathode-SE interface from a theoretical standpoint. From a modelling perspective, Ceder, Ong, and Wang [56] outlines the principles that should be employed when modelling SEs and Gao et al. [94] discusses the techniques used for investigating ionic transport. Given the extensiveness of the literature on this topic, we will instead focus on what is directly relevant specifically to research carried out in this work.

2.2.2 $\text{Li}_7\text{La}_3\text{Zr}_2\text{O}_{12}$

Cubic $\text{Li}_7\text{La}_3\text{Zr}_2\text{O}_{12}$ (c-LLZO) has a high Li-ion conductivity of 10^{-4} Scm^{-1} [205], a high shear modulus of 59 GPa[206], and the largest thermodynamic stability window with reference to lithium metal[36, 347, 349] of current solid electrolyte materials. However, at low temperatures ($< 150^\circ\text{C}$) c-LLZO is not stable and transitions to the less conductive tetragonal LLZO (t-LLZO) phase.[98] Attempts have been made to retain the more desirable c-LLZO by Al doping on lithium sites, with some success.[98, 234]

When in contact with a Li anode, dendrite growth has been shown to be a challenge in solid electrolytes. For LLZO, dendrite growth has caused short circuits in the cells after relatively short periods[238, 280]. Cheng, Sharafi, and Sakamoto observed this growth directly and found the process occurs mostly through grain boundaries.[60] Recently, Kim et al. confirmed these observations and investigated the use of an interlayer buffer to restrict Li propagation through grain boundaries.[152]

There has been a wide effort to understand dendrite formation through modelling[53, 92, 296]. For example, Tian, Xu, and Qi used DFT to investigate dendrite growth through analysis of c-LLZO and t-LLZO bulk and slab surface energies via the total density of states (TDOS) [296]. The authors found that t-LLZO forms at the surface of bulk c-LLZO, even with Al-doping[183, 240], and extra states appear in the band gap for the slab structures, which do not appear in the bulk, potentially allowing electrons to be trapped on the surface of LLZO. Electrons localised primarily around Li^+ and La^{3+} ions on the surface lead to the nucleation of lithium metal, which can result in lithium growth through grain boundaries and pores in the LLZO, eventually forming dendrites[238]. This analysis was also conducted on $\text{Li}_2\text{PO}_4\text{N}$ (LiPON), where no electron trapping was found to occur, indicating that LiPON could be a suitable coating to prevent dendrite and t-LLZO formation.

Gao, Jalem, and Tateyama attributed the dendrite growth mechanism to the under-coordination of Zr present on some of the stable interfaces of LLZO with Li,[92] leading to inhomogeneous Li depletion, which has been linked to Li metal deposition and dendrite formation. It is unclear whether the suggested cause by Gao, Jalem, and Tateyama is complementary evidence of Tian, Xu, and Qi's electron trapping theory or a separate cause of interface dendrite growth. However, the papers do differ on the choice of surface. Tian, Xu, and Qi used Li and La rich surfaces, which were determined to be more stable by Thompson et al., who used DFT to investigate 6 different LLZO slabs for the (100) and (110) planes.[295] In contrast, Gao, Jalem, and Tateyama drew upon results presented in several methods[53, 295, 335] and performed DFT calculations on a wider range of surfaces, finding (100) and (001) surfaces to be the most stable. The findings of these studies agree that Li and La-rich surfaces are the most stable. However, Gao, Jalem, and Tateyama calculated the interface formation energies of the Li-LLZO interfaces using the CALYPSO interface structure prediction method[93, 320]. This method determined the Zr-rich surfaces to be the most stable. Experimental observations corroborate these findings, also determining Zr to cause interfacial degradation[346]. It is apparent that the selected surface plays a large role in the conclusions one can make about important material processes. For this reason, we investigate the surfaces further using novel techniques in section 5.3.2.

Experimental measurements have suggested a non-uniform distribution of current on the surfaces as a possible cause of dendrite growth.[3, 116] Non-uniform current distribution produces random, local spikes in current density for short periods of time leading to a reduction of Li at these sites. Squires et al. used DFT to model the electronic conductivity in LLZO to probe the importance of the surface current to dendrite formation.[278] The authors determined that at room temperature, bulk c-LLZO was found to have negligible electron/electron-hole concentrations, indicating that bulk defects are not a significant factor in dendrite growth. However, these models did not account for other forms of defects,

such as grain boundary and surface effects.

Understanding Li-ion migration is key to improving battery conductivity. Xu et al. analysed the Li-ion migration path through LLZO using DFT with the nudged elastic band (NEB) method.[328] Two migration paths were observed, depending on Li concentration. Low Li_x ($\text{Li}_5\text{La}_3\text{Zr}_2\text{O}_{12}$) led to a higher energy, single hop, migration path, whereas higher Li_x ($\text{Li}_7\text{La}_3\text{Zr}_2\text{O}_{12}$), led to a lower energy, two hop, migration path. Using potentials-based MD Burbano et al. further investigated the Li-ion transport mechanisms by comparing ionic conductivity in t-LLZO and c-LLZO.[49] The authors found the longer time scale of potentials-based MD allowed the observation of a large sample of diffusion events in both LLZO structural forms. Diffusion events in t-LLZO were less common and mostly involved exactly 8 Li ions, which corresponds to the cyclic movement of Li ions around the 12 octahedral and tetrahedral ring sites in t-LLZO. This cyclic mechanism results in no net long-ranged diffusion of Li and hampers the ability of t-LLZO to conduct ions. AIMD investigations of the transport mechanism in LLZO have been conducted. However, the shorter time scale led to some key disagreements about the transport mechanism in c-LLZO.[49, 141, 191] It should also be noted that simulating c-LLZO, a disordered crystal, atomistically may require a more reasonable starting structure than what was available in the literature. We introduce a methodology to address this in section 4.2.

DFT calculations have determined Al doping reduces the energy barrier for Li-ions to move between octahedral and tetrahedral sites, increasing the ionic conductivity.[239, 241] More recent work by Bonilla et al., using potentials-based MD, supports these findings, finding increased conductivity in t-LLZO due to the Al forcing Li ions into previously inaccessible tetrahedral sites.[42] The authors also found Al doping in c-LLZO led to a slight decrease in conductivity. They attributed this to the tendency for Al to “trap” Li ions close to the dopant.

Experimental investigations of solid electrolyte interfaces are often challenging, making atomistic modelling a vital tool.[327] The interface stability properties of solid electrolyte materials in contact with an electrode are best described by its electrochemical stability window. The electrochemical stability window is defined by Zhu, He, and Mo as the range of voltages under which the interface configuration, which is a mixture of the electrode (Li) and the solid electrolyte, does not undergo a decomposition reaction.[347]

2.2.3 Interfaces with Solid Electrolytes

It has been widely reported in both experiment[115, 179] and theory[197] that certain solid electrolytes have an electrochemical stability window with reference to a Li anode between 0–5 V.[148, 179, 291] Mo, Ong, and Ceder reported a 3.6 eV band gap from a DFT calculation (c.f. section 1.2) for LGPS,[197] attributing the higher solid electrolyte stability observed to the passivation phenomenon forming an interphase layer at the interface of the anode-electrolyte.[154] More recent work by Zhu, He, and Mo has questioned this high stability window, using DFT to demonstrate that the stability windows, particularly of sulfides, are far smaller than originally thought.[349]

A smaller thermodynamic window increases the importance of the interphase layer formation. Zhu, He, and Mo determined that a range of solid electrolytes are unstable with respect to Li metal at low and high voltages, with the exception of LLZO, which appears to be kinetically stabilised at low voltages due to an unfavourable reduction energy of -0.02 eV per atom. Any potential outside of the thermodynamic stability window results in decomposition into lithium binary compounds unless otherwise kinetically stabilised. This is problematic for germanium and titanium-containing compounds as they form electronically conductive alloys upon decomposition.[349] This renders the proposed passivation process impossible[197, 349] as this degradation process would be sustained throughout the bulk cycling, severely limiting the efficacy of these materials as electrolytes. Such degradation can also increase interfacial resistance[254, 287]. Other solid electrolytes face different problems. As explained in sec. 2.2.2, LLZO forms the far less ionically conductive tetragonal LLZO at the surface. The Li-LiPON and Li-argyrodite interfaces were reported to degrade favourably, forming an ionically conductive and electronically insulating interphase consisting of Li_2O , Li_2S , Li_3P , Li_3N , and LiI .[349]

Further study by Zhu, He, and Mo sought to investigate the mechanism behind the degradation/instability at the surface.[347] In order to probe these mechanisms, the authors looked at several solid electrolytes (LGPS, LLZO, LiPON, NAISICON-type, LLTO) and calculated their chemical stability, electrochemical stability, and the equilibrium conditions at the interfaces. Examining the cathode-electrolyte interface, using lithium cobalt oxide (LCO) as the cathode, a similar pattern emerged: oxides were found to be far more stable than their sulfide counterparts. However, LLTO and LATP had the best electrochemical stability against LCO.

Studies looking into the interfacial resistance have been conducted,[145, 209, 265, 290] with the main source of resistance attributed to the electric double layer (EDL), which in liquid electrolytes consists of a capacitance and diffusion layer.[290] The EDL in solid electrolytes is made up of a space charge layer of point defects in ionic materials. [285] Tateyama et al. use the CALYPSO method to find low-energy surfaces[93] to probe the interface. The lithium chemical potential of these stable interfaces in the Helmholtz layer, corresponding to the negative of the Li-ion vacancy formation energy, was determined. These energies correspond to lithium moving from the electrode to the electrolyte, with the vacant lithium sites becoming a potential source of interfacial resistance. Okuno, Haruyama, and Tateyama use DFT calculations to compare the interfacial resistances of sulfide and oxide-based solid electrolytes with LCO cathodes.[209] The Li vacancy

formation energy at various interfaces and ion exchange across the interface were calculated. It was found that sulfide-based electrolytes had a higher interfacial resistance, due to the presence of more sites with a low vacancy formation energy on the surface. The authors also found the interfacial resistance to be dependent on the orientation of the crystals at the interface. The cause of interfacial resistance can also be attributed to the preparation of solid electrolyte surfaces.

A study by Lepley and Holzwarth used DFT to investigate the interface energies between the Li electrode and the compounds that make up the interphase layer of the electrolyte.[172] They defined the interface energy as:

$$\gamma_{ab}(\Omega) = \frac{E_{ab}(\Omega, A, n_a, n_b) - n_a E_a - n_b E_b}{A}, \quad (2.2)$$

where Ω is the interface configuration of atoms, E_{ab} is the energy of the complete system, E_x is the bulk energy per formula unit and A is the surface energy. Because the interface energy is intensive, calculating larger systems will give a converging value for γ_{ab} ,

$$\lim_{\Omega_s \rightarrow \Omega} [\gamma_{ab}(\Omega_s)] = \gamma_{ab}(\Omega), \quad (2.3)$$

where Ω_s is the atomic configuration in a sample of the interface volume. Because the exact matching of lattice constants between interfaces is unlikely, a semi-coherent interface is considered, meaning lattice strain needs to be taken into account. Using the lowest overall lattice energy structure and explicitly accounting for the lattice strain, the most probable interfaces could be found. The Li/Li₃PO₄, Li/Li₂O, and Li/Li₂S interfaces were found to be stable and the Li/Li₃PS₄ interface was found to be unstable.[172]

In response to the apparent poor stability of most solid electrolytes, many studies have attempted to simulate the effect of coating the electrolyte with an oxide layer[296, 324, 342]. As discussed in section 2.2.2, Tian, Xu, and Qi identified LiPON as a suitable coating material for LLZO by comparing the bulk and surface density of states[296]. The authors found no extra states on the surface structure, so concluded that no electron trapping would occur (the primary mechanism that they attributed to dendrite formation). Recently, Sang et al. proposed an artificial interphase layer between the Li anode and the solid electrolyte composed of a Li_{3a_b}N_aX_b compound, where X is a halide.[255] This material was investigated computationally by screening stable and metastable structures using the USPEX structure prediction software.[101, 207] The dynamic stability of the stable structures was found by analysing the phonon frequency spectrum by using PHONO3PY [213, 298, 299]. The temperature-dependant ionic transport properties were found using *ab initio* molecular dynamics (AIMD). (c.f. section 1.4)

Phase diagrams for various atomic configurations were then constructed using a cluster expansion, implemented through the Alloy-Theoretic Automated Toolkit (ATAT).[119, 315] Through these various computational techniques, Sang et al. found that Li₆NCl₃ to have the most favourable properties for use with sulfide-based solid electrolytes such as LGPS.[255]

Chapter 3

A Study of Graphite Nanoparticles

3.1 Abstract

The process of Li intercalation is fundamental to the operation of Li-ion batteries and the computational modelling of this process, as atomic resolution would be of great benefit to the rational design of improved battery materials. Towards this goal, we present an approach and workflow for the simulation of Li intercalation which uses electrostatic considerations. These considerations use the electrostatic potential found from Density Functional Theory (DFT) calculations as a guiding principle to find favourable sites for Li intercalation. We test the method on graphite-based models of anodic carbon, graphite nanoparticles. The study of nanoparticles using first-principles methods is made possible thanks to linear-scaling DFT which allows calculations on larger numbers of atoms than conventional DFT. We show how our approach can reproduce the well-known Li staging and we investigate the electronic structure of the nanoparticle obtained via atomic charges and density of states analysis. We also compute the open circuit voltages of the structures via a convex hull formalism and find reasonable agreement with experiment with respect to the degree of Li intercalation. Our approach provides a novel route to simulating the intercalation process and, combined with linear-scaling DFT, can be used to investigate intercalation in complex nanoscale electrode structures.

3.2 Introduction

Li-ion batteries are charged and discharged by the intercalation and deintercalation of Li within electrodes through an electrolyte.[11] (c.f. section 2.1) The most popular anode material is graphite due to its high Li storage capacity, electrochemical stability, cycling stability, and affordability.[89, 124, 150, 269, 293, 305, 343] (c.f. section 2.1.3) For this reason Li intercalation into graphite has been the subject of intense study both experimentally[74, 188, 243, 260, 323] and computationally[58, 97, 125, 193, 194, 222, 226]. Other graphite-like anode materials such as graphenelyne[338], biphenylene monolayers[117], or even doped graphite[337] have also been subject to intense study.

Despite this, the mechanisms surrounding the charging and discharging of the graphite anode are still not fully understood.[6, 67, 262]. Recent experimental and computational investigations have focused on the entropic contributions of different stage formations [193, 194, 222], the transition between Li stages [188], and the kinetics of Li intercalation [97, 193, 226]. Experimental results often differ from computational ones. For example, the voltage step profiles presented by Persson et al.[226] were unable to match the experimental results presented by Stevens and Dahn[279] even when including van der Waals (vdW) corrections.

A potential cause of the apparent mismatch between experiment and computation is that, until now, *ab-initio* calculations have been primarily performed on bulk graphite. Graphite, in batteries, often occurs at the micro- or nano-scales[9, 247]. The incidence of particles occurring at the nano-scale is likely to increase with cell age due to the prevalence of cracking as the volume expands and contracts upon charging and discharging.[288, 311] It is possible that to reconcile computational and experimental results, the unique structural properties of the nanoparticle must be accounted for. This has proven difficult to model at electron resolution due to the large number of electrons present in a nanoparticle. Conventional density functional theory (DFT) scales at $\mathcal{O}(n^3)$, where n is the number of atoms in the system, due to the need to perform computationally expensive processes such as diagonalization under the constraint of orthonormality (c.f. section 1.2.2). This puts an effective limit on the size of the system that can be studied using conventional DFT. Large-scale DFT calculations are possible due to the recent developments of linear-scaling DFT, where the computational cost scales at $\mathcal{O}(n)$. We use ONETEP[230] (c.f. section 3.3.1 for practical implementations of this program in the context of this work or c.f. section 1.3 for the core theory) because of the highly parallelizable nature of this program.

Previous work has investigated graphite systems with intercalated[220] and nucleated Li[33, 221]. These studies were performed on graphite slabs and we found energetic preferences for Li intercalation and nucleation at graphite edges. As experimentally used systems contain multiple edges, these types of effects can be studied in greater detail with a graphite nanoparticle. In this work, we advance understanding by focusing on Li intercalation into the graphite nanoparticle by adopting a novel Li placement strategy. This study can be further advanced to consider events of nucleation and dendrite formation on graphite nanoparticles by extending Li placement on surfaces as well (c.f. section 3.3.5).

Established methods such as cluster expansion[55, 233] have been used to simulate Li intercalation in bulk systems previously[226, 303]. However, these methods require the energy calculations of multiple extra configurations to find the lowest energy structures.[55] This is computationally expensive, particularly when performing these calculations on large systems. Ran et al.[233] partially address this issue by employing a group-subgroup transformation formalism to rigorously find structures for their bulk graphite system and eliminate a large portion of configurational space. This reduction of configurational space allowed them to identify a new extremely low ground state structure occurring at $\text{Li}_{0.0625}\text{C}_6$.

However, even with the impressive breakthroughs of Ran et al. an insurmountable disadvantage of this method is that it requires long-range, translational symmetry (i.e. the construction of a supercell).[321] Methods such as cluster expansion or group sub-group transformation are unsuitable for dealing with large systems of low long-range symmetries, such as nanoparticles. Recently, Shen, Horton, and Persson[266] demonstrated a method that used the charge density minimum for intercalating lithium ions and demonstrated it on a large number of common, bulk cathode materials. To insert Li they find the relaxed, unlithiated structures of the bulk cathode crystals and the respective local minima of charge density equating them to lithiation sites. The authors validated the use of charge density by calculating the binding energy of known Wyckoff sites in the crystals and compared them to their predictions. They found that the charge density predictions aligned with the Li atoms' site preference. They were also able to capture structural phenomena such as accurately reproducing which Li insertions would give topotactic insertions.

Given that the primary source of interaction in graphite intercalated compounds (GICs) between Li and C is electrostatic, we, instead, place Li atoms at the global minimum of the electrostatic potential within our system. After each lithiation this method should only find structures that are close to the ground-state and therefore reduce the number of calculations needed to be performed (c.f. section 3.3.4). To validate our model we will be looking for a number of structural and electronic phenomena that we would expect to occur in graphite. The phenomena we validate against are detailed below.

- **Li Staging:** Li intercalation occurs with a staging process whereby lithiation between graphite layers does not result in a uniform distribution. Li will preferentially populate sites between graphite layers that have already experienced some degree of lithiation, thus forming a layer of Li. The Li layers that form have a long-range symmetry that is dependent on the degree of global lithiation. The type of staging is dictated by the number of graphite layers

between Li layers. If there is only one (i.e. full or close to full lithiation) then this is a stage I compound, if there are two it is a stage II compound, and so on.[253]

- **AB to AA Graphite Shift:** Graphite's lowest energy state has its individual graphite sheets staggered. i.e. the centre of a graphite hexagon will have a carbon atom aligned directly above and below it. This is known as an AB structure. With increasing Li saturation the vdW forces between graphite sheets are weakened. They are replaced with Li-C interactions. As the lowest energy state for Li is directly above and below a centre of the graphite hexagon there is increasing preference, with increasing lithiation, for the graphite layers to slide over one another to accommodate the Li's optimum position.[136, 194] Therefore, a transition to an AA structure occurs where all C atoms in graphite layers are stacked directly on top of each other.
- **Charge Transfer:** Upon entering the graphite structure Li atoms give up their 2s electron to the C 2p orbitals. This plays an important role in the expansion of the graphite intercalated compound (GIC), as well as the aforementioned staging process[188]. Charge transfer can be probed through the analysis of local charges on atoms, as well as the electronic density of states (DOS).[316]
- **Voltage Step Profile:** Direct comparison to experimental open circuit voltage (OCV) measurements can be made by plotting the calculated voltages from the ground-state structures against the degree of lithiation.[226] To find the ground-state structures we draw a lower convex hull from all GICs we produce. These structures tend to be topotactic as we intercalate further until the threshold for the next structure is met.[266]

Comparison to experiment and prior computational studies through the aforementioned metrics will enable us to assess the quality of our model. We will also be able to highlight the differences that occur when moving to the nanoscale with our nanoparticle.

This work is structured so that in section 3.3.1 we briefly outline the linear-scaling DFT code that we use, ONETEP. In section 3.3.2, we benchmark exchange-correlation functionals that account for long-range forces for a graphite-like system and select the best functionals to move forward with. We then define our nanoparticle and calculation properties in section 3.3.3. The intercalation methodology is outlined in sections 3.3.4 and 3.3.5. We outline the results in section 3.4, splitting them into structure (section 3.4.1), local charge (section 3.4.2), electronic density of states (section 3.4.3), and voltage step profiles (section 3.4.4). Finally, we perform further calculations to investigate the cause of the lack of AB to AA shift as we intercalate our nanoparticle in section 3.4.5.

3.3 Methodology

3.3.1 ONETEP for Graphite

All calculations were performed with ONETEP, a linear-scaling DFT code, where the computational cost scales linearly with the number of atoms as opposed to cubic scaling in conventional DFT.[230, 272] ONETEP is based on reformulating DFT in terms of the one-particle density matrix. This matrix is expressed in terms of an atom-centred, non-orthogonal generalised Wannier functions (NGWFs).[271] The NGWFs are in turn expanded with a basis set of periodic sinc (psinc) functions which are related to plane waves through a unitary transformation.[201] This allows us to truncate the one-particle density matrix and thus achieve linear scaling for large enough systems.

3.3.2 Modelling Graphite Properties

When modelling graphite computationally using DFT, a careful approach to functional selection must be made. Intra-planar bonding can be reproduced easily enough with most functional choices, due to the well-defined nature of covalent bonds. However, the interplanar interactions are determined by weaker, long-range effects. These interactions are not accounted for with generalised gradient approximation (GGA) functionals[7, 128, 159, 164] and spuriously accounted for with local density approximation (LDA)[104] functionals. For this reason, many non-local functionals[39, 71, 153, 168, 252] and empirical correction terms[51, 106–108, 297] were developed.

This work aims to add Li atoms between the graphite layers at the most favourable sites. This adds a further layer of complication as the electrostatic interactions of Li-C are stronger than the C-C vdW interactions.[226] An accurate representation of vdW interactions is therefore essential for realistic Li intercalation.

Starting from pure graphite we consider a number of functionals to determine which one best models the interlayer binding energy and interlayer spacing. Our results were compared to other computational and experimental studies. We consider the following non-local functionals: rVV10[252], AVV10s[39], vdW-DF[71], vdW-DF2[168], optPBE[153], optB88[153]. We also consider PBE with the Grimme D2 empirical correction term[106].

The calculations were performed on a 640 atom graphite structure with periodic boundary conditions[230]. The structure is 10 layers high, with each layer consisting of 64 C atoms (c.f. Fig 3.1a). To find the interlayer spacing we follow the technique outlined by Bramley et al. to expand our unit cell.[44] We iterate upon this technique by only varying a single lattice parameter, or interlayer spacing (c), as demonstrated by Siersch et al.[268], between 2.978 and 4.964 Å. The kinetic energy cutoff was kept constant throughout (732.32 eV) while the number of psinc functions, that form our basis set (c.f. section 1.3.2), along the z-axis were increased.[270]

Plotting the total energies against the volume of the simulation cell allows us to fit a third-order Birch-Murnaghan equation shown in figure 3.1b.[38, 204, 268]. As only the interlayer spacing is varied this is what is displayed on the x-axis instead of volume. We use the least mean square method to fit this equation to our results. The minimum of this plot gives the lowest energy simulation cell volume and therefore the ideal interlayer spacing (c).

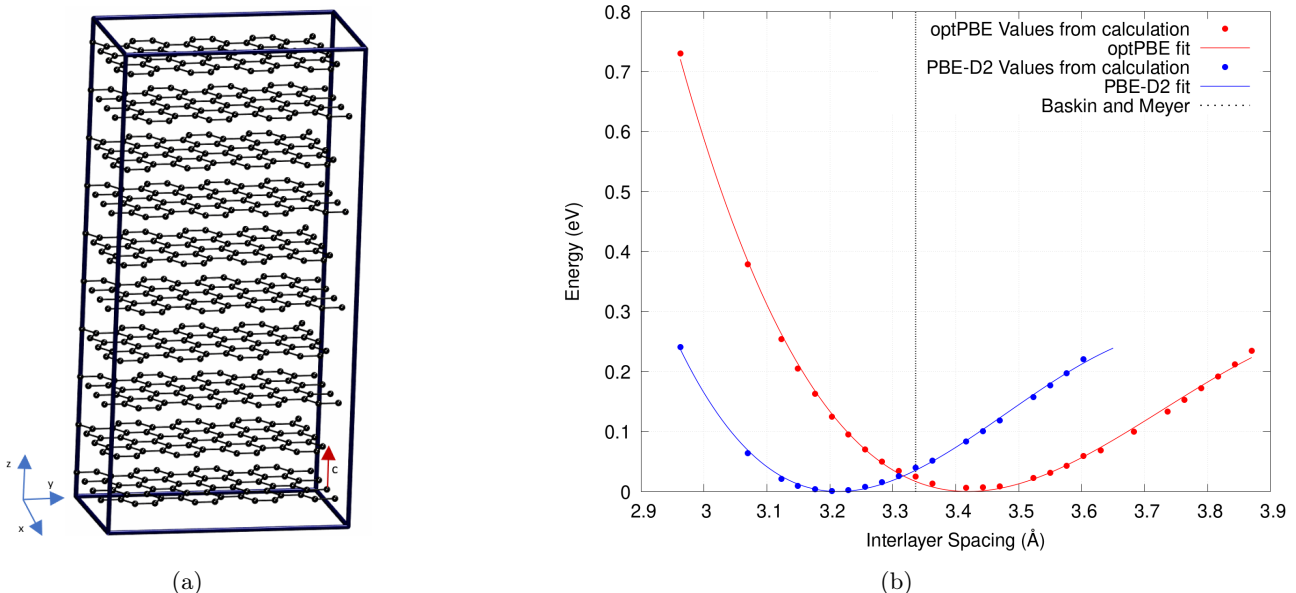


Figure 3.1: (a) Periodic graphite structure used to test various non-local functionals and empirical correction terms. (b) The relationship between the interlayer spacing of bulk graphite and the total energy. A third-order Birch-Murnaghan equation of state was used to fit this plot. Results of the optPBE non-local functional and PBE with the D2 correction term are shown.[44, 270] Experimental results by Baskin and Meyer are also shown.[24]

The interlayer binding energy, E_{int} , was found by considering the energy difference between the bulk, E_{bulk} , with the minimum energy interlayer spacing for each functional used, and that of infinitely separated graphene sheets, E_{sep} . In practice, we set our graphite system to have an interlayer spacing of 10.1 Å which should be far enough away that any long-range interactions are negligible.

$$E_{int} = \frac{E_{sep} - E_{bulk}}{N} \quad (3.1)$$

Where N is the number of layers in our system. The binding energies are presented in Table 3.1.

In this table, we compare our binding energy and interlayer spacing values to experimental data and to other published DFT results. We do this to validate our findings and to establish the functional that predicts the most realistic graphite properties. Attention should be drawn to the disparate experimental layer binding energy values cited in Table 3.1. There is no definitive way to find the interlayer binding energy of graphite experimentally in the literature. There have, however, been several attempts to find a good approximation that we include in our table[28, 178, 340].

[340] [340] are able to approximate the interlayer binding energy of graphite by adsorbing a polycyclic aromatic hydrocarbon (PAH) to a graphite surface. The PAHs are then desorbed at increasing temperature and the concentration is recorded giving a rate of desorption with temperature increase. This allows for the calculation of the activation energy using the Redhead peak analysis method[236] and Falconer-Madix isothermal analysis[79]. This was repeated for 4 different PAHs of increasing size. A relationship was found and extrapolated for pure graphite.

Liu et al.[178] find the binding energy by creating a graphite mesa with a known step height atop a graphite flake with atomically smooth surfaces. A second atomically smooth flake is created on a SiO_2 base which is attached to a microprobe. The graphite sheet is then placed over the mesa and moved over the edge until it buckles. By accounting for the geometries involved and modelling the vdW forces as “non-linear spring elements ... with force displacement relation derived from the Leonard-Jones potential” the binding energy can be found.

Benedict et al.[28] use collapsing carbon nanotubes. By varying the nanotube radii and number of walls, the resulting collapsed nanotubes were observed using transmission electron microscopy (TEM) which enabled a detailed analysis of the structures. The authors fed structures’ parameters into a continuum elasticity theory with a Lennard-Jones description of intersheet attraction.

Below we summarise the long-range functionals we test and what their original development operation.

- PBE-D2[106]
 - Not a vdW functional. It was developed by Grimme[106] as a correction that can be applied to any DFT calculation

Table 3.1: Comparison of interlayer spacing and binding energy results between experimental and other theoretical values

Interlayer Spacing (Å)				
Experiment	3.3360 ± 0.0005 [24]			
Functional	Our results (ONETEP)	Chen et al.[58] (VASP)	Hazrati, Wijs, and Brocks[125] (VASP)	Lenchuk, Adelhelm, and Mollenhauer[171] (VASP)
LDA	-	3.33	-	-
LDA-D2[106]	-	2.99	-	-
PBE[224]	-	4.42	4.40	3.99
PBE-D2[106, 224]	3.22	3.23	-	-
PBE-D3[108, 224]	-	-	-	3.34
rVV10[252]	3.36	-	-	-
AVV10s[39]	3.48	-	-	-
vdW-DF[71]	3.56	-	3.59	3.54
vdW-DF2[168]	3.51	3.51	3.51	-
optPBE[153]	3.44	3.45	3.44	-
optB88[153]	3.36	3.36	3.36	3.32
optB86b[153]	-	-	3.31	3.29

Layer Binding Energy (meV/atom)				
Experiment	52 ± 5 Zacharia, Ulbricht, and Hertel[340] 31 ± 2 Liu et al.[178] 35 ± 15 Benedict et al.[28]			
Functional	Our results (ONETEP)	Chen et al.[58] (VASP)	Hazrati, Wijs, and Brocks[125] (VASP)	Lenchuk, Adelhelm, and Mollenhauer[171] (VASP)
LDA	-	23.7	-	-
LDA-D2[106]	-	114.9	-	-
PBE[224]	-	0.9	1.0	-
PBE-D2[106, 224]	54.5	55.2	-	-
PBE-D3[108, 224]	-	-	-	53
rVV10[252]	70.4	-	-	-
AVV10s[39]	65.3	-	-	-
vdW-DF[71]	54.0	-	52.7	53
vdW-DF2[168]	53.4	52.1	52.0	-
optPBE[153]	64.0	63.7	63.7	-
optB88[153]	70.7	69.6	69.5	70
optB86b[153]	-	-	69.9	70

- It showed particular promise on large scale biological systems
- rVV10[252]
 - Is a revision of VV10[313] that allows for usage with a plane wave framework
 - It reported good interlayer spacing in graphite
- AVV10s[39]
 - Refits VV10 with the goal to improve weakly bonded and close packed solids
 - Reports slightly worse interlayer binding modelling than the original VV10
- vdW-DF[71]
 - Includes vdW forces by expanding to the second order a term in the long range part of the correlation functional
 - Shown to give realistic descriptions of rare gases and benzene dimers
 - Uses rPBE[224] as its exchange functional
- vdW-DF2[168]
 - Improves upon vdW-DF by using a different exchange functional (rPW86[225])
 - Shows improved binding curves (close to that of accurate quantum calculations) on 22 different duplexes
- optPBE[153]
 - Again, improves upon vdW-DF using different exchange functionals. Uses a combination of PBE and RPBE[114] as well as some other corrections
 - The exact proportion of PBE and RPBE present in the exchange functional was found by fitting for the S22 data set[147]
 - Overbinds some molecules such as methane but accurately predicts the energy ordering of water hexamers which a particularly tough test for DFT[258]
- optB88[153]
 - Was developed in the same paper as optPBE. It uses B88[27] as exchange-correlations and corrected to mitigate its tendency to underbind
 - Outperforms optPBE on the S22 dataset

Chen et al.[58] found PBE with the Grimme D2 dispersion correction to perform the best. They also find the C_{33} elastic modulus for comparison between functionals. Hazrati, Wijs, and Brocks[125] chose the optB88 functional to move forward in their calculations. They selected it because it gave the best overall structure, which is reflected in our results, and this was deemed to be the most important feature for the type of calculations they were doing. However, they also note that optPBE performs equally well due to its better prediction of binding energy. Lenchuk, Adelhelm, and Mollenhauer[171] found vdW-DF to best recreate the structural and thermodynamic properties of graphite and Li intercalated graphite. It was the only functional to correctly estimate the shape of the voltage step profile without the need for correction.

With no apparent *best* functional we ran calculations using the Grimme D2 functional correction term[106] championed by Chen et al.[58] as well as the optPBE non-local functional[153] as it gave close to experimental values for both metrics. This will allow a comparison of both the most common approaches to modelling vdW interactions, non-local functionals and empirical correction terms, for our system.

3.3.3 Nanoparticle

Our nanoparticle consists of 484 C atoms and is terminated with 108 H atoms. It is 4-layers thick with each layer consisting of 121 carbons and 27 hydrogens (figure 3.2). This structure was constructed using *Materials Studio*[37]. Dangling carbon sigma bonds are terminated with H atoms because it is a naturally occurring structure, described by Andersson et al.[9]. This size of structure is considerably smaller than even the smallest nanoparticles used in anodes which typically consist of 1000s of atoms.[9] This size was chosen as it has been shown that polycyclic aromatic hydrocarbon (PAH) dimers reach an assymtopic limit of interaction energy with increasing monomer C atom count[300]. Circumcoronene ($C_{54}H_{18}$) was shown by Totton, Misquitta, and Kraft[300] to be approaching that limit. A similar limit was observed with the binding energy PAH adsorbing on to graphene with respect to number of aromatic rings by James and Swathi[142]. We use this limit as a guide for our individual layer size. By more than doubling the C atom count in each sheet, compared to that of Circumcoronene, we are confident that our system is close enough to the limit to exhibit graphite-like binding energies. To ensure the completion of our calculations in a reasonable time frame, a necessity to validate the methods we wish to look at in this paper, we abstain from increasing the size of our nanoparticle further. The structure has enough layers

to exhibit most of the natural properties of Li intercalation, such as staging and stacking which need several layers of C atoms to occur. Although, we do expect differences compared to bulk staging as evidence points to a minimum of 8 layers required to fully describe this process.[166]

Graphite-like structures such as this can be intercalated up to the LiC_6 limit. A 484 C atom nanoparticle should therefore have around 80 Li sites. However, this is not a bulk structure and adsorption occurs both above and below the nanoparticle. Therefore an extra layer of sites needs to be accounted for. This would increase the number of lithiation sites to approximately 100. However, for the reasons that will be explained in section 3.3.5, only the 60 internal Li intercalations are modelled. It should also be noted, given the geometry of our nanoparticle, if we were to assume all Li is perfectly spaced, as we discuss in section 3.4.5, then the maximum Li intercalation limit is 42.

All nanoparticle calculations were performed using the generalised gradient approximation (GGA) exchange-correlation functional, PBE[224] with the Grimme D2[106] dispersion correction or using the non-local optPBE functional[153] (c.f. section 3.3.2). We use a kinetic energy cut-off value of 830 eV and a NGWF radii of $9.0 \text{ } a_0$. The core electrons are represented using projected augmented waves (PAW)[40] from well-established[29] GBRV pseudopotential library.[95] For Li, all electrons were treated as valence because we expect Li electrons to move from the Li to the graphite structure. We do not want to artificially restrict this charge transfer by treating the $1s_2$ electrons as core electrons. Calculations were performed with ensemble-DFT (EDFT)[251] (c.f. section 1.3.3), spin polarisation, and utilised the quasi-Newton Broyden-Fletcher-Goldfarb-Shanno (BFGS) algorithm due to its stability and efficiency[263]. Our geometry optimisation calculations use a displacement convergence tolerance of $1.5 \times 10^{-2} a_0$, an energy convergence tolerance of $1.5 \times 10^{-6} E_h$, and a force convergence tolerance of $3 \times 10^{-3} E_h a_0^{-1}$. Periodic boundary conditions have been used. A sufficiently large, cubic simulation cell with volume $2.362 \times 10^5 \text{ } a_0^3$ was used to reduce interactions between the nanoparticle and its periodic images. [127, 230] This gives us a vacuum between particles of over $53 \text{ } a_0$ inline with the nanoparticle planes and $74 \text{ } a_0$ orthogonal to the nanoparticle planes (c.f. figure 3.2).

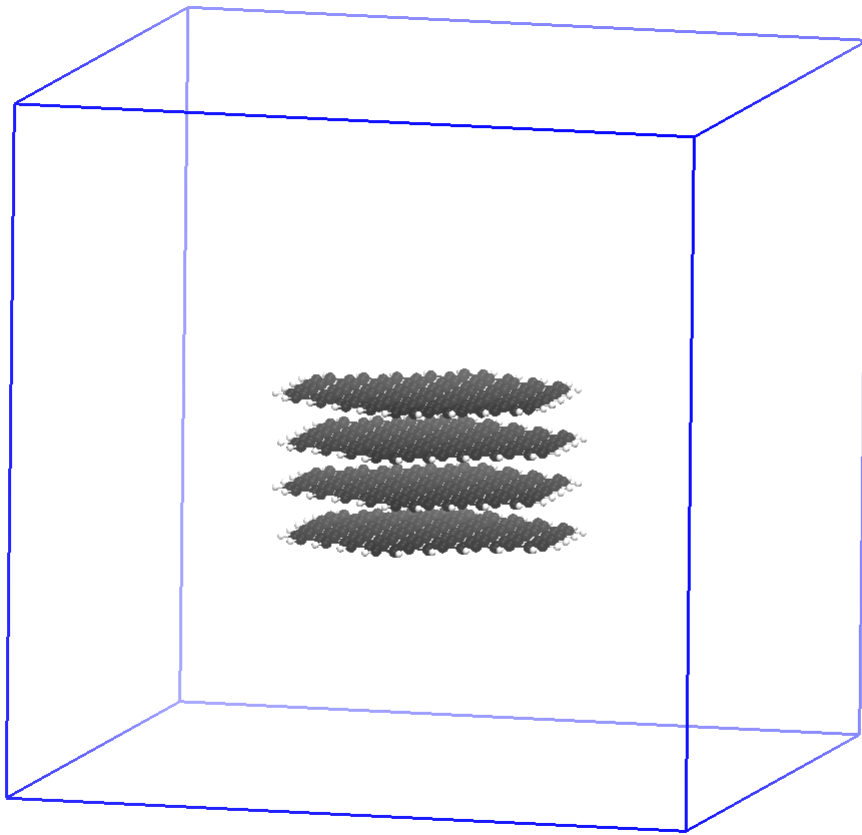


Figure 3.2: Our nanoparticle in a $50\text{\AA} \times 50\text{\AA} \times 50\text{\AA}$ simulation cell

3.3.4 Intercalation Process

To place highly polarizable Li atoms in a structure, the optimal sites of intercalation need to be found. Chevrier and Dahn did this for amorphous Si anodes by identifying the largest open spaces available to the ion.[61] Shen, Horton, and Persson did this via the use of charge density (c.f. section 3.2).[266]. We use the electrostatic potential minimum. The main interaction between an intercalated Li atom and the graphite is electrostatically driven. Therefore, using the electrostatic potential as a guide for finding favourable intercalation sites is a reasonable assumption to make.

Here, we describe the practical procedure of the calculations undertaken. First, our initial unintercalated structure is relaxed with a DFT geometry optimisation. The electrostatic potential of this relaxed structure is output as a voxel cube file in ONETEP. We find the minimum value voxel in the simulation cell and translate the voxel's position to real space Cartesian coordinates. We then place a Li atom at this position. The script that processes the voxel cube file is provided in thesis data. Then, we relax the structure with the newly-added Li atom, find the position where electrostatic potential of this new structure is minimum and place the next Li atom at the position of this minimum. We then run a single point calculation, find the position where electrostatic potential is minimum, and place the third Li atom at this minimum. We repeat this process alternating between single point calculations and full geometry optimisation calculations until our structure is fully lithiated. Single point calculations are considerably lower in computational cost and given that our structure is relaxed regularly we do not expect a significant change in Li placement. We also perform a full geometry relaxation on our final structure. The workflow of this process is demonstrated in figure 3.3

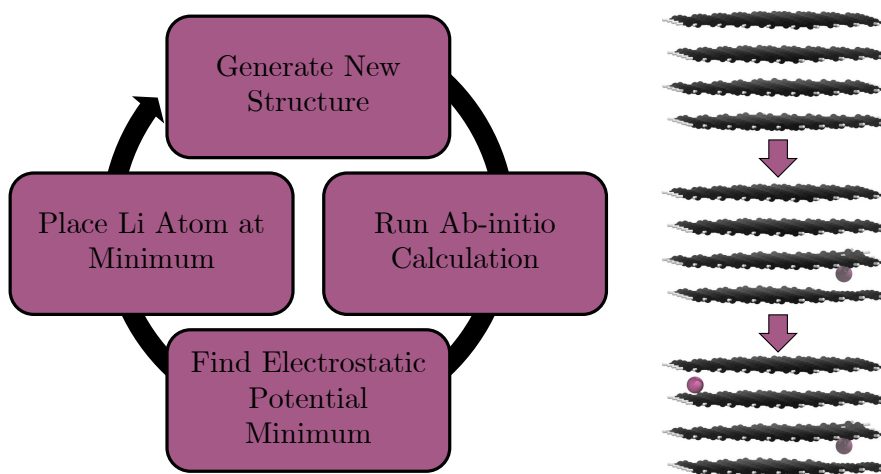


Figure 3.3: The workflow employed (left) to intercalate a graphite nanoparticle (right) with Li atoms using the electrostatic potential as a guide for Li placement. Li atoms are in pink, C atoms in black, and H atoms in white.

This workflow while simplistic does allow a relatively fast computation of what a Li intercalation process could look like. Improvements to this procedure are discussed in section 3.6.4.

3.3.5 Placement restriction

Initial nanoparticle calculations with the PBE-D2 functional had no restrictions on where the lithium could be placed. We observed pseudo-stage II lithium distribution up to the 21st lithiation (c.f. figure 3.4b) if we ignore the Basal plane adsorption. After this, populating of the central layer occurred and the structure became stage I. As we continued to lithiate, Li-metal accumulation on the basal planes was observed (c.f. figure 3.4c).

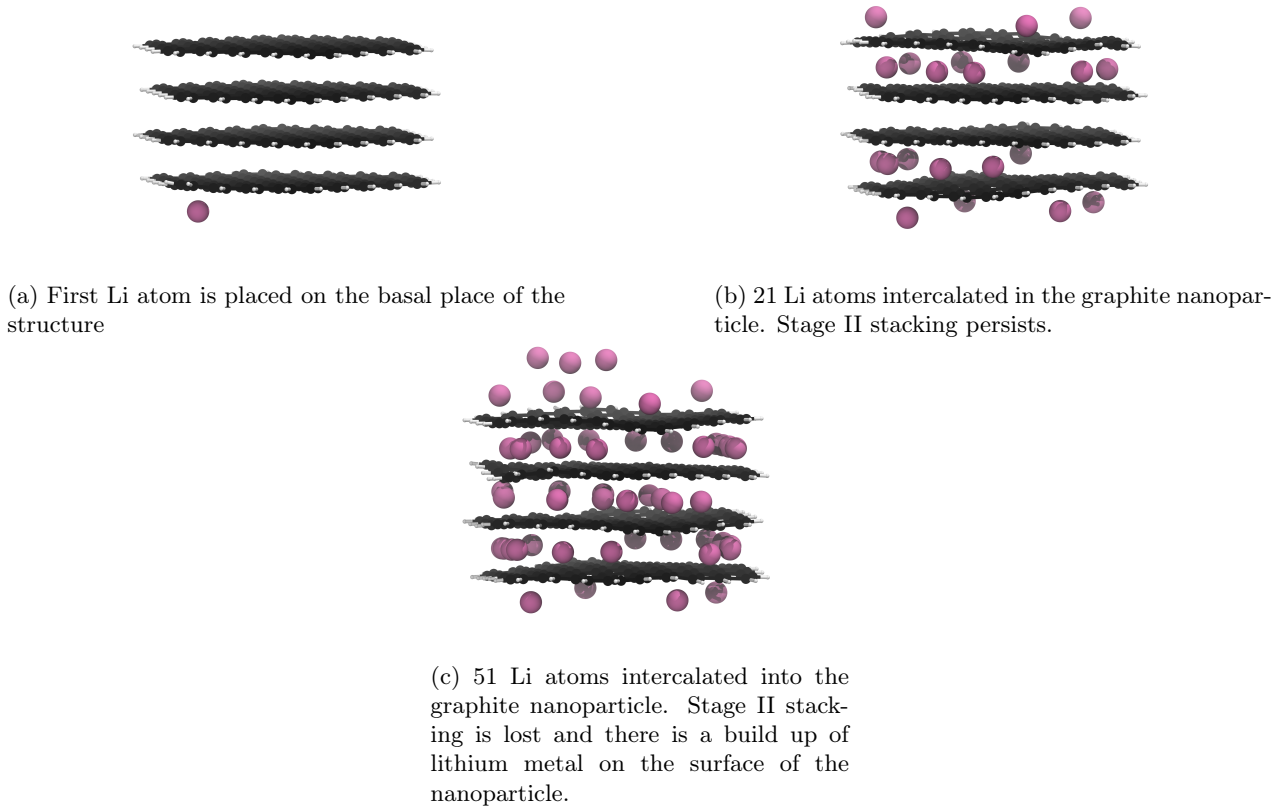


Figure 3.4: Li intercalation of graphite nanoparticle with unrestricted placement of Li. Li atoms are in pink, C atoms in black, and H atoms in white.

The results yielded from the unrestricted placement of Li warrant further investigation, particularly with reference to Li-metal formation being more favourable than intercalation. Li-plating on anodes is an active area of research[20, 221] and is a topic that should be pursued in another project. Li on individual layers are not expected to interact significantly with Li on other layers[226]. For this reason we restricted lithium placement between the highest and lowest carbon atoms along the z-axis as any atoms adsorbed on the basal plane are unlikely to affect the internal structure. Because adsorption has been prevented, 60 Li atoms is now the theoretical maximum intercalation.

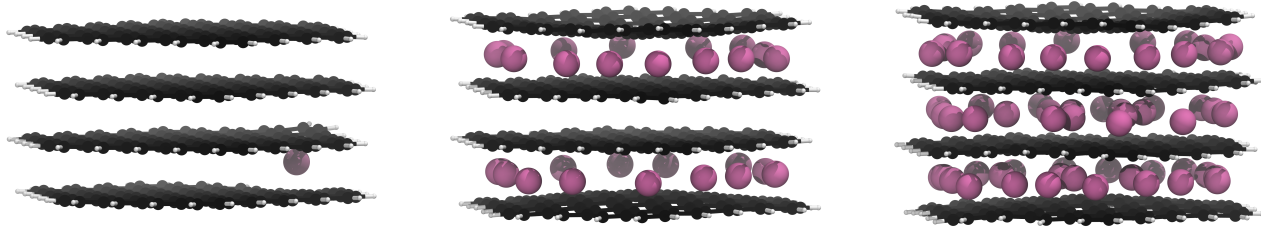
In our optPBE functional calculations the structure of the graphite sheets became so flared that the Li were still able to adsorb to the basal plane as they could technically still be placed on the basal plane but below/above the highest/lowest C atom. To prevent this we added a 1 Å lithiation restriction zone around the highest and lowest C atoms.

3.4 Results and Discussion

Using the procedure described in sections 3.3.4 and 3.3.5 we intercalate our nanoparticle with Li atoms consecutively. This process is performed twice with different exchange-correlation functionals: PBE, with the D2 correction term, and optPBE (c.f. section 3.3.2).

3.4.1 Structure

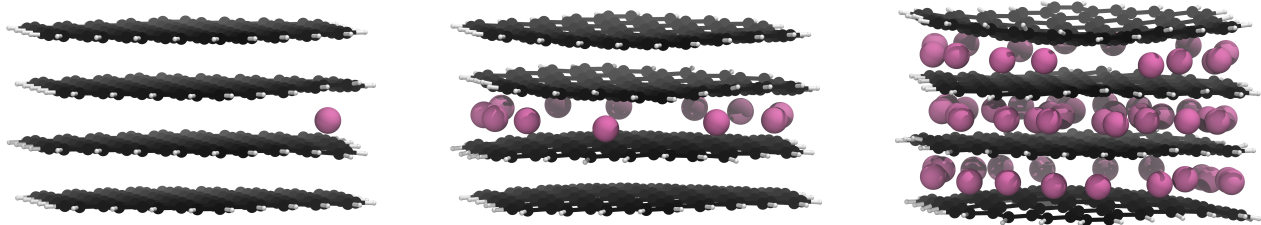
For the PBE-D2 functional we observe the formation of a stage II structure up to the 29th lithiation (c.f. figure 3.5b). This is approximately half of the theoretical lithiation maximum for intercalation of internal layers. If our system had aligned with the staging mechanism observed in bulk graphite[194], all sites in the upper and lower layers would be occupied before the filling of the central layer, i.e. a stage II structure up to the 40th lithiation. Further lithiations past the half-lithiated (30 Li) structure result in an early collapse to a stage I structure as the central layer is populated. The formation of a stage II structure is a promising result and demonstrates that the nanoparticle follows similar behaviour to what was observed by computational studies on bulk graphite.[194, 226].



(a) 1st lithiation, Li atoms fill the lower and upper layers after this point. (b) 29th lithiation, Li atoms start filling the central layer after this point. (c) 60th lithiation is the theoretical maximum lithiation.

Figure 3.5: Significant geometry optimised GIC structures from Li intercalation with Li placement restrictions (c.f. 3.3.5), using PBE with the D2 correction term. Li atoms are in pink, C atoms in black, and H atoms in white.

A similar pattern is observed for our optPBE calculations, whereby the initial intercalation layer choice makes future intercalations into that layer more likely (c.f. figure 3.6a). However, because our initial Li intercalation occurs in the central layer, with half as many possible sites available for stage II population, the breakdown to stage I occurs earlier (c.f. figure 3.6b).



(a) 1st lithiation, Li atoms fill the central layer after this point. (b) 12th lithiation, Li atoms start filling the upper and lower layers after this point. (c) 60th lithiation is the theoretical maximum lithiation.

Figure 3.6: Significant geometry optimised GIC structures from Li intercalation with Li placement restrictions (c.f. 3.3.5), using the optPBE correction functional. Li atoms are in pink, C atoms in black, and H atoms in white.

In both the optPBE and PBE-D2 calculations the early breakdown of stage II to stage I is observed. This breakdown is unlike the dilute phase transitions that are observed by Dahn[67] and is instead due to the intercalation model preferring Li placement around the edges of the nanoparticle. We discuss the cause of this edge site preference in later sections (c.f. 3.4.2 and 3.4.5). The preference appears to be strong enough to forgo population in the centre of an already populated layer for an edge site on a different layer.

Both generated final structures (figures 3.5c and 3.6c) have an uneven distribution of Li atoms in individual layers. In the PBE-D2 structure, the upper layer has 17 Li atoms, the middle has 21 atoms, and the lower has 22. For optPBE, the disparity is more pronounced with the upper layer having 15 Li atoms, the central layer having 27 Li atoms, and the lower layer having 18 Li atoms.

This uneven distribution can be partially attributed to the preference of Li to populate the edges of the nanoparticle. This is because the edge-site preference is strong enough to overcome intra-layer Li-Li repulsion interactions thereby increasing the maximum capacity of individual layers in the nanoparticle. In the final structure for our PBE-D2 calculations (c.f. figure 3.5c) some Li atoms were found to be within 2.7 Å of each other, as opposed to the 4.3 Å typically observed in bulk GICs. The same is true for our optPBE calculations. These structures are not fully saturated as there are numerous lithiation sites unfilled in the centre of the upper and lower layers. This is surprising, as if this were realised in experiments it could provide a route to exceeding the 372 mAhg⁻¹ theoretical limit of energy storage for graphite without the stacking of layers of solid Li, as was observed by Kühne et al.[160]

A theoretical study on how the particle size distribution of graphite affects the cell performance is presented by Röder et al.[247] In this paper, they find that distributions with smaller graphite nanoparticles are less likely to degrade and have higher internal capacities compared to distributions with larger particles. Our observations of closer than typical Li placement in our nanoparticle could partially explain the increased capacity observed by Röder et al.[247]

While lithiation occurs primarily around the edge sites, at later intercalations, both functionals begin to favour the filling of the centre of the central layer over available edge sites on the upper and lower layers. This phenomenon appears earlier in the optPBE calculations than in the PBE-D2 calculations. This led to the final structure of our optPBE calculations (c.f. figure 3.6c) having a significantly more heavily populated central layer than its PBE-D2 counterpart (c.f. figure 3.5c). This demonstrates the drastic effect that different interpretations of the long-range forces have on the electrostatic potential of GICs. The earlier population of the centre of the nanoparticle in our optPBE calculations indicates either that the electrostatic potential is lowered in the centre of the central layer or the edge site electrostatic potential is raised at the upper and lower layer edge sites relative to our PBE-D2 calculations. We find the latter of these conclusions to be more likely for the reasons given below.

In our PBE-D2 calculations, we observe a 19.7% increase in interlayer spacing at the edges of the nanoparticle, where the majority of the lithiation occurs, and a 7.5% increase at the centre of the nanoparticle, where less lithiation occurs. For our optPBE calculations, we observe a 17.4% increase at the edge and a 2.88% decrease in the centre. It is likely that the geometry of our structures, decided in part by the interpretation of the long-range forces, is the direct cause for the different preferences of edge and centre sites between both functionals. The decreased space afforded to the edge sites in the optPBE calculations relative to the PBE-D2 calculations likely meant the electrostatic potential was slightly higher and the global minimum was now located within the relatively unaffected centre of the central layer. Experimental results observe a uniform 10.4% increase in interlayer spacing when comparing graphite (3.35 Å) to its fully lithiated GIC (3.70 Å)[274]. We would expect a larger increase in interlayer spacing in our nanoparticle compared to bulk calculations due to our structure being intercalated in a vacuum. This is because the nanoparticle lacks the pressure along the z-axis which is present in bulk graphite and serves to compact the structure. While this explains the larger than bulk graphite increases at the edges, it does not explain optPBE's decreasing centre, particularly when considering that the centre of the optPBE nanoparticle is more filled than its PBE-D2 equivalent. One possible description of this effect is that due to the lower uniformity of Li distribution and the lack of external pressure on the outer graphite layers increased deformation was allowed to occur. This increased "flaring" of the outer graphite layers can only be attributed to optPBE's interpretation of long-range forces. For PBE-D2 The C-C bond length increases by 0.012 ± 0.007 Å as we intercalated to 60 Li. For optPBE the bond length increased by 0.015 ± 0.007 Å. This bond length increase occurs primarily around the edges where the H termination occurs causing shorter C-C bonds due to the slight electronegativity difference (c.f. section 3.4.2). We do not anticipate this small an increase in bond length and therefore surface area to have a significant effect on properties such as Li capacity.

Given the uniqueness of our structure and how little literature there is surrounding the intercalation of graphite nanoparticles, it is hard to say which method out of optPBE and PBE-D2 generates the most realistic structure. For this reason, we will continue with the analysis of both.

We observe no shift from an AB to an AA structure, something we would expect to see if this were a bulk structure. We explore the cause behind this in section 3.4.5.

3.4.2 Mulliken Population Analysis

To obtain some insight into the distribution of charges, we use Mulliken population analysis[202] to partition the total charge density into point charges associated with individual atoms as intercalation occurs.

The Mulliken population analysis[202] allows us to monitor how the electron population associated with each atom evolves as more lithium is intercalated.

A molecular orbital (MO), ψ_i , can be constructed from a linear combination of atomic orbitals (LCAO), χ_m localised around an atom, k , in the following manner.[203]

$$\psi_i = \sum_{m_k} c_{im_k} \chi_{m_k} \quad (3.2)$$

Where c_{im_k} is the occupancy of each AO. The MO's population, $N(i)$, can be split into *net atomic population* and *overlap population* terms.

$$N(i) = N(i) \sum_{m_k} c_{im_k}^2 + 2N(i) \sum_{l>k} c_{im_k} c_{in_l} S_{m_k n_l} \quad (3.3)$$

By summing *net atomic population* with half of the *overlap population* we can obtain the *gross atomic population* on a given atom, which can then be written as

$$N(k) = N(c_m^2 + c_m c_n S_{mn}) \quad (3.4)$$

we can rewrite this for a general case

$$N(i; m_k) = N(i) c_{im_k} \left(c_{im_k} + \sum_{l \neq k} c_{in_l} S_{m_k n_l} \right) \quad (3.5)$$

where $N(i; m_k)$ is the partial gross population in MO ψ_i and AO χ_{m_k} on atom k . The subtotal in ϕ_i on atom k can be found by summing equation 3.5 for all orbitals.

$$\sum_m N(i; m_k) = N(i; k) \quad (3.6)$$

The total gross population in χ_{m_k} can be found by summing equation 3.5 for all of ψ_i .

$$\sum_i N(i; m_k) = N(m_k) \quad (3.7)$$

We can now define the *gross charge* on an atomic orbital or an atom as

$$Q(m_k) = N_0(m_k) - N(m_k) \text{ and } Q(k) = N_0(k) - N(k) \quad (3.8)$$

where $N_0(m_k)$ is the number of electrons in χ_m and $N_0(k)$ is the number of electrons in the ground state of atom k .

For both functionals, in the unlithiated structures, this technique reveals that the edge C atoms, those directly bonded to H atoms, have a slight negative charge due to the difference in electronegativity (c.f. figure 3.7a and 3.7c). This leads to Li placement at sites closer to the more negatively charged C atoms. The placement of Li atoms at edge sites, which donate their electrons to the graphite structure (c.f. section 3.4.3), exacerbates the effect leading to more negatively charged edges in the lithiated structures (figure 3.7b). Another possible cause for the edge accumulation of Li atoms is the topological spin polarisation of the graphite edges as was observed by Peng et al. [220] The authors note the prevalence of this effect is most extreme for zig-zag edges that are H-terminated. However, upon analysing the spin density of our nanoparticle at various stages of lithiation we saw no evidence of spin polarised states emerging as the ground-state.

For both our calculations it is apparent that places where Li has intercalated result in a greater population of electrons in the surrounding carbons (c.f. figure 3.7b and 3.7d). This replicates what has been observed in the literature for bulk graphite.[132]

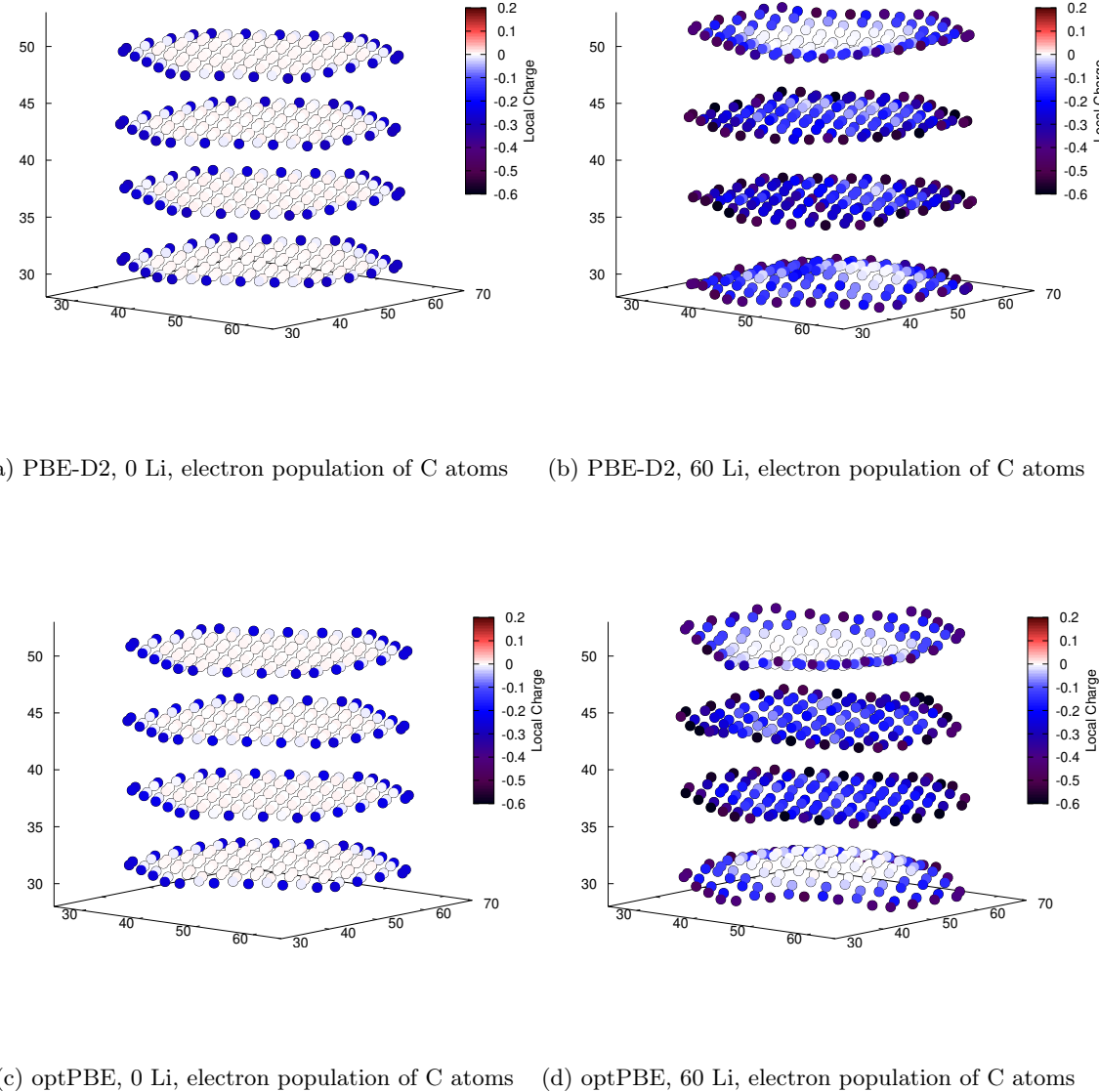


Figure 3.7: Mulliken population analysis for C atoms for the fully unlithiated (a and c) and fully lithiated (b and d) graphite nanoparticles. The axes are the spatial coordinates within the simulation cell in bohr and the colour indicates the charge of individual C atoms. More detailed images for all individual atoms can be found in SI:2

Looking at the mulliken charges of all elements in figures 3.8 and 3.9 we can see the inter-element disparity in charge more clearly

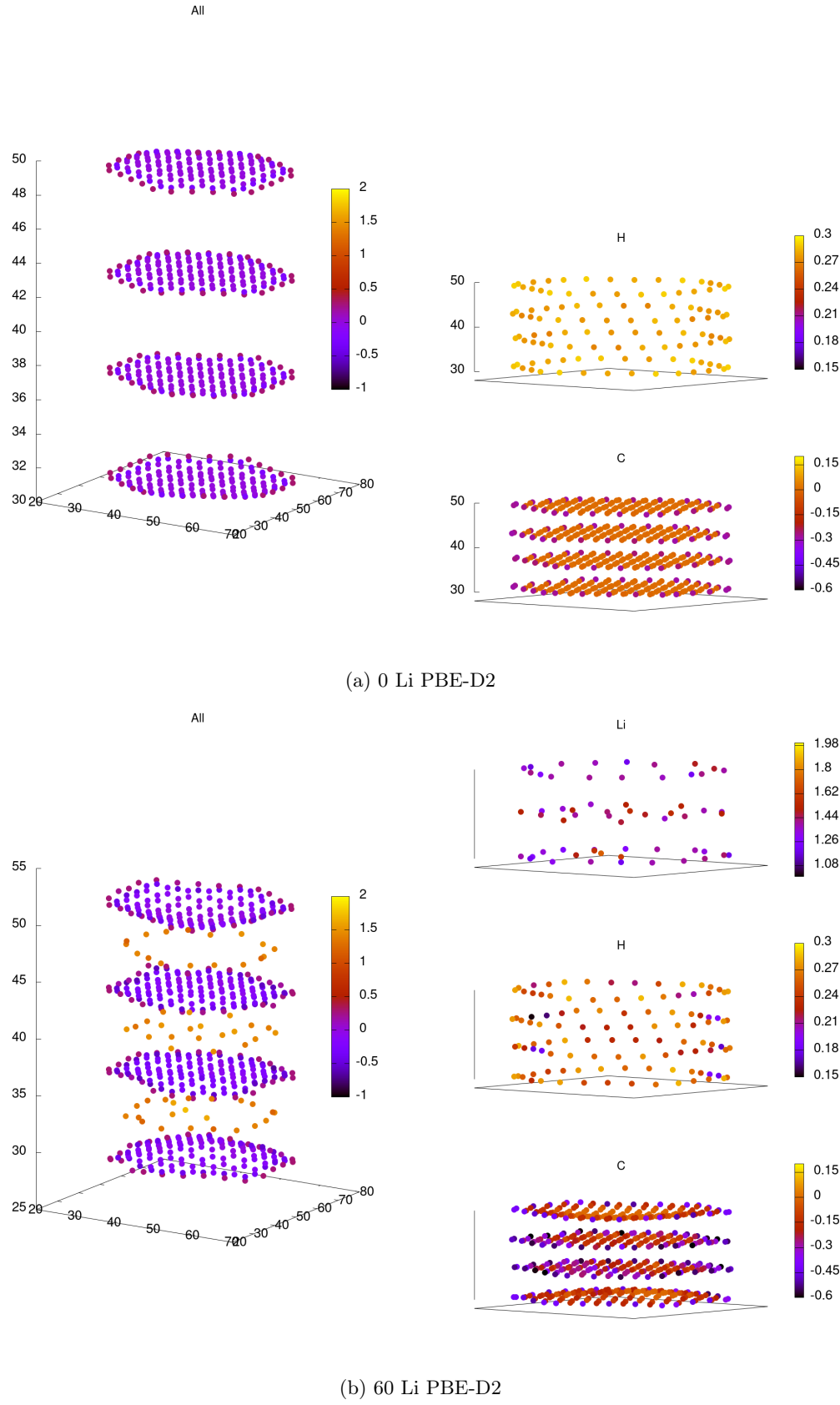


Figure 3.8

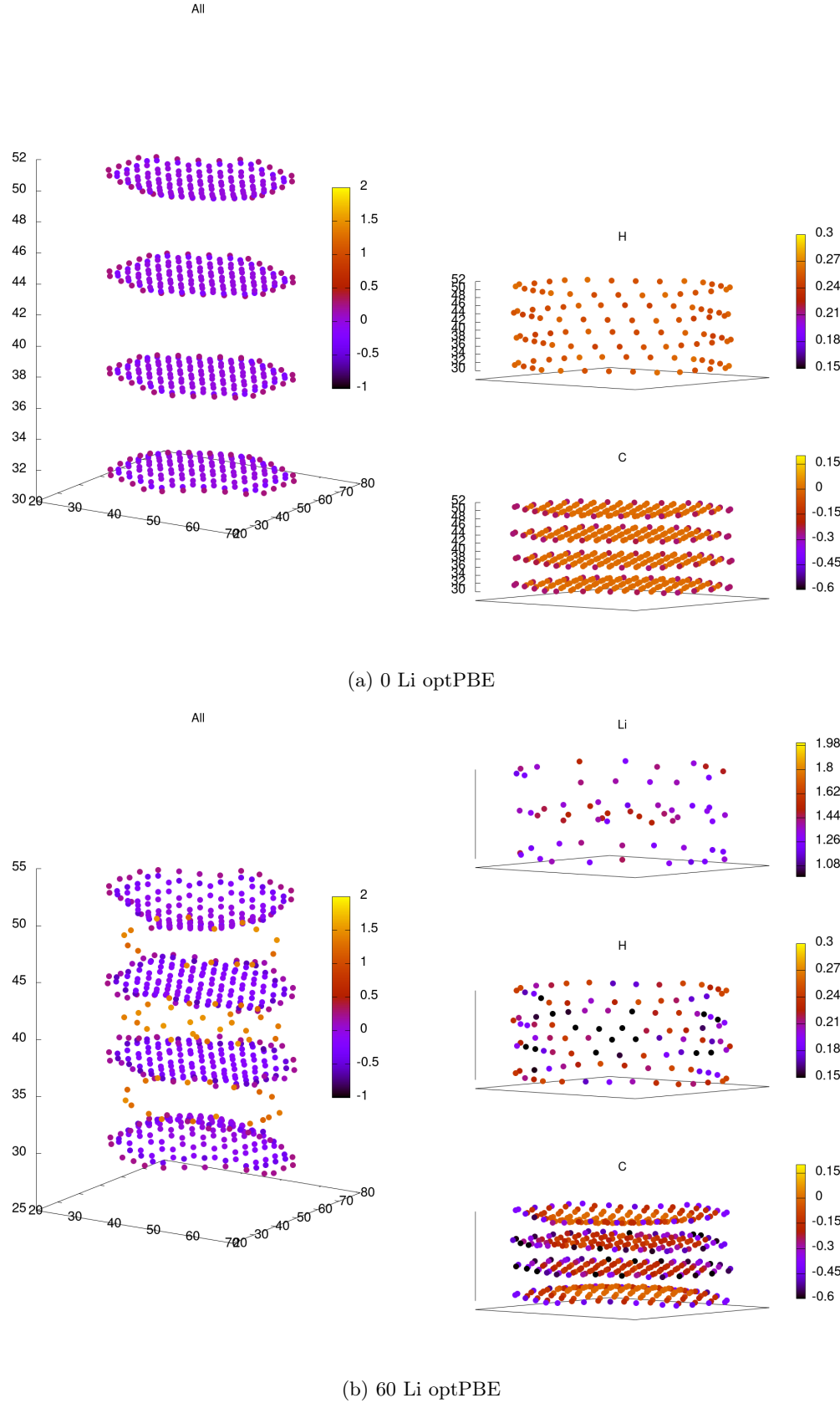


Figure 3.9

Mulliken population analysis has some known flaws. Such as an unrealistic build up of electron density on electropositive atoms[34, 203], sensitivity to different basis sets[182] and a poor representation of compounds with significant ionic character[64]. These issues are addressed with more modern techniques, such as the derived electrostatic and chemical (DDEC) approach[185] or natural population analysis[237]. In future work, we hope to use these techniques to compliment this analysis.

3.4.3 Density of States

Further evidence for the transfer of electrons from the Li to the graphite nanoparticle can be found by examining the electronic density of states (DOS).

Comparing the total DOS (TDOS) of the nanoparticle to that of its fully lithiated counterpart and shifting both graphs so their Fermi levels occur at 0 reveals a shift in the TDOS to the left as lithiation occurs (c.f. figure 3.10). The increase in states below the Fermi level with lithiation is predictable for a system to which we add more electrons. However, by analysing the partial DOS (PDOS) (c.f. figure 3.11) for individual angular momentum channels and the local DOS (LDOS) (c.f. figure 3.12) for each atom type, we can assign the electrons being added largely occur in the C 2p states and very little is added to the Li 2s states. This is clear evidence of the donation from the intercalant band to the graphitic band.

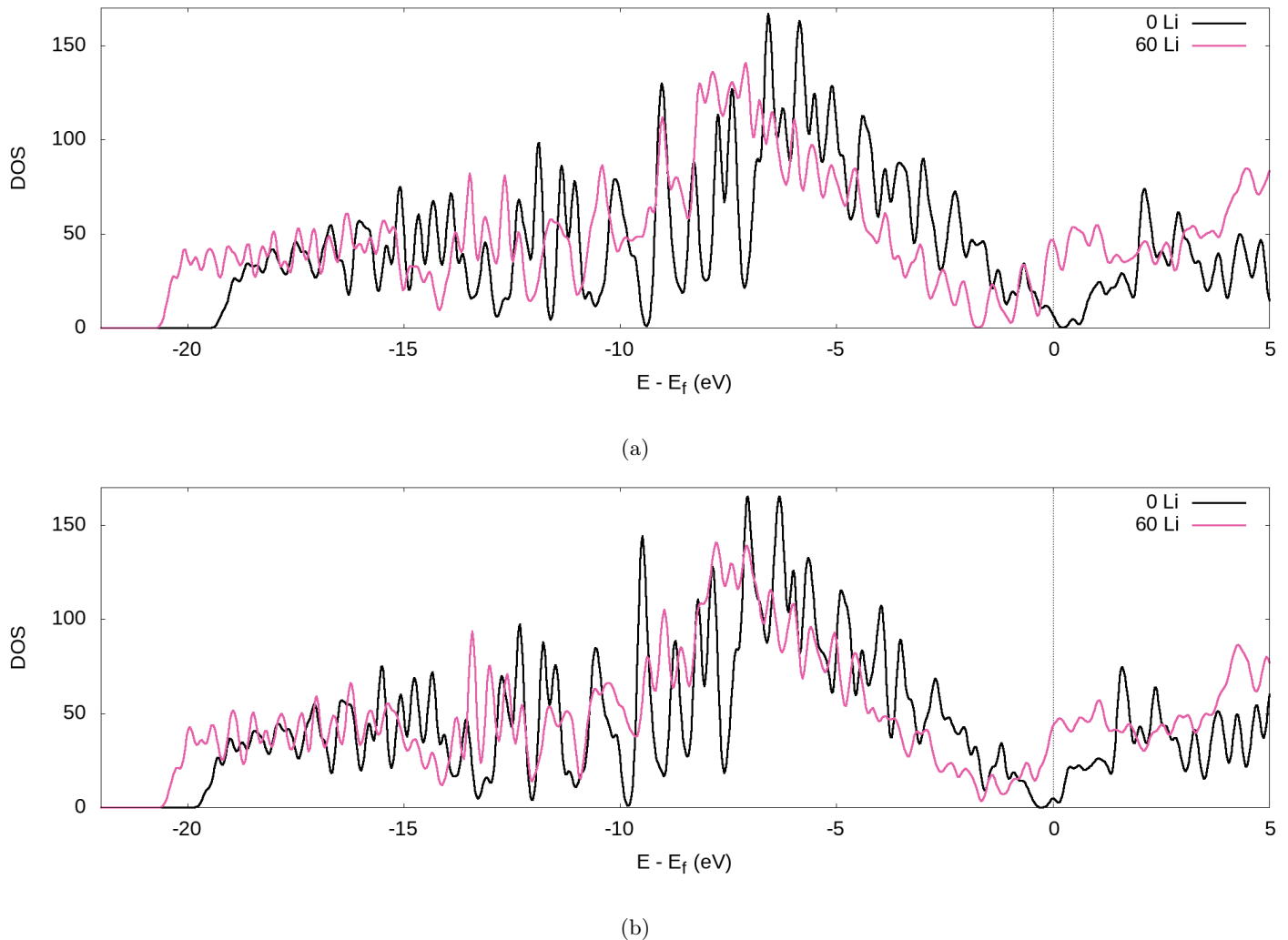


Figure 3.10: TDOS of the graphite nanoparticle compared to the fully lithiated graphite nanoparticle, for our (a) PBE-D2 and (b) optPBE calculations.

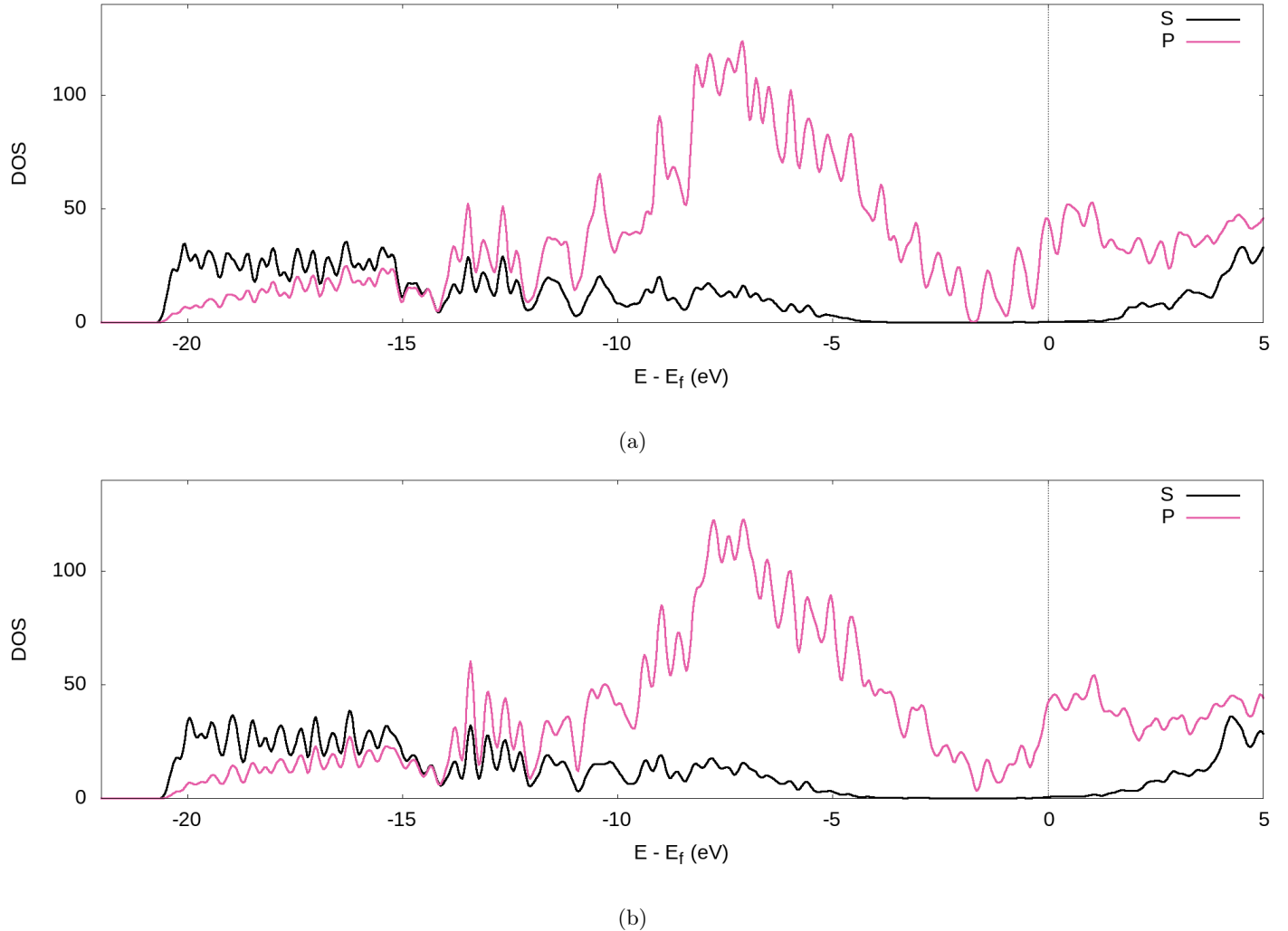


Figure 3.11: PDOS of the fully lithiated graphite nanoparticle, for our (a) PBE-D2 and (b) optPBE calculations.

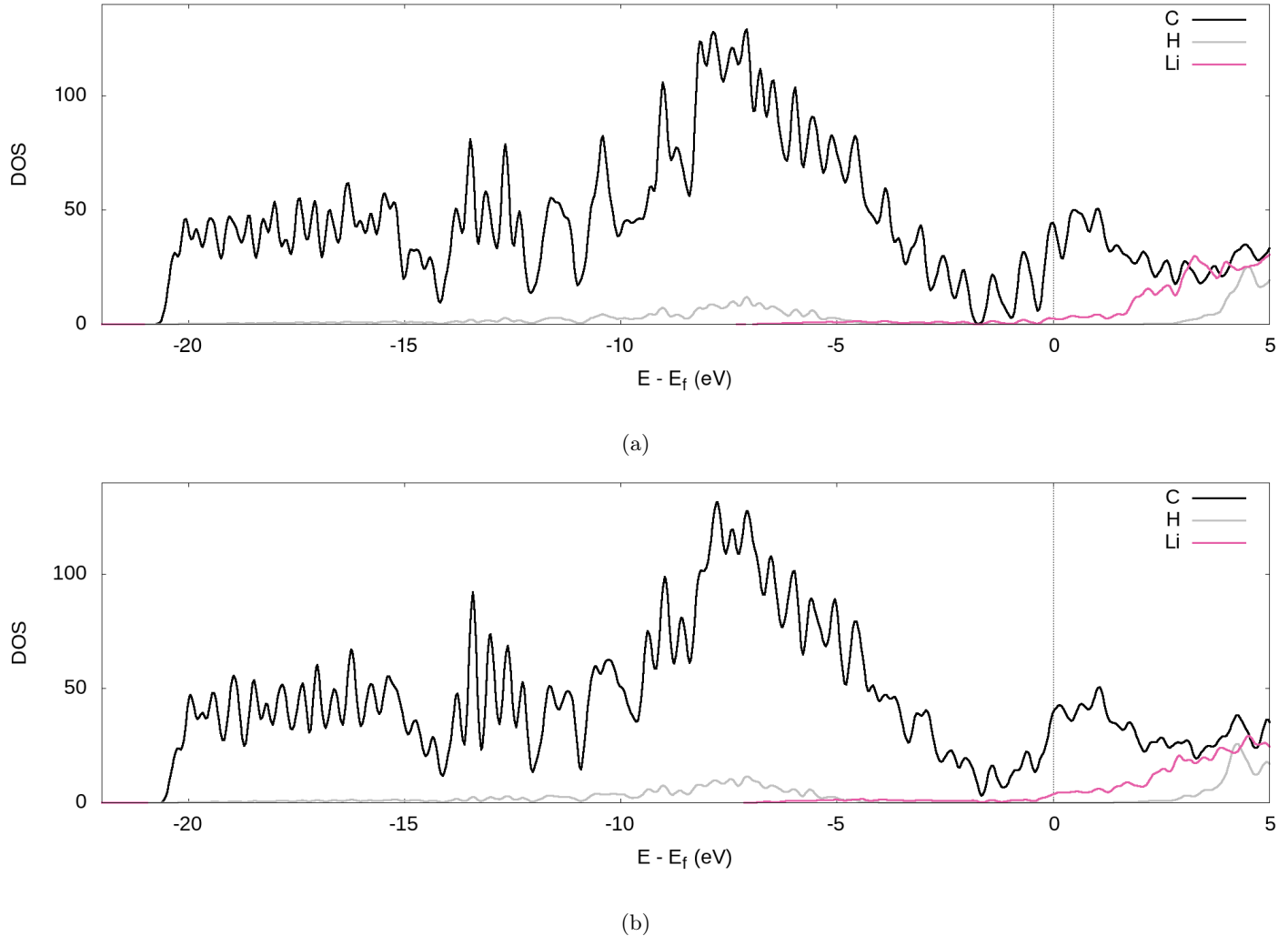


Figure 3.12: LDOS of the fully lithiated graphite nanoparticle, for our (a) PBE-D2 and (b) optPBE calculations.

These findings are supported by previous theoretical studies on bulk graphite[121, 132, 248, 339] and experimental studies[188]. The experimental findings of Mathiesen et al. went on to associate the charge transfer with the elongation of the interlayer carbon interactions and subsequent staging processes.[188] Something we observe in our structure (c.f. section 3.4.1).

3.4.4 Voltage Step Profiles

We can directly compare the results of the intercalation procedure to that of experiment by computing a thermodynamically relevant observable quantity, the intercalation voltage. The Li intercalation reaction into the graphite nanoparticle, G, can be written as



where, n is the number of intercalated Li into the graphite nanoparticle: $n = 0$ for a fully unlithiated graphite structure and $n = N$ for a fully lithiated graphite structure ($N = 60$ for our graphite nanoparticle (c.f. section 3.3.5)). To plot a voltage step profile from *ab-initio* calculations, we need to find the ground-state structures during lithiation of the graphite nanoparticle. These structures can be found by plotting the formation energy (E_f) against the number of Li intercalated (n) and connecting these points by a lower convex hull. The ground-state structures are those that lie on this convex hull. The formation energy of lithiated graphite nanoparticles can be calculated with respect to the two end states of fully unlithiated ($n = 0$) and fully lithiated ($n = N$) as:

$$E_f(n) = E_{\text{Li}_n\text{G}} - \left(1 - \frac{n}{N}\right) E_{\text{G}} - \frac{n}{N} E_{\text{Li}_N\text{G}}, \quad (3.10)$$

Here E is the DFT calculated energy. We can ignore the contributions of entropy at 0 K, while Pressure-volume contributions are also expected to be small.[19, 138, 194, 244] The calculated formation energy (E_f) is shown in figures 3.13a and 3.13b for the geometry optimized structures. We draw the convex hull using the convex hull finder QHULL[22].

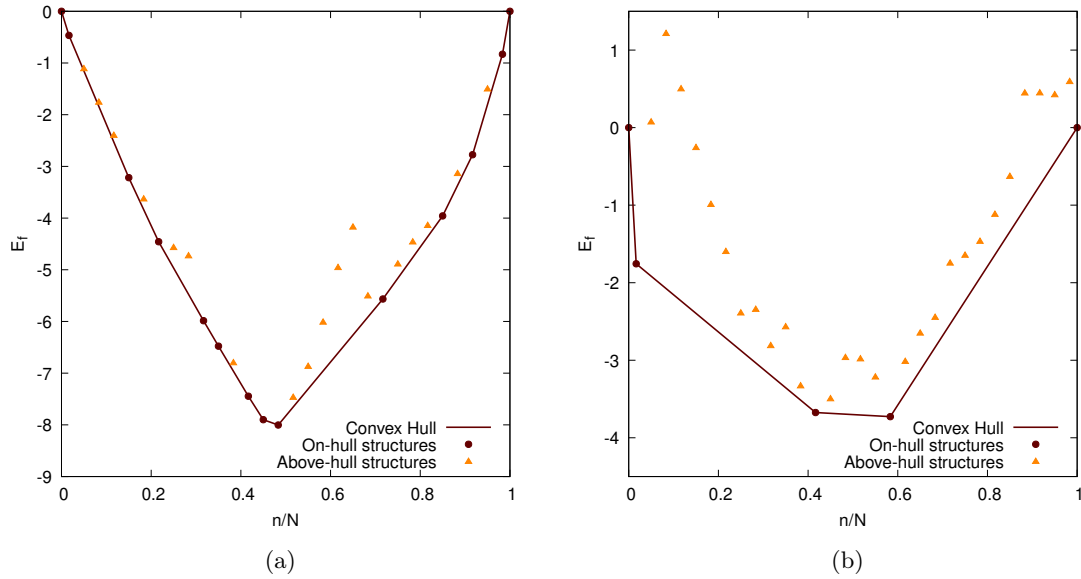


Figure 3.13: The formation energy of the Li intercalated graphite nanoparticles as a function of the degree of lithiation (n/N). $N = 60$ for our graphite nanoparticle, cf. sec. 3.3.5 The Li intercalation proceeds via the convex hull (shown as brown line). The points on the convex hull (shown as brown circles) are the ground-states. The structures above the convex hull are shown with yellow triangles. Two different DFT functionals are considered: (a) PBE-D2 and (b) optPBE

The Li intercalation process proceeds along the convex hull via the identified ground-state structures. The intercalation reaction from a ground-state with n_1 Li to the next ground-state with n_2 Li can be written as



The intercalation voltage produced during this intercalation step from n_1 to n_2 can be calculated from the Nernst equation:[19]

$$V_{n_1 \rightarrow n_2} = -\frac{\Delta E}{e\Delta n} = -\frac{E_{\text{Li}_{n_2}\text{G}} - E_{\text{Li}_{n_1}\text{G}} - (n_2 - n_1)E_{\text{Li(BCC)}}}{e(n_2 - n_1)} \quad (3.12)$$

where e is the elementary charge. We performed a separate calculation to calculate the energy $E_{\text{Li(BCC)}}$ of bulk lithium in its lowest energy body centred cubic (BCC) structure using the same calculation parameters as we used for the nanoparticle (c.f. section 3.3.4).

The intercalation voltage step profile is shown in figure 3.14 for both considered DFT functionals. PBE-D2 and optPBE nanoparticles vary in terms of shape and voltage range. With PBE-D2's profile occurring between approximately -0.4 and 0.9 V and optPBE's between approximately -0.2 and 1.75. The PBE-D2 voltage step profile has a very shallow initial step of about 0.2 V, whereas optPBE has an initial step of about 1.7 V. Both share an approximate plateau between 0.0 and 0.4 n/N . PBE-D2 has a drop just before 0.5 n/N before consistently decreasing. optPBE has two shallow drops in voltage occurring at around 0.4 and 0.6 n/N before plateauing. The PBE-D2 voltage step profile eventually decreases below 0 V at the around 0.9 n/N . For optPBE the drop below 0 V occurs much earlier at around 0.4 n/N . The drop below 0 V indicates that it has no longer become thermodynamically favourable for Li to intercalate into the nanoparticle at the position of lowest electrostatic potential.

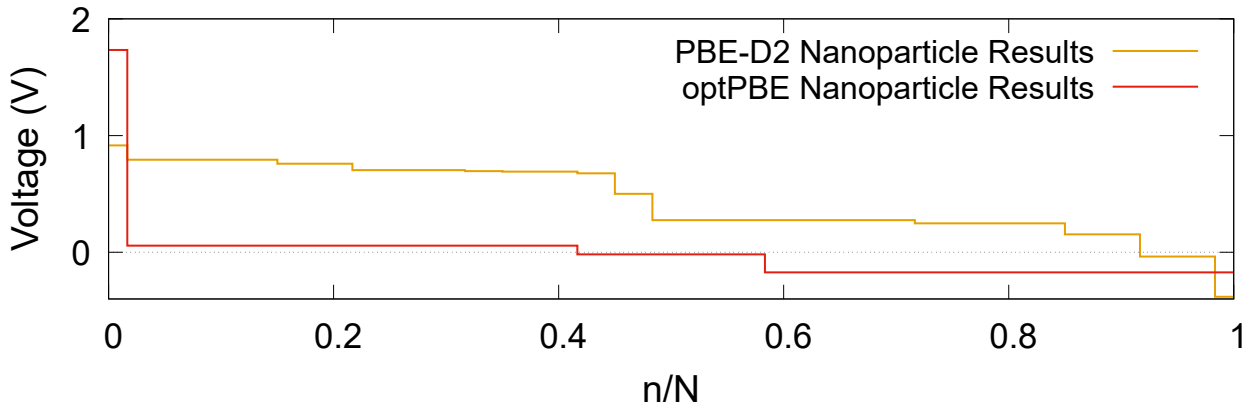


Figure 3.14: The computed Li intercalation voltage step profiles using two DFT functionals: PBE-D2 and optPBE

Given that our nanoparticle, when intercalated using both functionals, becomes saturated before reaching the theoretical maximum, discussed in section 3.3.3, we could elect to stop the intercalation as soon as intercalation becomes unfavourable. This is a more ‘natural’ method of determining our nanoparticle’s Li capacity. We visualise this in figure 3.16. Where N_0 is the number of Li atoms present in the on-hull structure that upon intercalation results in a negative intercalation voltage. A more intuitive visualisation for the the insertion energies of on-hull structures (c.f. figure 3.15). We calculate the insertion energy as a slight reformulation of equation 3.12:

$$E_{ins} = \frac{\Delta E}{\Delta n} = \frac{E_{Li_{n_2}G} - E_{Li_{n_1}G} - (n_2 - n_1)E_{Li(BCC)}}{(n_2 - n_1)} \quad (3.13)$$

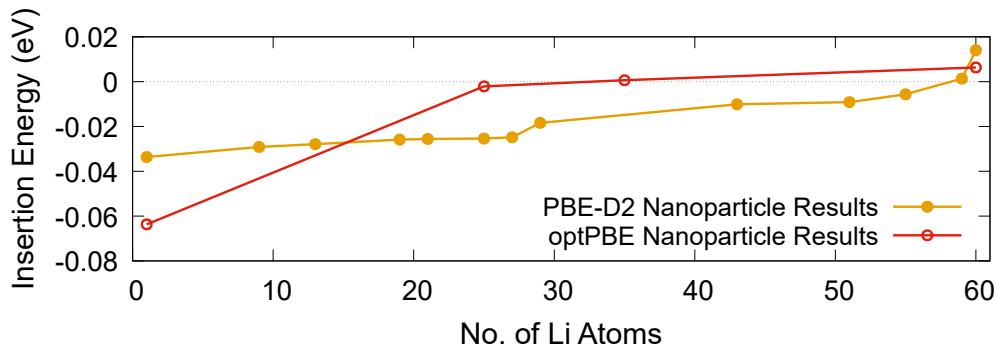


Figure 3.15: Insertion energy (eV) for on-hull structures with increasing lithiation for optPBE (red) and PBE+D2 (orange)

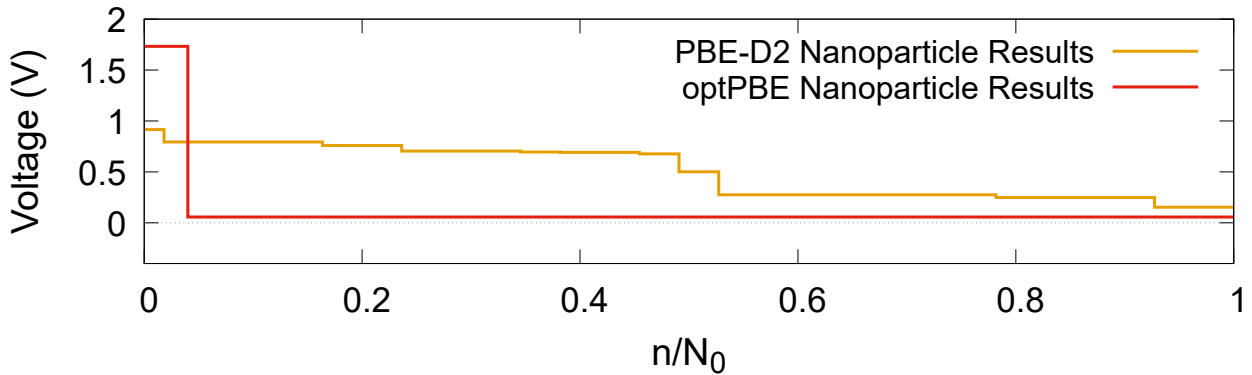


Figure 3.16: The computed Li intercalation voltage step profiles, where intercalation stops once it becomes thermodynamically unfavourable, using two DFT functionals: PBE-D2 and optPBE

For PBE-D2 the central decrease caused by the stage II to stage I transition is moved forward and more inline with that of experiment (c.f. figure 3.17b). For optPBE the result of this new saturation limit is less clear due to the lack of on-hull structures generated in figure 3.13b. For this reason we will use the theoretical maximum as our intercalation limit so we

can see how the voltage, beyond the thermodynamically unfavourable limit, evolves. We acknowledge that this means comparisons between experiment and our structure may not be as direct but we still believe they have value, particularly when comparing Li arrangements inside the nanoparticle.

Other computational results that have focused on the bulk graphite are shown in figure 3.17a and are compared to our nanoparticle results. Even when modelling bulk graphite, computational voltage step profiles appear to vary extensively in magnitude and shape. Several factors affect the plots in such a way such as the selection of a different pseudopotential, dispersion corrections, and the exchange-correlation functionals.

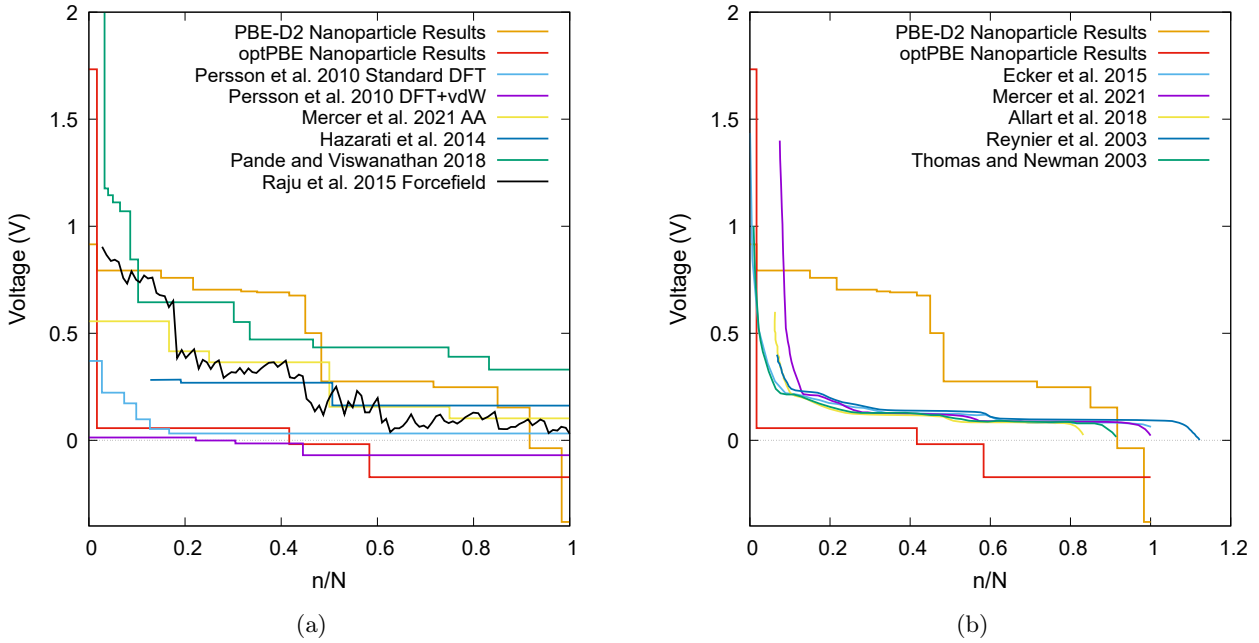


Figure 3.17: (a) A comparison of computational voltage step profiles with increasing lithiation adapted from references: Persson et al.[226], Mercer et al.[194], Hazrati, Wijs, and Brocks[125], Pande and Viswanathan[212], Raju et al.[232]. (b) a comparison of experimentally determined OCVs with increasing lithiation adaption from references: Ecker et al.[76], Mercer et al.[194], Allart, Montaru, and Gualous[6], Reynier, Yazami, and Fultz[243], Thomas and Newman[294].

We also compare our results with experimentally observed open circuit voltage (OCV) profiles in figure 3.17b. We note that PBE-D2 produces a voltage step profile that typically results in more favourable intercalations than that of experiment until the nanoparticle becomes saturated (i.e. when the voltage step profile becomes negative). Our PBE-D2 nanoparticle's voltage step profile's shape is also different from that of experimental OCVs (figure 3.17b). Some parallels can be drawn in terms of curve shape, such as the plateaus in both occurring around 0.1 to 0.5 n/N . The dip that occurs around 0.5 n/N in our PBE-D2 voltage step profile corresponds to the stage II to stage I transition is also present in experimental results. However, little resemblance can be observed beyond this point. Experimental results predict a plateau above 0.6 n/N whereas our PBE-D2 nanoparticle results continue to decrease. In comparison, our optPBE results predict a less favourable intercalation beyond the first intercalation with respect to experiment. According to this profile, it is apparent that optPBE predicts no favourable intercalation for this structure beyond the 0.4 n/N lithiation. When comparing the shape of this profile to that of experiment we see that the plateaus occurring at around 0.1 to 0.5 n/N are loosely replicated, the decrease at 0.6 n/N and the plateau from 0.5 to 1 are replicated well. We can conclude from this comparison that there is a significant difference between intercalation behaviour in our nanoparticle and that of bulk scale charging of an experimental anode. We can also conclude that, with the methodology we implement, the choice of functional has a large impact on the intercalation voltage, either through the geometry of the structure they produce or their energetic interpretation of such structures, and a careful selection will need to be made in future work.

The differences between experimental plots and our nanoparticle results can, in part, be explained by the increased ratio of terminated C atoms in our system compared that of a larger, more realistic nanoparticle. Indeed, it has been shown in a number of theoretical studies that an increased H atom to C atom ratio has a noticeable effect on binding energy.[142, 175, 300] Given the well-documented sensitivity of the Li intercalation process to the interlayer binding of graphite, deviations are to be expected. We would also expect an experimental OCV to be effected by some of the different environmental factors such as having the experiment be performed at 298.15 K, the use of highly ordered pyrolytic graphite (HOPG), being mixed with carbon binder, being in a functioning lithium half-cell, or being in the presence of a mixture of ethylene carbonate and dimethyl carbonate as electrolyte which leads to the eventual formation of a solid electrolyte interphase (SEI). Whereas, our simulations occur in a vacuum, for a single nanoparticle of graphite, at 0 K and therefore would not exhibit any environmental effects. Another source of potential error is non-local DFT's known issue with modelling highly polarizable ions such as Li[48] due to the use of atomic rather than ionic volumes[105]. Anniés et al.[10] identify this issue for Pande and Viswanathan's[212] DFT based Ising model which performs well for low Li abundance stages

but not for high Li abundance stages. Further advancements can be made by considering graphite nanoparticles in electrolyte environments at applied voltage as in experimental electrochemistry. In the recent years, we have developed computational models for performing DFT simulations in electrolyte under potential control which could be the next step in this direction.[31, 32, 75]

3.4.5 AB Pinning

As we report in section 3.4.1, we observe no shift from an AB to an AA structure in our graphite nanoparticle as it is lithiated, something that we would expect to occur in a graphite-like compound. To investigate the cause of this lack of structural change we compare the energies of AA structures against that of AB structures. We compare the relative energies of the completely unfilled and completely filled nanoparticle with ideal Li spacing, Li_{42}G (c.f. section 3.3.3).

All calculations were performed with the parameters described in section 3.3.3 using the optPBE exchange-correlation functional. All structures were relaxed using geometry optimisation.

Table 3.2: Comparison of energies per atom of graphite nanoparticle of different stackings and lithiation

592 atom nanoparticle					
Structure	AB 0 Li	AA 0 Li	AB 42 Li electrostatically distributed	AB 42 Li perfectly distributed	AA 42 Li perfectly distributed
eV/atom	-131.0469	-131.0423	-136.0106	-136.0168	-136.0220

The results in Table 3.2 show that for the empty graphite nanoparticle structure, the AB structure is 4.6 meV/atom lower in energy than the AA structure. This is expected given that the AB structure of graphite is lower in energy than that of AA graphite.[136] We also note that for the comparison of the filled nanoparticle with perfect Li spacing the AB structure is 5.2 meV/atom higher in energy than the AA structure. This is also expected as full GICs are typically lower in energy in the AA configuration.[136]

Attention should be drawn to the nanoparticle filled with perfectly spaced Li is 6.2 meV/atom lower in energy than the filled nanoparticle with lithium spacing generated by our method of intercalation (c.f. section 3.3.4). This is also to be expected given that we only use electrostatic potential as a guide for low energy sites and not as a definitive global minimum.

Given that the perfectly filled AB structure was relaxed with a geometry optimisation and it remained in the AB configuration, we can conclude that there is a local energy minimum for this carbon configuration. It is unclear whether the energy barrier to transition to from the AB structure to the AA is significant. Mercer et al.[194] perform climbing image nudged elastic band calculations on this transition for bulk graphite and find no significant energy barrier. However, they do find meta-stable carbon sheet stackings as we do. They attribute their meta-stable stackings to the increased configuration entropy particularly present during de-lithiation caused by residual Li left in stage II ‘empty’ interlayer spaces. Our meta-stable states instead occur during lithiation where AB does not transition to AA. We can not attribute this to the increased configurational entropy of our system as a purely stage II AB structure is observed well beyond the expected lithiation limit for the transition to AA to occur (i.e. no ‘residual’ Li atoms are present in the empty layer until well beyond the point we would expect the AB to AA transition to occur). Of course, our calculations are performed at 0 K and we acknowledge there may be other entropic contributions that would destabilise our AB structure, such as the Li moving away from the edge. This leaves the geometry of our structure causing a significant energy barrier to transition from AB to AA as our leading explanation. Li-C binding at graphite edges has been reported to be stronger than Li-C binding in the bulk.[169, 198, 220] Given the edge site presence of our structure, enhanced Li-C binding could cause an energy barrier to transition that is not present in bulk graphite.

In support of this explanation we note that due to the way Li is distributed in the nanoparticle we made using our method, deformation in the graphite structure occurs that would allow for closer, central, inter-layer C-C bonds. Furthermore, the edge-favouring distribution of Li means that shifting layers would leave some Li atoms outside the nanoparticle which would either lead to a higher total energy due to the loss of enhanced edge Li-C interactions, if the atoms were to remain outside the particle, or would require a large Li atom reorganisation which will not occur without including a way of modelling the kinetics of Li during intercalation.

Therefore we believe that no AB to AA shift is observed in our structure as we intercalate with Li due to the local minimum AB being stabilised by the emptier outer intercalation layers and Li edge preference allowing the graphite sheets to flare and interact as if they were unintercalated as well as the possible AA structure being destabilised through edge accumulation meaning that an AA transition would lead to large scale deintercalation. This effect is allowed to occur because we provide no mechanism through which the Li can move and reorganise themselves. Unlike Mercer et al.’s[194] reported meta stable structures delaying the transition of AA to AB we are likely observing a kinetic trap where Li not having the energy to diffuse through the graphite structure at this temperature means that the AB structure is pinned as the most stable state for this arrangement of Li.

3.5 Conclusions

In this study, we have demonstrated the feasibility of performing multiple *ab-initio* calculations on entire graphite nanoparticles at various stages of charge. We also demonstrated a novel intercalation method whereby lithiation is dictated by the electrostatic global minimum. This method provides a suitable alternative to other intercalation schemes such as cluster expansion[226], with the advantage of being applicable to systems without long-range symmetry such as nanoparticles. Despite drastic structural and environmental differences of our nanoparticle to that of experiments, Li staging, Li to C charge transfer, and the formation of an OCV-like voltage step profile all occur readily. However, our nanoparticle results diverge from that of other bulk graphite results due to a preference for intercalation occurring at the edge sites. We believe the edge site preference is caused by the slight polarisation of edge C atoms by the more electropositive H atom terminations, which consequently creates an electrostatic potential minimum. The effect of this Li distribution is shown in the distribution of local charges and leads to an increased polarisation of the outer C atoms as more Li to C charge transfer occurs. We also found the edge accumulation of Li to be a likely cause of the nanoparticle structure being unable to transition from an AB to an AA configuration.

Going forward, the availability of linear-scaling DFT we will be able to make more realistic atomistic models of intercalation. The same technique demonstrated here can be used in the future for more sophisticated models. These improvements could include structural refinements to our nanoparticle such as increased scale and edge terminations that better reflect a battery environment. Improvements to the model could include the inclusion of temperature-dependent Li intercalation, the addition of a kinetic model to our Li atoms that would enable them to diffuse through graphite and away from the edges, and the use of a solvent and electrolyte model.[31, 32, 75]

3.6 Supplementary Results and Discussion

In this section I will discuss research that is relevant to the current project but does not fit with the main body. I have separated to not interfere with the primary narrative.

3.6.1 Bulk

The idea of this work is based off initial calculations obtained by Dr. Felix Hanke. We present an analysis of the results of these calculations which eventually lead to the work presented in sections 3.1 to 3.5

Having implemented the methodology refinements outlined in section 3.3.5 we applied the workflow shown in figure 3.3 to the bulk system described in section 3.3.4.

We then found the important structures of this system by plotting a convex hull. The full details of this will be given in section 3.4.4. The plots shown in figure 3.18 were obtained through 2 different dispersion forces approximations. The results shown in figure 3.18a uses the TS09 dispersion correction developed by Tkatchenko and Scheffler[297]. This method was able to reproduce Li staging and a shift from AB to AA stacking perfectly. However, the energies are not correct and no convex hull is formed.

The results shown in figure 3.18b use the Grimme D2 dispersion functional[106] for reasons outlined in section 3.3.4. The convex hull formed here is an improvement over figure 3.18a as important structures can be found other than that of the initial and final structures. However, analysis of the structure involves a placement of Li atoms too close to each other. So while energies have improved with this choice of dispersion correction the structure has degraded. A similar pattern was observed by Hanke[118].

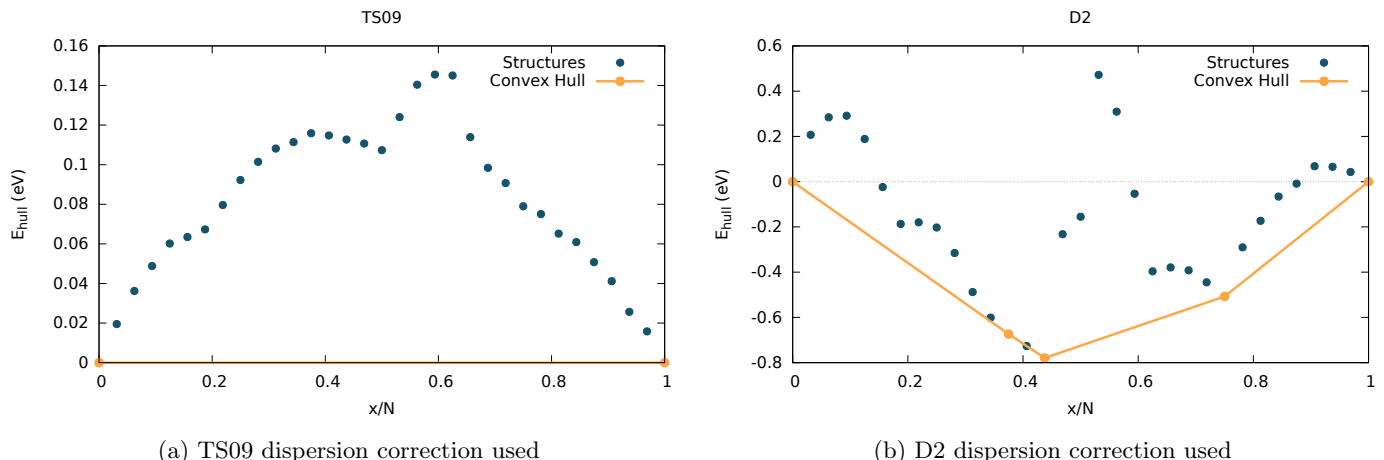


Figure 3.18: Plot of the divergence from linearity of energies as lithiation occurs (E_{Hull}) against the fraction of Li (x) in lithiation sites (N). Section 3.4.4 has more details.

While the energies appear nonsensical for the TS09 results, it should be noted that shape and magnitude of the convex hull values are highly sensitive to even slight deviations in energy. Examples of this are given in section 3.4.4.

Interestingly, when the structures generated by the TS09 functional were relaxed in a D2 framework the convex hull produced was vastly improved (c.f. figure 3.19). Combining TS09 and D2 dispersion corrections gave an intercalation process whereby the Li atoms were placed with a perfect staging process and AB to AA shift as well as giving a sensible convex hull.

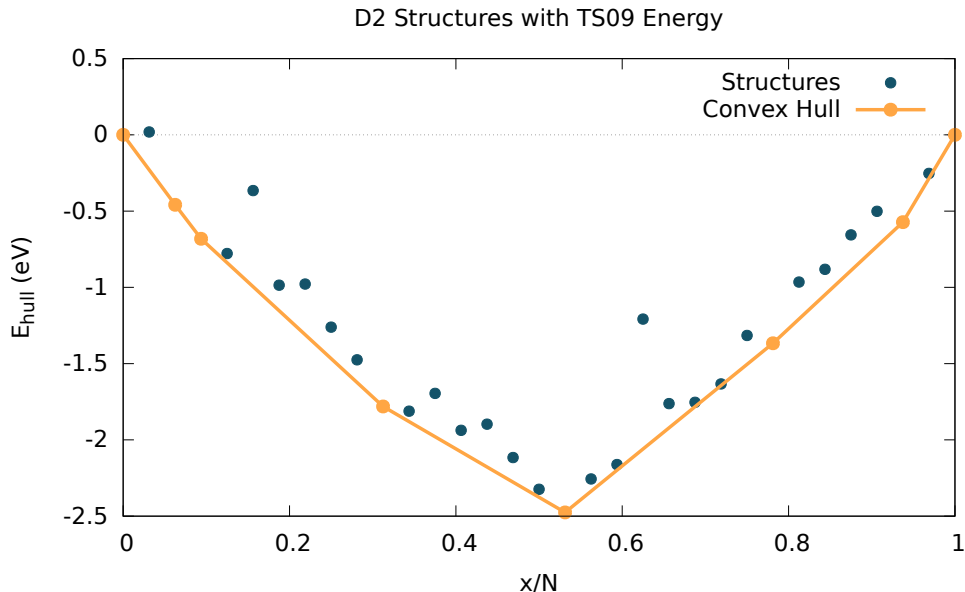


Figure 3.19: Convex Hull of the structures generated using TS09 dispersion correction but allowed to relax in an environment with the D2 dispersion correction.

Justifying the combination of two dispersion correction in a single workflow is tricky and falls outside the scope of my research. However, figure 3.19 does give us hope that by modelling the electrostatic potential at a higher accuracy, good structures and energies can be found in more scientifically justifiable way. This gives us a clear mandate for finding a more appropriate method to modelling dispersion interactions. We discuss the use of dispersion functionals in section 3.3.2. Perhaps the use of such functionals will yield the desired result. We are currently undertaking calculations using the optPBE and vdW-DF functionals.

Despite the apparent trade off we make between structure and energy, we do still get close to the right structure using our D2 results; Li staging and AB to AA stacking occurs naturally without paramaterisation. This coupled with the apparent improvement in energy over TS meant that we are confident moving forward with the D2 dispersion correction for the nanoparticle.

3.6.2 Different Terminations of the Nanoparticle

In Li-ion batteries, graphite nanoparticles are not terminated by H. Instead, an complex SEI layer is formed[8], which is briefly discussed in section 2.1. Recreating this SEI layer precisely would be an ambitious end-goal for this project. It would require considerable scaling up and refinement of our current model to achieve. For the immediate future an approximation, such as a different atomic termination, may suffice.

The composition of the SEI contains multiple precipitates from reduced decompositions of solvents, salts, Li-ions and impurities from the electrolyte. The part of the SEI closest to the edge of the graphite (for highly ordered graphite specifically) was found to primarily contain inorganic lithium carbonates and organic lithium alkali carbonates. By terminating our structure with carbonate like groups, or even just oxygen, we would expect to observe significant effects on lithium placement due to the apparent importance of our hydrogen termination in lithiation.

To investigate the importance of termination we compared the current slightly electropositive H-termination to that of highly electronegative F-termination. We replaced all hydrogens with fluorine atoms and performed a geometry optimisation calculation on the new structure, which is shown in figure 3.20.

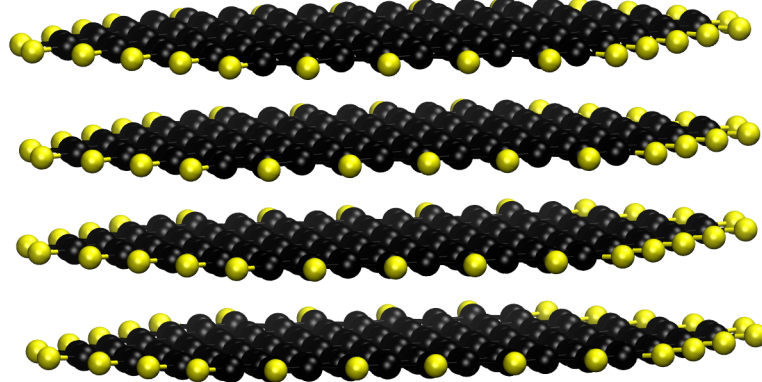


Figure 3.20: Graphite nanoparticle terminated with fluorine atoms. F: Yellow, C: Black

It should be noted that the geometry optimisation calculation was carried out using the old method, i.e. without spin relaxation. However, the number of electrons is even and no artificial spin polarisation should occur. The density of state plots (figures 3.21a and 3.21c) reveal a large peak at around -32eV not present in the typical graphite nanoparticle. This is more easily seen in figure 3.22. Given that fluorine and s-orbitals seem to be the main contributors, we can conclude this peak is a contribution from the fluorine 2s orbital. The 1s orbital, like carbon, is included in the pseudopotential.

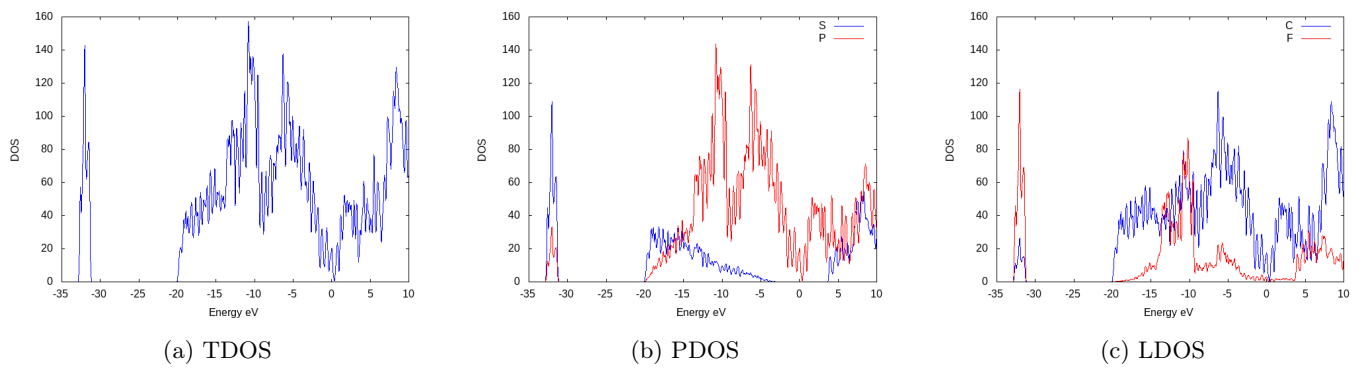


Figure 3.21: DOS plots for graphite nanoparticle terminated with F.

The comparison of F-termination against that of H-termination also reveals the DOS has shifted right with the band gap appearing to the right-hand side of the Fermi level (set to 0). This is due to the electronegative nature of fluorine withdrawing electrons from the carbon structure. It will be interesting to observe the interplay between the “right-shifting” F-termination with the “left-shifting” lithium intercalation and how this will effect the overall structure.

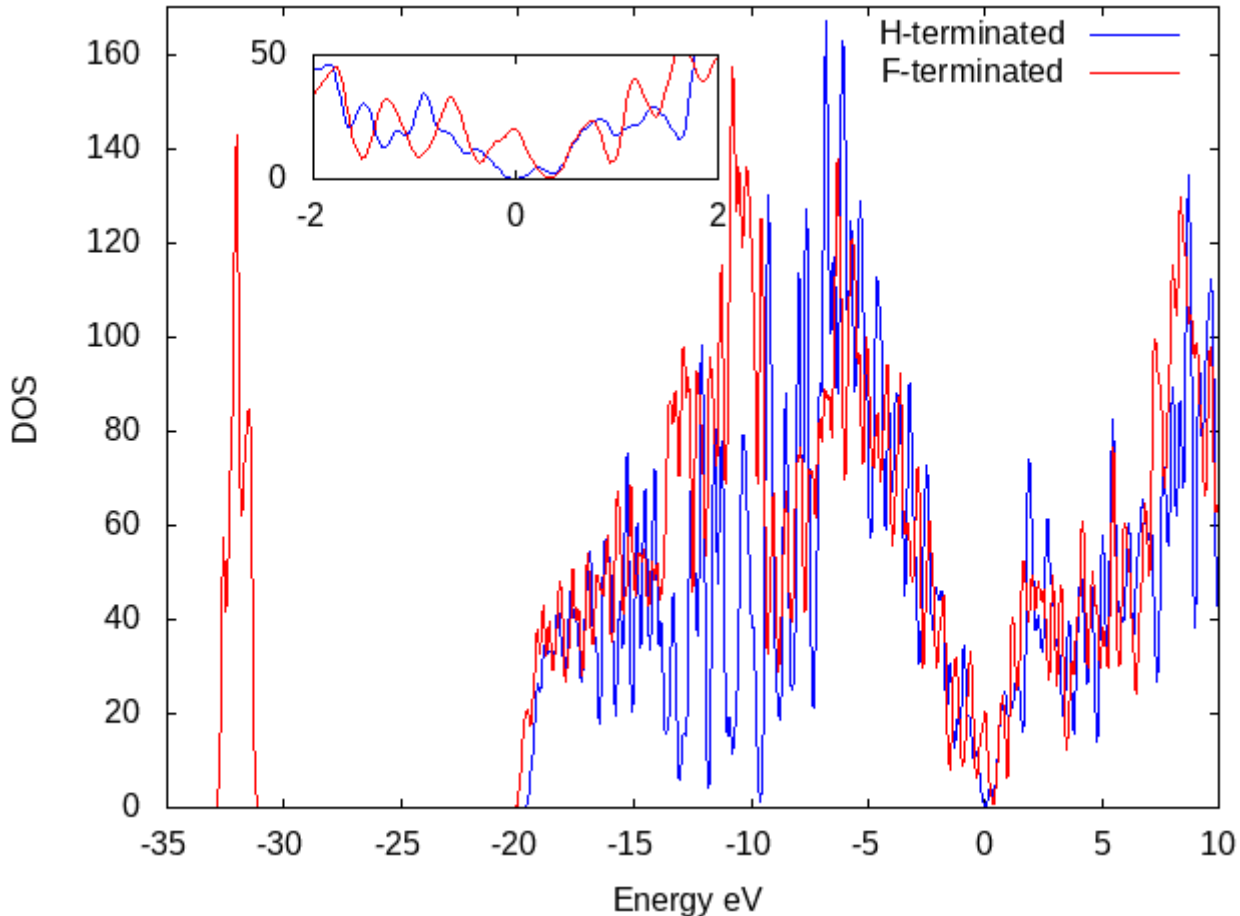


Figure 3.22: Comparison of TDOS between a H-terminated and F-terminated graphite nanoparticle.

The Mulliken population analysis of this structure (figure 3.23) is of particular interest as the charge build-up on the outer carbons was one of the key reasons for substituting the termination atoms. The termination with F, as expected, has had the opposite effect compared to the termination of H. There is now a charge depletion on the outer carbons which have a charge of around +0.4. The fluorines appear to have taken most of this charge giving them an average charge of around -0.23. We also note that the F-termination has resulted in a ripple effect in the charge with the carbons attached to the outer carbons being slightly negatively charged (-0.05 to -0.1). We predict this will have large ramifications for structure should we intercalate this compound with Li.

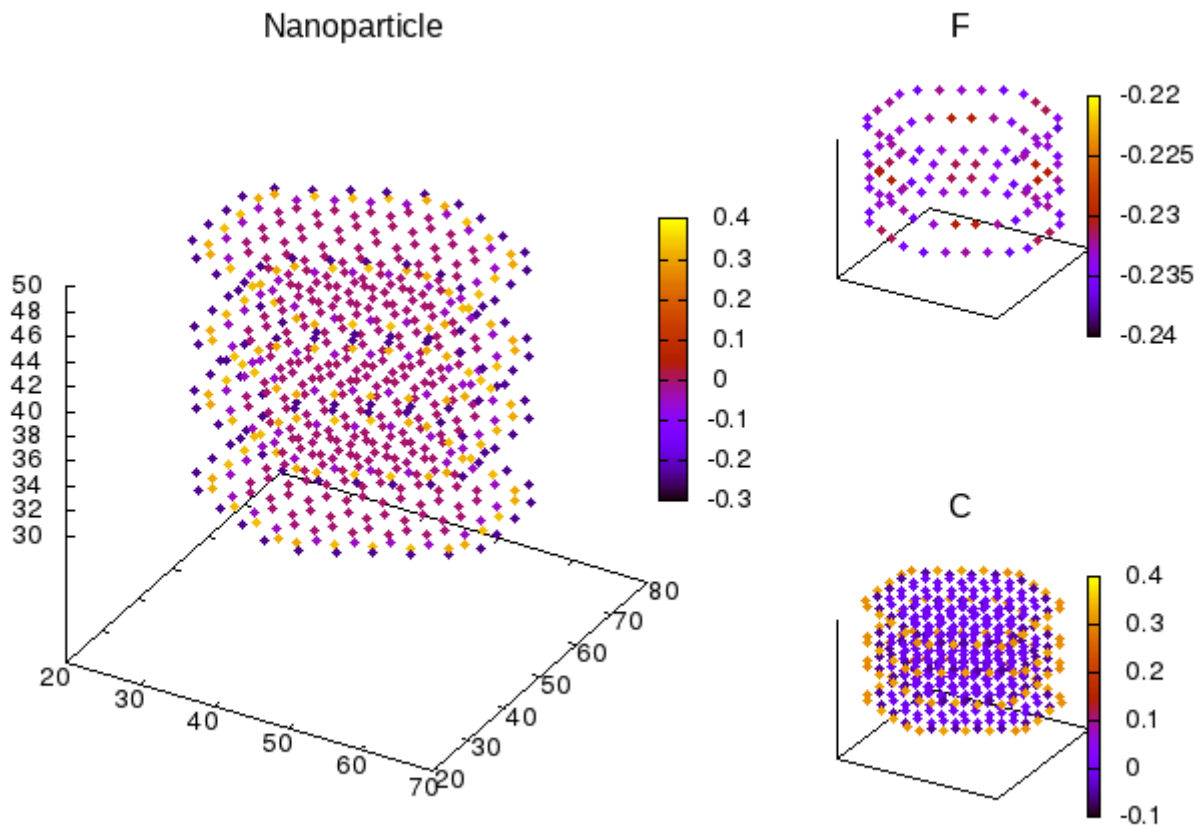


Figure 3.23: Mulliken population analysis of F-terminated graphite nanoparticle

No lithium intercalation calculations have been performed as of yet. This is in part due to ongoing research in the literature on how to best terminate our nanoparticle. Our termination with F, whilst being present in many SEIs, was mostly academic. We wished to see how the electronegativity affected our electron density and make predictions on how this would affect our lithiation. Should we intend to perform costly lithiation calculations we will need to make a more careful choice of termination. Perhaps a termination that will be more representative of the conditions of graphite in the presence of an SEI (c.f. section 2.1.2).

3.6.3 A Posteriori Dispersion Correction

To see the effect that different slight changes in the way the dispersion forces are calculated we perform *a posteriori* dispersion correction calculations on all our geometry optimised structures found using PBE with a D2 dispersion correction.

We use the following dispersion corrections

- D2[106], the original (c.f. section 3.3.2)
- D3[108],
- D3-M[108, 273]
- D3-BJ [107, 108]
- D3-BJM [107, 108, 273]
- D4[51]

Convex hull calculations are shown in figure 3.24 and were plotted with equation 3.10. The lower hulls are found using Qhull[22]

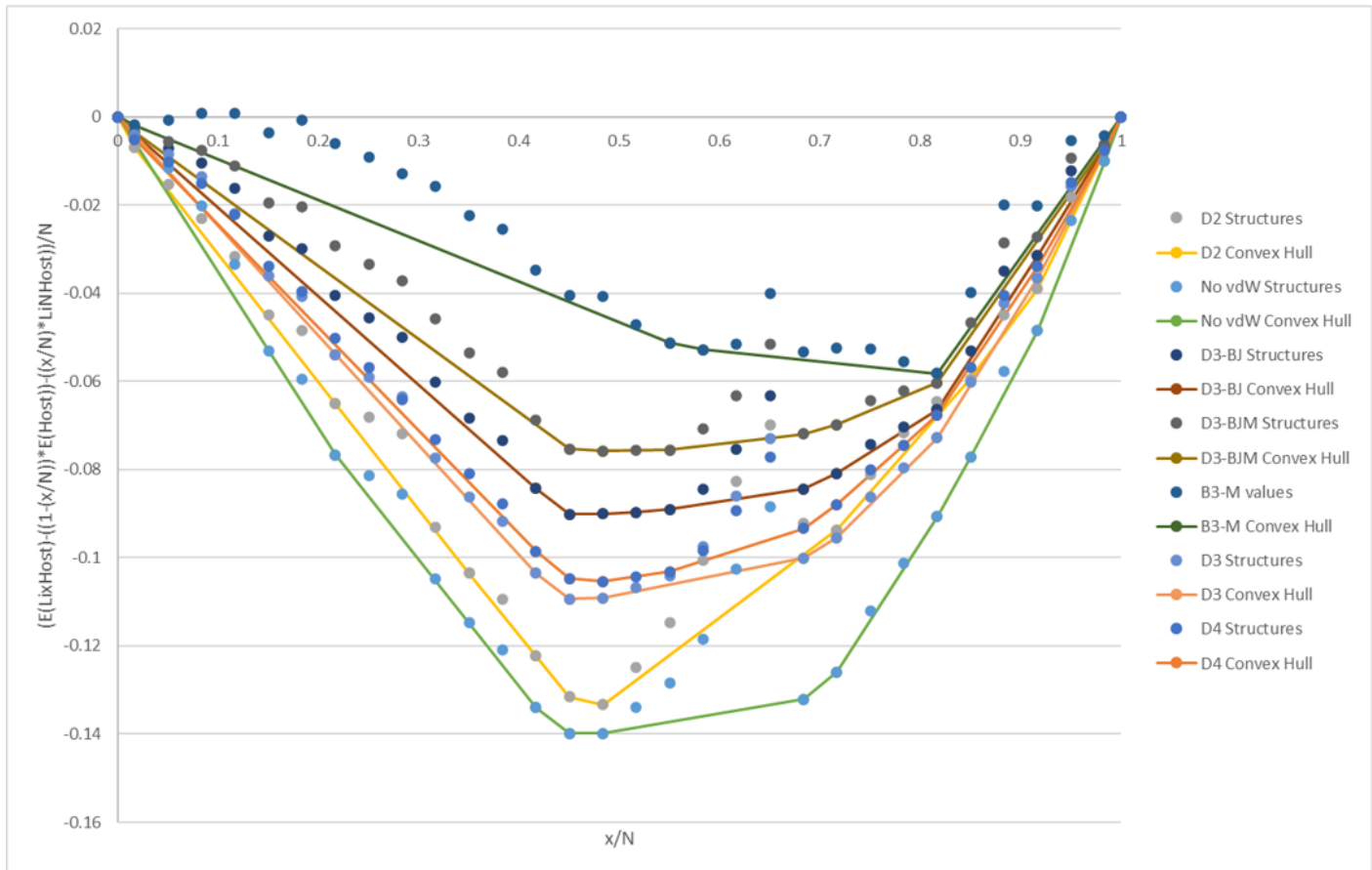


Figure 3.24: *A posteriori* convex hulls for a range of dispersion corrections with different parameterisations

The convex hull changes both in magnitude and shape with the different dispersion corrections applied.

Using the convex hulls generated in figure 3.24 and equation 3.12 we can create voltage step profiles for each dispersion correction (c.f. figure 3.25).

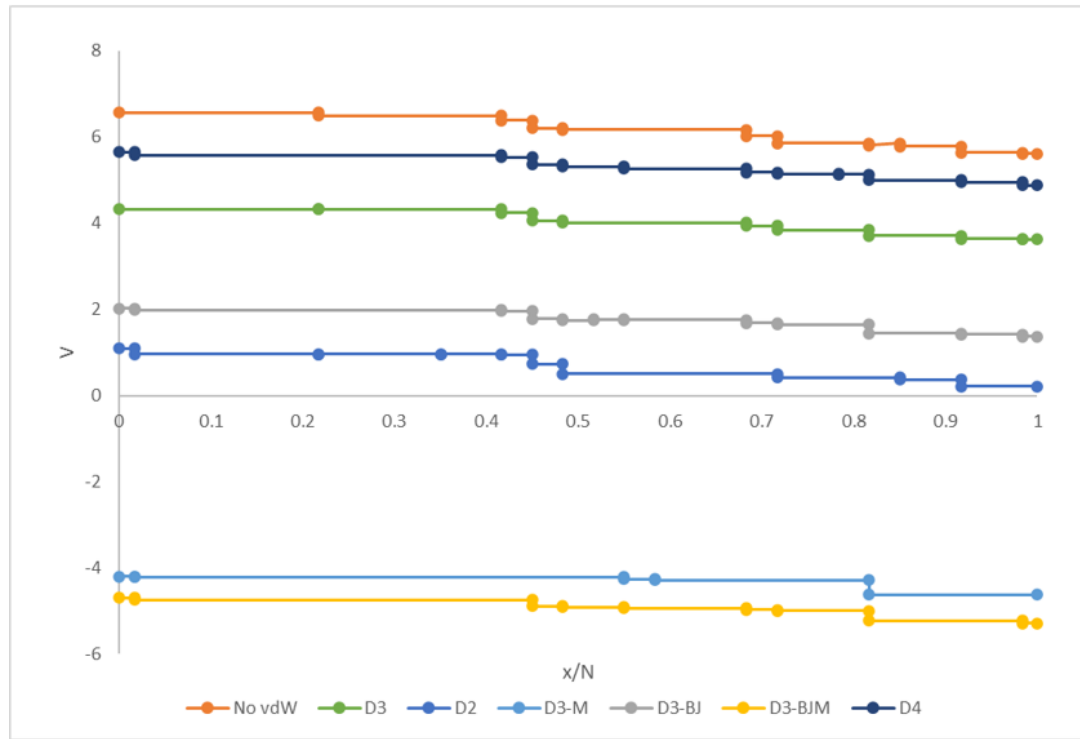


Figure 3.25: *A posteriori* convex hulls for a range of dispersion corrections with different parameterisations

The voltage step profiles are largely similar in shape with the exceptions of D3-M and D3-BJM with the [273] damping

terms being the underlying factor. We also note there is a large range in voltages.

We shall not go too in depth in the analysis as the results have already shown the intended purpose of this exercise, to demonstrate the sensitivity of the voltage step profile. To analyse deeper would be pointless because of the *a posteriori* nature of these calculations. The structures have already been determined using the electrostatic potentials generated using PBE-D2. It is therefore only natural that the D2 correction is the only result that gives a sensible voltage step magnitude.

3.6.4 Confidence of Lithium Placement

One possible methodology to quantify the likelihood of a Li placement being ‘realistic’ is to observe the spatial spread of the 50 lowest iso-values output by the electrostatic potential. Plotting these values in real space gives figure 3.26.

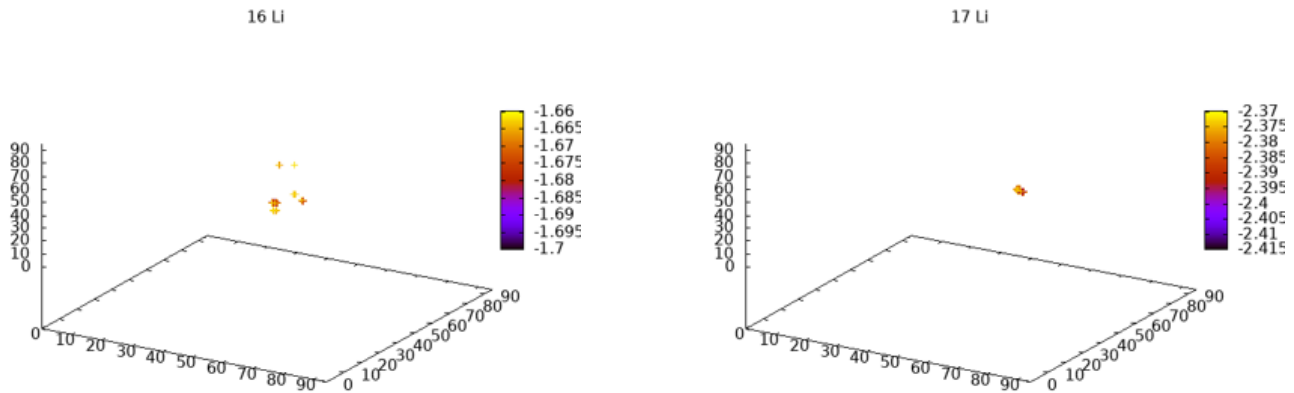


Figure 3.26: Confidence in lithium placement analysis for the placement of a lithium atom after the 16th and 17th lithiation. Plotted in real space, length units: bohr, colour bar: iso-value

Figure 3.26 demonstrates a typical pattern we see throughout the intercalation process. The electrostatic potential following the 16th lithiation, a single point energy calculation, is disperse. We can think of this as meaning our electrostatic potential energy surface is flatter than we would like, which results in an ill-defined minimum and many sites where the lithium could be placed. The electrostatic potential following our 17th lithiation, a geometry optimisation calculation, is much tighter. This can be thought of as a steep electrostatic potential energy surface with a well-defined minimum. This is a common pattern throughout the early lithiations of our graphite nanoparticle.

This analysis shows the accuracy trade-off we make when running a single point calculation compared to a geometry optimisation. However, there are exceptions to this pattern, particularly as our structure become more lithiated. Fig 3.27 shows a tight concentration of electrostatic potential around 1 potential site for the lithium to be placed. This occurs despite this following a single point calculation. These exceptions become more common as the system becomes more lithiated due to individual lithiations having less of an overall effect on the nanoparticle structure.

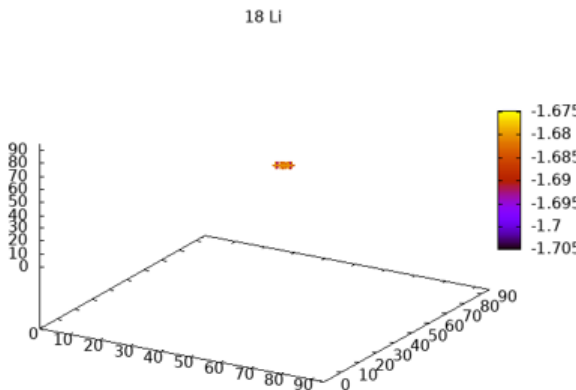


Figure 3.27: Confidence in lithium placement analysis for the placement of a lithium atom after the 18th lithiation, an exception to the pattern. Plotted in real space, length units: bohr, colour bar: iso-value

Refinements to this analysis need to be made. Specifically, the arbitrary use of the 50 voxels with the lowest iso-values. This provides a useful frame of reference when comparing lithiation calculations but does not provide a systematic method of qualifying how "good" a lithium placement is. Regardless, one could imagine a workflow whereby the necessity of a geometry optimisation was dictated by the variance of a number of voxels within a certain electrostatic energy range.

Chapter 4

A Study of Bulk c-LLZO

4.1 Abstract

Experimental and theoretical works have, to date, been unable to uncover the ground state configuration of solid electrolyte candidate cubic $\text{Li}_7\text{La}_3\text{Zr}_2\text{O}_{12}$ (c-LLZO). Computational studies rely on an initial low energy structure as a reference point. We present a methodology to identify energetically favourable configurations of c-LLZO for a crystallographically predicted structure. We begin by eliminating structures that involve overlapping Li atoms based on nearest neighbour counts. We further reduce the configuration space by eliminating symmetry images from all remaining structures. We then use a machine learning-based energetic ordering of all remaining structures. By considering the geometrical constraints that emerge from this methodology we determine that a large portion of previously reported structures may not be feasible or stable. The method developed here could be extended to other ion conductors. We provide a database of all structures generated with the aim of improving accuracy and reproducibility in future c-LLZO research.

4.2 Introduction

As is stated in section 2.2.1 solid electrolytes for Li-ion batteries promise higher energy density, improved safety, longer lifetimes[25], and reduced production costs compared to the current generation of liquid electrolyte commercial cells.[72, 198] Electrochemical and chemomechanical stability present a significant issue for a number of superionic solid state conductors[88]; Dendrite formation through the electrolyte causing the batteries to short-circuit has been reported even for the most stable solid electrolytes.[21, 53, 92, 280, 296]. $\text{Li}_7\text{La}_3\text{Zr}_2\text{O}_{12}$ (LLZO) has the best interfacial stability of all popular fast ion conducting solid electrolytes against metallic Li.[349] LLZO has two primary polymorphs, the highly conducting disordered cubic LLZO (*c*-LLZO) and ordered tetragonal LLZO (*t*-LLZO) with a Li diffusivity over two orders of magnitude smaller than the cubic phase.[17, 18] *c*-LLZO has a Hermann-Maguin space group of $Ia\bar{3}d$ with Li atoms partially occupying the 24*d* and 96*h* sites (c.f. Figure 4.1b). *c*-LLZO is not stable at room temperature but has been stabilised with a number of substitutional dopants on 24*d* sites[98, 162, 234, 267] The 24*d* site is tetrahedral and the 96*h* site occurs at a tetrahedral/octahedral interface.

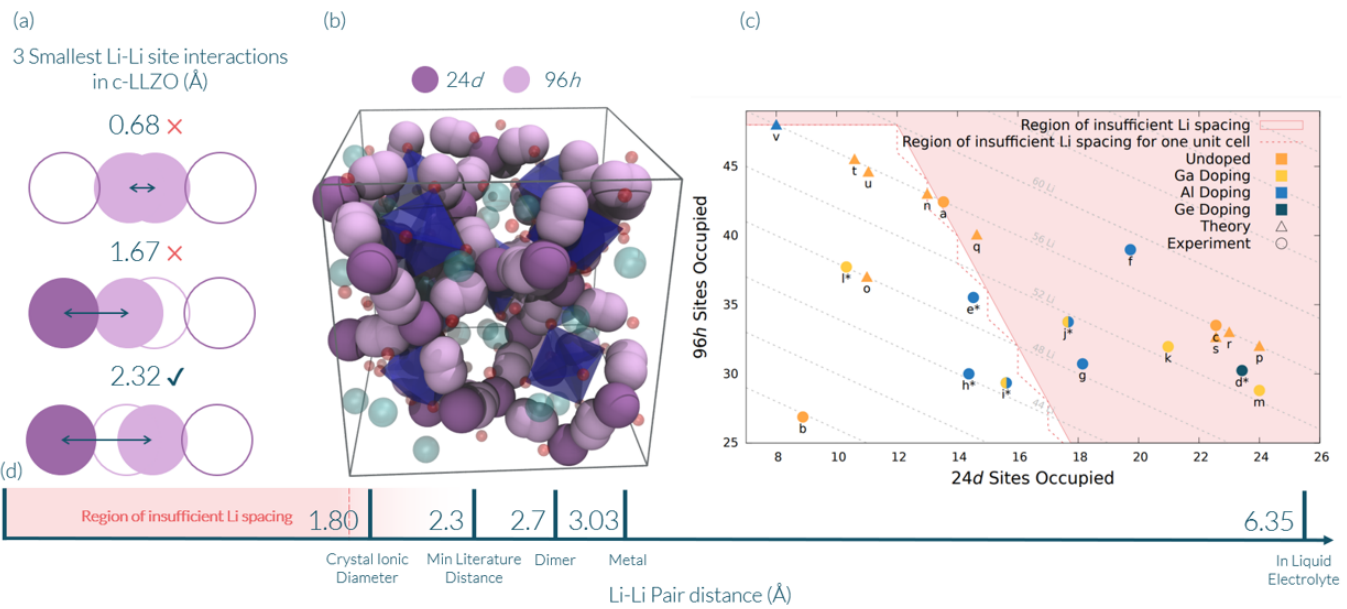


Figure 4.1: (a) examples of the 3 smallest site interactions from the centre of each atom. First and second neighbour Li sites are too close and cannot simultaneously contain a Li atom. (b) a unit cell of *c*-LLZO with all 24*d* (dark purple) and 96*h* (light purple) sites highlighted. O and La are represented by red and green spheres respectively, the Zr atoms are represented by the blue polyhedra. (c) shows experimental and theoretical site assignments and/or starting structures in the literature: a[326], b[98], c[17], d[46], e[50], f[126], g[314], h[241], i[241], j[241], k[246], l[134], m[314], n[21, 92, 239, 265, 295, 296, 334, 335], o[328], p[141, 149], q[191], r[257], s[309], t[309], u[112]. * indicates that experimental assignments used neutron diffraction, no * means the experimental assignments used x-ray diffraction. The region in red indicates the 24*d*:96*h* ratios that cannot exist without a Li-Li interaction below the crystal ionic diameter. The data for this image is provided in the Tables 4.2 and 4.3. (d) a scale showing the important Li-Li interactions distances recorded in the literature: Crystal Ionic Diameter,[263] Min Literature Distance[35], Dimer (in a vacuum) (c.f. figure 4.9), In Liquid Electrolyte (average Li-Li distance)[161] as well as our chosen cutoff point at 1.7 Å (red dashed line).

Despite the material's technological relevance and intensive study[4, 90, 112, 167, 259, 343] there is no consensus of *c*-LLZO's Li occupancy (c.f. Figure 4.1c). Here, we present a combinatorial study to find and rank all possible Li site occupancies. Previous computational studies often use one of the experimental values in Figure 4.1 as a starting point to obtain an idealised unit cell using a variety of methods (c.f. Table 4.3). The range of predicted structures in the literature indicates some disagreement about the ground state. Without knowing if the structures used are close to the ground state, more complicated thermodynamic and observable properties calculated from these structures may not be well described.

4.3 Reducing the Configuration Space

To find the most stable structures we intend to produce all possible structures of a c-LLZO unit cell and order them energetically to ascertain the presence of a significant energy difference in choice of structure. We also hope to elicit whether some of the structural properties, such as the 24*d*:96*h* ratio, are indicative of a structure's energy. We neglect to include the 48*g* site that occurs between the 96*h* sites as it is not reported in most refinements we find (c.f. Table 4.2 for references). The structures produced in this work are published alongside our results (c.f. section 4.7.1) in the hope that we can provide further clarity and improve reproducibility in this field of research.

The number of ways to populate 120 sites with 56 Li is $\binom{120}{56} \approx 7.4 \times 10^{34}$, rendering a brute-force combinatorial method unviable. To reduce this configuration space, we begin by eliminating all overlapping Li atoms (c.f. Figure 4.1a)[66] by imposing a minimal Li-Li distance. Here, we use 1.7 Å (c.f. section 4.7.4) which is less than 2 times the ionic radius of a Li atom and smaller than the minimum distance in t-LLZO (2.56 Å)[245], and significantly less than Li-Li distances in metallic Li. In practice, any minimal distance between 1.67 Å and 2.3 Å would be suitable for a numerical implementation.

This constraint on allowed Li-Li distances immediately limits the physically possible 24*d*:96*h* ratios. To describe the possible structures available under this simple geometric constraint, we outline the two major consequences this limit imposes.

1. A maximum of 48 out of 96*h* sites can be occupied at any one time: each 96*h* site exists as a pair within 0.68 Å of each other, at most one site can contain a Li atom.
2. Each of the 24*d* occupation eliminates 4 out of 96*h* sites as they are within 1.67 Å of this site.

We can use this information to narrow the range of Li site occupations

$$y_{96h} \text{ Occupancy} \leq \frac{N_{96h} \text{ sites}}{2}, \quad (4.1)$$

$$y_{96h} \text{ Occupancy} \leq N_{96h} \text{ sites} - 4x_{24d} \text{ Occupancy}, \quad (4.2)$$

where N_{96h} sites is the number of total 96*h* sites, y_{96h} Occupancy is the number of 96*h* sites occupied, and x_{24d} Occupancy is the number of 24*d* sites occupied. The area described in Eqs. 4.1 and 4.2, the unshaded area in Figure 4.1c, is the region with sufficient Li spacing at a given Li concentration. Outside of this area the structures, by necessity, will have a Li-Li interaction smaller than what we would expect to find in reality. For the stoichiometrically predicted case (56 Li atoms per unit cell), we observe that $8 \leq x_{24d}$ Occupancy ≤ 13.3 . This means the only stoichiometric 24*d*:96*h* ratios possible, for a single unit cell, are 8:48, 9:47, 10:46, 11:45, 12:44, and 13:43. This is how we refer to specific ratios throughout the rest of this communication.

By reducing the configuration space down to just these ratios we see an immediate large reduction in configuration space. The total number of structures (x) available for each 24*d*:96*h* ratio (i) for a single unit cell of a given Li occupancy (N), $N = 56$ for the stoichiometric case, can be calculated as

$$x_i = \binom{24}{i} + \binom{120 - 4i}{N - i}, \quad (4.3)$$

For a stoichiometric unit cell, we can calculate the total number of structures (x_{tot}) as

$$x_{\text{tot}} = \sum_{i=8}^{13} \left(\binom{24}{i} + \binom{120 - 4i}{56 - i} \right) \approx 1.93 \times 10^{25}, \quad (4.4)$$

Figure 4.1c shows a significant number of studies report structures that imply overlapping Li atoms with Li-Li distances smaller than 1.7 Å. For example, a structure with a 24*d*:96*h* ratio of 17:39 has a population of 17 24*d* sites necessitating that 68 (4×17) out of the 96 *h* sites will fall within 1.7 Å of an occupied 24*d* site. Trying to distribute 39 Li atoms amongst the remaining 28 ($96 - 68$) sufficiently spaced 96*h* sites is impossible so 11 of these Li atoms will occupy sites within 1.7 Å of another Li atom.

Having established the possible 24*d*:96*h* ratios, we can generate all allowed structures. We initially generate all possible 24*d* permutations for a given 24*d* occupancy, eliminating directly neighbouring 96*h* sites from consideration. We then populate the remaining 96*h* sites such that no two nearest neighbours are occupied simultaneously. The number of structures for each 24*d*:96*h* ratio, for one unit cell, are given in Table 4.1. We use the crystal structure sites reported by Buschmann et al.[50] as our framework to perform our generation in.

This method will generate all possible structures, approximately 2.3×10^8 , including symmetry-equivalent duplicates. To further reduce our large data set to unique conformations, we construct the upper triangular connectivity matrix of the Li sub-lattice for each structure. We define a connectivity matrix as the distances between each Li atom to every other Li atom. The matrix is then flattened and sorted to ensure uniformity in all matrices. This pre-processing of our structures decreases the memory required to store our structures compared to the full atomic structure of the crystal. A direct comparison of all structures to check symmetry would be computationally costly. We use local sensitive hashing (LSH)[173] to perform fast approximate similarity searches with further lower memory requirements than the unhashed data. The use of LSH optimises the pairwise comparison from scaling at $\mathcal{O}(N^2)$ to $\mathcal{O}(N)$, where N is the number of structures.¹ This symmetry comparison method is designed to work for large data sets of similar data, allowing us to perform symmetry checks on over 100 million structures in a reasonable time frame and attainable memory requirements, something that would be impractical to attempt with conventional methods[30, 298, 304]. The trade-off for increased speed and lower memory costs is the high specificity of the method. In practice, this method is limited to the comparison of monoatomic sub-lattices with predefined positions.

To validate our symmetry checking methodology we compare our results against that of more rigorous methods.[298] We use the atomic simulation environment (ASE) python package's symmetry equivalence check on the two smallest 24: d :96: h ratios (c.f. table 4.1): 12:44 and 13:43. Employing this technique we find that only approximately 1% of our structures are symmetrically unique, allowing a reduction by a further factor of approximately 100 (c.f. Table 4.1).

Table 4.1: The total number of c-LLZO structures for every possible 24: d :96: h ratio after limiting to the specific 24: d :96: h ratio(s), mandating all Li-Li interactions must be greater 1.7 Å, and ensuring the structures generated are symmetry unique

24:d:96:h	Ratio Limited	> 1.7 Å spacing	Symmetry unique
8:48	1.8×10^{25}	80,019,456	816,454
9:47	9.3×10^{23}	98,304,000	905,216
10:46	4.4×10^{22}	41,754,624	366,971
11:45	1.9×10^{21}	7,176,192	65,958
12:44	7.6×10^{19}	427,176	4,162
13:43	2.6×10^{18}	1,056	11
Total	1.9×10^{25}	227,682,504	2,158,772

¹The code and model for this symmetry checker was developed by Tom Demeyere for use in this body of research

4.4 Energetic Ordering of the Perfect Crystals

Having reduced the configuration space to around 2×10^6 structures (c.f. Table 4.1) we can energetically order our structures. Initially, we tried a number of classical forcefield tended to use already available methods such as force fields, which neglect explicitly modelling the electrons in favour of fitted potentials, or Density functional tight-binding (DFTB) which is based on a second-order expansion of the Kohn-Sham total energy functional.[77] (c.f. section 1.5 for the theoretical background and section 5.5 for the construction of the DFTB parameters used here).

Due to the limited number of forcefields available with La and Zr parameters and that we predict the majority of the energy differences to come from the unique Li configurations we believed that excluding non-Li elements may still be sufficient to energetically order our structures. Figure 4.2 demonstrates how the calculated ONETEP DFT energy compares to our fast energy calculator method. We perform our calculations on the 11 symmetrically unique structures predicted for the 13:43 ratio.

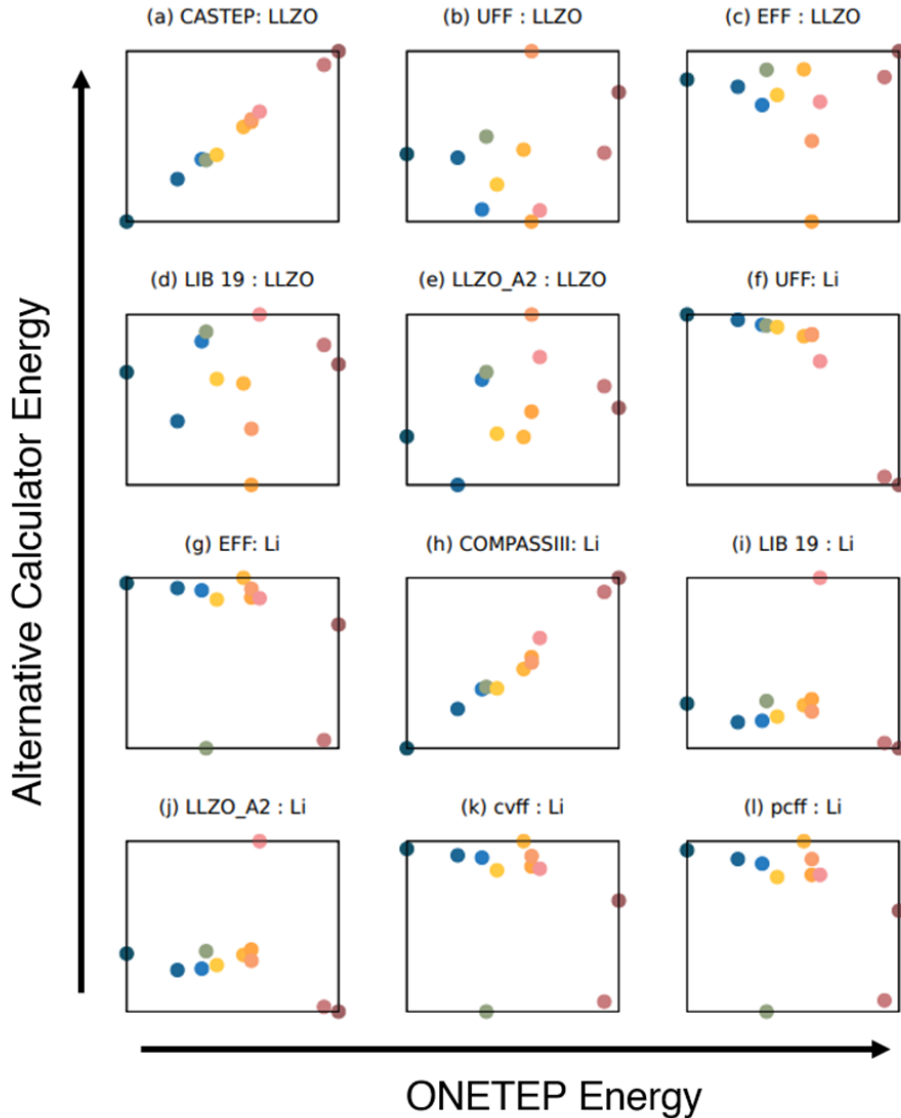


Figure 4.2: A comparison of the energetic ordering of all symmetry unique 13:43 structures for different energy calculators compared to our ONETEP calculations: (a) CASTEP[62]: DFT software used as our base line comparison, (b) and (f) FORCITE:[37] universal forcefield[235], (c) and (g) FORCITE:[37] custom forcefield that exclusively considers the coulombic interaction of atoms, (d) and (i) DFTB+[133]: Slater-Koster library developed for Li ion batteries[37] and extended to include La and Zr interactions (if required) with data from the LLZO_A2 Slater-Koster library (c.f. section 5.5), (e) and (j) DFTB+[133]: unpublished custom parameterised Slater-Koster file specifically for LLZO (c.f. section 5.5), (h) FORCITE:[37] using the COMPASSIII forcefield[282], (k) FORCITE:[37] using the cvff forcefield[113], (l) FORCITE:[37] using the pcff forcefield[283].

Orderings with "Li" in the title indicate that only the Li sublattice was used in the energy evaluation. "LLZO" indicates all atoms were used. Energy values are not included as they often (in the case of the Li only calculations) do not correspond to real systems. We are only interested in the ordering.

Pure electrostatic summation does not appear to be sufficient in this case (c.f. figure 4.2(g)), which is why additional

non-bonded terms such as van der Waals interactions appear necessary. The most successful method we found was COMPASSIII when applied only to the Li sublattice. It was able to order the 13:43 with a correlation coefficient of 0.991.

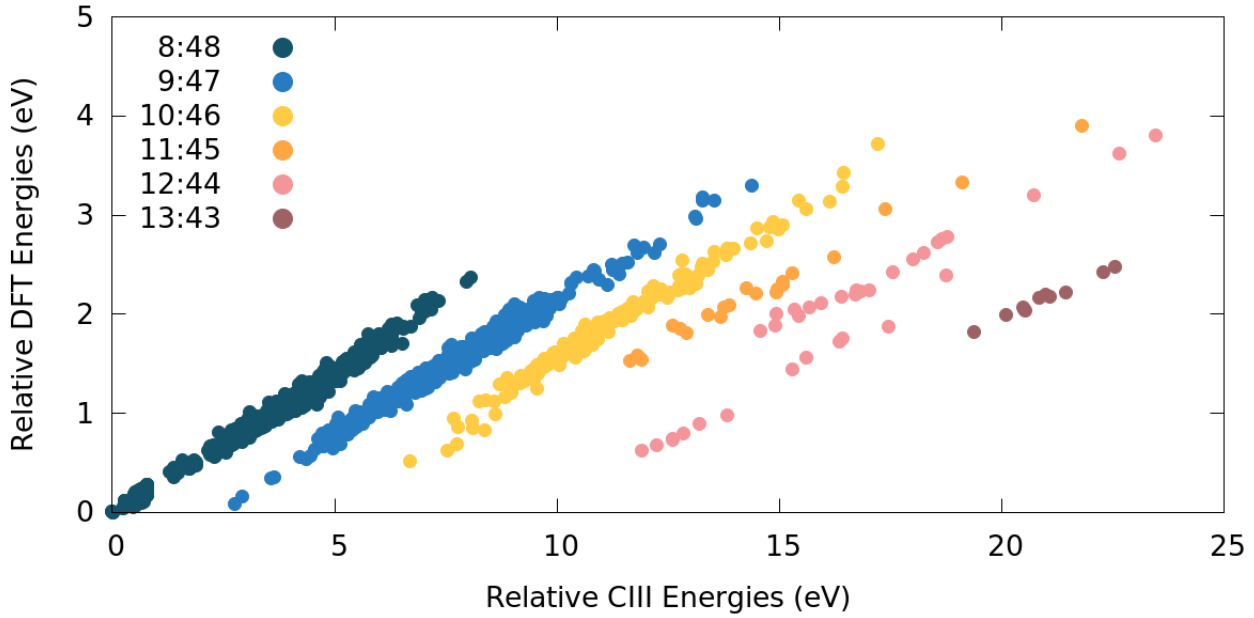


Figure 4.3: A comparison of 1235 relative DFT energies to that of COMPASSIII

Figure 4.3 shows that COMPASSIII, when only evaluated for Li atoms, predicts a more pronounced separation of energies depending on the 24d:96h ratio than is predicted by ONETEP, while good intra-ratio ordering is retained. This is the best we could do with easily available force fields, but ultimately insufficient for structural ordering. For this reason, we developed the multiple linear regression model. No results in the main part of the paper are actually built on COMPASSIII.

To achieve this in a reasonable time frame, we perform DFT calculations on small subsets of the total number of structures. The results are then used to fit a multiple linear regression (MLR) model. The DFT calculations were performed on 2 major subsets of structures. The first subset was the 200 energetically lowest structures according to the COMPASSIII forcefield,[5, 282]. The second subset was a random selection of approximately 1000 structures across the entire configuration space to ensure good coverage. In total 1235 single-point DFT calculations were performed.

All DFT calculations were performed with the ONETEP code, where the computational cost scales linearly with the number of atoms as opposed to cubic scaling in conventional DFT (c.f. section 1.3).[230, 272] The following settings were used for our ONETEP calculations. Functional: PBE[224], Kinetic Energy Cut-off: 830 eV, Pseudopotentials: CASTEP on-the-fly generated pseudopotentials[62], NGWF Radii: 10.0 Bohr, NGWF number: (Li: 5, La: 17, Zr: 10, O: 5)

Because some structures have Li distributed in such a way that non-identity symmetry operations are possible there will be variation in the contribution of configurational entropy to the total energy. We calculated the configurational entropy for all structures and have included it in all results presented in this work, unless stated otherwise. We discuss how we calculated configurational entropy in section 4.7.6.

Because we are working with only the crystallographically predicted structures the base LaZrO structure remains unchanged with each configuration and therefore all energetic changes are due to Li placement. We acknowledge that in reality, the geometry does change considerably depending on the Li environment[149]. However, this is a suitable assumption to make to energetically order the crystallographically predicted structures we generate. Therefore, an expression of all types of Li interactions would be a sufficient descriptor for predicting the energies of c-LZO structures. The DFT energies were paired with a numerical representation of the structure and fit using a multiple linear regression model (MLR). The structures were represented by a frequency occurrence list of all possible Li-Li interactions. This representation is a reformulation of the connectivity matrix of the Li sub-lattice used for the symmetry reduction described section 4.3 and is shown visually in figure 4.4.

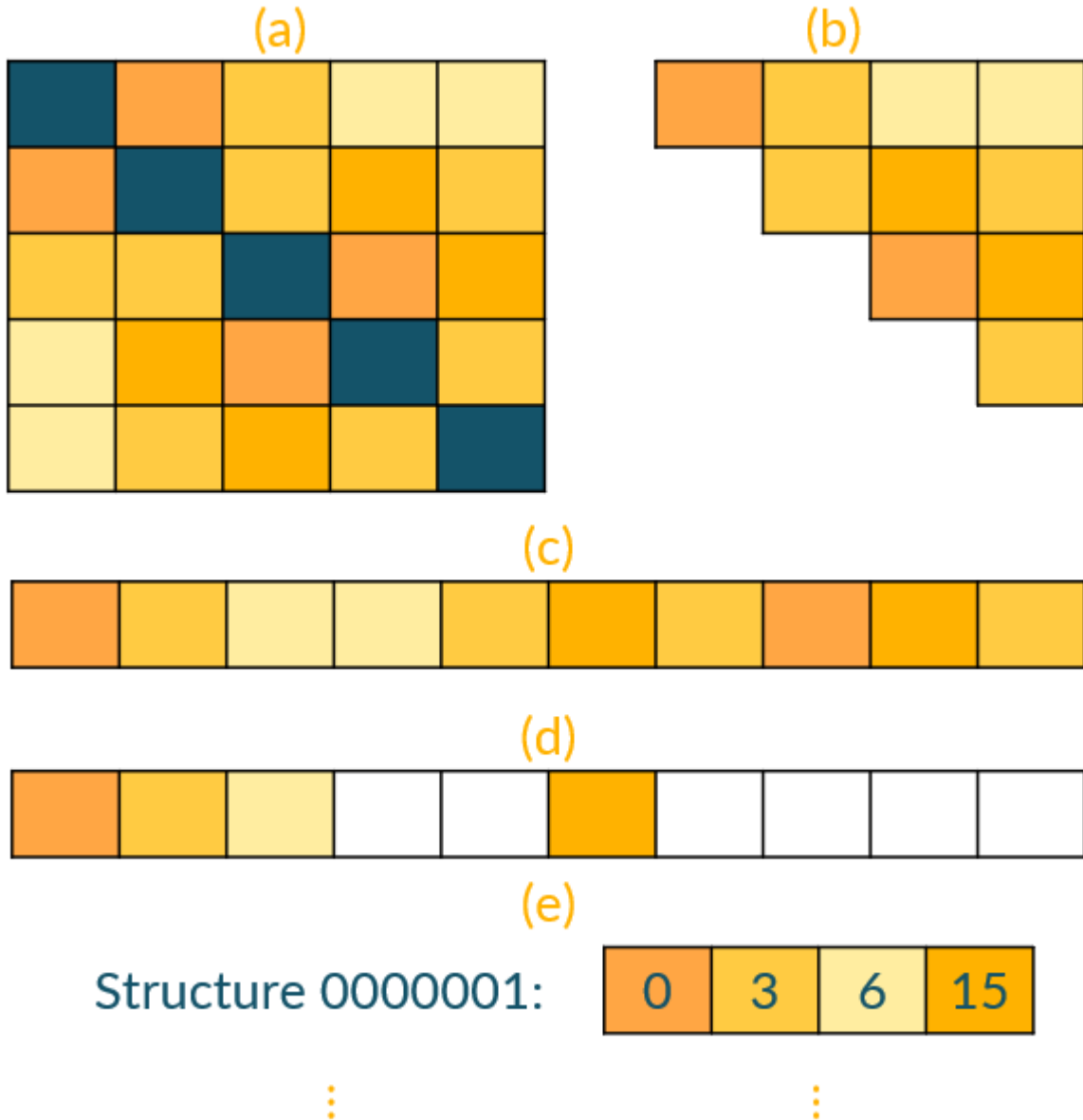


Figure 4.4: Demonstration of how the geometry data is processed for Li sublattice a 5×5 matrix with 4 unique distances is used here to make the individual processes easier to observe. We will describe the individual processes as if they were applied to the real system (a) The 120×120 minimum periodic distances between all possible Li sites are calculated, (b) the upper triangular matrix is taken, (c) The matrix is flattened containing only non-zero values, (d) the unique values are found and isolated (there are 86 unique distances for our system), (e) each cLLZO structure tallies the number of each type of interaction present which serves as a unique representation of that structure containing a large portion of the geometric information of the Li sublattice.

The data were split into test and training sets with a 1:3 ratio. We found through applying this model to our test set a correlation of 0.9996 (c.f. Figure 4.5a) with DFT energies with a mean average error of 0.0325 eV.

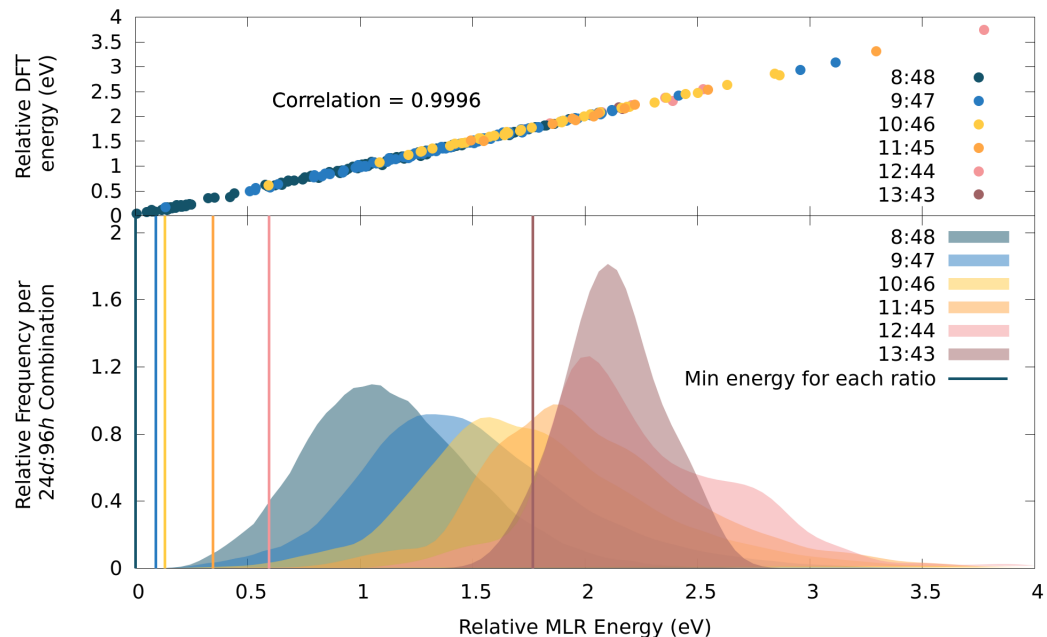


Figure 4.5: (above) the parity plot of the test set of ONETEP total energies compared to MLR predicted energies for each 24d:96h ratio. (below) The relative frequency of energy occurrences for each 24d:96h ratio.

All structures are found to occur within a range of 5.7 eV of our lowest energy structure. 17 out of the 20 lowest energy structures have a ratio of 8:48 (c.f. Figure 4.5b) with the 17th, 19th, and 20th lowest being 9:47. The average energy for all structures occurs at 1.47 eV higher than the ground state structures. The average energy for each ratio increases with increasing 24d occupancy, indicating an energetic preference to avoid 24d occupation where possible. There are 5 structures, all 8:48, within 0.026 eV (1 kT at 298 K) of the lowest energy structure we find (c.f. Figure 4.6). The four lowest energy structures have very similar atomic coordinates, all have the same 24d configuration with only slight variations in the 96h configuration, except for the fourth lowest structure which has different 24d and 96h structures. We perform geometry optimisation calculations on the final 5 structures and find the energy gap between them narrows further.

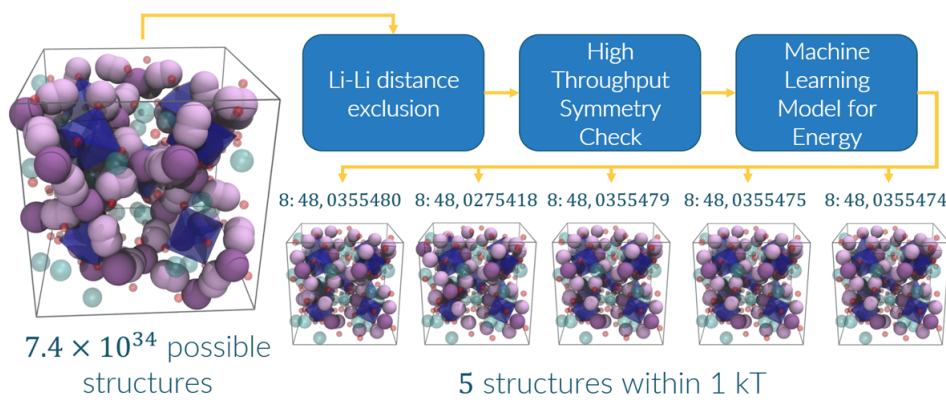


Figure 4.6: The workflow we employ to find our 4 final structures from given occupancies. Above each structure is its respective 24d:96h ratio and unique identity number in the c-LLZO database we have built (c.f. SI section 4.7.1)

We note that our energetic ordering procedure does not include vibrational entropic contributions and assumes a reasonable retention of ordering upon geometry relaxation, which are both approximations. We acknowledge the necessity of finding a good energetic ordering for the optimised structure of c-LLZO and have made preliminary efforts towards that. We assess the effect of geometry relaxation on a small dataset in section 4.5. A large-scale energy prediction of the geometry-optimised structures falls outside the scope of this communication.

It should be stressed that pure c-LLZO is not stable at room temperature and requires dopants (typically of Al or Ga on the 24d sites[308]). However, the structures we provide alongside this work should provide an excellent starting point for all future studies on dopants. The addition of dopants will significantly increase the complexity of this problem. Before attempting such a feat we believe understanding the potential energy surface of the geometry optimised structures to be more pressing.

4.5 Energetic Ordering of the Optimised Crystals

To assess what effect the geometry relaxed structures have on the overall ordering and also to compare our low energy structures to that of a random selection we perform 20 geometry optimisation calculations. We use the settings outlined in section 4.4 as well as the following geometry optimisation settings for the Broyden-Fletcher-Goldfarb-Shanno (BFGS)[263] optimisation algorithm

- Energy tolerance: 1.0E-6 Hartree

- Force tolerance: 0.002 Ha/Bohr

- Displacement tolerance: 0.005 Bohr

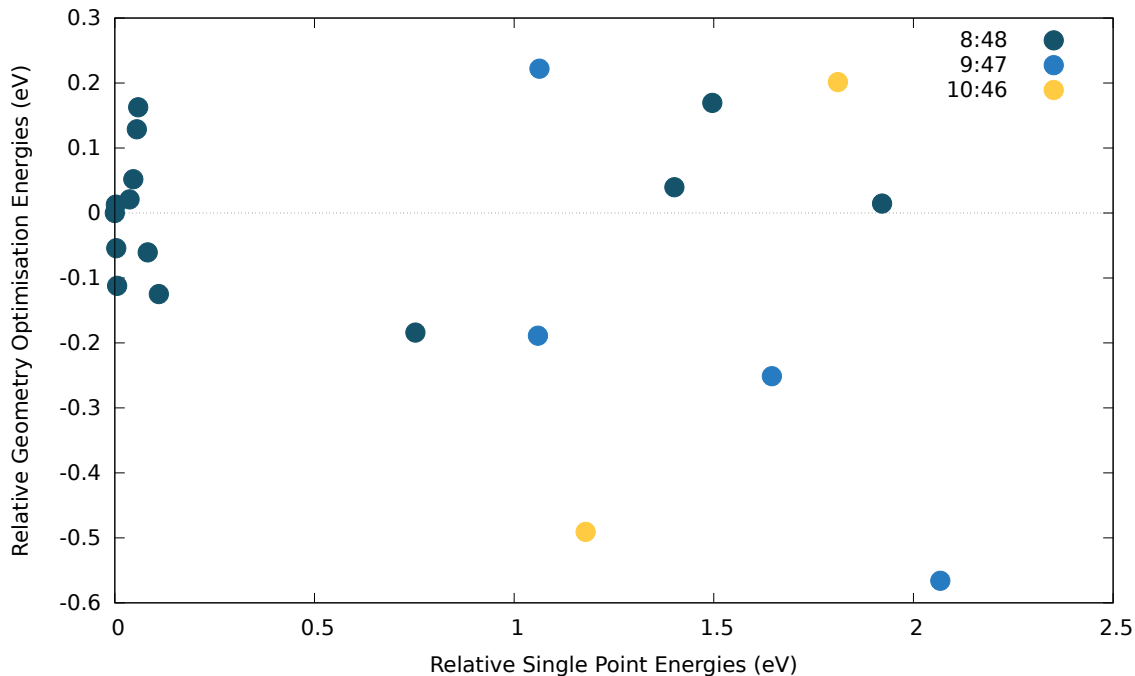


Figure 4.7: A comparison of the energetic ordering of 10 lowest structures according to MLR and 10 random structures for single-point (SP) and geometry-optimisation (GO) calculations. All energies are relative to the 355474 result for each calculation type

Figure 4.7 demonstrates no correlation between the single-point structures and their geometry-optimised counterparts. We observe three types of site change upon relaxation. 96h to 96h, 96h to 48g and 96h to 24d listed in order of frequency occurred. None of these site changes correlated significantly with the geometry optimised energy. The 96h to 24d transition was only recorded once and yielded our lowest overall energy structure (structure label 1095859): 0.58 eV lower in energy than the geometry optimised lowest energy single point structure. The 96h to 24d transition meant that the ratio of the structure changed from 9:47 to 10:46, the only time we have observed such a feature.

In figure 4.8a there is a negative correlation between the mean distance moved of all Li atoms in the c-LLZO structure and the increasing energy of the final optimised c-LLZO structure. This indicates that the more the Li atoms move from their original crystallographic site the lower in energy the structure. Figure 4.8b shows a weaker negative correlation between distance to a crystallographic site and energy. These results indicate that from the structures assessed movement from the original sites is preferable to attain lower energies and movement to another site is not necessary in order to attain a lower energy structure.

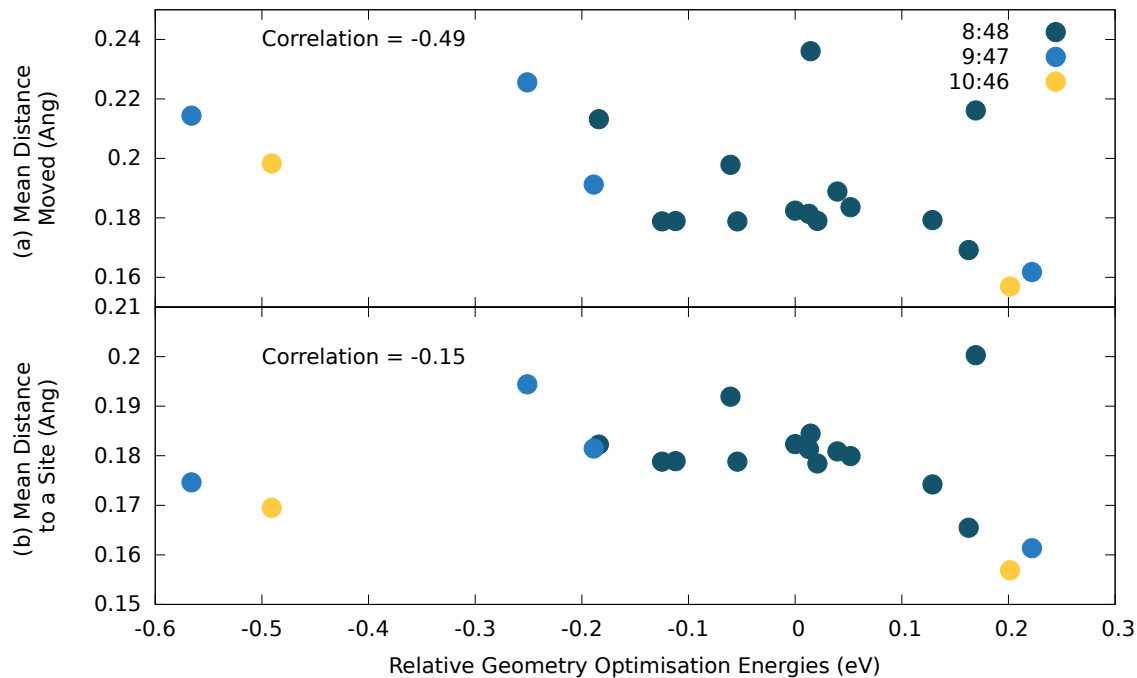


Figure 4.8: The relationships of the energy of 20 geometry optimised c-LLZO structures with (a) the mean distance moved by the individual Li atoms from their original crystallographically predicted site and (b) the mean distance of all Li atoms from a crystallographically identified Li site. Colours identify the 24d:96h ratio of the starting structure.

From this initial investigation, we can conclude that there is unlikely to be a good correlation between low-energy “perfect” crystal structures and that of their optimised counterparts. To resolve this there we need a way to find the energies of the optimised structures. There are two ways of doing this

1. Predict the optimised energy from the unoptimised structures
2. Optimise the structures and find the energy

For item 1, one could imagine an extension of the MLR model presented in section 4.4. Where the data of the initial structural positions is related to the energy of the optimised structures instead of the crystallographically predicted ones. It is unclear if this would be a good technique as the initial structure may not be predictive enough for the final energy. We would also, like the original MLR model, not get the structures, cell parameters, or forces out from this model, and would have to trust its assessment of our input structures.

Item 2 is problematic as there is no reasonable forcefield or DFTB model that can accurately simulate this system (c.f. figure 4.2). A possible avenue is to generate a machine learned-potential (MLP) using techniques such as ACE[73] or DeepMD[317]. We have started the process of generating the structures of training these models and have over 10,000 DFT calculations performed to date. The advantage of an MLP over the MLR model previously discussed would be that we get all the details we would from a conventional DFT calculation at a fraction of the cost. This method also has the added benefit of being extendable to simulate other structures such as t-LLZO and Li-LLZO interfaces as will be necessary to screen in chapter 5. Both of these methods will be evaluated as soon as we have sufficient data to attempt them.

4.6 Conclusion

In summary, we have created a fast evaluation procedure to generate and energetically order all crystallographically predicted structures for crystals with partially occupied sites. We have used the basis of this procedure, disallowing structures with atoms too close to each other, to highlight that a large proportion of experimental and theoretical literature are predicting or working with structures that are not reflective of a real system (c.f. Figure 4.1). It is our hope that in providing all possible structures we can bring further accuracy and reproducibility to future computational LLZO research.

4.7 Supplementary Results and Discussion

Here, we collect results found that while relevant are not necessary to formulate our conclusions above.

4.7.1 Data

All structures, ONETEP input and output files, and codes used in this work can be accessed at
<https://doi.org/10.5258/SOTON/D2704>

4.7.2 Experimental Literature Summary Table

Table 4.2: All Experimental papers we could find that explicitly report the site occupancies of the $24d$ and $96h$ sites. The second column shows the paper and the reported stoichiometry. The third column reports the method used with "X-ray" referring to some form of X-ray diffraction and "Neutron" referring to any presence of Neutron powder diffraction being present in the assignment. The remaining columns are taken directly from the respective papers and standardised to report the proportion of sites occupied out of total sites and the number of atoms that would result in a full cubic structure

* Ga occupies some of the La $24c$ sites. We have also approximated the $12a$ and $12b$ sites to be the same as the $24d$ sites, as well as the two $48e$ Li sites to be $96h$ so we can compare with the other structures.

† a significant portion of Li reported was unassigned

	Paper Assigned Stoichiometry	Method	Li $24d$ Fraction (Occupancy)	Dopant $24d$ Frac- tion (Occupancy)	Li $96h$ Fraction (Occupancy)	Total Assigned Sites Occupied
a	Xie et al.[326] $\text{Li}_7\text{La}_3\text{Zr}_2\text{O}_{12}$	X-ray	0.564 (13.53)	-	0.442 (42.43)	55.96
b	Geiger et al.[98] $\text{Li}_{4.47}\text{La}_3\text{Zr}_2\text{O}_{12}$	X-ray	0.37 (8.88)	-	0.28 (26.88)	35.76
c	Awaka et al.[17] $\text{Li}_7\text{La}_3\text{Zr}_2\text{O}_{12}$	X-ray	0.94 (22.56)	-	0.349 (33.504)	56.08
d	Brugge, Kilner, and Aguadero[46] $\text{Li}_{6.6}\text{Ge}_{0.1}\text{La}_3\text{Zr}_2\text{O}_{12}$	Neutron	0.943 (22.64)	Ge 0.033 (0.8)	0.315 (30.24)	53.68
e	Buschmann et al.[50] $\text{Li}_{6.06}\text{Al}_{0.2}\text{La}_3\text{Zr}_2\text{O}_{12}$	Neutron	0.54 (12.96)	Al 0.0653 (1.44)	0.37 (35.52)	49.92
f	Hiebl et al.[126] $\text{Li}_7\text{Al}_{0.33}\text{La}_3\text{Zr}_2\text{O}_{12}$	X-ray	0.712 (17.08)	Al 0.11 (2.64)	0.406 (38.976)	58.696
g	Wagner et al.[314] $\text{Li}_{6.03}\text{Al}_{0.08}\text{La}_3\text{Zr}_2\text{O}_{12}$	X-ray	0.68 (16.32)	Al 0.076 (1.824)	0.32 (30.72)	48.864
h	Rettenwander et al.[241]† $\text{Li}_{5.5}\text{Al}_{0.19}\text{La}_3\text{Zr}_2\text{O}_{12}$	Neutron	0.54 (12.848)	Al 0.064 (1.528)	0.31 (30.0)	44.376
i	Rettenwander et al.[241]† $\text{Li}_{5.5}\text{Al}_{0.20}\text{Ga}_{0.05}\text{La}_3\text{Zr}_2\text{O}_{12}$	Neutron	0.57 (13.65)	Al 0.066 (1.584), Ga 0.016 (0.384)	0.31 (29.344)	44.96
j	Rettenwander et al.[241]† $\text{Li}_{6.3}\text{Al}_{0.12}\text{Ga}_{0.08}\text{La}_3\text{Zr}_2\text{O}_{12}$	Neutron	0.67 (16.08)	Al 0.039 (0.944), Ga 0.027 (0.64)	0.35 (33.752)	51.416
k	Robben et al.[246]* $\text{Li}_{6.25}\text{Ga}_{0.52}\text{La}_{2.67}\text{Zr}_2\text{O}_{12}$	X-ray	0.811 (19.464)	Ga 0.063 (1.512)	0.315 (31.68)	52.656
l	Howard et al.[134] $\text{Li}_{5.5}\text{Ga}_{0.5}\text{La}_3\text{Zr}_2\text{O}_{12}$	Neutron	0.263 (6.312)	Ga 0.167 (4.008)	0.393 (37.728)	48.048
m	Wagner et al.[314] $\text{Li}_{6.58}\text{Ga}_{0.016}\text{La}_3\text{Zr}_2\text{O}_{12}$	X-ray	0.984 (23.616)	Ga 0.016 (0.384)	0.30 (28.8)	52.8

4.7.3 Theoretical Literature Summary Table

Table 4.3: All theoretical studies we could find who explicitly report their 24d:96h ratio and a brief summary of how their structures were generated. If a dopant is present it is included in the total 24d:96h ratio. We should note that under the majority of these schemes the 24d:96h ratio is likely not maintained after allowing their structure to relax or move but the final ratio is rarely reported.
 † Methodology is discussed further in text

	Paper	Li 24d:96h Ratio	Method
n	Tian, Xu, and Qi[296]	13:43	Use experimentally defined ratio[326] and generate 10 random structures
n	Gao, Jalem, and Tateyama[92]	13:43	Use experimentally defined ratio[326] and generate 10 random structures
n	Yu et al.[335]	13:43	Unpublished electrostatic minimisation method
n	Thompson et al.[295]	13:43	Unpublished electrostatic minimisation method
n	Sharafi et al.[265]	13:43	Unpublished electrostatic minimisation method
n	Sharafi et al.[264]	13:43	Unpublished electrostatic minimisation method
n	Yu and Siegel[334]	13:43	perform a quasi-random distribution of Li while keeping the occupancy of sites set
n	Barai et al.[21]	13:43	quasi-random distribution
n	Rettenwander et al.[239]	13:43 (Al)	Highest symmetry possible (for computational costs)
o	Zhang, Liu, and Yu[343]	11:37	Use experimentally defined ratio[17]* and geometry relaxes structure. Explanation is not given as to why the total number of Li changes
p	Xu et al.[328]	24:32	Fill all 24d sites, randomly distribute the 96h then perform a geometry relaxation
p	Karasulu et al.[149]	24:32	Created fully lithiated cell and reduced the symmetry to the $R\bar{3}c$ space group then sequentially introduced vacancies
q	Jalem et al.[141]	14.64:40.05	AIMD at 1800 K
r	Meier, Laino, and Currioni[191]	23:33	120 randomly distributed structures with ratio given by experiment[17]
s	Santosh et al.[257]	22.56:32.64	Started with experimental results[17] and optimised
t	Verduzco, Marinero, and Strachan[309]	10.59:45.51	Average occupancies after 25 ps of AIMD at 1273 and 1773 K
u	Verduzco, Marinero, and Strachan[309]	11.05:44.60	Average occupancies after 25 ps of AIMD at 1273 and 1773 K
v	Haarmann, Rohrer, and Albe[112]	8:48 (Al)	Combinatorial Software + AIMD [†]

Haarmann, Rohrer, and Albe[112] perform the most rigorous exploration of c-LLZO we found. They use the generalised combinatorial structure generation software, Supercell,[208] to generate a number of possible structures. However, due to the large number of structures in typical c-LLZO cell, let alone a 2x2x2 supercell with an Al present, they limited the configuration space by only placing 48 Li exclusively at 48g sites and relying on ab-initio molecular dynamics (AIMD) and geometry relaxation to move the Li into the correct 96h site. They allow the remaining Al and Li atoms the freedom of the 24d sites and generate all combinations, selecting the supercell with the lowest Coulombic energy to proceed with. There are 2 issues with this procedure. Firstly, the choice of initial structure was mostly for convenience of a smaller phase space and a low energy structures is not necessarily guaranteed even with AIMD. Secondly, as we show in figure 4.2

using, the Coulombic forces alone is not sufficient to energetically order c-LLZO structures.

4.7.4 Dimer in Vacuum

To find the optimal inter-atomic distance of a Li-dimer we performed 30 single-point calculations in a large unit cell to prevent self-interaction. We use the same, relevant, settings as used in section 4.4

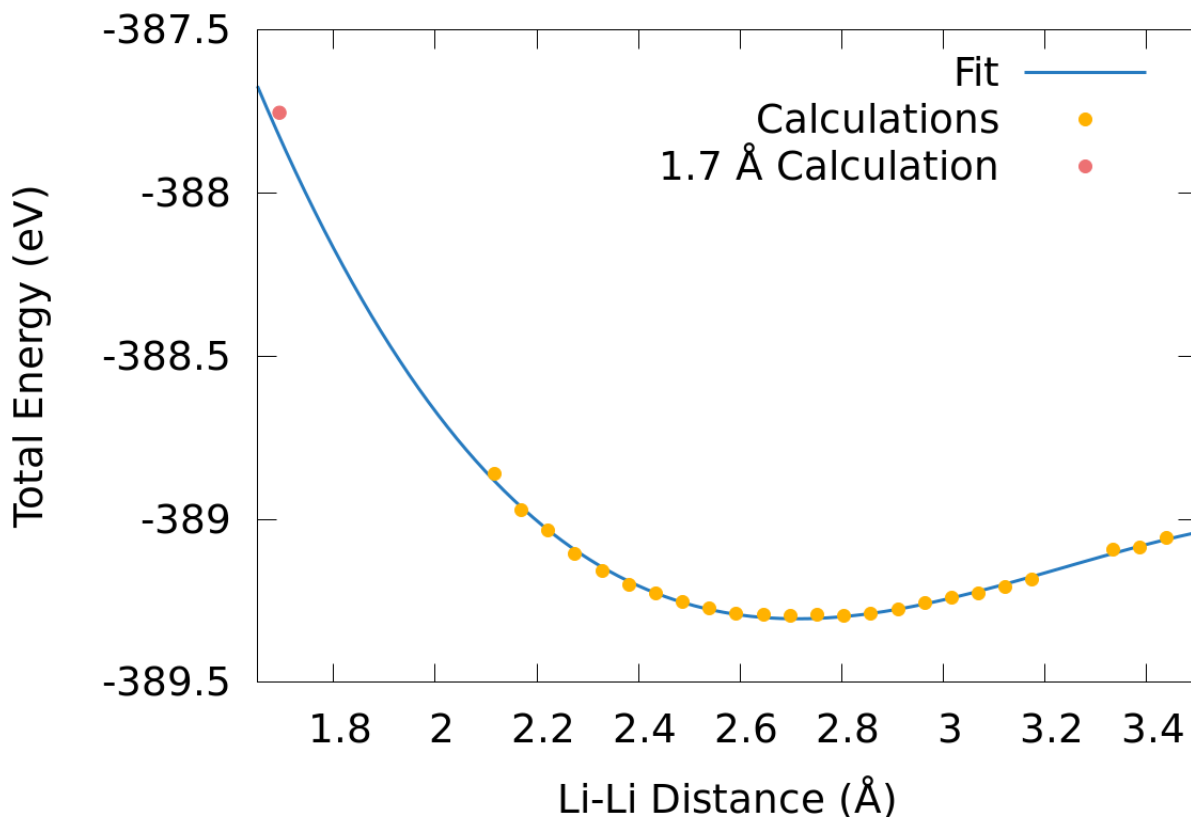


Figure 4.9: The energy of a Li Dimer with changing inter-atomic distance, the fit is a 3rd order polynomial of the calculations close to the optimal distance (yellow). the 1.7 Å calculation (red) is displayed for comparison.

Using the fit in figure 4.9 we find the minimum energy likely to occur at approximately 2.7 Å. We also observe the large energy penalty for Li atoms approaching 1.7 Å of each other.

4.7.5 Symmetry Against Energy

Each generated c-LLZO structure will have a symmetry that is a reduced version of the *Ia3d* space group of the general crystal. We have assigned the new space groups for all 2×10^6 symmetry unique structures, knowing the group we can plot the order of the group against the predicted multiple linear regression (MLR) energy

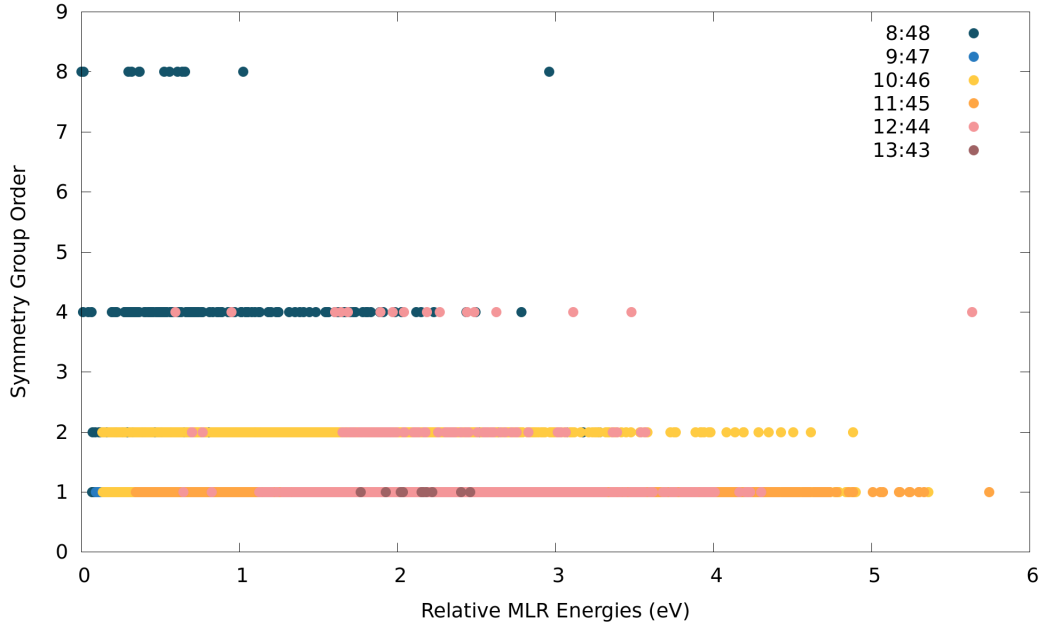


Figure 4.10: MLR energies compared to the order of the individual structure space group, for each $24d:96h$

The most symmetric ratio appears to be 8:48 followed by 12:44 and finally 10:46 with very few odd-numbered 24d occupancies having more symmetry operations higher than 1 (the identity). There does appear to be a slight correlation between lower energy and higher symmetry.

We tested including the symmetry of the structure in our MLR model in section 4.4 but found it made a negligible difference to overall results.

4.7.6 Configurational Entropy

The number of configurations that contribute to configurational entropy for each individual structure can be calculated as the number of symmetry operations (the order) belonging to the $Ia\bar{3}d$ (96) space group which is then divided by the order of the distributed Li structures.

$$\frac{O_{Ia\bar{3}d}}{O_{\text{Li Sublattice}}} = \Omega \quad (4.5)$$

We can then use this number in the following equation to get the configurational entropy, S_{config}

$$-TS_{\text{config}} = -k_B T \ln(\Omega) \quad (4.6)$$

Where T is the temperature and k_B is the Boltzmann constant. The vast majority of structures do not have any symmetry operations other than the identity so belong to space group P1. However, some structures have more than the identity operator available to them and will therefore have different entropic contributions. For this reason, the configurational entropy will need to be considered when energetically ordering our structures. We find structures with space group orders of 1, 2, 4, and 8 (c.f. figure 4.10).

Table 4.4: All space group orders we recorded and their configurational entropic contributions at 298.15 K

Space group order of the Li sublattice	Number of occurrences	Configurational Entropy Contribution at Room Temperature (eV)
1	2154949	0.1173
2	3635	-0.09946
4	174	-0.08165
8	14	-0.06384

Table 4.4 shows that the maximum energy difference that can occur due to configurational entropy is 53 meV. We can also see that only 0.18% of the structures are going to have a different S_{config} than the majority, therefore ordering will be minimally affected.

Chapter 5

A Study of LLZO Interfaces

5.1 Abstract

One of the major obstacles in including the solid-state electrolyte $\text{Li}_7\text{La}_3\text{Zr}_2\text{O}_{12}$ (LLZO) in modern battery packs is the formation of dendrites at the $\text{Li}|\text{LLZO}$ interface. Experimentally, electrochemical interfaces are challenging to probe. This provides a niche in which theory can deliver insights. In this work, we present the progress we have made towards simulating the $\text{Li}|\text{LLZO}$ interface using linear-scaling DFT and high-accuracy surface energies. We also present a methodology to compute the configuration space structures necessary for thoroughly sampling solid-state interfaces which we apply to the system in question and find a minimum, well-sampled, configuration space of 1.04×10^7 structures. To get to this number we find all possible Miller plane combinations, find all possible t-LLZO cuts, create a scheme for sampling inter-slab translations, provide a methodology to finding low-strain commensurate interfaces, and present the results of large-scale DFT calculations on the $\text{Li}|t\text{-LLZO}$ interface that find a reasonable inter-slab distance value. Finally, having established our configuration space, we present our efforts towards the creation of density functional tight-binding Slater-Koster libraries specific to LLZO. During the process, we demonstrate a general workflow for solid-state systems. We find that our Slater-Koster libraries are able to reproduce DFT values for the total electronic density of states at the Fermi level of bulk t-LLZO. However, further parameterisation is required in order to apply these libraries to $\text{Li}|\text{LLZO}$ interfaces, particularly the Li-O element-pair interaction.

5.2 Introduction

We have already established the necessity of using solid electrolytes in section 2.2.1, as well as the importance of their interfaces in section 2.2.3 and the particular merits of using LLZO in sections 2.2.2 and 4.2. Here, We will instead focus our efforts on presenting the necessity of simulating the Li|t-LLZO|c-LLZO interphase.

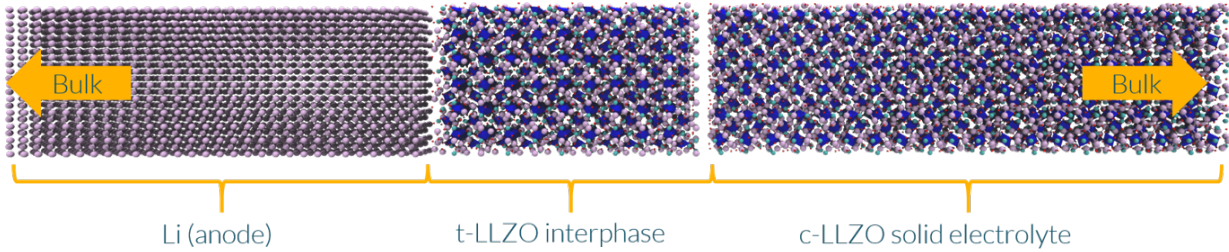


Figure 5.1: Representation of the Li|t-LLZO|c-LLZO structure with a 5 unit-cell thick t-LLZO interphase.

Ma et al.[183] found that when placed in contact with a Li anode a c-LLZO forms a 5 unit-cell thick t-LLZO-like interface. Previous computational efforts at simulating this interface have often focused on the Li|t-LLZO interface[92, 139]. t-LLZO is computationally more convenient to work with as the Li atoms fully occupy their respective sites, unlike c-LLZO (c.f. chapter 4). Dendrite formation in LLZO-based batteries will often exceed the length scale of the t-LLZO-like interphase so in order to produce an accurate representation of that growth, or at least the environment in which that growth occurs in, the full interphase will need to be simulated. Furthermore, simulating the full interphase will enable us to study the driving forces causing the formation of the less ionically conductive t-LLZO polymorph and provide insights on how its formation can be mitigated.

The eventual goal is to simulate this entire interphase. In this chapter, we will outline the progress we have made towards this goal. Including individual surface calculations for Li and t-LLZO, the creation of new energy calculator techniques with the aim of screening potential interfaces, and finally some preliminary results from our Li|t-LLZO calculations.

5.3 Surfaces

Surface energy calculations serve two primary purposes. Firstly, they allow a direct comparison between the literature values and our own. This allows us to validate that our methods are working well before moving on to more complex systems. The second reason is that we need surface energies to calculate the interfacial energies. Therefore high-accuracy surface energies will be vital to ensure good interface evaluation in section 5.4

5.3.1 Li Surfaces

Li is the anode of choice for solid electrolytes as it enables a far higher density than the most common anode used today graphite (c.f. chapter 3). The Li surface, given its monoatomic nature, is exceedingly simple to simulate. This is because any cut along any Miller index plane will be valid energetically, i.e. the surface energy will be the same if we choose the plane behind or in front instead. This is not the case for polyatomic crystals as we will see in section 5.3.2

Surface energies have been typically calculated with the following equation for ultra-thin films (UTF).

$$E_s(i) = \lim_{i \rightarrow \infty} \frac{1}{2A} (E_i - nE_b) \quad (5.1)$$

Where E_s is the surface energy, A is the surface area, E_i is the energy per unit cell of the i -layer film, E_b is the bulk energy of the infinite solid per unit cell, and n is the number of equivalent formula units present in the UTF. E_i was then obtained for a reasonably large value of i and E_b was then determined with an independent calculation.[26, 81] Other methods that iterate upon this have also been demonstrated, such as freezing the bottom layers of the slab[256]

Boettger discovered that this method diverges as i increases[41]. He proposed the following correction.

$$E_s(i) = \frac{1}{2A} (E_i - i\Delta E), \quad \Delta E = E_i - E_{i-1} \quad (5.2)$$

This provides a replacement bulk energy that is calculated in the same manner as the UTF energy. This will lead to a convergence of energy with increasing i . This does have the disadvantage of having to perform an extra calculation. Fiorentini and Methfessel improved on this method by increasing the convergence rate.[83]. They note that as i becomes large a linear relationship emerges.

$$E_i \approx 2E_s + iE_b \quad (5.3)$$

By fitting the calculated UTF energies to a straight line, we can find the bulk energy in a way where the surface energy does not diverge with increasing i and converges quicker than the method proposed by Boettger (equation 5.2). Once the bulk energy is found, we can use it in equation 5.1 to obtain our surface energy. This method requires more calculations than Boettger's in order to obtain a proper linear fit. How this is implemented practically is shown below

$$E_s(i) = \frac{1}{2A} (E_i - i\Delta E), \quad \Delta E = \frac{E_i - E_x}{i - x} \quad (5.4)$$

where E_x is the energy of a UTF of x thickness smaller than i but sufficiently large to display bulk-like properties in its centre.

We attempt to replicate the results of Fiorentini and Methfessel for the low-index surfaces of Li. Here, we use ONETEP (c.f. section 1.3) to perform DFT calculations on all structures. We use the same relevant settings as used in section 4.5. However, because our structure is a metal we need to use EDFT as discussed in section 1.3.3. All values were obtained by using a constant vacuum length. The Fiorentini and Methfessel (F+M) value for surface energy is found by taking the average predicted surface energy of the four largest UTFs.

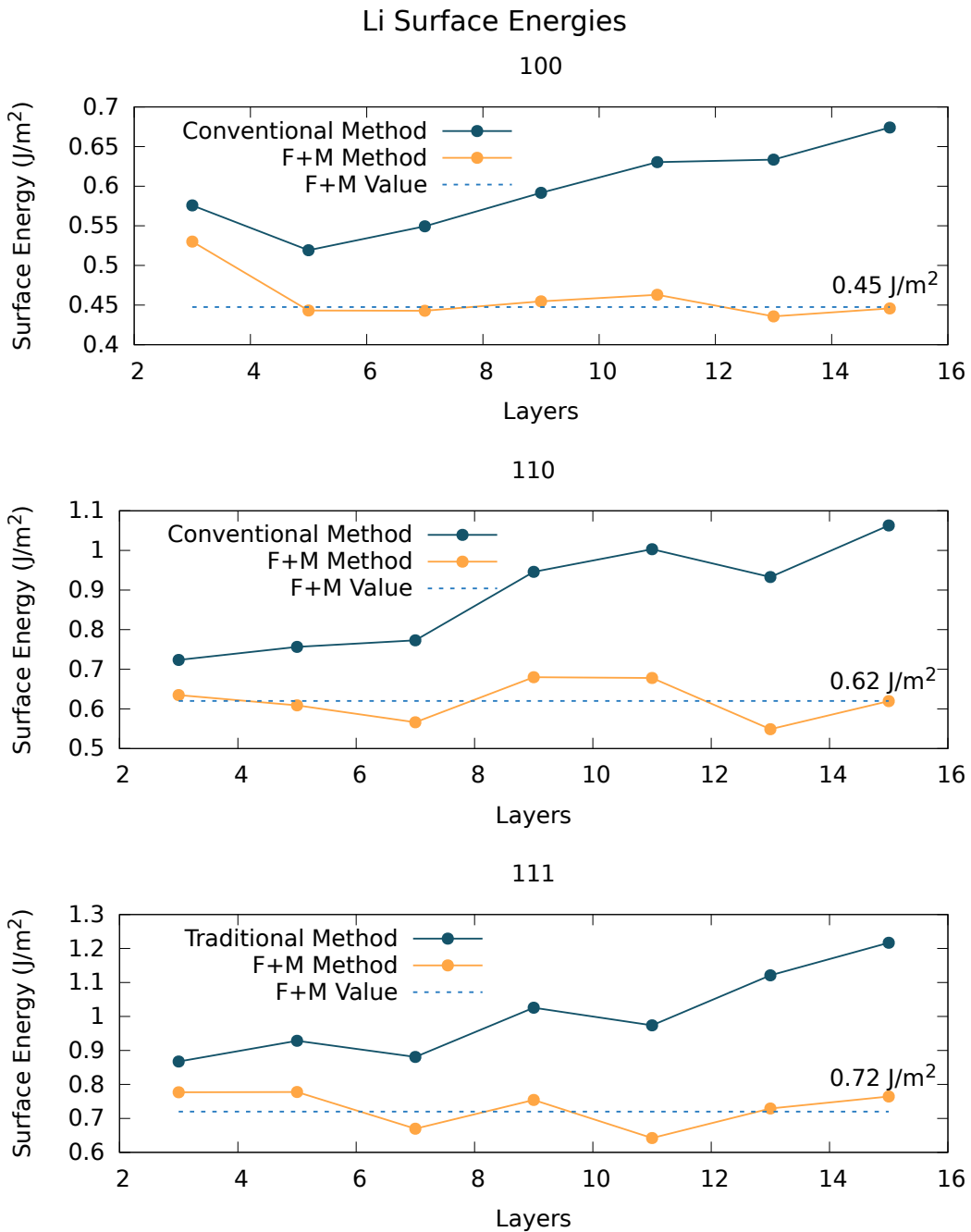


Figure 5.2: Comparison of Fiorentini and Methfessel method to that of conventional surface energy calculations for an increasing thickness of UTF. The surfaces sampled are that of Li{100} (top), Li{110} (middle), and Li{111} (bottom).

Using these methods we find a surface ordering of {100} < {110} < {111}. That is what has been predicted by the literature, however values for the {110} and {111} are higher than predicted.[301]. We suspect the waviness in the Fiorentini and Methfessel method values in figure 5.2 stems from the noise generated by different cell sizes leading to a mismatch in the psinc point grid that we use for our basis (c.f. section 1.3.2). What this means for our calculations is a slightly different kinetic energy cutoff term. We correct this in figure 5.3 for the {100} surface and in later calculations by ensuring the unit cell length remains fixed instead of the length of the vacuum.

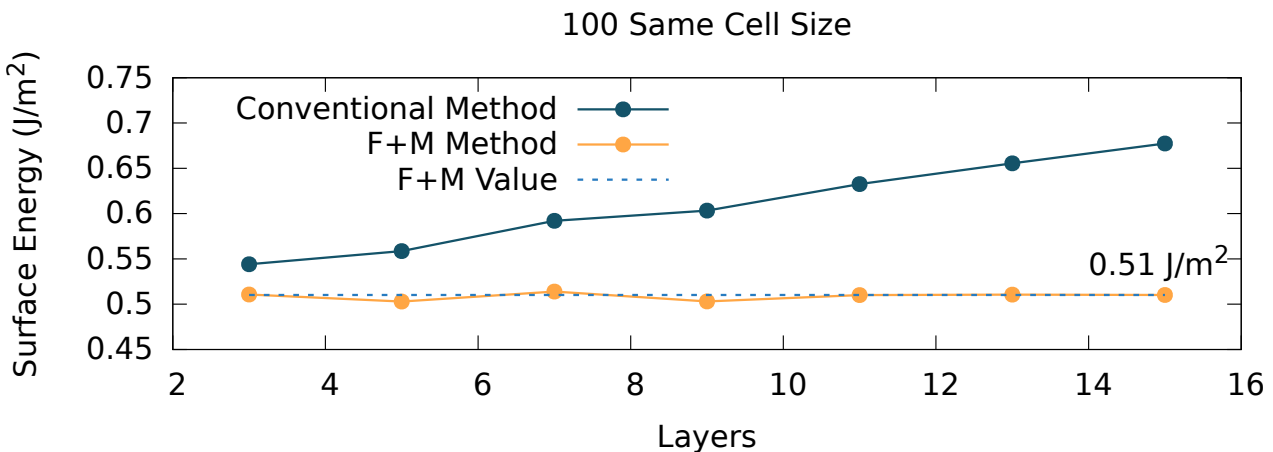


Figure 5.3: Comparison of the Fiorentini and Methfessel method to that of conventional surface energy calculations for increasing thickness of UTF. The {100} surface is used here. Unlike figure 5.2 we keep the unit cell the same size instead of the vacuum. This plot is smoother and converges to a different energy.

5.3.2 t-LZO Surfaces

For t-LZO surfaces, we can use the method outlined in section 5.3.1. However, the problem is complicated by the need to make a choice of termination. To establish this we cut the surface and select a thickness so that the surfaces on either side of the UTF are symmetrically the same, this is done by visually using MATERIALS STUDIO[37].

Next, we can collate all the different atomic positional values of this cut and find unique values along the axis normal to the surface. We then divide by two (as the surface is now symmetric), this number represents all unique possible terminations. For each of these terminations we need to adjust the thickness of the UTF so that the surfaces are symmetric again. This process is time-intensive and prone to human error, efforts to automate this process should be made in the future.

For the {100} cut of t-LZO we can choose 21 different terminations (c.f. table 5.1). We convert the t-LZO structure to an orthogonal cell for ease of generating interfaces in section 5.4.2. There is however a further complication. In equation 5.1 the surface energy is established under the assumption that your slab is constructed with the same ratio as your chemical formula.

Table 5.1: A table showing the different types of excess atoms for different t-LZO symmetric surfaces

Surface	Excess Li	Excess La	Excess Zr	Excess O	Total Atoms	Formula within 1 Å of the surface
Cut 1	4	4	4	0	204	$\text{Li}_4\text{La}_4\text{Zr}_4\text{O}_8$
Cut 2	4	4	4	8	212	$\text{Li}_4\text{La}_4\text{Zr}_4\text{O}_8$
Cut 3	4	4	4	16	220	$\text{Li}_4\text{La}_4\text{Zr}_4\text{O}_8$
Cut 4	5	1	2	12	236	Li_4O_{12}
Cut 5	5	5	2	12	240	$\text{Li}_4\text{La}_2\text{O}_8$
Cut 6	5	5	2	20	248	$\text{Li}_4\text{La}_2\text{O}_8$
Cut 7	6	2	0	8	256	$\text{Li}_4\text{La}_2\text{O}_8$
Cut 8	14	2	0	8	264	$\text{Li}_8\text{La}_2\text{O}_4$
Cut 9	14	2	0	16	272	$\text{Li}_8\text{La}_2\text{O}_8$
Cut 10	14	2	0	24	280	Li_8O_{12}
Cut 11	0	4	4	0	296	$\text{Li}_4\text{La}_4\text{Zr}_4\text{O}_8$
Cut 12	0	4	4	8	304	$\text{La}_4\text{Zr}_4\text{O}_8$
Cut 13	0	4	4	16	312	$\text{La}_4\text{Zr}_4\text{O}_8$
Cut 14	1	1	2	4	320	$\text{Li}_4\text{La}_4\text{Zr}_4\text{O}_8$
Cut 15	9	1	2	4	328	Li_8O_8
Cut 16	9	1	2	12	336	Li_8O_{12}
Cut 17	2	2	0	0	340	$\text{Li}_8\text{La}_2\text{O}_8$
Cut 18	2	2	0	8	348	$\text{Li}_4\text{La}_2\text{O}_8$
Cut 19	10	2	0	8	356	$\text{Li}_4\text{La}_2\text{O}_8$
Cut 20	10	2	0	16	364	$\text{Li}_4\text{La}_2\text{O}_8$
Cut 21	10	2	0	24	372	Li_4O_{12}

However, none of the surfaces displayed in table 5.1 are an exact multiple of the chemical formula for t-LZO ($\text{Li}_7\text{La}_3\text{Zr}_2\text{O}_{12}$)

and have an excess of at least one type of atom. This means we need to extend equation 5.1 to account for this:

$$E_s(i) = \frac{1}{2A} \left(E_i - nE_b - \sum_j \mu_j m_j \right), \quad (5.5)$$

where j is the atomic species, μ the chemical potential, and m the number of excess atoms above what is given by n formula units. We use equation 5.5 to calculate the surface energies for all unoptimised unique cuts of the t-LLZO $\{100\}$ surface. For these calculations, we use the same ONETEP settings as used in chapter 4.

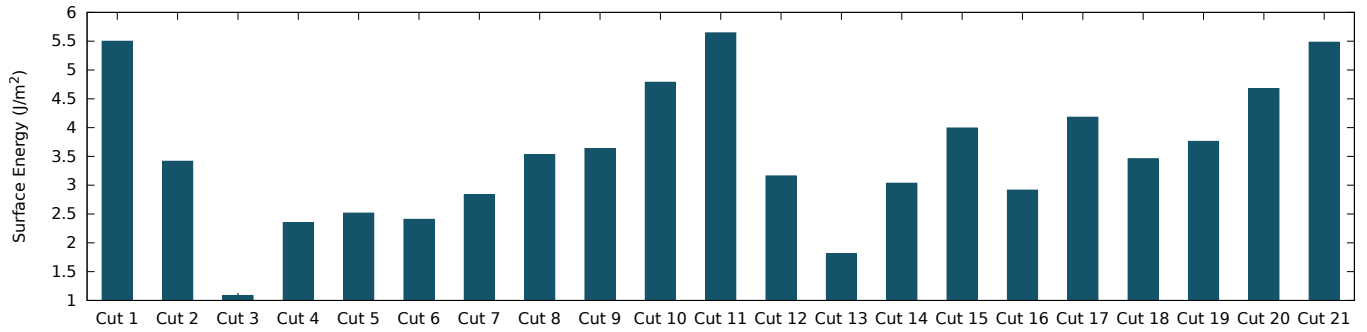


Figure 5.4: Initial surface energy values for single-point calculations of the 21 possible cuts of $\{100\}$ t-LLZO using the Oxide Set 1 chemical potentials from table 5.2 and equation 5.5

We note in figure 5.4 that Cut 3 and Cut 13 are particularly low in energy. However, we should stress that these are surface energies of unoptimised structures. We would expect there to be a significant difference moving to optimised structures. This figure primarily serves to demonstrate the differences surface terminations have on the surface energy of this structure. We also note these surface energies were calculated with equation 5.5 which we have shown in section 5.3.1 can give inaccurate values. We will instead apply the Fiorentini and Methfessel method[83] to this structure by modifying equation 5.4 to be

$$E_s(i) = \frac{1}{2A} \left(E_i - i\Delta E - \sum_j \mu_j m_j \right), \quad \Delta E = \frac{E_i - E_x}{i - x}, \quad (5.6)$$

and applying it to Cut 1 from table 5.1. We chose Cut 1 primarily due to its small atom count. All structures used for this surface energy calculation are geometry-optimised.

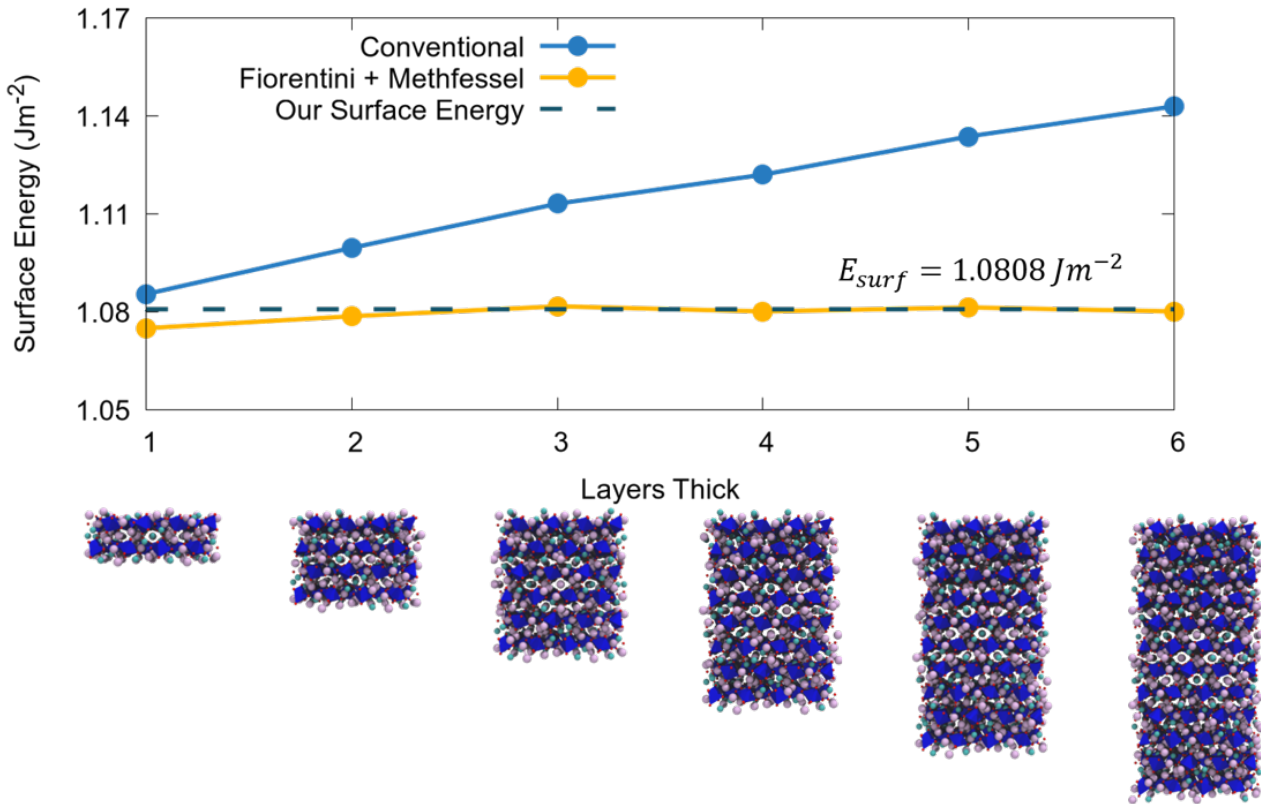


Figure 5.5: The Fiorentini and Methfessel method applied to the t-LLZO {100} Cut 1 (c.f. table 5.1). the Fiorentini and meth vessel values are from equation 5.6, the conventional method is included for comparison and is calculated from equation 5.5, and the surface energy value is calculated by taking an average of all converged terms (in this case 3, 4, 5, and 6 layers thick)

As can be seen in figure 5.5 convergence is achieved at a layer thickness of 3 unit cells. Taking an average of the four thickest values we find a surface energy of $1.08 \frac{J}{m^2}$.

All of the surface energy calculations performed in this section require chemical potentials for the 4 elements present in LLZO. Finding the chemical potentials for a four-species system is a non-trivial task and is discussed further in section 5.3.3.

5.3.3 Chemical Potentials

The chemical potential of a system can be defined as

$$\mu = \frac{G}{N} \quad (5.7)$$

To calculate the chemical potential in solids we assume the pV contributions to be small[63] and therefore we can say $G = F$ where F is the electronic Helmholtz free energy which can be directly found through DFT calculations (c.f. sections 1.2 and 1.3.3). A simplistic method of finding the chemical potential for a multi-component system such as LLZO is by calculating F for each element in its conventional state at room temperature. This means the lowest energy metal crystals for Li, La, and Zr and the diatomic gas for O. To find the pure element values shown in table 5.2 we perform ONETEP calculations using the same settings used in chapter 4.

While this is an easy and simple way of calculating the chemical potential for these elements, it is not reflective of the environments the elements reside in as a part of t-LLZO. To properly compute this we can take the following formula

$$\mu_{\text{LLZO}} = 7\mu_{\text{Li}} + 3\mu_{\text{La}} + 2\mu_{\text{Zr}} + 12\mu_{\text{O}} \quad (5.8)$$

and solve for each μ_i where i is an element in LLZO. In an oxygen environment the metals are oxidised so a more appropriate reference state is binary oxides of the metals. To this end, we can create the following equations based on low energy (on-hull) structures[140] selected from LLZO's decomposition products forming at the reduction onset when in

contact with a Li anode (Li_2O , Zr_3O , and La_2O_3).[348]

$$\mu_{\text{Li}2\text{O}} = 2\mu_{\text{Li}} + \mu_{\text{O}} \quad (5.9)$$

$$\mu_{\text{Zr}3\text{O}} = 3\mu_{\text{Zr}} + \mu_{\text{O}} \quad (5.10)$$

$$\mu_{\text{La}2\text{O}_3} = 2\mu_{\text{La}} + 3\mu_{\text{O}} \quad (5.11)$$

which we can rearrange for all none O elements as

$$\mu_{\text{Li}} = \frac{\mu_{\text{Li}2\text{O}} - \mu_{\text{O}}}{2} \quad (5.12)$$

$$\mu_{\text{Zr}} = \frac{\mu_{\text{Zr}3\text{O}} - \mu_{\text{O}}}{3} \quad (5.13)$$

$$\mu_{\text{La}} = \frac{1}{2}\mu_{\text{La}2\text{O}_3} - \frac{3}{2}\mu_{\text{O}} \quad (5.14)$$

we label this Oxide Set 1 in table 5.2 of course any oxide could in theory be chosen (For Oxide Set 2 we choose Li_2O_2 , ZrO_2 , and La_2O_3). To solve these equations we need a value for μ_{O} . A common assumption to make is that O is in equilibrium with the gas phase therefore it can calculated as

$$\mu_{\text{O}}(T, p) = U_{\text{O}_2} + F_{\text{O}_2}^{\text{trans}}(T) + F_{\text{O}_2}^{\text{vib}}(T) + F_{\text{O}_2}^{\text{rot}}(T) + k_B T \ln \left(\frac{p}{p_0} \right) \quad (5.15)$$

where U_{O_2} is the internal energy of O_2 calculated from DFT. $F_{\text{O}_2}^{\text{trans}}(T)$, $F_{\text{O}_2}^{\text{vib}}(T)$, and $F_{\text{O}_2}^{\text{rot}}(T)$ are the translational, vibrational, and rotational free energies for a diatomic O_2 molecule respectively, for a given temperature. The free energy (Helmholtz energy, as we neglect pV contributions) can be found from

$$F = -k_B T \ln z \quad (5.16)$$

where z is the partition function. Each of the free energies in equation 5.15 for a single O_2 molecule can be calculated with the following partition functions

$$z_{\text{trans}} = \left(\frac{\sqrt{2\pi 8m_{\text{O}_2} k_B T}}{h} \right)^{\frac{3}{2}} \left(\frac{k_B T}{p} \right) \quad (5.17)$$

where m_{O_2} is the mass of an O_2 molecule.

$$z_{\text{vib}} = \frac{e^{\frac{-h\nu}{2k_B T}}}{1 - e^{\frac{-h\nu}{k_B T}}} \quad (5.18)$$

where ν is a value obtained from infrared absorption spectroscopy, here we use 1580.36 cm^{-1} as reported by Atkins and De Paula's *Atkins' Physical chemistry*[14].

$$z_{\text{rot}} = \frac{8\pi^2 I k_B T}{h^2} \quad (5.19)$$

where I is the impulse which takes the form

$$I = m_{\text{O}} r_{\text{O-O}}^2 \quad (5.20)$$

for O_2 , where m_{O} is the mass of an oxygen atom and $r_{\text{O-O}}$ is the O_2 bond length. Converting the partition functions into Helmholtz free energy using equation 5.16 and summing the results, assuming atmospheric pressure, we find a value for μ_{O} and subsequently values for our other chemical potentials.

Table 5.2: The different chemical potentials calculated for each element type in LLZO.

Element	Pure Element (eV)	Oxide Set 1	Oxide Set 2
Li	-7.1814	-7.2897	-7.2912
La	-39.8119	-40.1414	-40.1414
Zr	-48.1356	-48.2208	-48.5018
O	-15.7748	-15.9634	-15.9634

The selection of μ_O has a large effect on the predicted surface energies.[242] In figure 5.6 the effect is demonstrated for explicitly changing the chemical potential but such an effect can be achieved by changing the temperature and pressure as well.

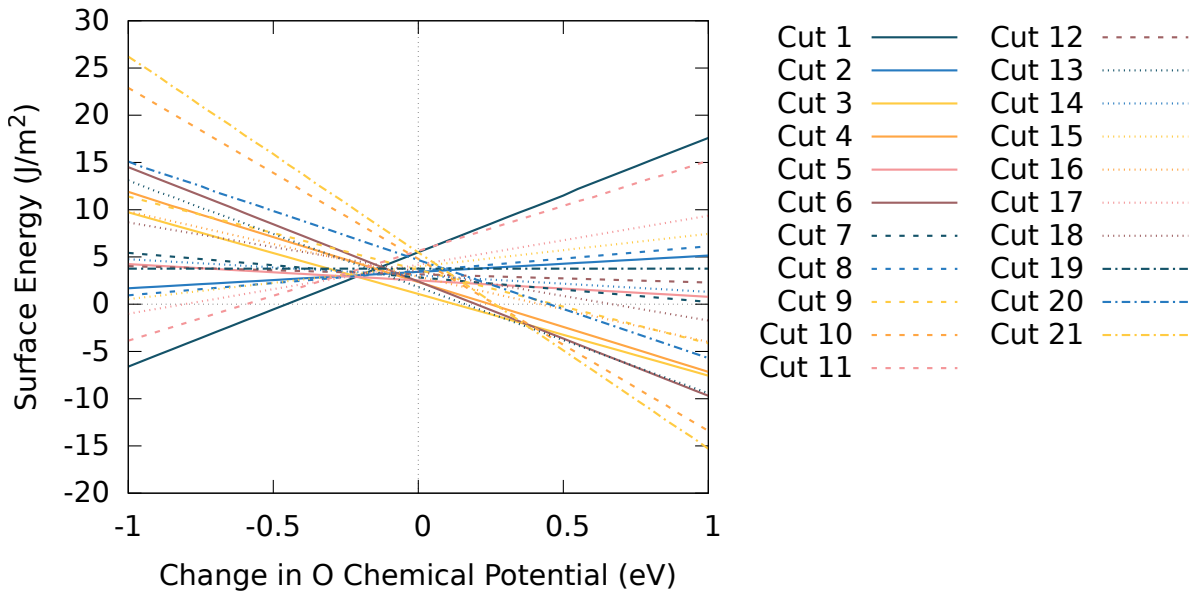


Figure 5.6: Effect of different chemical potentials of oxygen on the surface energies of all 21 {100} t-LLZO surfaces using Oxide Set 1 and the relationships defined in equations 5.12, 5.13, and 5.14

5.4 Interfaces

Having established a suitable method to obtain surface energies in sections 5.3.1, 5.3.2, and 5.3.3 we can now move on to creating interfaces. The Li:t-LLZO interface is the simplest to create and therefore will be the subject of this section. There are a large number of possible interface structures even for our simplest interface. It is unclear which ones should be considered ‘representative’ of a real system. Our approach to resolve this issue is two-fold:

1. Create a means of generating all necessary interfaces that need to be screened (c.f. sections 5.4.1 to 5.4.7)
2. Create a tool to evaluate the energy of these structures (c.f. section 5.5)

5.4.1 Interface Parameters

There are a number of factors that dictate whether an interface is appropriate. We can reduce these factors down to 11 major, general parameters

- 1. Miller indices of surface A
- 2. Miller indices of surface B
- 3. Slab thickness of A
- 4. Slab thickness of B
- 5. Surface termination of surface A
- 6. Surface termination of surface B
- 7. Inter-slab Distance
- 8. Relative compressibility of unit cells
- 9. Relative rotation of surfaces
- 10. Relative u,v translation of surfaces
- 11. Degree of non-commensurate lattice strain T_S threshold

To iterate over all of these parameters thereby creating an 11-dimensional array of all possible surfaces would be thorough but somewhat unnecessary. We can instead make some assumptions, based on the specific characteristics of our system, that will severely reduce the number of structures required to screen.

By assuming our slabs have an energetically converged thickness, which can be identified from our UTF calculations (c.f. figures 5.3 and 5.5), the thickness changes beyond that point are unlikely to affect the interfacial energy in any meaningful way. We can therefore set parameters 3 and 4 to be constants. For pure Li, there is only 1 type of surface termination so we can remove parameter 6. Because t-LLZO has a much higher bulk modulus than Li[103, 336], we only allow the Li cell to stretch or contract as needed when the interface is made, which removes parameter 8. We will also assume, once established, that the value of acceptable total strain (T_S) will remain constant for all types of interface, removing parameter 11, exact values of total lattice strain are calculated for the t-LLZO{100}|Li{100} in section 5.4.2. Finally, as long as we iterate over a sufficiently large range of Miller indices we will capture all relative rotations, eliminating parameter 9. This turns our 11-dimensional configuration space into a 5-dimensional one (parameters 1, 2, 5, 7, 10).

5.4.2 Commensurate Interfaces

To study interfaces between two crystalline species we require commensurate surfaces (i.e. surfaces that have similar lattice vectors) so that no artificial strain is introduced into the system when performing calculations. The degree of ‘fit’ for each lattice vector can be calculated as the total lattice strain which is a combination of strain along the u and v lattice vectors.

$$T_s = \min_{u_{tLLZO}, v_{tLLZO}} \sqrt{(S_u^2 + S_v^2)}, \quad (5.21)$$

where u_{tLLZO} and v_{tLLZO} are the number of unit cell multiples along the u and v directions in a t-LLZO cell respectively. We find T_s by summing the strain along each vector direction. S_u and S_v can be expanded as

$$S_u = \min_{u_{Li}} \left| 1 - \frac{a_{Li} u_{Li}}{a_{tLLZO} u_{tLLZO}} \right|, \quad S_v = \min_{v_{Li}} \left| 1 - \frac{b_{Li} v_{Li}}{b_{tLLZO} v_{tLLZO}} \right|, \quad (5.22)$$

where a_{Li} and b_{Li} are the lattice lengths of the chosen Li surface, a_{tLLZO} and b_{tLLZO} are the lattice lengths of the chosen t-LLZO surface, and u_{Li} and v_{Li} are the number of unit cell expansions along their respective lattice vectors chosen

so that the strain is minimised for a given t-LLZO supercell. By varying the size of the t-LLZO surface supercell and applying equation 5.21 we can easily identify low-strain combinations.

Table 5.3: Total interfacial strains of the best Li match for different t-LLZO 2D supercells. Here we compare the t-LLZO {100} and Li {100} interface. The t-LLZO unit cell was made to be orthogonal through a transformation. The columns represent the number of equivalent unit cells present in the supercell along the v axis, the rows represent the same but for the u axis. The colour gradient represents the degree of strain (red is high, green is low)

Li (100)	u	4	7	11	15	18	22	26	30	33	37
v	tLLZO (100)	1	2	3	4	5	6	7	8	9	10
4	1	8.480%	6.665%	3.760%	3.760%	3.970%	3.760%	3.721%	3.970%	3.760%	3.686%
8	2	8.480%	6.665%	3.760%	3.760%	3.970%	3.760%	3.721%	3.970%	3.760%	3.686%
12	3	8.480%	6.665%	3.760%	3.760%	3.970%	3.760%	3.721%	3.970%	3.760%	3.686%
15	4	8.115%	6.194%	2.841%	2.841%	3.113%	2.841%	2.790%	3.113%	2.841%	2.742%
19	5	7.764%	5.726%	1.580%	1.580%	2.029%	1.580%	1.486%	2.029%	1.580%	1.395%
23	6	7.655%	5.579%	0.911%	0.911%	1.565%	0.911%	0.735%	1.565%	0.911%	0.527%
27	7	7.640%	5.557%	0.766%	0.766%	1.486%	0.766%	0.546%	1.486%	0.766%	0.189%
31	8	7.660%	5.585%	0.952%	0.952%	1.589%	0.952%	0.785%	1.589%	0.952%	0.595%
35	9	7.695%	5.633%	1.200%	1.200%	1.750%	1.200%	1.073%	1.750%	1.200%	0.943%
39	10	7.734%	5.687%	1.430%	1.430%	1.915%	1.430%	1.325%	1.915%	1.430%	1.222%

In Table 5.3, we find that 19 combinations with $T_s \leq 1\%$ and 80 combinations with $T_s \leq 5\%$. The lowest strain combination being

$$\begin{aligned} \text{Li} : & u(37), v(27), \\ \text{t-LLZO} : & u(10), v(8), \end{aligned}$$

with a T_s of 0.189%. We note that with increasing t-LLZO size we generally observe a lower strain. This is expected as for a larger size t-LLZO cell, a more precise number of Li unit cell lengths can be used and a more accommodating fit found. The drawback of this is that the cost of these calculations can quickly become impractical even for linear-scaling DFT (c.f. section 1.3). We have calculated the atoms required for each of these assuming a 2-thick t-LLZO slab, with cuts 1 or 22 from figure 5.4 surfaces and a 10-thick {100} Li surface. The thicknesses are determined by the values that are considered close to converged in figures 5.3 and 5.5.

Table 5.4: Minimum number of atoms required to build the best Li match for different t-LLZO 2D supercells. Here we compare the t-LLZO {100} and Li {100} interface. The t-LLZO unit cell was made to be orthogonal through a transformation. The columns represent the number of equivalent unit cells present in the supercell along the v axis, the rows represent the same but for the u axis. The colour gradient represents the number of atoms required (red is high, green is low)

Li (100)	u	4	7	11	15	18	22	26	30	33	37
v	tLLZO (100)	1	2	3	4	5	6	7	8	9	10
4	1	706	1332	2038	2744	3370	4076	4782	5488	6114	6820
8	2	1412	2664	4076	5488	6740	8152	9564	10976	12228	13640
12	3	2118	3996	6114	8232	10110	12228	14346	16464	18342	20460
15	4	2744	5188	7932	10676	13120	15864	18608	21352	23796	26540
19	5	3450	6520	9970	13420	16490	19940	23390	26840	29910	33360
23	6	4156	7852	12008	16164	19860	24016	28172	32328	36024	40180
27	7	4862	9184	14046	18908	23230	28092	32954	37816	42138	47000
31	8	5568	10516	16084	21652	26600	32168	37736	43304	48252	53820
35	9	6274	11848	18122	24396	29970	36244	42518	48792	54366	60640
39	10	6980	13180	20160	27140	33340	40320	47300	54280	60480	67460

The best matching structure for the {100} interfaces shown above would require 47000 atoms ($\text{Li}_{19980}|\text{Li}_{7980}\text{La}_{3360}\text{Zr}_{2240}\text{O}_{13440}$). Which is beyond our current computational resources and may not even be necessary. Looking at table 5.3 we can see several strain minima occurring at far lower atom counts when cross-referencing with table 5.4. We would like to examine the lowest atom instances of a $T_s \leq 5\%$ and $T_s \leq 1\%$ which would have atom counts of 2038 ($\text{Li}_{880}|\text{Li}_{342}\text{La}_{144}\text{Zr}_{96}\text{O}_{576}$) and 12008 ($\text{Li}_{5060}|\text{Li}_{2052}\text{La}_{864}\text{Zr}_{576}\text{O}_{3456}$) respectively. Further examinations of these structures, as well as a high strain-low atom count structure, will give us an indication of the effect of strain on overall system effects such as surface reconstructions and anode-electrolyte interaction. This will also provide us with a target T_s to stay below for other interfaces.

5.4.3 Miller Planes

A Next, we must decide on the ranges and resolution that we want to probe our configuration space. For parameters 1 and 2, we will produce all unique permutations of the miller indices up to $\{222\}$. We can calculate the number of surfaces for t-LLZO and Li with

$$p_{t\text{LLZO}} = ((n+1)^3 - 1) - x(n) \quad (5.23)$$

$$p_{\text{Li}} = \frac{(n+1)^3}{3} - y(n) \quad (5.24)$$

Where n is the max miller index number, x is a unknown function that we find after we have found all surfaces and compared the equivalent and y is a sequence shown by Bos[43]¹. For $n = 2$, $p_{t\text{LLZO}} = 26$, the ‘-1’ in equation 5.23 comes from the fact there is no $\{000\}$ plane . For Li, this number is significantly less as $\{001\}=\{010\}=\{100\}$. Also, surfaces that are multiples of other surfaces are the same i.e. $\{001\}=\{002\}=\{003\}$. Therefore only surfaces that are not permutations of each other or are a multiple of a lower index miller plane are allowed, resulting in 6 unique surfaces up to the $\{222\}$ limit: $\{100\}$, $\{110\}$, $\{111\}$, $\{201\}$, $\{211\}$ and $\{221\}$ (c.f. figure 5.9). The total number of unique miller plane combination, p_{Miller} , can be calculated as

$$p_{\text{Miller}} = p_{t\text{LLZO}} p_{\text{Li}} \quad (5.25)$$

For $n = 2$, $p_{\text{Miller}} = 78$.

5.4.4 Surface Cuts

To establish the size of parameter 5 we must iterate through all possible 26 miller index surfaces using the method described in section 5.3.2.

Table 5.5: Estimates of the possible numbers of terminations for each miller plane for t-LLZO

Miller Indeices	Number of possible terminations
001	10
002	10
010	22
011	42
012	38
020	22
021	39
022	34
100	22
101	42
102	38
110	21
111	38
112	32
120	42
121	62
122	73
200	22
201	39
202	0
210	42
211	62
212	73
220	0
221	37
222	0
Total	862

For this table we wrote a custom open-access program called Symmetric Surface Finder (SSF)[130]. Further to this script, it is apparent that some of these cuts produce the same surface. removing the duplicate planes we are left with **410 surfaces**. We note that some surfaces yield no surfaces. This is a limitation of using only symmetric slabs.

¹The exact form of this equation was attempted to be solved in our office with a prize of a pint. It consumed a significant amount of people’s time until Tom Demyere found that this was an unsolved mathematical problem that, at best, could be approximated with the referenced sequence. He won a half-pint

5.4.5 Inter-Slab Distance

The optimal inter-slab distance can be calculated by finding the minimum energy of two interfaces that we slowly increase the gap between. Ideally, this would be done by geometry-optimising each structure. We use the minimum size, $T_S \leq 5\%$ structure calculated in table 5.3 of

$$\begin{aligned} \text{Li} : & u(11), v(4), \\ \text{t-LLZO} : & u(3), v(1). \end{aligned}$$

To reduce computational cost we reduced the thicknesses of both slabs to a 1-thick {100} t-LLZO slab (c.f. table 5.5) and a 6-thick Li {100} slab this reduces the size of structure required for each calculation from 1332 (c.f. table 5.4) to 1110 atoms. This interface was optimised using ONETEP and used the same settings as we used in section 4.5. The structure we generate is shown in figure 5.7

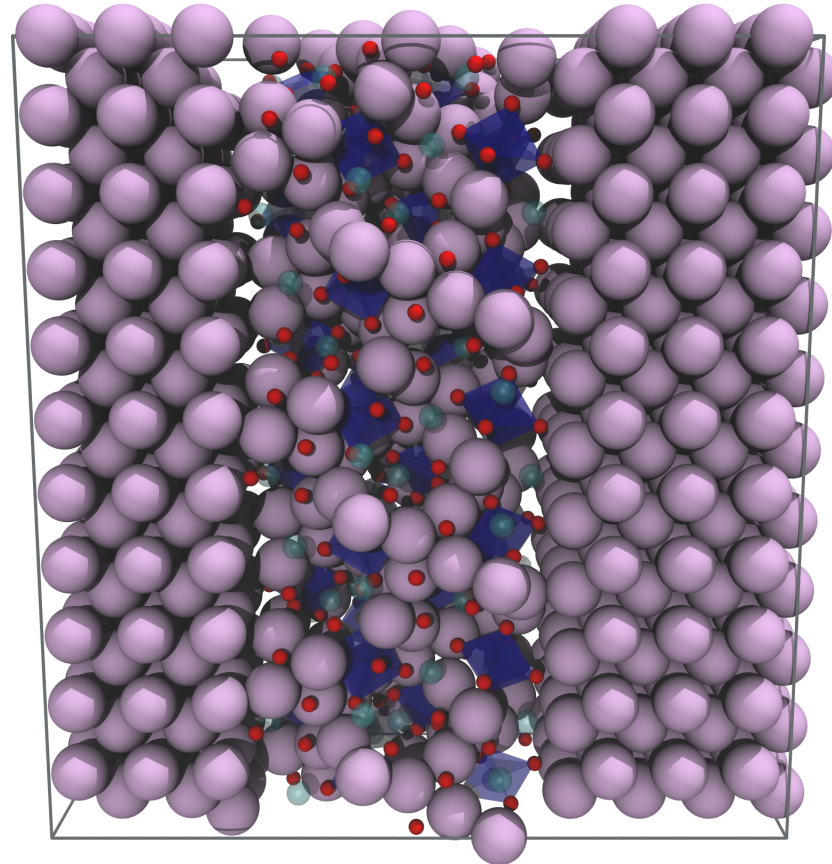


Figure 5.7: geometry-optimised structure of the near-commensurate, t-LLZO{100}|Li{100} interface.

To ensure the correct interslab distance has been attained we take an unoptimised version of the structure shown in figure 5.7 and perform ONETEP single-point calculations using the settings we used in section 4.4 and vary the interslab distance. We report the results of this in figure 5.8.

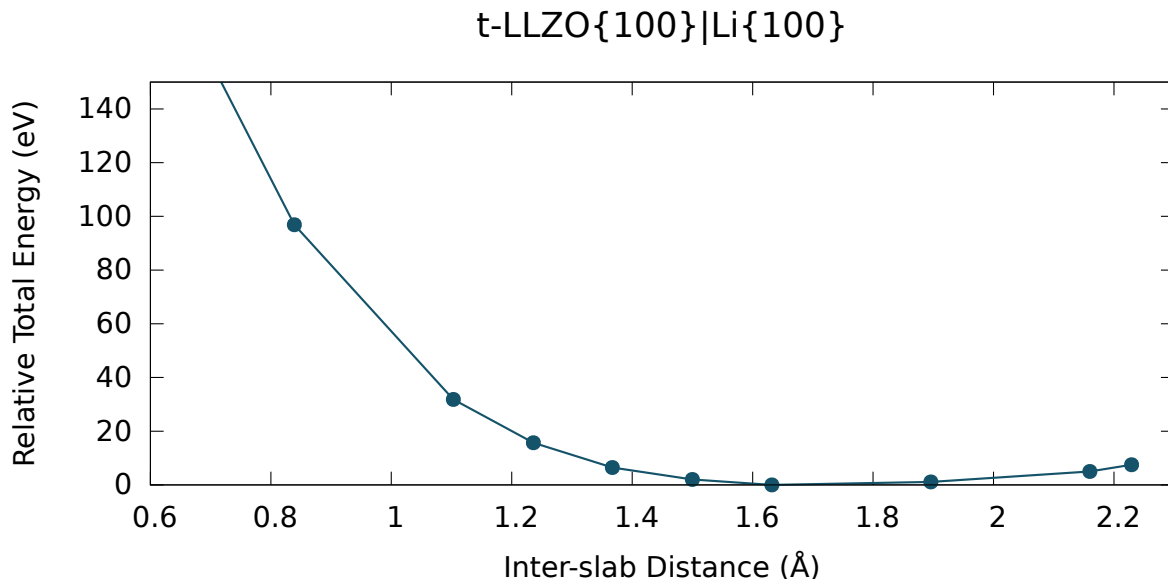


Figure 5.8: How total energy varies with inter-slab distance. Each point represents a single-point calculation performed.

Because we do not have a vacuum that we can expand into to keep the cell the same (c.f. the differences between figures 5.3 and 5.2), we have to employ the strategy used in section 3.3.2 where we expand the cell while being mindful of the psinc basis grid in order to keep the kinetic energy cut off constant. We can see the results of this method in figure 5.8. We observe that the minimum occurs around 1.6-1.7 Å. To establish whether this inter-slab distance is universal to the Li|t-LLZO interface further calculations should be performed. If a universal inter-slab distance can be found then we would be able to remove parameter 7 from consideration.

5.4.6 Relative Inter-slab Translation

Relative u , v translation is dependent on the minimum size surface structure that can translate into itself (i.e. it is dependent on the lattice parameters of the smallest two-dimensional unit cell from either surface). In all cases, for our system, the smallest repeatable surface structure belongs to Li. This means the amount of possible translatable distance is entirely dependent on the Miller plane of our Li surface (c.f. figure 5.9).

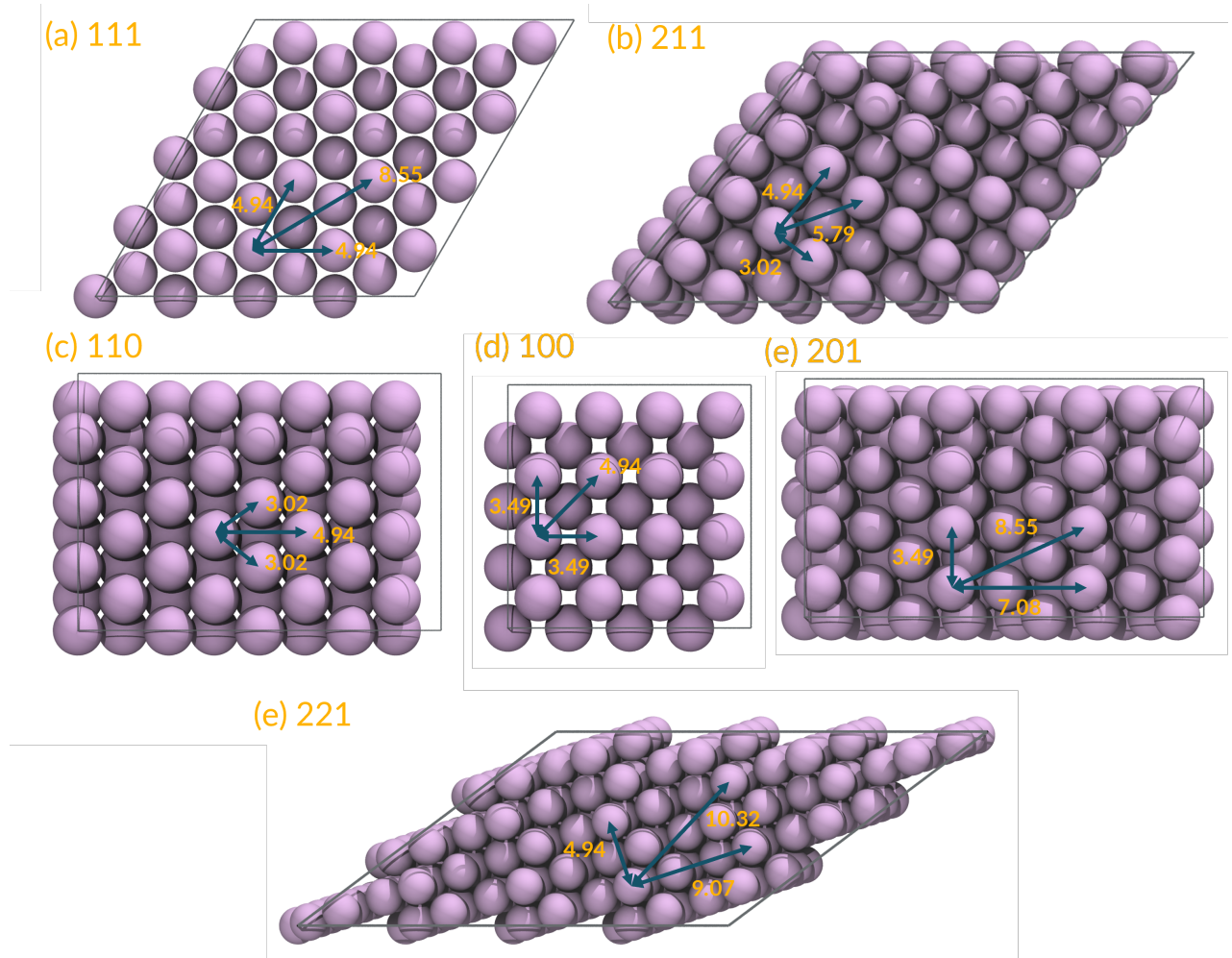


Figure 5.9: Comparison of the 6 unique Li surfaces with a miller index ≤ 2 and the significant reduced unit cell parameters of each surface structure.

We can divide each of the areas of the repeatable surface unit cells into a sample point grid that are evenly distributed with an arbitrary accuracy. In table 5.6 we choose our sample density d to be greater than 1 sample per 2 \AA^2 and calculate the number of symmetrically unique samples p we require for each unique Li surface. This number is calculated by equation 5.26

$$\lceil p \rceil = \frac{A}{2d} \quad (5.26)$$

where A is the surface area of the smallest repeatable surface unit cell. We divide by two because half of the unit cell should be sufficient to sample all unique points.

Table 5.6: Areas of repeatable surface unit cells for all unique Li surfaces with miller indices ≤ 2 along with the number sample points to ensure a greater than 2 \AA^2 per point coverage (d)

Surface	Area (\AA^2)	Number of sample points $d > 2$
100	12.18	4
110	17.24	5
111	42.24	11
201	24.71	5
211	14.92	3
221	44.80	11
Total	156.09	39

For this sample density, we find 28 unique sample points, where each sample point represents a 2 dimensional translation of the Li surface against that of t-LLZO. To quantify if this sample density is reasonable further calculations will need to be performed.

5.4.7 Configuration Space

To find an estimate of the number of structures possible, C , under the regime of relevant parameters we have defined as well as making the following assumptions:

1. All relevant surfaces for our interface are covered when the Miller indices are ≤ 2
2. We have counted the correct number of t-LLZO interface cuts using our visual method of ensuring symmetry
3. The chosen slabs are thick enough to exhibit bulk-like properties
4. A universal inter-slab distance value exists
5. The relative u, v translation grid is sufficiently sampled

we can write

$$p_{\text{Miller}(2)} \times p_{\text{tLLZO-term}} \times p_{u,v} = C \quad (5.27)$$

where $p_{\text{Miller}(2)}$ is the number of possible Miller plane combinations ≤ 2 , $p_{\text{tLLZO-term}}$ is the total number of different t-LLZO surface cuts for each t-LLZO miller plane ≤ 2 , and $p_{u,v}$ is the total number of samples for the repeatable surface structures all 6 unique Li miller planes ≤ 2 where $d > 2$. Substituting in the relevant values we find $C \approx 1.25 \times 10^6$

Having established the size of the configuration space that we need to sample it is apparent that performing DFT calculations for all structures would be computationally intractable. In the next section, we will show the progress we have made towards developing fast interfacial energy evaluators that could be used to effectively screen several million structures in a reasonable time frame.

5.5 DFTB parameterisation for LLZO

We have discussed theory of density functional tight-binding (DFTB) in section 1.5. Given its potential of producing near-DFT accuracy at a fraction of the computational cost, if correctly parameterised, this theory is ideal for quickly evaluating a large number of similar structures. Therefore it is an ideal tool for a configuration space discussed in section 5.4.7. No published DFTB Slater-Koster library exists for the LLZO combination of elements so we needed to create our own. To do this we have used the DFTB+ parameterisation procedure outlined in MATERIALS STUDIO.[37]

5.5.1 Library Development

In this section, we discuss the development of three Slater-Koster libraries that share a number of element-pair parameters between them.

1. LIB19_LLZO: Library that creates the electronic parameters and the short-range element-pair potentials for La and Zr. It acts as an extension to the interactions of the already parameterised LIB 2019 library[37]
2. LLZO_A2: Library that takes all of the created electronic and short-range element-pair parameters from LIB19_LLZO and also parameterises the Li and O short-range element-pair interactions
3. LLZO_Al: Library containing all the electron and short-range element pair interactions from LLZO_A2 and also extends that library to include all Al electronic and short-range element-pair interactions. (Not yet validated)

All libraries used the LIB 2019 Electronic parameters as we found that they are unlikely to change even with the different chemical environments that the library is designed for. LIB19_LLZO was developed because a Slater-Koster library had already been developed and made available for use in MATERIALS STUDIO that focuses on interactions in Li-ion batteries (c.f. section 2.1) known as LIB 2019. This library contained interactions we required in our library (Li-Li, O-O, and Li-O). Extending this already ‘battery-themed’ library was a natural choice and had the potential to save us time. The goal was therefore to generate all relevant pair-wise interactions for LLZO excluding those that are included in the LIB 2019 library and extend this library (c.f. table 5.7 for a summary). We will refer to the new extended library as LIB19_LLZO throughout the rest of this chapter

Table 5.7: A summary of the element-pair interactions produced for each of the Slater-Koster libraries we develop. The L_L are the element-pair interactions we parameterise for LIB19_LLZO, L19 are the interactions provided by the LIB 2019 library. L_A2 and L_Al denote the element-pair interactions used to develop LLZO_A2 and LLZO_Al respectively

Atom	Li	La	Zr	O	Al
Li	L19/LA2				
La	L_L	L_L			
Zr	L_L	L_L	L_L		
O	L19/LA2	L_L	L_L	L19/LA2	
Al	LA1	LA1	LA1	LA1	LA1

To extend the LIB 2019 library for LIB19_LLZO we needed to achieve three goals

1. Parameterise the electronic terms for La and Zr
2. Parameterise the repulsive terms for all non-LIB 2019 interactions
3. Merge and evaluate the new library

A workflow of the process we used to achieve these goals is presented in figure 5.10

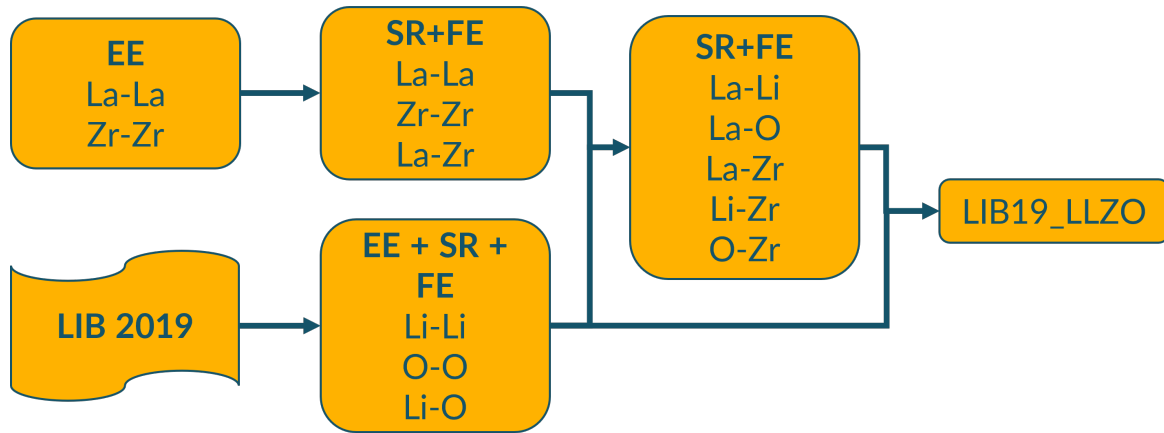


Figure 5.10: Workflow used to create the LIB19_LLZO Slater-Koster file. Where EE is the electronic parameter generation (c.f. section 5.5.2), SR is the short-range potential fitting (c.f. section 5.5.3), and FE is the final evaluation (c.f. section 5.5.2). Each subprocess is carried out for the element-pairs denoted underneath the header. The Li and O parameters were extracted from the LIB 2019 Slater-Koster File available on MATERIALS STUDIO[37] and were not calculated by us.

To extend the LIB19_LLZO by reparameterising the necessary element-pair interactions LIB 2019 and to include Al we needed to achieve a further 3 goals

1. Parameterise the electronic terms for Al
2. Parameterise the short-range potential terms for the missing Li and O element pairs as well as all Al element pairs
3. Merge and evaluate the new libraries

A workflow on how we aim to achieve this is presented in figure 5.11

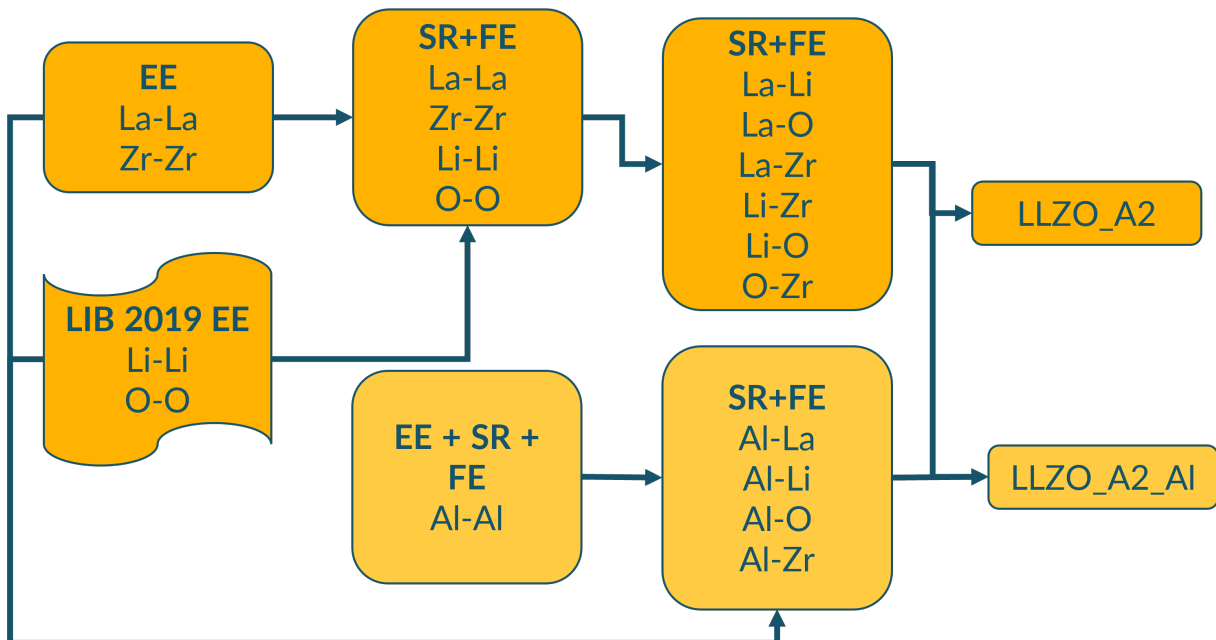


Figure 5.11: Workflow used to create the LLZO_A2 and LLZO_A2_Al Slater-Koster files. Where EE is the electronic parameter generation (c.f. section 5.5.2), SR is the short-range potential fitting (c.f. section 5.5.3), and FE is the final evaluation (c.f. section 5.5.2). Each subprocess is carried out for the element-pairs denoted underneath the header. The Li and O parameters were extracted from the LIB 2019 Slater-Koster File available on MATERIALS STUDIO[37] and were not calculated by us.

Both of the workflows presented here require multiple complex subprocesses. We attempt to condense and generalise these subprocesses in the following sections

5.5.2 Electronic term parameterisation

To create electronic parameters we chose different on-hull, or close-to-hull, pure element structures that we geometry-optimised (GO) with DFT code DMOL³[68, 69]. For all elements, we used structures provided by Materials Project[140].

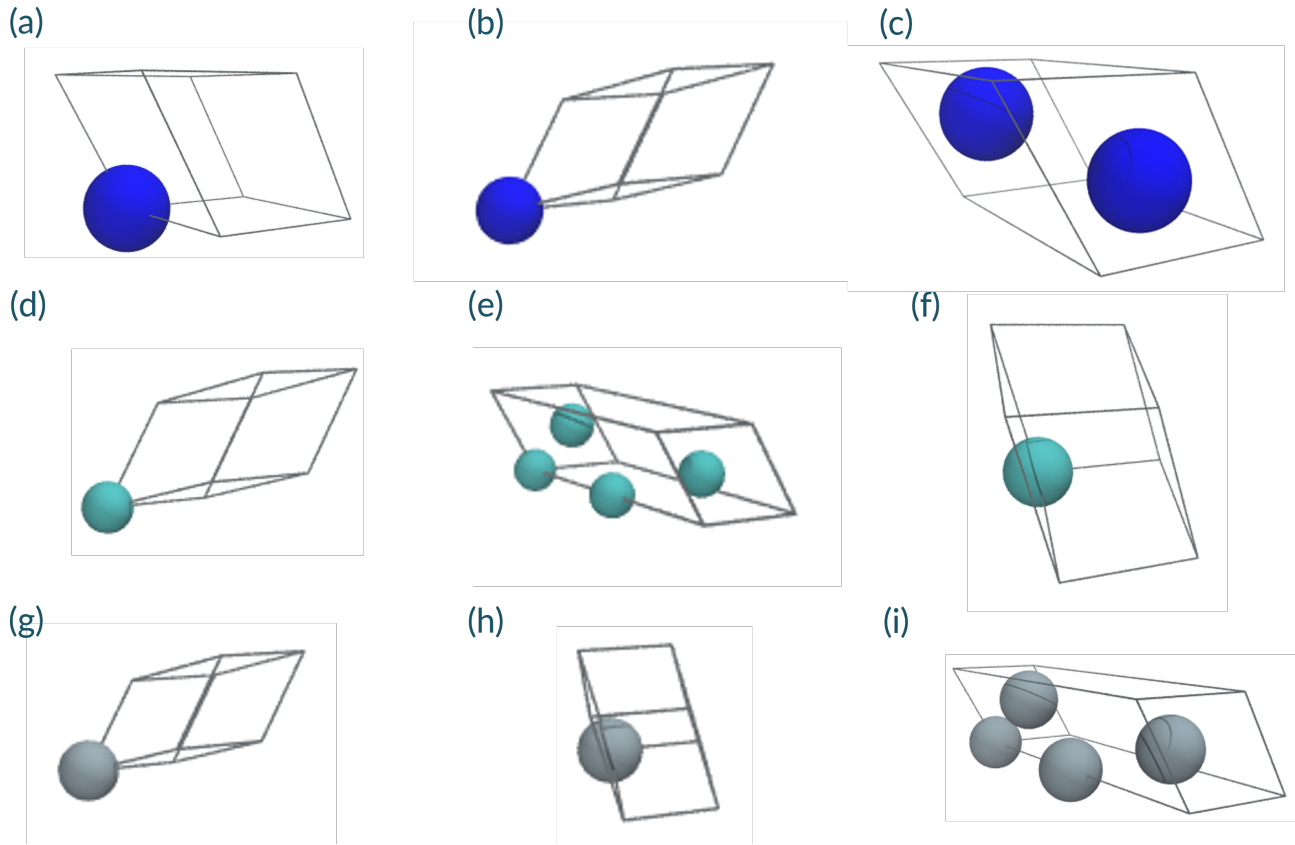


Figure 5.12: geometry-optimised Zr ((a), (b), and (c)) and La ((d), (e), and (f)) structures we used to find the electronic parameters for the LIB19_LLZO Slater-Koster library. The Al ((g), (h), and (i)) structures we used to find the electronic parameters for the LLZO_Al Slater-Koster library are also shown.

To obtain the optimised structures in figure 5.12 with DMOL³ we used the following settings:

- GO energy tolerance: 1×10^{-5} Ha
- GO max force tolerance: 2×10^{-3} Ha/Å
- GO max displacement tolerance: 5×10^{-3}
- Exchange-Correlation Functional: PBE[225]
- self-consistent field tolerance: 1×10^{-6}
- Basis set: DNP 4.4
- K-point mesh: $6 \times 6 \times 6$

We used these settings for the rest of this section unless we explicitly state otherwise

The Hamiltonian matrix for DFTB is defined in equation 1.113. The off-diagonal elements of this matrix, found in equation 1.115 need parameterisation of the x and r_0 terms. The style of parameterisation in the mentioned equation calculates the potential as a superposition of atomic potentials which is then used to calculate the wavefunction. For our parameterisation we treat the off-diagonal elements in the following form

$$H_{\mu\nu} = \langle \phi_\mu^\alpha | \hat{T} + V_0(n_\alpha + n_\beta) | \phi_\nu^\beta \rangle \quad (5.28)$$

meaning that the potential is a superposition of atomic electron densities. This means that the single electron densities and single electron wavefunctions can be calculated with different compression radii.[144] This can lead to a better fit of our system but can lead to over-fitting. We now had three parameters to fit, the wavefunction compression radii r_1 , the atomic electron density compression radii r_2 , and the power term x .

We then generated a given number of permutations of different values for these parameters and compared the band structures produced to that of DMOL³'s. The parameter set with the lowest mean average error (MAE) of band structure for all structures was selected as the electronic parameter for that element. Table 5.8 shows the optimal values we found.

Table 5.8: Electronic parameter set for La, Zr, and Al.

Element	r_1	r_2	x
La	2	7.25	5
Zr	1.64	13	8
Al	1.75	10	3

We note that the r_2 value for Zr consistently gave marginally better accuracy for higher terms. We show the plots of how increasing r_2 affected each of the structure's band structure MAE

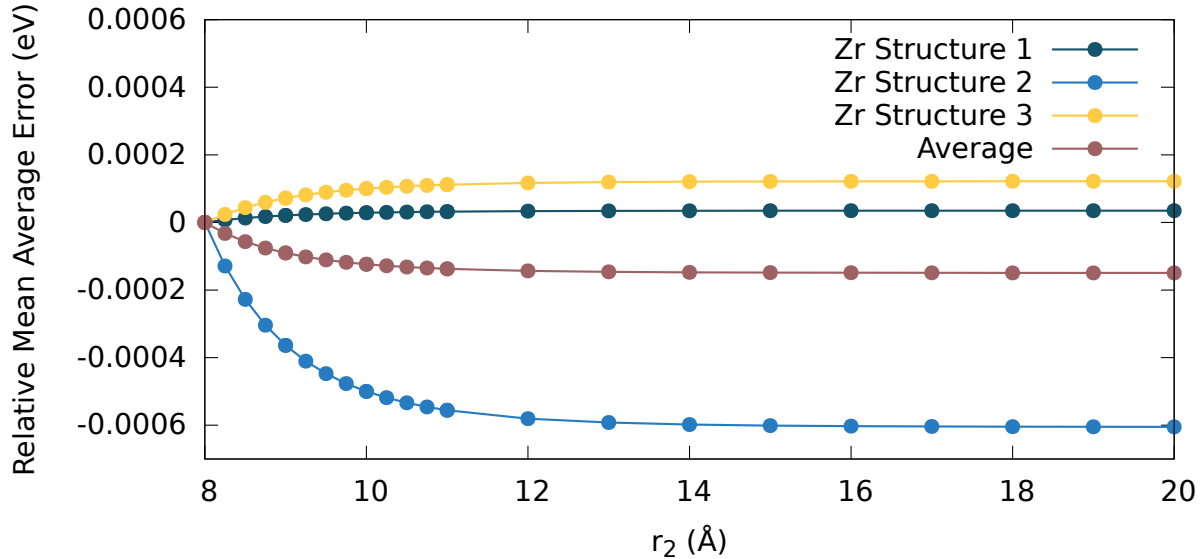


Figure 5.13: The Mean average error change with an increasing electron density compression parameter for each of the Zr structures shown in figure 5.12

In figure 5.13, we can clearly see only one structure of the three is benefiting from a higher r_2 value (this structure is shown in figure 5.12c) while the others slightly increase. Beyond a $r_2 = 13$ there are minimal average MAE improvements. In the interest of keeping the parameterisation transferable, we elected to choose our Zr r_2 to have a value of 13.

5.5.3 Repulsive term parameterisation for LLZO pair interactions

With the electronic terms for all individual elements available to us, we generated the short-range, repulsive fit for the following element-pairs

- La-La
- La-O
- Zr-Zr
- La-Li
- Li-Zr
- O-Zr

for the LIB19_LLZO library, this is extended to include the following element pairs

- Li-Li
- O-O
- Li-O

for the LLZO_A2 library, and a final extension is performed, to include

- Al-La
- Al-Zr
- Al-Al
- Al-Li
- Al-O

for the LLZO_Al library.

To find a good fit for each of these interactions we created a set number of systems consisting of materials containing the element-pairs. The materials used would ideally have involved a low-atom number to keep the computational cost of multiple calculations low and a low energy-above-hull so as to sample ground-state-like structures. For most cases, these structures were sourced from Materials Project[140]. Two appropriate structures were typically selected. We also create a dimer of the element pair meaning we use three binary structures per atom-pair to create our repulsive term.

The structures are then optimised using DMOL³. These optimised structures can then be used for a DFTB+ parameterisation calculation. Example settings for such an interaction are shown in table 5.9. This table was then modified if we found that some parts of the fit required further parameterisation. Once the settings are chosen we can perform a DFTB+ parameterisation calculation. Here each of the steps in table 5.9 represents an individual DFT calculation using DMOL³.

All The data generated is fit to a pairwise polynomial basis set. The energies can be expressed as linear combination of these polynomials.

$$U_{e_\alpha e_\beta} = \sum_\nu C_{e_\alpha e_\beta, \nu} f_{e_\alpha e_\beta, \nu}(r_{\alpha\beta}), \quad (5.29)$$

where U is the repulsive, short-range potential for the element-pair $e_\alpha e_\beta$, C are the polynomial coefficients, f the polynomial which is dependent on the associated atom pair distance $r_{\alpha\beta}$, and ν is the term of the associated polynomial. To ensure sufficient decay a cut-off distance r_{cut} is set.

$$f_{e_\alpha e_\beta, \nu}(r_{\alpha\beta}) = \begin{cases} (r_{\alpha\beta} - r_{\text{cut}})^\nu & \text{if } r_{\alpha\beta} < r_{\text{cut}} \\ 0 & \text{otherwise,} \end{cases} \quad (5.30)$$

The parameterisation procedure tests a number of different r_{cut} values to find the and selects the one with the lowest accumulated squared fitting error for all conformations (c.f. figure 5.14). Often the lowest error r_{cut} is not the most transferable so a number of fits are carried forward to the final evaluation. We are aware of more advanced automated fitting schemes and it could be a potential area to improve on in future work.[96, 102, 144]

Table 5.9: Example settings used for paramaterisation calculation performed using DFTB+ on MATERIALS STUDIO. The generator column indicates the type of deformation that is performed on the corresponding structure; Stretch involves changing the inter-atomic distance of the dimer, Scale changes the lattice parameters of a crystal, Perturb involves the movement of a single atom relative to the rest of the crystal. The Steps column indicates the number of samples to take for each generator. The Force column indicates whether the forces are included in the fit or just the energy. The Relative Weight column indicates how much each generator for a given crystal contributes to the overall fit. The Max Compression/Expansion columns mark the range under which the steps are distributed for each generator. The Number of Shells column is solely for the Perturb generator and indicates the number of radial steps to take in between the equilibrium position and that of the distance defined in Max Perturbation. The Weight Function Width describes the tightness of the Gaussian used that contributes to the final model. Tighter widths are typically used to provide information over a smaller region and therefore should not contribute to region in the pair interaction considered ‘far-away’

Structure	Generator	Steps	Force	Relative Weight	Max. Compression/ Perturbation	Max Expansion	Number of Shells	Weight Function Width
Dimer	Stretch	61	Yes	4	60%	60%	-	40
Crystal 1	Scale	21	No	1	10%	15%	-	7.5
Crystal 2	Scale	21	No	1	10%	15%	-	7.5
Crystal 1	Scale	41	No	1	40%	60%	-	40
Crystal 1	Perturb	41	Yes	4	10%	-	10	5

A further check that we can perform is to visually ensure there are no major oscillations in the individual pair-potentials. Figure 5.14 shows element-pair potentials that are fit for different r_{cut} .

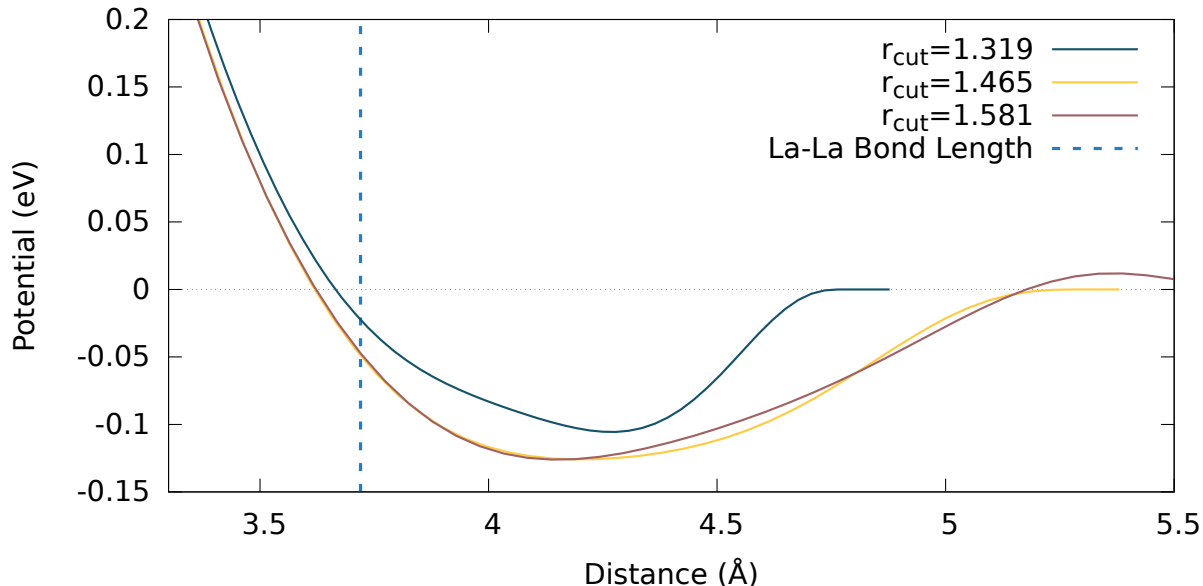


Figure 5.14: La-La element pair potentials for different cut-off values (r_{cut}). The cut-off value is a multiple of the La-La bond length (3.72 Å [140]).

A good curve will be smooth, indicating structures will tend towards a certain bond length without getting trapped in local minima, which occurs when we have either under or over-fitted. In figure 5.14, both $r_{\text{cut}} = 1.465$ and $r_{\text{cut}} = 1.581$ are smooth enough. We selected $r_{\text{cut}} = 1.465$ to proceed to the final evaluation as it carries less risk of being over-fitted.

Some species have an increasingly lower error with an increasingly higher cut-off value. This is typical when we parameterise against structures with finely separated nearest-neighbour atom shells such as Zr. To avoid over-fitting, we try to find a reasonable cutoff below $1.6 \times$ the typical elemental bond length.

Sometimes we were unable to find enough binary crystals to parameterise the way we do in table 5.9. For the La-Zr there was only 1 reported structure on the Materials Project database. In these situations, we instead increased the number of points sampled in both this structure and the dimer.

5.5.4 Pair-interaction Evaluation

To evaluate whether our pair interaction is suitable for inclusion in the entire library we examined how closely DFTB+ can replicate DFT's structure prediction for a number of element pair structures.

Firstly, we had to decide which structures we would evaluate against. As many structures as possible should be evaluated to properly assess the quality of the parameterisation in as many different environments as possible. We typically used all structures listed on Materials Project below an atom count of 20.

We then checked the quality of the structural optimisation for our parameterised interaction. We did this by selecting different bond angles and lengths to measure in the DFTB+ against the DMOL³ optimised structures. Typically, we selected one example of each type of bond length/angle for each structure. For example, for LiO we selected a Li-Li, O-O, and Li-O bond lengths and a Li-Li-Li, Li-O-Li, and O-O-O bond angle. By performing this for all structures we could garner insight into how good our fit was. If we intuitively felt that the fit was producing good enough structures then we merged the structure to the main library.

In most cases, multiple short-range potential fits were advanced to this stage and the ones with the lowest error in the predicted structure were the fit included in the library. The potential that yielded the lowest error in structure prediction compared to that of DFT was selected to be merged into the main Slater-Koster library. If no candidates produced acceptable results we would add extra systems or samples to our short-range potential fit in table 5.9. An example of a rejected potential is shown in table 5.10

Table 5.10: A table showing the differences for specified bond lengths and angles for a set of unique La O binary structures to evaluate the quality of a repulsive potential fit.

Structure	Total Atoms	La-La 1 Error	La-La 2 Error	O-O Error	La-O 1 Error	La-O 2 Error	O-La-O 1 Error	O-La-O 2 Error	La-O-La 1 Error
La2O3_3	5	0.29321	-	-	0.21786	-	1.08128	0.42627	-
La2O3_4	5	0.16404	-	-	1.03213	-	0.11432	3.67342	-
La2O3_7	15	0.54835	-	-	0.13804	-	6.56776	35.67542	-
La2O3_8	5	0.29144	-	-	0.21943	-	1.11406	0.17957	-
LaO2_1	6	0.26121	-	-	0.32219	-	5.49567	-	-
LaO3_10	8	0.74606	-	0.10422	0.01774	-	2.84586	-	8.93695
LaO3_5	8	0.1809	0.34184	-	-	-	2.29215	1.05251	-
LaO_9	2	-	-	-	0.26845	0.23474	-	-	1.19069
LaO_dimer	2	-	-	-	0.01712	-	-	-	-
Average Bond Length Error				0.299943	Average Angle Error				5.046138

Table 5.10 shows how the geometry-optimised structures of DFT and our parameterised DFTB+ model compare. This analysis is particularly useful as it allows us to spot places in configuration space that are not properly sampled. For the fit shown table 5.10, we refit our short-range potential this time including the La₂O₃_7 crystal in the parameterisation.

5.5.5 Library Evaluation

Once all element pair interactions were included, we evaluated the quality of our libraries with materials of a higher complexity than binary compounds. The quality is determined for the LIB19_LLZO and the LLZO_A2 libraries by computing the bulk t-LLZO total electronic density of states (DOS).

We show the t-LLZO DOS in figure 5.15.

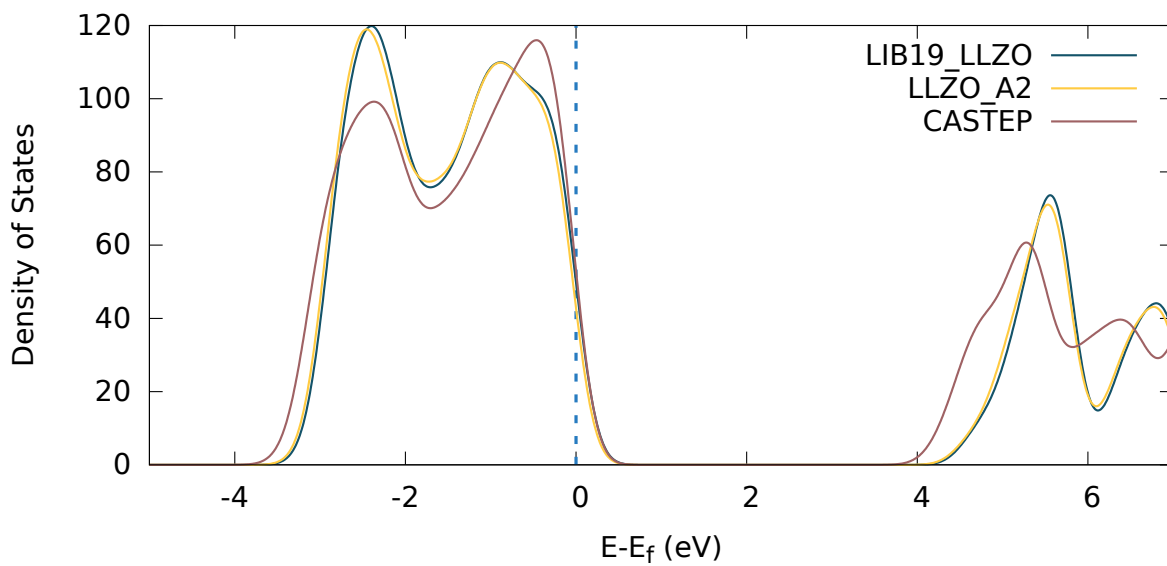


Figure 5.15: Bulk t-LLZO total electronic density of states for the two fully evaluated DFTB+ Slater-Koster libraries we produced compared to DFT code CASTEP. All densities of states have been shifted so that 0 aligns with the Fermi level (dashed blue line)

The DOS results were encouraging. Both libraries reproduce DFT results close to the Fermi level and predicted a similar-sized band gap.

Next, we attempted to optimise a t-LLZO surface. We chose Cut 1 from table 5.1 due to its low atom count. We initially tried this with LIB19_LLZO (c.f. figure 5.16).

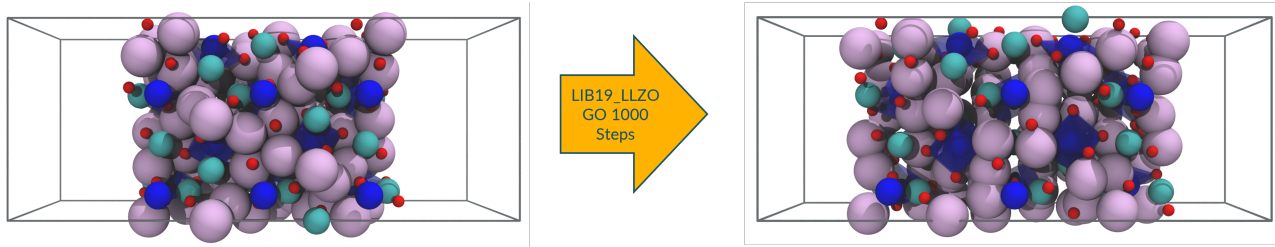


Figure 5.16: The effect of the LIB19_LLZO DFTB+ Slater-Koster library on the geometry of a t-LLZO surface after 1000 geometry-optimisation steps. This calculation did not ever reach the optimisation criteria.

After 1000 geometry steps with DFTB the calculation had not reached any of our geometry-optimisation criteria (energy tolerance: 0.01 kcal/mol, force tolerance: 0.05 kcal/mol/Å, stress tolerance: 0.02 GPa, displacement tolerance: 5×10^{-4} Å). It was apparent beyond this point the surface was expanding across the entire simulation cell as atoms were trying to move away from each other and there was no reason to continue the simulation.

All surface tests, like the one in figure 5.16, returned similar results. The surfaces stretched normal to the surfaces. This could have indicated that the LIB19_LLZO library is unable to handle ‘dangling bonds’ caused by the cleaving of a surface. In figure 5.17, we showed that a similar effect occurs for the bulk structure when we allowed the cell to relax.

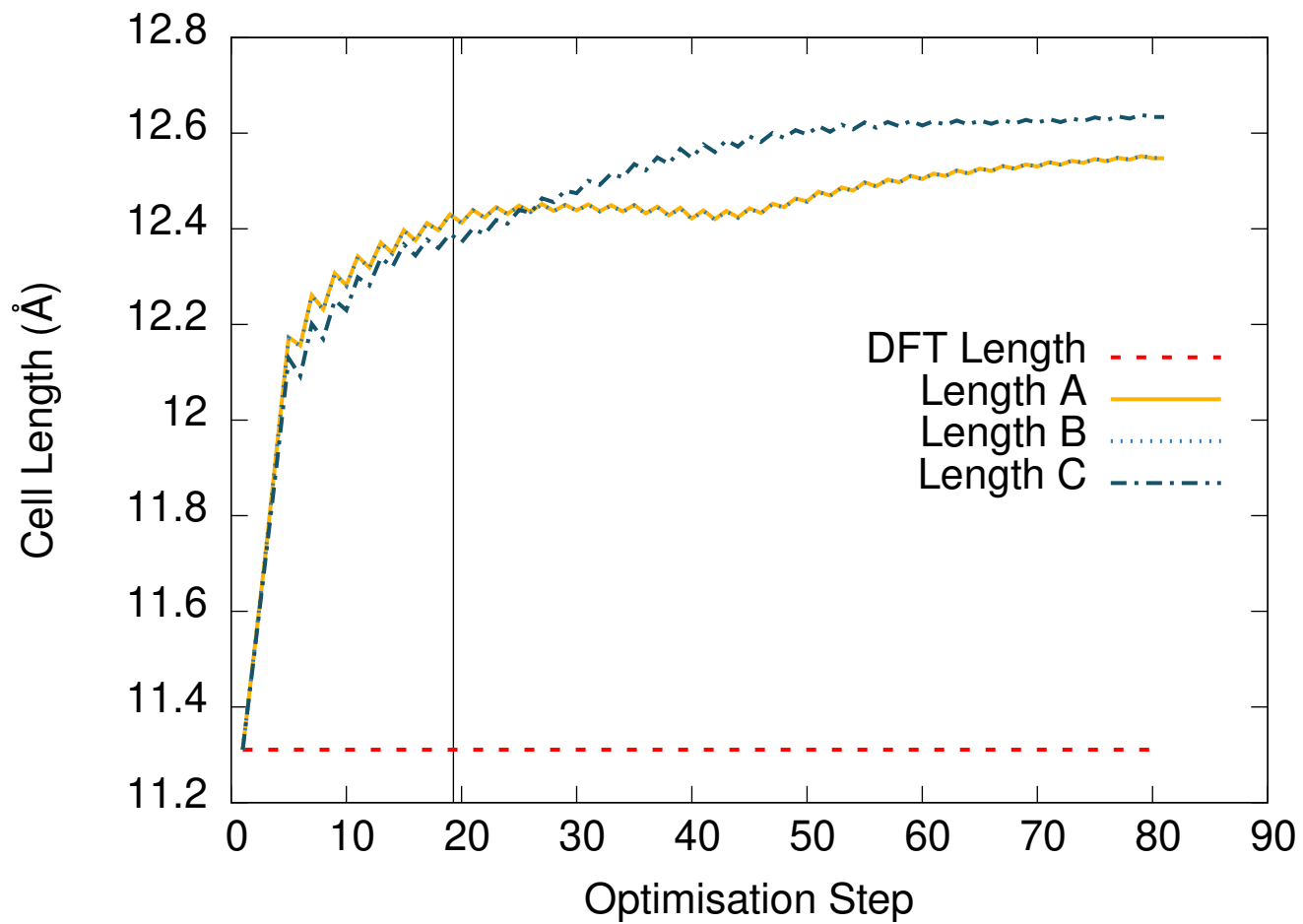


Figure 5.17: t-LLZO cell lengths with increasing geometry-optimisation step for the LIB19_LLZO DFTB+ library when compared to DFT

It is apparent that this is a deeper issue than not accounting for ‘dangling bonds’ and one that likely lies with the element-pair parameterisation. The expansions observed in both figures 5.16 and 5.17 could also be explained by the fact that the LIB 2019 library’s values are primarily parameterised for liquids and not for the solid-state, the type of systems we are interested in. This could have led to the lattice expansion we observed in t-LLZO. This was confirmed when we found that the LIB 2019 library was unable to replicate the DFT energy differences or ordering of different Li-O binary crystals (c.f. figure 5.18).

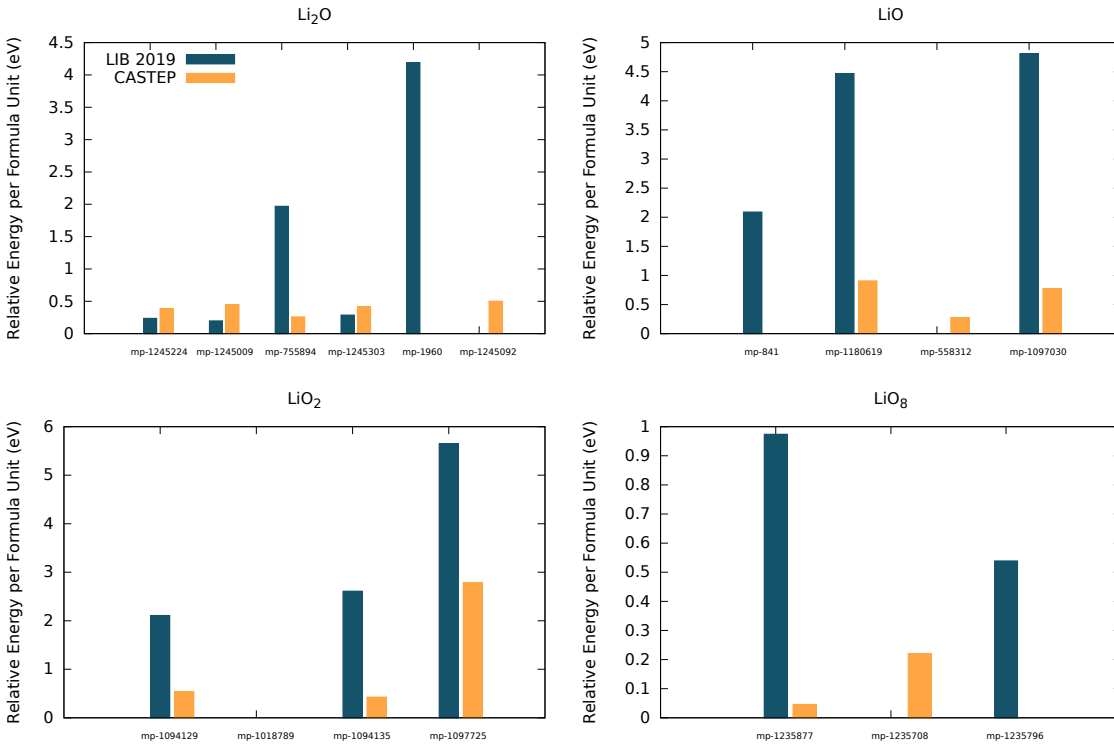


Figure 5.18: Comparing the CASTEP DFT energies to those predicted by the LIB 2019 library for DFTB+. We compare four separate groups of Li O binary compounds. The base formula unit is denoted at the top of each graph and the specific structure corresponds to the materials project[140] structure code.

For this reason, we reparameterised the Li-Li, Li-O, and O-O pair potentials for the solid-state which lead to the formation of the LLZO_A2 library discussed throughout this section.

To see if our own parameterisation on crystal structures made any improvement we performed another test where we varied the lattice parameter in order to ascertain the relationship the element-pair potentials impose on the energies of real systems.¹ We use the lowest energy Li and LiO structures reported on materials project[140] for the calculations in figure 5.19.

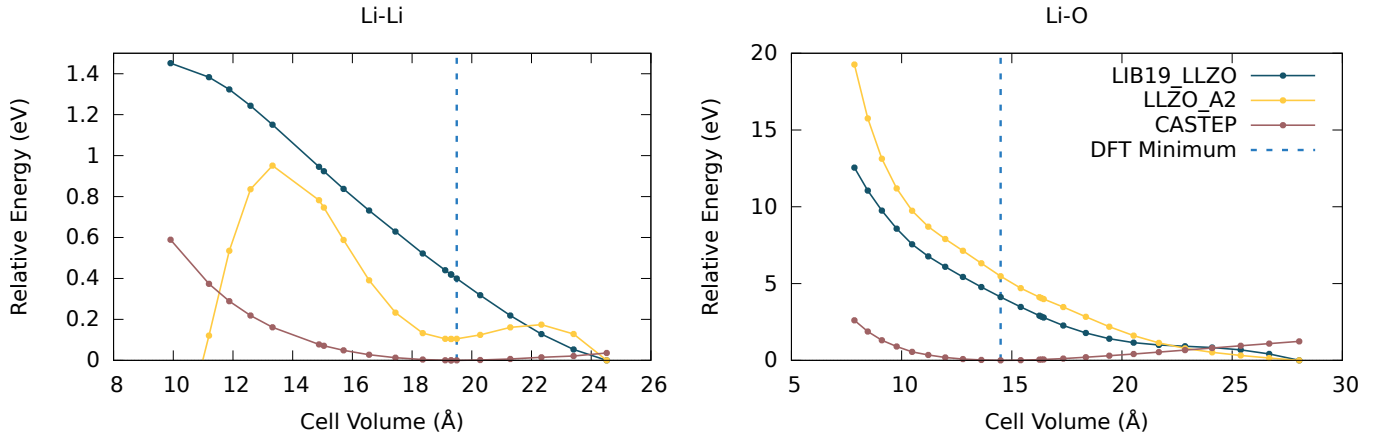


Figure 5.19: Energy change with increasing lattice parameters for Li-O and Li-Li compounds. The energy is evaluated with the DFT program CASTEP and the DFTB+ Slater-Koster libraries LIB19_LLZO and LLZO_A2. All calculations performed were single-point

Figure 5.19 shows that some progress has been made with the Li-Li interaction. Ignoring the artifacts that occur when the Li atoms are too far or too close to one another² the lowest energy cell volume was predicted exactly as DFT did. Efforts will need to be made to improve the gradient around this minimum as the steepness of Li-Li getting close is currently far too punishing. The Li-O element pair interaction has not improved at all with our solid-state parameterisation. We

¹This is very similar to the setup required to obtain a Birch-Murnaghan plot[38] which we perform for graphite in figure 3.1b.

²This can be easily rectified by sampling more in these regions

have made several attempts to improve this interaction, shown in figure 5.20, by changing parameters such as r_{cut} and changing some of the weights and samplings in the Li-O equivalent of table 5.9.

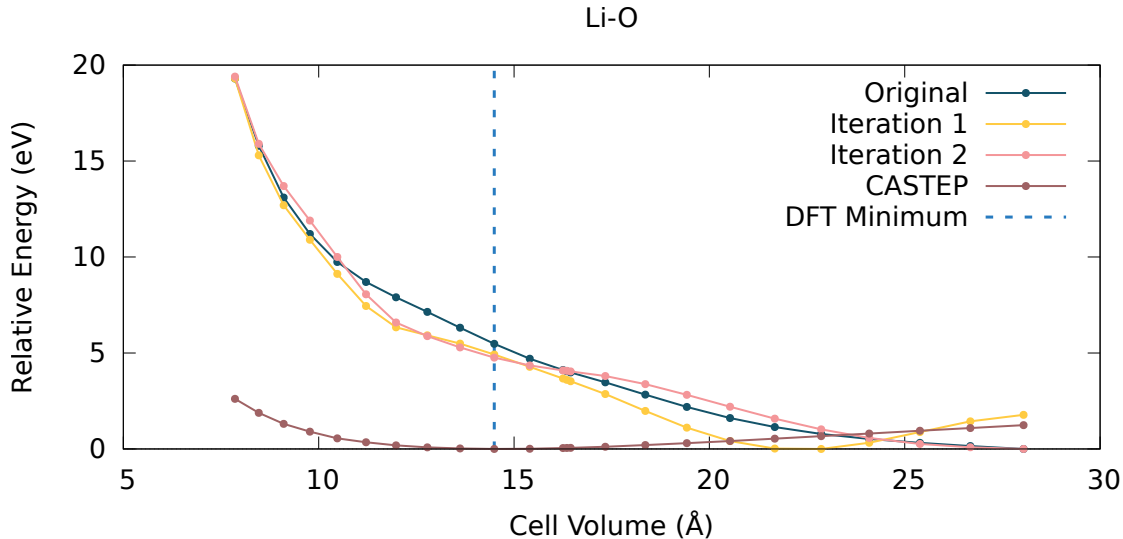


Figure 5.20: The Li-O element-pair short-range interaction for different parameterisation set versions of LLZO_A2 Slater-Koster library

However, while slight improvements have been made using these techniques (e.g. the formation of a shoulder at approximately the correct cell volume for iteration 2 in figure 5.20) further work, specifically reparameterising the Li-O element-pair short-range interaction, is required. None of the Slater-Koster libraries can be published alongside this thesis as they were developed during a 3-month placement with BIOVIA at their facility in Cambridge and subsequently belong to them.

5.6 Conclusion

In this chapter, we have made significant progress toward simulating the Li|t-LLZO|c-LLZO interphase. We have calculated Li surface energies to a high-accuracy using the Fiorentini and Methfessel method which was then applied to a t-LLZO surface for the first time using the linear-scaling DFT program ONETEP. We have developed the necessary chemical potentials to produce reasonable surface energies and shown the effect of the change on them on all 21 t-LLZO {100} surfaces. We have also developed a thorough method of sampling the Li|t-LLZO configuration space by making several reasonable approximations that reduced the 11-dimensional scheme to three-dimensions. This reduction included calculations to determine a potential universal Li|t-LLZO inter-slab distance and the determination of low-strain, low-atom count candidate interfaces. With a good estimate of the size of the configuration space and a means of generating it, we then moved on to a fast energy evaluator. Towards this end, we have parameterised three Slater-Koster libraries for the DFTB+ program of which we have evaluated two. None of the libraries in their current state are sufficient to perform the interface evaluations to the accuracy we require to screen our interfaces. We attribute the problem with these parameters to the LIB 2019 library interactions being parameterised primarily for liquid interactions and our own reparameterisation for the solid-state not being mature enough to achieve our accuracy.

Chapter 6

Conclusions

In this thesis we have aimed to demonstrate the significant role that simulation can play when investigating the interfaces of electrochemical systems. Specifically, we have focused on leveraging recent linear-scaling DFT developments of increased speed and efficiency to garner new insights into systems sizes that we were previously unable to simulate. With new system sizes and complexities come new challenges and the ambition of what we were trying to simulate often required innovation in terms of the methods we use to approach these systems.

In chapter 3 we investigated the lithium intercalation of a graphite nanoparticle. In this body of research we showcased how a high surface area to volume ratio dramatically effects its intercalation properties. The underlying methodology to produce these results involved several hundred calculations of structures with approximately 600 atoms. Linear-scaling DFT enabled us to accomplish this feat in a reasonable time frame. A framework for Li intercalation had not been developed that was compatible with graphite nanoparticles prior to this work so we also had develop and refine our own. This research provided a new methodology for simulating the charging of anode that is independent of the constraints of requiring long-range translational symmetry as was typically required for bulk-like simulations.[226] Our method utilised the primary interaction between intercalant and graphite scaffold, electrostatics, to make predictions about low energy intercalation sites. From this methodology we developed a workflow that enabled us to simulate the charging of a graphite nanoparticle anode. The results of this workflow demonstrated experimentally observed, bulk-like characteristics such as the replication of Li staging, complete Li charge transfer, and the formation of a good voltage step profile based on a reasonable convex hull of structures. All of these bulk-like features occurred in a unparameterised scheme indicating the predictive power of our workflow. Perhaps more notably, were the observed divergences from bulk-like structure. Accumulation of the Li atoms around the edges of our systems indicate the particular importance interfaces have when predicting the properties of battery materials. The severity of this accumulation was enough to pin our graphite structure in AB environment despite literature (for bulk or bulk-like structures) indicating a shift to AA structure should occur. This accumulation was also sufficient to change the point at which a stage II to stage I transition occurs. We were able to attribute the edge accumulation of Li atoms due to the slight charge bias the termination of H atoms on our nanoparticle caused, highlighting the importance of this interface and its high environmental sensitivity.

In chapter 4 we demonstrated new methodologies for predicting, symmetrically screening, and energetically ordering all unique and low energy chrystrallographically occurring structures. These methods were applied to the particularly challenging system of c-LLZO which has a configuration space of 7.4×10^{34} , approximately 10 billion times the number of stars in the observable universe.[78]. By assuming that Li atoms are not able to get closer than 1.7 Å to each other we were able to reduce this configuration space to 2.3×10^8 structures. In so doing we were also able to demonstrate that a large portion of experimental and theoretical literature report or work with structures that are highly energetically unfavourable and unlikely to occur in reality. Knowing that some of the structures we produce with our generation algorithm were symmetrically indistinct we sought to find a methodology to remove them and reduce our configuration space further. When we found that no such program could handle the large volume of structures we had generated in a reasonable time frame we developed our own using local sensitivity hashing to perform fast symmetry comparisons on representations of Li sublattices. This reduced our configuration space to 2.2×10^6 . This significant reduction was still not enough to sample the configuration space with atomistic techniques, so we developed a new multiple linear regression technique to predict the energy of structure based off of their Li sublattice. This method used only around 1000 DFT calculations as its input. We demonstrated on a test set of over 200 structures the ability of our multiple linear regression model to predict the single point energy to a 99.96% accuracy when compared to DFT. From these predictions and further DFT tests to confirm we found only four chrystrallographically predicted structures to occur within 1kT at 298.15 K. We have published a data set of all our structures in the hope this will improve accuracy and reproducibility of future LLZO research.

To expand the utility of the research performed in chapter 4, we focused on developing a model for the Li|t-LLZO|c-LLZO interphase in chapter 5. In this chapter we highlight the significant progress made in performing high-accuracy surface energy calculations for large scale surfaces, often > 1000 atoms, using linear-scaling DFT. We have complimented the progress made in our surface calculations by developing a thorough scheme to fully sample the configuration space

of the Li|t-LLZO interface. This is achieved through further large-scale > 1000 atom calculations to determine inter-slab distance, the determination of low strain low atom count interfaces, and a rigorous scheme to sample inter-slab translations. We also began the development of a suitable fast energy evaluator for this interface in the form of several newly parameterised Slater-Koster libraries for the DFTB methodology, which were able to accurately replicate DFT electronic density of states close to the Fermi level.

We summarise the major achievements of this research as

- Developed a novel electrostatically driven intercalation procedure that predicts close-to-ground state structures for sequential charging/discharging of an electrode and applied it to a graphite nanoparticle.
- Generated all likely structures for the disordered crystal of solid electrolyte material c-LLZO, and energetically ordered them using a multiple linear regression model based purely on the geometry of our Li sublattice
- Provided the framework to begin a thorough study of the Li|LLZO interface by performing high accuracy surface energy calculations, creating a means of thoroughly sampling the Li|LLZO configuration space, and creating new fast energy evaluation tools that can be developed to effectively screen this space for low energy interfaces

All of these projects have contributed or, we hope, will contribute to the current atomistic understanding of modern battery material interfaces and their rational design.

6.1 Outlook and Future Work

For the graphite nanoparticle simulations, demonstrated in chapter 3, improvements to the model have already been discussed such as including the confidence of lithium placement (c.f. section 3.6.4) in whether the procedure chooses to perform a single point or geometry optimisation. Furthermore, a means could be developed to allow Li atoms to diffuse within the nanoparticle before each intercalation. Methods that could achieve this include kinetic Monte Carlo or even molecular dynamics. With respect to the chosen system several improvements could be made in order to make it more realistic. Given that we have demonstrated the ability of this model to replicate key phenomena and that we have access to and expertise with linear-scaling DFT a larger, more realistic, nanoparticle could be investigated. Terminations on this nanoparticle could be adjusted to be more in-fitting with a solid electrolyte interphase (SEI) environment. Finally, a full interface could be built between our nanoparticle and a SEI-like system using a similar scheme to one presented in section 5.4. Further to this, varying the choice of intercalant has a large appeal as the battery industry tries to transition away from the Li economy due the cost/abundance of Li[13]. Hard carbon (HC) has been proposed as replacement anode for graphite and significant research has been done to simulate it[2, 59, 151, 170, 192, 199, 210, 211]. Modelling an analogue of HC would be well within the capabilities of ONETEP. The lack of long range symmetry would also mean that the intercalation workflow could provide a workable means of “charging” our system. The primary limitation of such a method is generating representative structures of HC that can be run using DFT. Work is underway to generate such structures using swarm intelligence algorithms[341].

In chapters 4 and 5, we discuss the solid electrolyte material LLZO. Before considering the interface present for c-LLZO we need to establish the geometry of the bulk, something the literature has been unable to do. Having formed all crystallographically predicted structures and ranked them energetically, we need to establish a method of predicting their geometry optimised counterparts, or at least the crystallographically predicted structures that will yield low energy optimised structures. We have already mentioned our desire to build a machine learned potential (MLP) for our system and the progress made to simulating a sufficient fraction of configuration space in section 4.5. Once sufficient low energy, relaxed structures have been found we can progress to building surfaces in the manner outlined in section 5.3.2. One could also imagine extending this c-LLZO MLP to include t-LLZO and Li bulk and eventually the interfaces these three materials rendering the issues we are having developing accurate DFTB Slater-Koster libraries in section 5.5 obsolete. Given the large volume of data produced throughout this research this should be an achievable goal and a high impact extension of this work that could be completed in the near-future. We are currently collaborating with Professor Qiong Cai’s group at the university of Surrey to make such an MLP a reality. Development of such a model would make the screening of interface configuration space mentioned in section 5.4.7 relatively trivial as well as enabling us to run MD simulations over long time scales. Such results would allow for the probing of commercially applicable questions such as ‘how does pressure affect ion conductivity?’ and ‘how can we prevent the formation of the t-LLZO interphase’.

We would also like to highlight the diversity of new methodologies we have developed in this work. These methodologies allowed us to work around issues specific to the systems that interested us but given that the majority of these workflows were developed within an *ab-initio* framework they are fully transferable to other similar systems. We list a few examples below

- The electrostatically driven intercalation workflow would be ideal for investigating intercalation of other anode structures such SiO_x, hard carbon or any structure where the primary intercalant-scaffold interaction is electrostatic. The intercalant also need not be limited to just Li, there is no reason this could not be a successful scheme for other potential battery charge carriers such as Na, Mg, or Al.
- The multiple linear regression model is applicable to any solid electrolyte with well defined crystallographic sites.
- the rigorous interface scheme we develop is applicable to all solid-solid interfaces with the correct information supplied.

Bibliography

- [1] Joseph W. Abbott and Felix Hanke. "Kinetically Corrected Monte Carlo-Molecular Dynamics Simulations of Solid Electrolyte Interphase Growth". In: *Journal of Chemical Theory and Computation* 18.2 (Feb. 2022). Publisher: American Chemical Society, pp. 925–934. ISSN: 15499626. DOI: 10.1021/acs.jctc.1c00921.
- [2] Ryan A. Adams, Arvind Varma, and Vilas G. Pol. "Carbon Anodes for Nonaqueous Alkali Metal-Ion Batteries and Their Thermal Safety Aspects". en. In: *Advanced Energy Materials* 9.35 (Sept. 2019), p. 1900550. ISSN: 1614-6832, 1614-6840. DOI: 10.1002/aenm.201900550. URL: <https://onlinelibrary.wiley.com/doi/10.1002/aenm.201900550> (visited on 02/28/2024).
- [3] Frederic Aguesse et al. "Investigating the dendritic growth during full cell cycling of garnet electrolyte in direct contact with Li metal". In: *ACS Applied Materials and Interfaces* 9.4 (2017), pp. 3808–3816. ISSN: 19448252. DOI: 10.1021/acsam.6b13925.
- [4] K. Ajith et al. "A correlative study on electrochemical and optical properties of LLZO (Li₇La₃Zr₂O₁₂) garnet electrolyte". In: *Materials Today: Proceedings*. Vol. 50. ISSN: 22147853. Elsevier Ltd, 2020, pp. 2836–2839. DOI: 10.1016/j.matpr.2020.08.812.
- [5] Reinier L. C. Akkermans, Neil A. Spenley, and Struan H. Robertson. "COMPASS III: automated fitting workflows and extension to ionic liquids". In: *Molecular Simulation* 47.7 (May 2021). Publisher: Taylor and Francis Ltd., pp. 540–551. ISSN: 0892-7022. DOI: 10.1080/08927022.2020.1808215. URL: <https://www.tandfonline.com/doi/full/10.1080/08927022.2020.1808215>.
- [6] David Allart, Maxime Montaru, and Hamid Gualous. "Model of Lithium Intercalation into Graphite by Potentiometric Analysis with Equilibrium and Entropy Change Curves of Graphite Electrode". In: *Journal of The Electrochemical Society* 165.2 (Feb. 2018), A380–A387. ISSN: 0013-4651. DOI: 10.1149/2.1251802jes. URL: <https://iopscience.iop.org/article/10.1149/2.1251802jes>.
- [7] Mark J. Allen and David J. Tozer. "Helium dimer dispersion forces and correlation potentials in density functional theory". In: *The Journal of Chemical Physics* 117.24 (Dec. 2002), pp. 11113–11120. ISSN: 0021-9606. DOI: 10.1063/1.1522715. URL: <http://aip.scitation.org/doi/10.1063/1.1522715>.
- [8] Seong Jin An et al. "The state of understanding of the lithium-ion-battery graphite solid electrolyte interphase (SEI) and its relationship to formation cycling". In: *Carbon* 105 (2016). Publisher: The Authors, pp. 52–76. ISSN: 00086223. DOI: 10.1016/j.carbon.2016.04.008. URL: <http://dx.doi.org/10.1016/j.carbon.2016.04.008>.
- [9] Odd E. Andersson et al. "Structure and electronic properties of graphite nanoparticles". In: *Physical Review B* 58.24 (Dec. 1998), pp. 16387–16395. ISSN: 0163-1829. DOI: 10.1103/PhysRevB.58.16387. URL: <https://linkinghub.elsevier.com/retrieve/pii/0379677991910359>.
- [10] Simon Anniés et al. "Accessing Structural, Electronic, Transport and Mesoscale Properties of Li-GICs via a Complete DFTB Model with Machine-Learned Repulsion Potential". In: *Materials* 14.21 (Nov. 2021), p. 6633. ISSN: 1996-1944. DOI: 10.3390/ma14216633. URL: <https://www.mdpi.com/1996-1944/14/21/6633>.
- [11] M. Armand and J.-M. Tarascon. "Building better batteries". In: *Nature* 451.7179 (Feb. 2008), pp. 652–657. ISSN: 0028-0836. DOI: 10.1038/451652a. URL: <http://www.nature.com/articles/451652a>.
- [12] Emilio Artacho et al. "The SIESTA method: developments and applicability". en. In: *Journal of Physics: Condensed Matter* 20.6 (Jan. 2008), p. 064208. ISSN: 0953-8984. DOI: 10.1088/0953-8984/20/6/064208. URL: <https://dx.doi.org/10.1088/0953-8984/20/6/064208> (visited on 09/12/2023).
- [13] Gaurav Assat and Jean-Marie Tarascon. "Fundamental understanding and practical challenges of anionic redox activity in Li-ion batteries". en. In: *Nature Energy* 3.5 (Apr. 2018), pp. 373–386. ISSN: 2058-7546. DOI: 10.1038/s41560-018-0097-0. URL: <https://www.nature.com/articles/s41560-018-0097-0> (visited on 03/05/2024).
- [14] P. W. Atkins and Julio De Paula. *Atkins' Physical chemistry*. Tenth edition. Oxford ; New York: Oxford University Press, 2014. ISBN: 978-0-19-969740-3.
- [15] Peter W. Atkins. *Molecular quantum mechanics*. 1. eng. Reprint. Oxford: Clarendon Press, 1977. ISBN: 978-0-19-855129-4.
- [16] D Aurbach et al. "New insights into the interactions between electrode materials and electrolyte solutions for advanced nonaqueous batteries". In: *Journal of Power Sources* 81-82 (Sept. 1999), pp. 95–111. ISSN: 03787753. DOI: 10.1016/S0378-7753(99)00187-1. URL: <https://linkinghub.elsevier.com/retrieve/pii/S0378775399001871>.

- [17] Junji Awaka et al. "Crystal Structure of Fast Lithium-ion-conducting Cubic Li₇La₃Zr₂O₁₂". In: *Chemistry Letters* 40.1 (Jan. 2011), pp. 60–62. ISSN: 0366-7022. DOI: 10.1246/cl.2011.60. URL: <http://www.journal.csj.jp/doi/10.1246/cl.2011.60>.
- [18] Junji Awaka et al. "Synthesis and structure analysis of tetragonal Li₇La₃Zr₂O₁₂ with the garnet-related type structure". In: *Journal of Solid State Chemistry* 182.8 (Aug. 2009), pp. 2046–2052. ISSN: 00224596. DOI: 10.1016/j.jssc.2009.05.020. URL: <https://linkinghub.elsevier.com/retrieve/pii/S002245960900228X>.
- [19] M. K. Aydinol, A. F. Kohan, and G. Ceder. "Ab initio calculation of the intercalation voltage of lithium-transition-metal oxide electrodes for rechargeable batteries". In: *Journal of Power Sources* 68.2 (1997), pp. 664–668. ISSN: 03787753. DOI: 10.1016/S0378-7753(96)02638-9.
- [20] Daniel R. Baker and Mark W. Verbrugge. "Modeling Overcharge at Graphite Electrodes: Plating and Dissolution of Lithium". In: *Journal of The Electrochemical Society* 167.1 (Sept. 2020), p. 013504. ISSN: 0013-4651. DOI: 10.1149/2.0042001JES. URL: <https://iopscience.iop.org/article/10.1149/2.0042001JES>.
- [21] Pallab Barai et al. "The Role of Local Inhomogeneities on Dendrite Growth in LLZO-Based Solid Electrolytes". In: *Journal of The Electrochemical Society* 167.10 (Jan. 2020). Publisher: The Electrochemical Society, p. 100537. ISSN: 0013-4651. DOI: 10.1149/1945-7111/ab9b08. URL: <https://iopscience.iop.org/article/10.1149/1945-7111/ab9b08>.
- [22] C. Bradford Barber, David P. Dobkin, and Hannu Huhdanpaa. "The Quickhull Algorithm for Convex Hulls". In: *ACM Transactions on Mathematical Software* 22.4 (1996), pp. 469–483. ISSN: 00983500. DOI: 10.1145/235815.235821.
- [23] Charles S. Barrett. "A Low Temperature Transformation in Lithium". In: *Physical Review* 72.3 (Aug. 1947). Publisher: American Physical Society, pp. 245–245. DOI: 10.1103/PhysRev.72.245. URL: <https://link.aps.org/doi/10.1103/PhysRev.72.245> (visited on 09/14/2023).
- [24] Y. Baskin and L. Meyer. "Lattice Constants of Graphite at Low Temperatures". In: *Physical Review* 100.2 (Oct. 1955), pp. 544–544. ISSN: 0031-899X. DOI: 10.1103/PhysRev.100.544. URL: <https://link.aps.org/doi/10.1103/PhysRev.100.544>.
- [25] J B Bates et al. *Thin-film lithium and lithium-ion batteries*. Tech. rep. Publication Title: Solid State Ionics Volume: 135. 2000, pp. 33–45. URL: www.elsevier.com/locate/ssi.
- [26] Inder P. Batra et al. "Dimensionality and size effects in simple metals". In: *Physical Review B* 34.12 (1986), pp. 8246–8257. ISSN: 01631829. DOI: 10.1103/PhysRevB.34.8246.
- [27] A. D. Becke. "Density-functional exchange-energy approximation with correct asymptotic behavior". In: *Physical Review A* 38.6 (Sept. 1988). Publisher: American Physical Society, pp. 3098–3100. DOI: 10.1103/PhysRevA.38.3098. URL: <https://link.aps.org/doi/10.1103/PhysRevA.38.3098> (visited on 07/28/2023).
- [28] Lorin X Benedict et al. *CHEMICAL PHYSICS LETTERS ELSEVIER Microscopic determination of the interlayer binding energy in graphite*. Tech. rep. Publication Title: Chemical Physics Letters Volume: 286. 1998, pp. 490–496.
- [29] Joseph W. Bennett et al. "Hexagonal ABC semiconductors as ferroelectrics". In: *Physical Review Letters* 109.16 (Oct. 2012). ISSN: 00319007. DOI: 10.1103/PhysRevLett.109.167602.
- [30] Arihant Bhandari, Puneet Jindal, and Jishnu Bhattacharya. "Discovery of new ground state structures for Li₄Mn₂O₅ and V₂O₅ from first principles". In: *Computational Materials Science* 159 (Mar. 2019). Publisher: Elsevier B.V., pp. 454–459. ISSN: 09270256. DOI: 10.1016/j.commatsci.2018.12.040.
- [31] Arihant Bhandari et al. "Electrochemistry from first-principles in the grand canonical ensemble". In: *The Journal of Chemical Physics* 155.2 (July 2021), p. 024114. ISSN: 0021-9606. DOI: 10.1063/5.0056514. URL: <https://doi.org/10.1063/5.0056514> (visited on 07/28/2023).
- [32] Arihant Bhandari et al. "Electronic structure calculations in electrolyte solutions: Methods for neutralization of extended charged interfaces". In: *The Journal of Chemical Physics* 153.12 (Sept. 2020), p. 124101. ISSN: 0021-9606. DOI: 10.1063/5.0021210. URL: <https://doi.org/10.1063/5.0021210> (visited on 07/28/2023).
- [33] Arihant Bhandari et al. "Li nucleation on the graphite anode under potential control in Li-ion batteries". In: *Journal of Materials Chemistry A* (2022). ISSN: 2050-7488. DOI: 10.1039/D2TA02420A. URL: <http://xlink.rsc.org/?DOI=D2TA02420A>.
- [34] F. Matthias Bickelhaupt et al. "The carbon-lithium electron pair bond in (CH₃Li)_n (n = 1, 2, 4)". In: *Organometallics* 15.13 (1996), pp. 2923–2931. ISSN: 02767333. DOI: 10.1021/om950966x.
- [35] J. M. Bijvoet and A. Karssen. "X-ray investigation of the crystal structure of lithium oxide". en. In: *Recueil des Travaux Chimiques des Pays-Bas* 43.10 (1924). _eprint: <https://onlinelibrary.wiley.com/doi/pdf/10.1002/recl.19240431002> pp. 680–684. ISSN: 0165-0513. DOI: 10.1002/recl.19240431002. URL: <https://onlinelibrary.wiley.com/doi/abs/10.1002/recl.19240431002> (visited on 09/14/2023).
- [36] Tobias Binninger et al. "Comparison of computational methods for the electrochemical stability window of solid-state electrolyte materials". In: *Journal of Materials Chemistry A* 8.3 (2020). arXiv: 1901.02251 Publisher: Royal Society of Chemistry, pp. 1347–1359. ISSN: 2050-7488. DOI: 10.1039/C9TA09401F. URL: <http://xlink.rsc.org/?DOI=C9TA09401F>.

- [37] BIOVIA. *Materials Studio 23.1.0.3829*. San Diego, Dassault Systemes, 2023.
- [38] Francis Birch. "Finite Elastic Strain of Cubic Crystals". en. In: *Physical Review* 71.11 (June 1947), pp. 809–824. ISSN: 0031-899X. DOI: 10.1103/PhysRev.71.809. URL: <https://link.aps.org/doi/10.1103/PhysRev.71.809> (visited on 07/28/2023).
- [39] Torbjörn Björkman. "van der Waals density functional for solids". In: *Physical Review B* 86.16 (Oct. 2012), p. 165109. ISSN: 1098-0121. DOI: 10.1103/PhysRevB.86.165109. URL: <https://link.aps.org/doi/10.1103/PhysRevB.86.165109>.
- [40] P. E. Blöchl. "Projector augmented-wave method". In: *Physical Review B* 50.24 (Dec. 1994), pp. 17953–17979. ISSN: 0163-1829. DOI: 10.1103/PhysRevB.50.17953. URL: <https://link.aps.org/doi/10.1103/PhysRevB.50.17953>.
- [41] J. C. Boettger. "Nonconvergence of surface energies obtained from thin-film calculations". In: *Physical Review B* 49.23 (June 1994), pp. 16798–16800. ISSN: 0163-1829. DOI: 10.1103/PhysRevB.49.16798. URL: <https://link.aps.org/doi/10.1103/PhysRevB.49.16798>.
- [42] Mauricio R. Bonilla et al. "Exploring Li-ion conductivity in cubic, tetragonal and mixed-phase Al-substituted Li₇La₃Zr₂O₁₂ using atomistic simulations and effective medium theory". In: *Acta Materialia* 175 (2019), pp. 426–435. ISSN: 13596454. DOI: 10.1016/j.actamat.2019.06.033.
- [43] Jurjen N. E. Bos. A048134. URL: <https://oeis.org/A048134> (visited on 09/21/2023).
- [44] Gabriel Bramley et al. "Reconciling Work Functions and Adsorption Enthalpies for Implicit Solvent Models: A Pt (111)/Water Interface Case Study". In: *Journal of Chemical Theory and Computation* 16.4 (Apr. 2020), pp. 2703–2715. ISSN: 1549-9618. DOI: 10.1021/acs.jctc.0c00034. URL: <https://pubs.acs.org/doi/10.1021/acs.jctc.0c00034>.
- [45] Christian Brouder et al. "Exponential Localization of Wannier Functions in Insulators". In: *Physical Review Letters* 98.4 (Jan. 2007). arXiv: cond-mat/0606726, p. 046402. ISSN: 0031-9007. DOI: 10.1103/PhysRevLett.98.046402. URL: <https://link.aps.org/doi/10.1103/PhysRevLett.98.046402>.
- [46] R. H. Brugge, J. A. Kilner, and A. Aguadero. "Germanium as a donor dopant in garnet electrolytes". In: *Solid State Ionics* 337 (Sept. 2019). Publisher: Elsevier B.V., pp. 154–160. ISSN: 01672738. DOI: 10.1016/j.ssi.2019.04.021.
- [47] H. Bryngelsson et al. "How dynamic is the SEI?" In: *Journal of Power Sources* 174.2 (Dec. 2007), pp. 970–975. ISSN: 03787753. DOI: 10.1016/j.jpowsour.2007.06.050.
- [48] Tomáš Bučko et al. "Tkatchenko-Scheffler van der Waals correction method with and without self-consistent screening applied to solids". In: *Physical Review B* 87.6 (Feb. 2013), p. 064110. ISSN: 1098-0121. DOI: 10.1103/PhysRevB.87.064110. URL: <https://link.aps.org/doi/10.1103/PhysRevB.87.064110>.
- [49] Mario Burbano et al. "Sparse Cyclic Excitations Explain the Low Ionic Conductivity of Stoichiometric Li₇La₃Zr₂O₁₂". In: *Physical Review Letters* 116.13 (2016). arXiv: 1511.08883, pp. 1–6. ISSN: 10797114. DOI: 10.1103/PhysRevLett.116.135901.
- [50] Henrik Buschmann et al. "Structure and dynamics of the fast lithium ion conductor "li₇La₃Zr₂O₁₂"". In: *Physical Chemistry Chemical Physics* 13.43 (2011), pp. 19378–19392. ISSN: 14639076. DOI: 10.1039/c1cp22108f.
- [51] Eike Caldeweyher, Christoph Bannwarth, and Stefan Grimme. "Extension of the D3 dispersion coefficient model". In: *The Journal of Chemical Physics* 147.3 (July 2017), p. 034112. ISSN: 0021-9606. DOI: 10.1063/1.4993215. URL: <http://aip.scitation.org/doi/10.1063/1.4993215>.
- [52] Katherine Calvin et al. *IPCC, 2023: Climate Change 2023: Synthesis Report. Contribution of Working Groups I, II and III to the Sixth Assessment Report of the Intergovernmental Panel on Climate Change* [Core Writing Team, H. Lee and J. Romero (eds.)]. IPCC, Geneva, Switzerland. en. Tech. rep. Edition: First. Intergovernmental Panel on Climate Change (IPCC), July 2023. DOI: 10.59327/IPCC/AR6-9789291691647. URL: <https://www.ipcc.ch/report/ar6/syr/> (visited on 09/24/2023).
- [53] Pieremanuele Canepa et al. "Particle Morphology and Lithium Segregation to Surfaces of the Li₇La₃Zr₂O₁₂ Solid Electrolyte". In: *Chemistry of Materials* 30.9 (May 2018). arXiv: 1804.05165 Publisher: American Chemical Society, pp. 3019–3027. ISSN: 15205002. DOI: 10.1021/acs.chemmater.8b00649.
- [54] R. Car and M. Parrinello. "Unified Approach for Molecular Dynamics and Density-Functional Theory". In: *Physical Review Letters* 55.22 (Nov. 1985), pp. 2471–2474. ISSN: 0031-9007. DOI: 10.1103/PhysRevLett.55.2471. URL: <https://linkinghub.elsevier.com/retrieve/pii/S0012369216318542>.
- [55] G. Ceder. "A derivation of the Ising model for the computation of phase diagrams". In: *Computational Materials Science* 1.2 (1993), pp. 144–150. ISSN: 09270256. DOI: 10.1016/0927-0256(93)90005-8.
- [56] Gerbrand Ceder, Shyue Ping Ong, and Yan Wang. "Predictive modeling and design rules for solid electrolytes". In: *MRS Bulletin* 43.10 (2018), pp. 782–788. ISSN: 08837694. DOI: 10.1557/mrs.2018.210.
- [57] D. M. Ceperley and B. J. Alder. "Ground State of the Electron Gas by a Stochastic Method". In: *Physical Review Letters* 45.7 (Aug. 1980), pp. 566–569. DOI: 10.1103/PhysRevLett.45.566. URL: <https://link.aps.org/doi/10.1103/PhysRevLett.45.566> (visited on 08/07/2023).
- [58] Xiaobin Chen et al. "Interlayer interactions in graphites". In: *Scientific Reports* 3 (2013), pp. 1–5. ISSN: 20452322. DOI: 10.1038/srep03046.

- [59] Xiaoyang Chen et al. "Understanding of the sodium storage mechanism in hard carbon anodes". en. In: *Carbon Energy* 4.6 (Nov. 2022), pp. 1133–1150. ISSN: 2637-9368, 2637-9368. DOI: 10.1002/cey2.196. URL: <https://onlinelibrary.wiley.com/doi/10.1002/cey2.196> (visited on 02/29/2024).
- [60] Eric Jianfeng Cheng, Asma Sharafi, and Jeff Sakamoto. "Intergranular Li metal propagation through polycrystalline Li_{6.25}Al_{0.25}La₃Zr₂O₁₂ ceramic electrolyte". In: *Electrochimica Acta* 223 (2017), pp. 85–91. ISSN: 00134686. DOI: 10.1016/j.electacta.2016.12.018.
- [61] V. L. Chevrier and J. R. Dahn. "First Principles Studies of Disordered Lithiated Silicon". en. In: *Journal of The Electrochemical Society* 157.4 (Feb. 2010). Publisher: IOP Publishing, A392. ISSN: 1945-7111. DOI: 10.1149/1.3294772. URL: <https://iopscience.iop.org/article/10.1149/1.3294772/meta> (visited on 07/28/2023).
- [62] Stewart J. Clark et al. "First principles methods using CASTEP". In: *Zeitschrift fur Kristallographie* 220.5-6 (2005), pp. 567–570. ISSN: 00442968. DOI: 10.1524/zkri.220.5.567.65075.
- [63] Daniel A. Cogswell and W. Craig Carter. "Thermodynamic phase-field model for microstructure with multiple components and phases: The possibility of metastable phases". In: *Physical Review E* 83.6 (June 2011). Publisher: American Physical Society, p. 061602. DOI: 10.1103/PhysRevE.83.061602. URL: <https://link.aps.org/doi/10.1103/PhysRevE.83.061602> (visited on 09/17/2023).
- [64] John B. Collins and Andrew Streitwieser. "Integrated spatial electron populations in molecules: Application to simple molecules". In: *Journal of Computational Chemistry* 1.1 (1980), pp. 81–87. ISSN: 1096987X. DOI: 10.1002/jcc.540010111.
- [65] Hazel Cox and Adam L. Baskerville. "The Series Solution Method in Quantum Chemistry for Three-Particle Systems". In: *Advances in Quantum Chemistry*. Vol. 77. ISSN: 00653276. Elsevier Inc., 2018, pp. 201–240. ISBN: 978-0-12-813710-9. DOI: 10.1016/bs.aiq.2018.02.003. URL: <http://dx.doi.org/10.1016/bs.aiq.2018.02.003>.
- [66] Edmund J. Cussen. "The structure of lithium garnets: cation disorder and clustering in a new family of fast Li⁺ conductors". In: *Chem. Commun.* 4 (2006), pp. 412–413. ISSN: 1359-7345. DOI: 10.1039/B514640B. URL: <http://xlink.rsc.org/?DOI=B514640B>.
- [67] J. R. Dahn. "Phase diagram of LixC₆". In: *Physical Review B* 44.17 (Nov. 1991). ISBN: 0163-1829, pp. 9170–9177. ISSN: 0163-1829. DOI: 10.1103/PhysRevB.44.9170. URL: <https://link.aps.org/doi/10.1103/PhysRevB.44.9170>.
- [68] B. Delley. "An all-electron numerical method for solving the local density functional for polyatomic molecules". In: *The Journal of Chemical Physics* 92.1 (1990), pp. 508–517. ISSN: 00219606. DOI: 10.1063/1.458452.
- [69] B. Delley. "From molecules to solids with the DMol3 approach". In: *The Journal of Chemical Physics* 113.18 (Nov. 2000), pp. 7756–7764. ISSN: 0021-9606. DOI: 10.1063/1.1316015. URL: <https://doi.org/10.1063/1.1316015> (visited on 09/21/2023).
- [70] A. N. Dey and B. P. Sullivan. "The Electrochemical Decomposition of Propylene Carbonate on Graphite". In: *Journal of The Electrochemical Society* 117.2 (1970), p. 222. ISSN: 00134651. DOI: 10.1149/1.2407470. URL: <https://iopscience.iop.org/article/10.1149/1.2407470>.
- [71] M. Dion et al. "Van der Waals Density Functional for General Geometries". In: *Physical Review Letters* 92.24 (June 2004). arXiv: cond-mat/0402105, p. 246401. ISSN: 0031-9007. DOI: 10.1103/PhysRevLett.92.246401. URL: <https://link.aps.org/doi/10.1103/PhysRevLett.92.246401>.
- [72] Mahmut Dirican et al. "Composite solid electrolytes for all-solid-state lithium batteries". In: *Materials Science and Engineering: R: Reports* 136 (Apr. 2019). Publisher: Elsevier Ltd, pp. 27–46. ISSN: 0927796X. DOI: 10.1016/j.mser.2018.10.004. URL: <https://linkinghub.elsevier.com/retrieve/pii/S0927796X18301797>.
- [73] Ralf Drautz. "Atomic cluster expansion for accurate and transferable interatomic potentials". In: *Physical Review B* 99.1 (Jan. 2019). Publisher: American Physical Society, p. 014104. DOI: 10.1103/PhysRevB.99.014104. URL: <https://link.aps.org/doi/10.1103/PhysRevB.99.014104> (visited on 09/25/2023).
- [74] M. S. Dresselhaus and G. Dresselhaus. "Advances in Physics Intercalation compounds of graphite". In: *Advances in Physics* 51.1 (1981). ISBN: 0001-8732, pp. 1–186. ISSN: 0001-8732. DOI: 10.1080/00018738100101367.
- [75] Jacek Dziedzic et al. "Practical Approach to Large-Scale Electronic Structure Calculations in Electrolyte Solutions via Continuum-Embedded Linear-Scaling Density Functional Theory". In: *The Journal of Physical Chemistry C* 124.14 (Apr. 2020), pp. 7860–7872. ISSN: 1932-7447. DOI: 10.1021/acs.jpcc.0c00762. URL: <https://pubs.acs.org/doi/abs/10.1021/acs.jpcc.0c00762>.
- [76] Madeleine Ecker et al. "Parameterization of a Physico-Chemical Model of a Lithium-Ion Battery". In: *Journal of The Electrochemical Society* 162.9 (2015), A1836–A1848. ISSN: 0013-4651. DOI: 10.1149/2.0551509jes.
- [77] M. Elstner et al. "Self-consistent-charge density-functional tight-binding method for simulations of complex materials properties". In: *Physical Review B - Condensed Matter and Materials Physics* 58.11 (1998), pp. 7260–7268. ISSN: 1550235X. DOI: 10.1103/PhysRevB.58.7260.
- [78] ESA. *How many stars are there in the Universe?* en. URL: https://www.esa.int/Science_Exploration/Space_Science/Herschel/How_many_stars_are_there_in_the_Universe (visited on 09/26/2023).

- [79] John L. Falconer and Robert J. Madix. "Desorption rate isotherms in flash desorption analysis". In: *Journal of Catalysis* 48.1-3 (1977), pp. 262–268. ISSN: 10902694. DOI: 10.1016/0021-9517(77)90099-9.
- [80] Theodosios Famprikis et al. "Fundamentals of inorganic solid-state electrolytes for batteries". In: *Nature Materials* 18.12 (Dec. 2019). Publisher: Springer US, pp. 1278–1291. ISSN: 1476-1122. DOI: 10.1038/s41563-019-0431-3. URL: <http://dx.doi.org/10.1038/s41563-019-0431-3>.
- [81] Peter J. Feibelman. "Static quantum-size effects in thin crystalline, simple-metal films". In: *Physical Review B* 27.4 (1983), pp. 1991–1996. ISSN: 01631829. DOI: 10.1103/PhysRevB.27.1991.
- [82] Kun Feng et al. "Silicon-Based Anodes for Lithium-Ion Batteries: From Fundamentals to Practical Applications". en. In: *Small* 14.8 (Feb. 2018), p. 1702737. ISSN: 1613-6810, 1613-6829. DOI: 10.1002/smll.201702737. URL: <https://onlinelibrary.wiley.com/doi/10.1002/smll.201702737> (visited on 03/05/2024).
- [83] Vincenzo Fiorentini and M. Methfessel. "Extracting convergent surface energies from slab calculations". In: *Journal of Physics Condensed Matter* 8.36 (1996). arXiv: cond-mat/9610046, pp. 6525–6529. ISSN: 09538984. DOI: 10.1088/0953-8984/8/36/005.
- [84] V. Fock. "Nherungsmethode zur Lsung des quantenmechanischen Mehrkrperproblems". In: *Zeitschrift fr Physik* 61.1-2 (Jan. 1930), pp. 126–148. ISSN: 1434-6001. DOI: 10.1007/BF01340294. URL: <http://link.springer.com/10.1007/BF01340294>.
- [85] Rosamaría Fong, Ulrich von Sacken, and J. R. Dahn. "Studies of Lithium Intercalation into Carbons Using Non-aqueous Electrochemical Cells". en. In: *Journal of The Electrochemical Society* 137.7 (July 1990). Publisher: IOP Publishing, p. 2009. ISSN: 1945-7111. DOI: 10.1149/1.2086855. URL: <https://iopscience.iop.org/article/10.1149/1.2086855/meta> (visited on 08/21/2023).
- [86] Michelle M. Franci et al. "Self-consistent molecular orbital methods. XXIII. A polarization-type basis set for second-row elements". en. In: *The Journal of Chemical Physics* 77.7 (Oct. 1982), pp. 3654–3665. ISSN: 0021-9606, 1089-7690. DOI: 10.1063/1.444267. URL: <https://pubs.aip.org/jcp/article/77/7/3654/89785/Self-consistent-molecular-orbital-methods-XXIII-A> (visited on 08/09/2023).
- [87] Christoph Freysoldt, Sixten Boeck, and Jörg Neugebauer. "Direct minimization technique for metals in density functional theory". In: *Physical Review B - Condensed Matter and Materials Physics* 79.24 (2009), pp. 1–4. ISSN: 10980121. DOI: 10.1103/PhysRevB.79.241103.
- [88] Chengyin Fu et al. "Universal chemomechanical design rules for solid-ion conductors to prevent dendrite formation in lithium metal batteries". en. In: *Nature Materials* 19.7 (July 2020). Number: 7 Publisher: Nature Publishing Group, pp. 758–766. ISSN: 1476-4660. DOI: 10.1038/s41563-020-0655-2. URL: <https://www.nature.com/articles/s41563-020-0655-2> (visited on 06/12/2023).
- [89] Ruijan Fu et al. "Comparison of Lithium-Ion Anode Materials Using an Experimentally Verified Physics-Based Electrochemical Model". In: *Energies* 10.12 (Dec. 2017), p. 2174. ISSN: 1996-1073. DOI: 10.3390/en10122174. URL: <http://www.mdpi.com/1996-1073/10/12/2174>.
- [90] Till Fuchs et al. "Current-Dependent Lithium Metal Growth Modes in "Anode-Free" Solid-State Batteries at the Cu|LLZO Interface". In: *Advanced Energy Materials* 13.1 (Jan. 2023). Publisher: John Wiley and Sons Inc. ISSN: 16146840. DOI: 10.1002/aenm.202203174.
- [91] C. K. Gan, P. D. Haynes, and M. C. Payne. "Preconditioned conjugate gradient method for the sparse generalized eigenvalue problem in electronic structure calculations". In: *Computer Physics Communications* 134.1 (2001), pp. 33–40. ISSN: 00104655. DOI: 10.1016/S0010-4655(00)00188-0.
- [92] Bo Gao, Randy Jalem, and Yoshitaka Tateyama. "Surface-Dependent Stability of the Interface between Garnet Li₇La₃Zr₂O₁₂ and the Li Metal in the All-Solid-State Battery from First-Principles Calculations". en. In: *ACS Applied Materials & Interfaces* 12.14 (Apr. 2020), pp. 16350–16358. ISSN: 1944-8244, 1944-8252. DOI: 10.1021/acsami.9b23019. URL: <https://pubs.acs.org/doi/10.1021/acsami.9b23019> (visited on 09/14/2023).
- [93] Bo Gao et al. "Interface structure prediction via CALYPSO method". In: *Science Bulletin* 64.5 (Mar. 2019). Publisher: Science China Press, pp. 301–309. ISSN: 20959273. DOI: 10.1016/j.scib.2019.02.009. URL: <https://doi.org/10.1016/j.scib.2019.02.009>.
- [94] Yirong Gao et al. "Classical and Emerging Characterization Techniques for Investigation of Ion Transport Mechanisms in Crystalline Fast Ionic Conductors". en. In: *Chemical Reviews* 120.13 (July 2020), pp. 5954–6008. ISSN: 0009-2665, 1520-6890. DOI: 10.1021/acs.chemrev.9b00747. URL: <https://pubs.acs.org/doi/10.1021/acs.chemrev.9b00747> (visited on 09/14/2023).
- [95] Kevin F. Garrity et al. "Pseudopotentials for high-throughput DFT calculations". In: *Computational Materials Science* 81 (2014). arXiv: 1305.5973 Publisher: Elsevier B.V., pp. 446–452. ISSN: 09270256. DOI: 10.1016/j.commatsci.2013.08.053. URL: <http://dx.doi.org/10.1016/j.commatsci.2013.08.053>.
- [96] Michael Gaus et al. "Automatized Parametrization of SCC-DFTB Repulsive Potentials: Application to Hydrocarbons". In: *The Journal of Physical Chemistry A* 113.43 (Oct. 2009). Publisher: American Chemical Society, pp. 11866–11881. ISSN: 1089-5639. DOI: 10.1021/jp902973m. URL: <https://doi.org/10.1021/jp902973m> (visited on 09/26/2023).

- [97] E. M. Gavilán-Arriazu et al. "The kinetic origin of the Daumas-Hérold model for the Li-ion/graphite intercalation system". In: *Electrochemistry Communications* 93.July (2018). Publisher: Elsevier, pp. 133–137. ISSN: 13882481. DOI: 10.1016/j.elecom.2018.07.004. URL: <https://doi.org/10.1016/j.elecom.2018.07.004>.
- [98] Charles A. Geiger et al. "Crystal chemistry and stability of "Li₇La₃Zr₂O₁₂" garnet: A fast lithium-ion conductor". In: *Inorganic Chemistry* 50.3 (2011), pp. 1089–1097. ISSN: 00201669. DOI: 10.1021/ic101914e.
- [99] Luigi Genovese et al. "Daubechies wavelets as a basis set for density functional pseudopotential calculations". In: *The Journal of Chemical Physics* 129.1 (July 2008), p. 014109. ISSN: 0021-9606. DOI: 10.1063/1.2949547. URL: <https://doi.org/10.1063/1.2949547> (visited on 09/12/2023).
- [100] M. J. Gillan et al. "Order-N first-principles calculations with the conquest code". In: *Computer Physics Communications*. Proceedings of the Conference on Computational Physics 2006 177.1 (July 2007), pp. 14–18. ISSN: 0010-4655. DOI: 10.1016/j.cpc.2007.02.075. URL: <https://www.sciencedirect.com/science/article/pii/S0010465507001658> (visited on 09/12/2023).
- [101] Colin W. Glass, Artem R. Oganov, and Nikolaus Hansen. "USPEX-Evolutionary crystal structure prediction". In: *Computer Physics Communications* 175.11-12 (2006), pp. 713–720. ISSN: 00104655. DOI: 10.1016/j.cpc.2006.07.020.
- [102] Nir Goldman et al. "Semi-Automated Creation of Density Functional Tight Binding Models through Leveraging Chebyshev Polynomial-Based Force Fields". In: *Journal of Chemical Theory and Computation* 17.7 (July 2021). Publisher: American Chemical Society, pp. 4435–4448. ISSN: 1549-9618. DOI: 10.1021/acs.jctc.1c00172. URL: <https://doi.org/10.1021/acs.jctc.1c00172> (visited on 09/26/2023).
- [103] Goodfellow. *Supplier Data - Lithium (Li) (Goodfellow)*. en. Section: Materials Article. Feb. 2003. URL: https://www_azom_com/article.aspx?ArticleID=1841 (visited on 09/19/2023).
- [104] Tim Gould, S. Lebègue, and John F. Dobson. "Dispersion corrections in graphenic systems: a simple and effective model of binding". In: *Journal of Physics: Condensed Matter* 25.44 (Nov. 2013), p. 445010. ISSN: 0953-8984. DOI: 10.1088/0953-8984/25/44/445010. URL: <https://iopscience.iop.org/article/10.1088/0953-8984/25/44/445010>.
- [105] Tim Gould et al. "A Fractionally Ionic Approach to Polarizability and van der Waals Many-Body Dispersion Calculations". In: *Journal of Chemical Theory and Computation* 12.12 (Dec. 2016). arXiv: 1703.08786 Publisher: American Chemical Society, pp. 5920–5930. ISSN: 15499626. DOI: 10.1021/acs.jctc.6b00925.
- [106] Stefan Grimme. "Semiempirical GGA-type density functional constructed with a long-range dispersion correction". In: *Journal of Computational Chemistry* 27.15 (Nov. 2006), pp. 1787–1799. DOI: 10.1002/jcc.20495. URL: <http://doi.wiley.com/10.1002/jcc.20495>.
- [107] Stefan Grimme, Stephan Ehrlich, and Lars Goerigk. "Effect of the damping function in dispersion corrected density functional theory". In: *Journal of Computational Chemistry* 32.7 (May 2011), pp. 1456–1465. ISSN: 01928651. DOI: 10.1002/jcc.21759. URL: <http://aip.scitation.org/doi/10.1063/1.3382344>.
- [108] Stefan Grimme et al. "A consistent and accurate *ab initio* parametrization of density functional dispersion correction (DFT-D) for the 94 elements H-Pu". In: *The Journal of Chemical Physics* 132.15 (Apr. 2010), p. 154104. ISSN: 0021-9606. DOI: 10.1063/1.3382344. URL: <http://aip.scitation.org/doi/10.1063/1.3382344>.
- [109] Jeffrey C. Grossman et al. "Towards an assessment of the accuracy of density functional theory for first principles simulations of water". In: *The Journal of Chemical Physics* 120.1 (Jan. 2004), pp. 300–311. ISSN: 0021-9606. DOI: 10.1063/1.1630560. URL: <http://aip.scitation.org/doi/10.1063/1.1630560>.
- [110] M. Grüning, O. V. Gritsenko, and E. J. Baerends. "Exchange-correlation energy and potential as approximate functionals of occupied and virtual Kohn-Sham orbitals: Application to dissociating H₂". In: *The Journal of Chemical Physics* 118.16 (Apr. 2003), pp. 7183–7192. ISSN: 0021-9606. DOI: 10.1063/1.1562197. URL: <https://doi.org/10.1063/1.1562197> (visited on 08/07/2023).
- [111] Ashim Gurung et al. "A review on strategies addressing interface incompatibilities in inorganic all-solid-state lithium batteries". In: *Sustainable Energy & Fuels* 3.12 (2019), pp. 3279–3309. ISSN: 2398-4902. DOI: 10.1039/C9SE00549H. URL: <http://xlink.rsc.org/?DOI=C9SE00549H>.
- [112] Lisette Haarmann, Jochen Rohrer, and Karsten Albe. "On the Origin of Zero Interface Resistance in the Li_{6.25}Al_{0.25}La₃Zr₂: An Atomistic Investigation". In: *ACS Applied Materials and Interfaces* 13.44 (Nov. 2021). Publisher: American Chemical Society, pp. 52629–52635. ISSN: 19448252. DOI: 10.1021/acsami.1c15400.
- [113] A. T. Hagler, E. Huler, and S. Lifson. "Energy functions for peptides and proteins. I. Derivation of a consistent force field including the hydrogen bond from amide crystals". In: *Journal of the American Chemical Society* 96.17 (Aug. 1974). Publisher: American Chemical Society, pp. 5319–5327. ISSN: 0002-7863. DOI: 10.1021/ja00824a004. URL: <https://doi.org/10.1021/ja00824a004> (visited on 09/14/2023).
- [114] B. Hammer, L. B. Hansen, and J. K. Nørskov. "Improved adsorption energetics within density-functional theory using revised Perdew-Burke-Ernzerhof functionals". In: *Physical Review B* 59.11 (Mar. 1999). Publisher: American Physical Society, pp. 7413–7421. DOI: 10.1103/PhysRevB.59.7413. URL: <https://link.aps.org/doi/10.1103/PhysRevB.59.7413> (visited on 07/28/2023).

- [115] Fudong Han et al. "A Battery Made from a Single Material". In: *Advanced Materials* 27.23 (June 2015), pp. 3473–3483. ISSN: 09359648. DOI: 10.1002/adma.201500180. URL: <http://doi.wiley.com/10.1002/adma.201500180>.
- [116] Fudong Han et al. "High electronic conductivity as the origin of lithium dendrite formation within solid electrolytes". In: *Nature Energy* 4.3 (2019). Publisher: Springer US, pp. 187–196. ISSN: 20587546. DOI: 10.1038/s41560-018-0312-z. URL: <http://dx.doi.org/10.1038/s41560-018-0312-z>.
- [117] Ting Han et al. "Biphenylene monolayer: a novel nonbenzenoid carbon allotrope with potential application as an anode material for high-performance sodium-ion batteries". In: *Physical Chemistry Chemical Physics* 24.18 (Apr. 2022). Publisher: Royal Society of Chemistry, pp. 10712–10716. ISSN: 1463-9076. DOI: 10.1039/D2CP00798C. URL: <http://xlink.rsc.org/?DOI=D2CP00798C>.
- [118] Felix Hanke. "Sensitivity analysis and uncertainty calculation for dispersion corrected density functional theory". In: *Journal of Computational Chemistry* 32.7 (May 2011). ISBN: 1096-987X, pp. 1424–1430. ISSN: 01928651. DOI: 10.1002/jcc.21724. URL: <http://doi.wiley.com/10.1002/jcc.21724>.
- [119] Gus L.W. Hart and Rodney W. Forcade. "Algorithm for generating derivative structures". In: *Physical Review B - Condensed Matter and Materials Physics* 77.22 (2008), pp. 1–12. ISSN: 10980121. DOI: 10.1103/PhysRevB.77.224115.
- [120] D. R. Hartree. "The Wave Mechanics of an Atom with a Non-Coulomb Central Field. Part I. Theory and Methods". In: *Mathematical Proceedings of the Cambridge Philosophical Society* 24.1 (Jan. 1928), pp. 89–110. ISSN: 0305-0041. DOI: 10.1017/S0305004100011919. URL: https://www.cambridge.org/core/product/identifier/S0305004100011919/type/journal_article.
- [121] C. Hartwigsen, W. Witschel, and E. Spohr. "Charge density and charge transfer in stage-1 alkali-graphite intercalation compounds". In: *Physical Review B* 55.8 (Feb. 1997), pp. 4953–4959. ISSN: 0163-1829. DOI: 10.1103/PhysRevB.55.4953. URL: <https://link.aps.org/doi/10.1103/PhysRevB.55.4953>.
- [122] Jeremy Harvey. *Computational chemistry*. Oxford chemistry primers. OCLC: on1005888564. Oxford, United Kingdom: Oxford University Press, 2018. ISBN: 978-0-19-875550-0.
- [123] Trevor Hastie, Robert Tibshirani, and J. H. Friedman. *The elements of statistical learning: data mining, inference, and prediction*. 2nd ed. Springer series in statistics. New York, NY: Springer, 2009. ISBN: 978-0-387-84857-0.
- [124] Cary M. Hayner, Xin Zhao, and Harold H. Kung. "Materials for Rechargeable Lithium-Ion Batteries". In: *Annual Review of Chemical and Biomolecular Engineering* 3.1 (July 2012), pp. 445–471. ISSN: 1947-5438. DOI: 10.1146/annurev-chembioeng-062011-081024. URL: <http://www.annualreviews.org/doi/10.1146/annurev-chembioeng-062011-081024>.
- [125] E. Hazrati, G. A. de Wijs, and G. Brocks. "Li intercalation in graphite: A van der Waals density-functional study". In: *Physical Review B* 90.15 (Oct. 2014), p. 155448. ISSN: 1098-0121. DOI: 10.1103/PhysRevB.90.155448. URL: <https://link.aps.org/doi/10.1103/PhysRevB.90.155448>.
- [126] C. Hiebl et al. "Proton Bulk Diffusion in Cubic Li₇La₃Zr₂O₁₂ Garnets as Probed by Single X-ray Diffraction". In: *Journal of Physical Chemistry C* 123.2 (Jan. 2019). Publisher: American Chemical Society, pp. 1094–1098. ISSN: 19327455. DOI: 10.1021/acs.jpcc.8b10694.
- [127] Nicholas D.M. Hine et al. "Electrostatic interactions in finite systems treated with periodic boundary conditions: Application to linear-scaling density functional theory". In: *Journal of Chemical Physics* 135.20 (2011). arXiv: 1109.1970, pp. 1–18. ISSN: 00219606. DOI: 10.1063/1.3662863.
- [128] Pavel Hobza, Ji? ?poner, and Tom? Reschel. "Density functional theory and molecular clusters". In: *Journal of Computational Chemistry* 16.11 (Nov. 1995). Publisher: Elsevier ISBN: 9780123694010, pp. 1315–1325. ISSN: 0192-8651. DOI: 10.1002/jcc.540161102. URL: <https://linkinghub.elsevier.com/retrieve/pii/B0123694019011505>.
- [129] P. Hohenberg and W. Kohn. "Inhomogeneous Electron Gas". In: *Physical Review* 136.3B (Nov. 1964). Publisher: American Physical Society, B864–B871. DOI: 10.1103/PhysRev.136.B864. URL: <https://link.aps.org/doi/10.1103/PhysRev.136.B864> (visited on 05/30/2023).
- [130] Julian Holland. *Symmetric Surface Finder*. Mar. 2024. URL: <https://github.com/julianholland/Symmetric-Surface-Finder>.
- [131] Julian Holland et al. "Ab initio study of lithium intercalation into a graphite nanoparticle". In: *Materials Advances* 3.23 (2022). Publisher: Royal Society of Chemistry (RSC), pp. 8469–8484. ISSN: 2633-5409. DOI: 10.1039/D2MA00857B. URL: <http://xlink.rsc.org/?DOI=D2MA00857B>.
- [132] N. A. W. Holzwarth, Steven G. Louie, and Sohrab Rabii. "Interlayer states in graphite and in alkali-metal-graphite intercalation compounds". In: *Physical Review B* 30.4 (Aug. 1984), pp. 2219–2222. ISSN: 0163-1829. DOI: 10.1103/PhysRevB.30.2219. URL: <https://link.aps.org/doi/10.1103/PhysRevB.30.2219>.
- [133] B. Hourahine et al. "DFTB+, a software package for efficient approximate density functional theory based atomistic simulations". In: *The Journal of Chemical Physics* 152.12 (Mar. 2020), p. 124101. ISSN: 0021-9606. DOI: 10.1063/1.5143190. URL: <https://doi.org/10.1063/1.5143190> (visited on 09/14/2023).
- [134] M. A. Howard et al. "Effect of Ga incorporation on the structure and Li ion conductivity of La₃Zr₂Li₇O₁₂". In: *Dalton Transactions* 41.39 (Oct. 2012), pp. 12048–12053. ISSN: 14779226. DOI: 10.1039/c2dt31318a.

- [135] IEA. *Greenhouse Gas Emissions from Energy Data Explorer – Data Tools*. en-GB. Aug. 2023. URL: <https://www.iea.org/data-and-statistics/data-tools/greenhouse-gas-emissions-from-energy-data-explorer> (visited on 09/24/2023).
- [136] Yoji Imai and Akio Watanabe. “Energetic evaluation of possible stacking structures of Li-intercalation in graphite using a first-principle pseudopotential calculation”. In: *Journal of Alloys and Compounds* 439.1-2 (2007), pp. 258–267. ISSN: 09258388. DOI: 10.1016/j.jallcom.2006.08.061.
- [137] International Transport Forum. *ITF Transport Outlook 2023*. en. ITF Transport Outlook. OECD, May 2023. ISBN: 978-92-821-4481-7. DOI: 10.1787/b6cc9ad5-en. URL: https://www.oecd-ilibrary.org/transport/itf-transport-outlook-2023_b6cc9ad5-en (visited on 09/24/2023).
- [138] Eric B. Isaacs, Shane Patel, and Chris Wolverton. “Prediction of Li intercalation voltages in rechargeable battery cathode materials: effects of exchange-correlation functional, van der Waals interactions, and Hubbard U”. In: (Mar. 2020). arXiv: 2003.01757. URL: <http://arxiv.org/abs/2003.01757>.
- [139] Rinton Iwasaki et al. “Density Functional Theory Studies on Li Metal Electrode/Garnet-Type Li₇La₃Zr₂O₁₂ Solid Electrolyte Interfaces for Application in All-Solid-State Batteries”. en. In: *physica status solidi (b)* 259.9 (2022). _eprint: <https://onlinelibrary.wiley.com/doi/pdf/10.1002/pssb.202100546>, p. 2100546. ISSN: 1521-3951. DOI: 10.1002/pssb.202100546. URL: <https://onlinelibrary.wiley.com/doi/abs/10.1002/pssb.202100546> (visited on 09/15/2023).
- [140] Anubhav Jain et al. “Commentary: The Materials Project: A materials genome approach to accelerating materials innovation”. In: *APL Materials* 1.1 (July 2013), p. 011002. ISSN: 2166-532X. DOI: 10.1063/1.4812323. URL: <https://doi.org/10.1063/1.4812323> (visited on 09/18/2023).
- [141] Randy Jalem et al. “Concerted migration mechanism in the Li ion dynamics of garnet-type Li₇La₃Zr₂O₁₂”. In: *Chemistry of Materials* 25.3 (2013), pp. 425–430. ISSN: 08974756. DOI: 10.1021/cm303542x.
- [142] Anto James and Rotti Srinivasamurthy Swathi. “Modeling the Adsorption of Polycyclic Aromatic Hydrocarbons on Graphynes: An Improved Lennard-Jones Formulation”. In: *Journal of Physical Chemistry A* (June 2022). Publisher: American Chemical Society. ISSN: 15205215. DOI: 10.1021/acs.jpca.2c01777.
- [143] J. F. Janak. “Proof that $\frac{\partial E}{\partial n_i} = \frac{\partial \epsilon}{\partial n_i}$ in density-functional theory”. en. In: *Physical Review B* 18.12 (Dec. 1978), pp. 7165–7168. ISSN: 0163-1829. DOI: 10.1103/PhysRevB.18.7165. URL: <https://link.aps.org/doi/10.1103/PhysRevB.18.7165> (visited on 05/24/2023).
- [144] Glen R. Jenness, Caitlin G. Bresnahan, and Manoj K. Shukla. “Adventures in DFTB: Toward an Automatic Parameterization Scheme”. In: *Journal of Chemical Theory and Computation* 16.11 (Nov. 2020). Publisher: American Chemical Society, pp. 6894–6903. ISSN: 1549-9618. DOI: 10.1021/acs.jctc.0c00842. URL: <https://doi.org/10.1021/acs.jctc.0c00842> (visited on 09/26/2023).
- [145] Zhouyang Jiang et al. “Reducing the Interfacial Resistance in All-Solid-State Lithium Batteries Based on Oxide Ceramic Electrolytes”. In: *ChemElectroChem* 6.12 (2019), pp. 2970–2983. ISSN: 21960216. DOI: 10.1002/celc.201801898.
- [146] R. O. Jones. “Density functional theory: Its origins, rise to prominence, and future”. en. In: *Reviews of Modern Physics* 87.3 (Aug. 2015), pp. 897–923. ISSN: 0034-6861, 1539-0756. DOI: 10.1103/RevModPhys.87.897. URL: <https://link.aps.org/doi/10.1103/RevModPhys.87.897> (visited on 05/24/2023).
- [147] Petr Jurečka et al. “Benchmark database of accurate (MP2 and CCSD(T) complete basis set limit) interaction energies of small model complexes, DNA base pairs, and amino acid pairs”. en. In: *Physical Chemistry Chemical Physics* 8.17 (Apr. 2006). Publisher: The Royal Society of Chemistry, pp. 1985–1993. ISSN: 1463-9084. DOI: 10.1039/B600027D. URL: <https://pubs.rsc.org/en/content/articlelanding/2006/cp/b600027d> (visited on 07/28/2023).
- [148] Noriaki Kamaya et al. “A lithium superionic conductor”. In: *Nature Materials* 10.9 (2011). Publisher: Nature Publishing Group, pp. 682–686. ISSN: 14764660. DOI: 10.1038/nmat3066. URL: <http://dx.doi.org/10.1038/nmat3066>.
- [149] Bora Karasulu et al. “Al/Ga-Doped Li₇La₃Zr₂O₁₂ Garnets as Li-Ion Solid-State Battery Electrolytes: Atomistic Insights into Local Coordination Environments and Their Influence on ¹⁷O, ²⁷Al, and ⁷¹Ga NMR Spectra”. In: *Journal of the American Chemical Society* 142.6 (Feb. 2020). Publisher: American Chemical Society, pp. 3132–3148. ISSN: 0002-7863. DOI: 10.1021/jacs.9b12685. URL: <https://doi.org/10.1021/jacs.9b12685> (visited on 10/03/2023).
- [150] Nitin A. Kaskhedikar and Joachim Maier. “Lithium Storage in Carbon Nanostructures”. In: *Advanced Materials* 21.25-26 (July 2009), pp. 2664–2680. ISSN: 09359648. DOI: 10.1002/adma.200901079. URL: <http://doi.wiley.com/10.1002/adma.200901079>.
- [151] Hoseong Kim et al. “Revisiting Lithium- and Sodium-Ion Storage in Hard Carbon Anodes”. en. In: *Advanced Materials* 35.12 (Mar. 2023), p. 2209128. ISSN: 0935-9648, 1521-4095. DOI: 10.1002/adma.202209128. URL: <https://onlinelibrary.wiley.com/doi/10.1002/adma.202209128> (visited on 03/05/2024).
- [152] Sewon Kim et al. “The Role of Interlayer Chemistry in Li-Metal Growth through a Garnet-Type Solid Electrolyte”. In: *Advanced Energy Materials* (2020). Publisher: Wiley-VCH Verlag. ISSN: 16146840. DOI: 10.1002/aenm.201903993.

- [153] Jiří Klimeš, David R. Bowler, and Angelos Michaelides. “Chemical accuracy for the van der Waals density functional”. In: *Journal of Physics Condensed Matter* 22.2 (2010). arXiv: 0910.0438. ISSN: 09538984. DOI: 10.1088/0953-8984/22/2/022201.
- [154] Takeshi Kobayashi, Atsuo Yamada, and Ryoji Kanno. “Interfacial reactions at electrode/electrolyte boundary in all solid-state lithium battery using inorganic solid electrolyte, thio-LISICON”. In: *Electrochimica Acta* 53.15 (June 2008), pp. 5045–5050. ISSN: 00134686. DOI: 10.1016/j.electacta.2008.01.071. URL: <https://linkinghub.elsevier.com/retrieve/pii/S0013468608001321>.
- [155] Wolfram Koch and Max C. Holthausen. *A chemist's guide to density functional theory*. eng. 2nd ed., 5. reprint. Weinheim: Wiley-VCH, 2008. ISBN: 978-3-527-30372-4.
- [156] Jorge Kohanoff. *Electronic structure calculations for solids and molecules: theory and computational methods*. OCLC: ocm63186207. Cambridge, UK ; New York: Cambridge University Press, 2006. ISBN: 978-0-521-81591-8.
- [157] W. Kohn and L. J. Sham. “Self-Consistent Equations Including Exchange and Correlation Effects”. en. In: *Physical Review* 140.4A (Nov. 1965), A1133–A1138. ISSN: 0031-899X. DOI: 10.1103/PhysRev.140.A1133. URL: <https://link.aps.org/doi/10.1103/PhysRev.140.A1133> (visited on 05/24/2023).
- [158] G. Kresse and J. Furthmüller. “Efficient iterative schemes for ab initio total-energy calculations using a plane-wave basis set”. In: *Physical Review B - Condensed Matter and Materials Physics* 54.16 (1996), pp. 11169–11186. ISSN: 1550235X. DOI: 10.1103/PhysRevB.54.11169.
- [159] Sándor Kristyán and Péter Pulay. “Can (semi)local density functional theory account for the London dispersion forces?” In: *Chemical Physics Letters* 229.3 (Oct. 1994), pp. 175–180. ISSN: 00092614. DOI: 10.1016/0009-2614(94)01027-7. URL: <https://linkinghub.elsevier.com/retrieve/pii/0009261494010277>.
- [160] Matthias Kühne et al. “Reversible superdense ordering of lithium between two graphene sheets”. en. In: *Nature* 564.7735 (Dec. 2018). Number: 7735 Publisher: Nature Publishing Group, pp. 234–239. ISSN: 1476-4687. DOI: 10.1038/s41586-018-0754-2. URL: <https://www.nature.com/articles/s41586-018-0754-2> (visited on 07/28/2023).
- [161] Narendra Kumar and Jorge M. Seminario. “Lithium-ion model behavior in an ethylene carbonate electrolyte using molecular dynamics”. In: *Journal of Physical Chemistry C* 120.30 (Aug. 2016). Publisher: American Chemical Society, pp. 16322–16332. ISSN: 19327455. DOI: 10.1021/acs.jpcc.6b03709.
- [162] Shota Kumazaki et al. “High lithium ion conductive Li₇La₃Zr₂O₁₂ by inclusion of both Al and Si”. In: *Electrochemistry Communications* 13.5 (May 2011), pp. 509–512. ISSN: 13882481. DOI: 10.1016/j.elecom.2011.02.035.
- [163] Franck Laloë. *Do We Really Understand Quantum Mechanics?* 1st ed. Cambridge University Press, Aug. 2012. ISBN: 978-1-107-02501-1. DOI: 10.1017/CBO9781139177160. URL: <https://www.cambridge.org/core/product/identifier/9781139177160/type/book> (visited on 05/24/2023).
- [164] D. C. Langreth et al. “Van der Waals density functional theory with applications”. In: *International Journal of Quantum Chemistry* 101.5 (2005), pp. 599–610. ISSN: 00207608. DOI: 10.1002/qua.20315.
- [165] Dominique Larcher et al. “Recent findings and prospects in the field of pure metals as negative electrodes for Li-ion batteries”. en. In: *Journal of Materials Chemistry* 17.36 (2007), p. 3759. ISSN: 0959-9428, 1364-5501. DOI: 10.1039/b705421c. URL: <http://xlink.rsc.org/?DOI=b705421c> (visited on 03/05/2024).
- [166] Eunseok Lee and Kristin A. Persson. “Li absorption and intercalation in single layer graphene and few layer graphene by first principles”. In: *Nano Letters* 12.9 (2012), pp. 4624–4628. ISSN: 15306984. DOI: 10.1021/nl3019164.
- [167] Kiwoong Lee et al. “Analyzing void formation and rewetting of thin in situ-formed Li anodes on LLZO”. In: *Joule* 6.11 (Nov. 2022). Publisher: Cell Press, pp. 2547–2565. ISSN: 25424351. DOI: 10.1016/j.joule.2022.09.009.
- [168] Kyuho Lee et al. “Higher-accuracy van der Waals density functional”. In: *Physical Review B* 82.8 (Aug. 2010). arXiv: 1003.5255, p. 081101. ISSN: 1098-0121. DOI: 10.1103/PhysRevB.82.081101. URL: <https://link.aps.org/doi/10.1103/PhysRevB.82.081101>.
- [169] Ermias Girma Legesse, Chi Liang Chen, and Jyh Chiang Jiang. “Lithium diffusion in graphene and graphite: Effect of edge morphology”. In: *Carbon* 103 (July 2016). Publisher: Elsevier Ltd, pp. 209–216. ISSN: 00086223. DOI: 10.1016/j.carbon.2016.03.016.
- [170] Hang Lei et al. “A review of hard carbon anode: Rational design and advanced characterization in potassium ion batteries”. en. In: *InfoMat* 4.2 (Feb. 2022), e12272. ISSN: 2567-3165, 2567-3165. DOI: 10.1002/inf2.12272. URL: <https://onlinelibrary.wiley.com/doi/10.1002/inf2.12272> (visited on 02/28/2024).
- [171] Olena Lenchuk, Philipp Adelhelm, and Doreen Mollenhauer. “Comparative study of density functionals for the description of lithium-graphite intercalation compounds”. In: *Journal of Computational Chemistry* 40.27 (Oct. 2019), pp. 2400–2412. ISSN: 0192-8651. DOI: 10.1002/jcc.26017. URL: <https://onlinelibrary.wiley.com/doi/abs/10.1002/jcc.26017>.
- [172] N. D. Lepley and N. A.W. Holzwarth. “Modeling interfaces between solids: Application to Li battery materials”. In: *Physical Review B - Condensed Matter and Materials Physics* 92.21 (2015), pp. 1–15. ISSN: 1550235X. DOI: 10.1103/PhysRevB.92.214201.

- [173] Jurij Leskovec, Anand Rajaraman, and Jeffrey D. Ullman. *Mining of massive datasets*. Second edition. OCLC: ocn900001321. Cambridge: Cambridge University Press, 2014. ISBN: 978-1-107-07723-2.
- [174] Ira N. Levine. *Quantum chemistry*. Seventh edition. Boston: Pearson, 2014. ISBN: 978-0-321-80345-0.
- [175] Bing Li et al. “Polycyclic Aromatic Hydrocarbons Adsorption onto Graphene: A DFT and AIMD Study”. In: *Materials* 11.5 (May 2018). Publisher: MDPI AG, p. 726. ISSN: 1996-1944. DOI: 10.3390/ma11050726. URL: <http://www.mdpi.com/1996-1944/11/5/726>.
- [176] Lin Lin and Jianfeng Lu. *A mathematical introduction to electronic structure theory: iterative solution of symmetric quasi-definite linear systems*. SIAM spotlights 4. Philadelphia: Society for Industrial and Applied Mathematics, 2019. ISBN: 978-1-61197-580-2.
- [177] Tongchao Liu et al. “In situ quantification of interphasial chemistry in Li-ion battery”. en. In: *Nature Nanotechnology* 14.1 (Jan. 2019). Number: 1 Publisher: Nature Publishing Group, pp. 50–56. ISSN: 1748-3395. DOI: 10.1038/s41565-018-0284-y. URL: <https://www.nature.com/articles/s41565-018-0284-y> (visited on 09/13/2023).
- [178] Ze Liu et al. “Interlayer binding energy of graphite: A mesoscopic determination from deformation”. In: *Physical Review B* 85.20 (May 2012), p. 205418. ISSN: 1098-0121. DOI: 10.1103/PhysRevB.85.205418. URL: <https://link.aps.org/doi/10.1103/PhysRevB.85.205418>.
- [179] Zengcai Liu et al. “Anomalous High Ionic Conductivity of Nanoporous -Li 3 PS 4”. In: *Journal of the American Chemical Society* 135.3 (Jan. 2013), pp. 975–978. ISSN: 0002-7863. DOI: 10.1021/ja3110895. URL: <https://pubs.acs.org/doi/10.1021/ja3110895>.
- [180] Maicon Pierre Lourenço et al. “FASP: a framework for automation of Slater–Koster file parameterization”. en. In: *Theoretical Chemistry Accounts* 135.11 (Oct. 2016), p. 250. ISSN: 1432-2234. DOI: 10.1007/s00214-016-2001-y. URL: <https://doi.org/10.1007/s00214-016-2001-y> (visited on 09/11/2023).
- [181] Per-Olov Löwdin. “Correlation Problem in Many-Electron Quantum Mechanics I. Review of Different Approaches and Discussion of Some Current Ideas”. In: *Advances in Chemical Physics*. Ed. by I. Prigogine. Hoboken, NJ, USA: John Wiley & Sons, Inc., Mar. 2007, pp. 207–322. ISBN: 978-0-470-14348-3. DOI: 10.1002/9780470143483.ch7. URL: <https://onlinelibrary.wiley.com/doi/10.1002/9780470143483.ch7> (visited on 05/24/2023).
- [182] H. P. Lüthi et al. “How well does the Hartree-Fock model predict equilibrium geometries of transition metal complexes? Large-scale LCAO-SCF studies on ferrocene and decamethylferrocene”. In: *The Journal of Chemical Physics* 77.4 (1982), pp. 2002–2009. ISSN: 00219606. DOI: 10.1063/1.444053.
- [183] Cheng Ma et al. “Interfacial Stability of Li Metal–Solid Electrolyte Elucidated via in Situ Electron Microscopy”. In: *Nano Letters* 16.11 (Nov. 2016), pp. 7030–7036. ISSN: 1530-6984. DOI: 10.1021/acs.nanolett.6b03223. URL: <https://pubs.acs.org/doi/10.1021/acs.nanolett.6b03223>.
- [184] Douglas R. MacFarlane et al. “Energy applications of ionic liquids”. en. In: *Energy Environ. Sci.* 7.1 (2014), pp. 232–250. ISSN: 1754-5692, 1754-5706. DOI: 10.1039/C3EE42099J. URL: <http://xlink.rsc.org/?DOI=C3EE42099J> (visited on 03/05/2024).
- [185] Thomas A. Manz and Nidia Gabaldon Limas. “Introducing DDEC6 atomic population analysis: Part 1. Charge partitioning theory and methodology”. In: *RSC Advances* 6.53 (2016). Publisher: Royal Society of Chemistry, pp. 47771–47801. ISSN: 20462069. DOI: 10.1039/c6ra04656h. URL: <http://dx.doi.org/10.1039/C6RA04656H>.
- [186] Richard M. Martin. *Electronic Structure: Basic Theory and Practical Methods*. 1st ed. Cambridge University Press, Apr. 2004. ISBN: 978-0-521-53440-6. DOI: 10.1017/CBO9780511805769. URL: <https://www.cambridge.org/core/product/identifier/9780511805769/type/book> (visited on 05/24/2023).
- [187] Nicola Marzari, David Vanderbilt, and M. C. Payne. “Ensemble density-functional theory for ab initio molecular dynamics of metals and finite-temperature insulators”. In: *Physical Review Letters* 79.7 (1997). arXiv: cond-mat/9703081, pp. 1337–1340. ISSN: 10797114. DOI: 10.1103/PhysRevLett.79.1337.
- [188] Jette K. Mathiesen et al. “Understanding the structural changes in lithiated graphite through high-resolution operando powder X-ray diffraction”. In: *Carbon* 153 (2019). Publisher: Elsevier Ltd, pp. 347–354. ISSN: 00086223. DOI: 10.1016/j.carbon.2019.06.103. URL: <https://doi.org/10.1016/j.carbon.2019.06.103>.
- [189] P. T. Matthews. *Introduction to quantum mechanics*. 3d ed. London ; New York [etc.]: McGraw-Hill, 1974. ISBN: 978-0-07-084036-2.
- [190] Donald A. McQuarrie. *Statistical mechanics*. Sausalito, Calif: University Science Books, 2000. ISBN: 978-1-891389-15-3.
- [191] Katharina Meier, Teodoro Laino, and Alessandro Curioni. “Solid-state electrolytes: Revealing the mechanisms of Li-Ion conduction in tetragonal and cubic LLZO by first-principles calculations”. In: *Journal of Physical Chemistry C* 118.13 (2014), pp. 6668–6679. ISSN: 19327447. DOI: 10.1021/jp5002463.
- [192] Michael P. Mercer et al. “Sodiation energetics in pore size controlled hard carbons determined via entropy profiling”. en. In: *Journal of Materials Chemistry A* 11.12 (2023), pp. 6543–6555. ISSN: 2050-7488, 2050-7496. DOI: 10.1039/D2TA09406A. URL: <http://xlink.rsc.org/?DOI=D2TA09406A> (visited on 02/28/2024).

- [193] Michael P. Mercer et al. "Transitions of lithium occupation in graphite: A physically informed model in the dilute lithium occupation limit supported by electrochemical and thermodynamic measurements". In: *Electrochimica Acta* 324 (2019). Publisher: Elsevier Ltd, p. 134774. ISSN: 00134686. DOI: 10.1016/j.electacta.2019.134774. URL: <https://doi.org/10.1016/j.electacta.2019.134774>.
- [194] Michael Peter Mercer et al. "Voltage hysteresis during lithiation/delithiation of graphite associated with metastable carbon stackings". In: *Journal of Materials Chemistry A* 9.1 (2021). Publisher: Royal Society of Chemistry, pp. 492–504. ISSN: 2050-7488. DOI: 10.1039/DOTA10403E. URL: <http://xlink.rsc.org/?DOI=DOTA10403E>.
- [195] N. David Mermin. "Thermal properties of the inhomogeneous electron gas". In: *Physical Review* 137.5A (1965), pp. 1–3. ISSN: 0031899X. DOI: 10.1103/PhysRev.137.A1441.
- [196] K. Mizushima et al. "Li_xCoO₂ (0 < x < -1): A new cathode material for batteries of high energy density". In: *Materials Research Bulletin* 15.6 (June 1980), pp. 783–789. ISSN: 00255408. DOI: 10.1016/0025-5408(80)90012-4. URL: <https://iopscience.iop.org/article/10.1143/JJAP.42.6131>.
- [197] Yifei Mo, Shyue Ping Ong, and Gerbrand Ceder. "First Principles Study of the Li₁₀GeP₂S₁₂ Lithium Super Ionic Conductor Material". In: *Chemistry of Materials* 24.1 (Jan. 2012), pp. 15–17. ISSN: 0897-4756. DOI: 10.1021/cm203303y. URL: <https://pubs.acs.org/doi/10.1021/cm203303y>.
- [198] Lucy M Morgan et al. "Pushing the boundaries of lithium battery research with atomistic modelling on different scales". In: *Progress in Energy* 4.1 (Jan. 2022). Publisher: IOP Publishing, p. 012002. ISSN: 2516-1083. DOI: 10.1088/2516-1083/ac3894. URL: <https://iopscience.iop.org/article/10.1088/2516-1083/ac3894>.
- [199] Ryohei Morita et al. "Combination of solid state NMR and DFT calculation to elucidate the state of sodium in hard carbon electrodes". en. In: *Journal of Materials Chemistry A* 4.34 (2016), pp. 13183–13193. ISSN: 2050-7488, 2050-7496. DOI: 10.1039/C6TA04273B. URL: <http://xlink.rsc.org/?DOI=C6TA04273B> (visited on 02/28/2024).
- [200] Arash A. Mostofi. "On Linear-Scaling Methods for Quantum Mechanical First-Principles Calculations". PhD thesis. University of Cambridge, 2004.
- [201] Arash A. Mostofi et al. "Preconditioned iterative minimization for linear-scaling electronic structure calculations". In: *Journal of Chemical Physics* 119.17 (2003), pp. 8842–8848. ISSN: 00219606. DOI: 10.1063/1.1613633.
- [202] R. S. Mulliken. "Electronic population analysis on LCAO-MO molecular wave functions. I". In: *The Journal of Chemical Physics* 23.10 (1955), pp. 1833–1840. ISSN: 00219606. DOI: 10.1063/1.1740588.
- [203] Robert Sanderson Mulliken and Walter C. Ermler. *Diatomeric molecules: results of ab initio calculations*. New York: Academic Press, 1977. ISBN: 978-0-12-510750-1.
- [204] F. D. Murnaghan. "The Compressibility of Media under Extreme Pressures". In: *Proceedings of the National Academy of Sciences* 30.9 (Sept. 1944). Publisher: Proceedings of the National Academy of Sciences, pp. 244–247. DOI: 10.1073/pnas.30.9.244. URL: <https://www.pnas.org/doi/10.1073/pnas.30.9.244> (visited on 07/28/2023).
- [205] Ramaswamy Murugan, Venkataraman Thangadurai, and Werner Weppner. "Fast lithium ion conduction in garnet-type Li₇La₃Zr₂O₁₂". In: *Angewandte Chemie - International Edition* 46.41 (2007), pp. 7778–7781. ISSN: 14337851. DOI: 10.1002/anie.200701144.
- [206] Jennifer E. Ni et al. "Room temperature elastic moduli and Vickers hardness of hot-pressed LLZO cubic garnet". In: *Journal of Materials Science* 47.23 (Dec. 2012), pp. 7978–7985. ISSN: 0022-2461. DOI: 10.1007/s10853-012-6687-5. URL: <http://link.springer.com/10.1007/s10853-012-6687-5>.
- [207] Artem R. Oganov and Colin W. Glass. "Crystal structure prediction using ab initio evolutionary techniques: Principles and applications". In: *Journal of Chemical Physics* 124.24 (2006). ISSN: 00219606. DOI: 10.1063/1.2210932.
- [208] Kirill Okhotnikov, Thibault Charpentier, and Sylvain Cadars. "Supercell program: A combinatorial structure-generation approach for the local-level modeling of atomic substitutions and partial occupancies in crystals". In: *Journal of Cheminformatics* 8.1 (2016). Publisher: BioMed Central Ltd. ISSN: 17582946. DOI: 10.1186/s13321-016-0129-3.
- [209] Yukihiko Okuno, Jun Haruyama, and Yoshitaka Tateyama. "Comparative study on sulfide and oxide electrolyte interfaces with cathodes in all-solid-state battery via first-principles calculations". In: *ACS Applied Energy Materials* 3.11 (2020), pp. 11061–11072. ISSN: 25740962. DOI: 10.1021/acsaem.0c02033.
- [210] Emilia Olsson, Jonathon Cottom, and Qiong Cai. "Defects in Hard Carbon: Where Are They Located and How Does the Location Affect Alkaline Metal Storage?" en. In: *Small* 17.18 (May 2021), p. 2007652. ISSN: 1613-6810, 1613-6829. DOI: 10.1002/smll.202007652. URL: <https://onlinelibrary.wiley.com/doi/10.1002/smll.202007652> (visited on 02/28/2024).
- [211] Jun Pan et al. "Revisit Electrolyte Chemistry of Hard Carbon in Ether for Na Storage". en. In: *JACS Au* 1.8 (Aug. 2021), pp. 1208–1216. ISSN: 2691-3704, 2691-3704. DOI: 10.1021/jacsau.1c00158. URL: <https://pubs.acs.org/doi/10.1021/jacsau.1c00158> (visited on 02/28/2024).
- [212] Vikram Pande and Venkatasubramanian Viswanathan. "Robust high-fidelity DFT study of the lithium-graphite phase diagram". In: *Physical Review Materials* 2.12 (2018). arXiv: 1607.05658 Publisher: American Physical Society, pp. 1–10. ISSN: 24759953. DOI: 10.1103/PhysRevMaterials.2.125401.

- [213] K. Parlinski, Z. Q. Li, and Y. Kawazoe. “First-principles determination of the soft mode in cubic ZrO₂”. In: *Physical Review Letters* 78.21 (1997), pp. 4063–4066. ISSN: 10797114. DOI: 10.1103/PhysRevLett.78.4063.
- [214] Robert G. Parr and Weitao Yang. *Density-functional theory of atoms and molecules*. eng. 1. iss. as ... paperback. International series of monographs on chemistry 16. New York, NY: Oxford Univ. Press [u.a.], 1994. ISBN: 978-0-19-509276-9.
- [215] M. C. Payne et al. “Iterative minimization techniques for ab initio total-energy calculations: Molecular dynamics and conjugate gradients”. In: *Reviews of Modern Physics* 64.4 (1992), pp. 1045–1097. ISSN: 00346861. DOI: 10.1103/RevModPhys.64.1045.
- [216] E. Peled. “The Electrochemical Behavior of Alkali and Alkaline Earth Metals in Nonaqueous Battery Systems—The Solid Electrolyte Interphase Model”. In: *Journal of The Electrochemical Society* 126.12 (Dec. 1979), pp. 2047–2051. ISSN: 0013-4651. DOI: 10.1149/1.2128859. URL: <https://iopscience.iop.org/article/10.1149/1.2128859>.
- [217] E. Peled, D. Golodnitsky, and G. Ardel. “Advanced Model for Solid Electrolyte Interphase Electrodes in Liquid and Polymer Electrolytes”. In: *Journal of The Electrochemical Society* 144.8 (Aug. 1997), pp. L208–L210. ISSN: 0013-4651. DOI: 10.1149/1.1837858. URL: <https://iopscience.iop.org/article/10.1149/1.1837858>.
- [218] E. Peled and S. Menkin. “Review—SEI: Past, Present and Future”. In: *Journal of The Electrochemical Society* 164.7 (June 2017). Publisher: The Electrochemical Society, A1703–A1719. ISSN: 0013-4651. DOI: 10.1149/2.1441707jes. URL: <https://iopscience.iop.org/article/10.1149/2.1441707jes>.
- [219] E. Peled et al. “Composition, depth profiles and lateral distribution of materials in the SEI built on HOPG-TOF SIMS and XPS studies”. In: *Journal of Power Sources* 97–98 (July 2001), pp. 52–57. ISSN: 03787753. DOI: 10.1016/S0378-7753(01)00505-5. URL: <https://linkinghub.elsevier.com/retrieve/pii/S0378775301005055>.
- [220] Chao Peng et al. “Lithium intercalation edge effects and doping implications for graphite anodes”. In: *Journal of Materials Chemistry A* 8.16 (2020). Publisher: Royal Society of Chemistry, pp. 7947–7955. ISSN: 20507496. DOI: 10.1039/c9ta13862e.
- [221] Chao Peng et al. “Mechanism of Li nucleation at graphite anodes and mitigation strategies”. en. In: *Journal of Materials Chemistry A* 9.31 (2021), pp. 16798–16804. ISSN: 2050-7488, 2050-7496. DOI: 10.1039/D1TA03447B. URL: <http://xlink.rsc.org/?DOI=D1TA03447B> (visited on 07/27/2023).
- [222] Eduardo M. Perassi and Ezequiel P.M. Leiva. “A theoretical model to determine intercalation entropy and enthalpy: Application to lithium/graphite”. In: *Electrochemistry Communications* 65 (2016). Publisher: Elsevier B.V., pp. 48–52. ISSN: 13882481. DOI: 10.1016/j.elecom.2016.02.003. URL: <http://dx.doi.org/10.1016/j.elecom.2016.02.003>.
- [223] John P. Perdew, Kieron Burke, and Matthias Ernzerhof. “Generalized Gradient Approximation Made Simple”. en. In: *Physical Review Letters* 77.18 (Oct. 1996), pp. 3865–3868. ISSN: 0031-9007, 1079-7114. DOI: 10.1103/PhysRevLett.77.3865. URL: <https://link.aps.org/doi/10.1103/PhysRevLett.77.3865> (visited on 08/07/2023).
- [224] John P. Perdew, Kieron Burke, and Yue Wang. “Generalized gradient approximation for the exchange-correlation hole of a many-electron system”. In: *Physical Review B* 54.23 (Dec. 1996), pp. 16533–16539. ISSN: 0163-1829. DOI: 10.1103/PhysRevB.54.16533. URL: <http://www.tandfonline.com/doi/abs/10.1080/13639080.2012.711944>.
- [225] John P. Perdew and Wang Yue. “Accurate and simple density functional for the electronic exchange energy: Generalized gradient approximation”. In: *Physical Review B* 33.12 (June 1986). Publisher: American Physical Society, pp. 8800–8802. DOI: 10.1103/PhysRevB.33.8800. URL: <https://link.aps.org/doi/10.1103/PhysRevB.33.8800> (visited on 07/28/2023).
- [226] Kristin Persson et al. “Thermodynamic and kinetic properties of the Li-graphite system from first-principles calculations”. In: *Physical Review B* 82.12 (Sept. 2010), p. 125416. ISSN: 1098-0121. DOI: 10.1103/PhysRevB.82.125416. URL: <https://link.aps.org/doi/10.1103/PhysRevB.82.125416>.
- [227] James C. Phillips and Leonard Kleinman. “New Method for Calculating Wave Functions in Crystals and Molecules”. en. In: *Physical Review* 116.2 (Oct. 1959), pp. 287–294. ISSN: 0031-899X. DOI: 10.1103/PhysRev.116.287. URL: <https://link.aps.org/doi/10.1103/PhysRev.116.287> (visited on 08/14/2023).
- [228] Warren E. Pickett. “Pseudopotential methods in condensed matter applications”. In: *Computer Physics Reports* 9.3 (Apr. 1989), pp. 115–197. ISSN: 0167-7977. DOI: 10.1016/0167-7977(89)90002-6. URL: <https://www.sciencedirect.com/science/article/pii/0167797789900026> (visited on 08/15/2023).
- [229] G. Pistoia, ed. *Lithium-ion batteries: advances and applications*. First edition. OCLC: ocn861211281. Amsterdam: Elsevier, 2014. ISBN: 978-0-444-59513-3.
- [230] Joseph C. A. Prentice et al. “The ONETEP linear-scaling density functional theory program”. In: *The Journal of Chemical Physics* 152.17 (May 2020). Publisher: AIP Publishing, LLC, p. 174111. ISSN: 0021-9606. DOI: 10.1063/5.0004445. URL: <http://aip.scitation.org/doi/10.1063/5.0004445>.
- [231] E. Prodan and W. Kohn. “Nearsightedness of electronic matter”. In: *Proceedings of the National Academy of Sciences* 102.33 (Aug. 2005), pp. 11635–11638. ISSN: 0027-8424. DOI: 10.1073/pnas.0505436102. URL: <http://www.pnas.org/cgi/doi/10.1073/pnas.0505436102>.

- [232] Muralikrishna Raju et al. "Reactive force field study of Li/C systems for electrical energy storage". In: *Journal of Chemical Theory and Computation* 11.5 (2015), pp. 2156–2166. ISSN: 15499626. DOI: 10.1021/ct501027v.
- [233] Yunbing Ran et al. "Towards prediction of ordered phases in rechargeable battery chemistry via group–subgroup transformation". In: *npj Computational Materials* 7.1 (Dec. 2021). Publisher: Nature Research, p. 184. ISSN: 2057-3960. DOI: 10.1038/s41524-021-00653-y. URL: <https://www.nature.com/articles/s41524-021-00653-y>.
- [234] Ezhiyil Rangasamy, Jeff Wolfenstine, and Jeffrey Sakamoto. "The role of Al and Li concentration on the formation of cubic garnet solid electrolyte of nominal composition $\text{Li}_7\text{La}_3\text{Zr}_2\text{O}_{12}$ ". In: *Solid State Ionics* 206 (Jan. 2012). Publisher: Elsevier B.V., pp. 28–32. ISSN: 01672738. DOI: 10.1016/j.ssi.2011.10.022. URL: <http://dx.doi.org/10.1016/j.ssi.2011.10.022>.
- [235] A. K. Rappe et al. "UFF, a full periodic table force field for molecular mechanics and molecular dynamics simulations". In: *Journal of the American Chemical Society* 114.25 (Dec. 1992). Publisher: American Chemical Society, pp. 10024–10035. ISSN: 0002-7863. DOI: 10.1021/ja00051a040. URL: <https://doi.org/10.1021/ja00051a040> (visited on 09/14/2023).
- [236] P. A. Redhead. "Thermal desorption of gases". In: *Vacuum* 12.5 (Sept. 1962), p. 274. ISSN: 0042207X. DOI: 10.1016/0042-207X(62)90543-2. URL: <https://linkinghub.elsevier.com/retrieve/pii/0042207X62905432>.
- [237] Alan E. Reed, Robert B. Weinstock, and Frank Weinhold. "Natural population analysis". In: *The Journal of Chemical Physics* 83.2 (July 1985), pp. 735–746. ISSN: 0021-9606. DOI: 10.1063/1.449486. URL: <http://aip.scitation.org/doi/10.1063/1.449486>.
- [238] Yaoyu Ren et al. "Direct observation of lithium dendrites inside garnet-type lithium-ion solid electrolyte". In: *Electrochemistry Communications* 57 (Aug. 2015). Publisher: Elsevier Inc., pp. 27–30. ISSN: 13882481. DOI: 10.1016/j.elecom.2015.05.001. URL: <https://linkinghub.elsevier.com/retrieve/pii/S1388248115001241>.
- [239] Daniel Rettenwander et al. "DFT study of the role of Al^{3+} in the fast ion-conductor $\text{Li}_{7-3x}\text{Al}_{3+x}\text{La}_3\text{Zr}_2\text{O}_{12}$ garnet". In: *Chemistry of Materials* 26.8 (2014), pp. 2617–2623. ISSN: 15205002. DOI: 10.1021/cm5000999.
- [240] Daniel Rettenwander et al. "Interface instability of fe-stabilized $\text{Li}_7\text{La}_3\text{Zr}_2\text{O}_{12}$ versus li metal". In: *Journal of Physical Chemistry C* 122.7 (2018), pp. 3780–3785. ISSN: 19327455. DOI: 10.1021/acs.jpcc.7b12387.
- [241] Daniel Rettenwander et al. "Structural and Electrochemical Consequences of Al and Ga Cosubstitution in $\text{Li}_7\text{La}_3\text{Zr}_2\text{O}_{12}$ Solid Electrolytes". In: *Chemistry of Materials* 28.7 (2016), pp. 2384–2392. ISSN: 15205002. DOI: 10.1021/acs.chemmater.6b00579.
- [242] Karsten Reuter and Matthias Scheffler. "First-Principles Atomistic Thermodynamics for Oxidation Catalysis: Surface Phase Diagrams and Catalytically Interesting Regions". In: *Physical Review Letters* 90.4 (Jan. 2003). Publisher: American Physical Society, p. 046103. DOI: 10.1103/PhysRevLett.90.046103. URL: <https://link.aps.org/doi/10.1103/PhysRevLett.90.046103> (visited on 09/17/2023).
- [243] Y. Reynier, R. Yazami, and B. Fultz. "The entropy and enthalpy of lithium intercalation into graphite". In: *Journal of Power Sources* 119–121 (June 2003). ISBN: 1626395217, pp. 850–855. ISSN: 03787753. DOI: 10.1016/S0378-7753(03)00285-4. URL: <https://linkinghub.elsevier.com/retrieve/pii/S0378775303002854>.
- [244] Yvan Reynier et al. "Entropy of Li intercalation of $\text{Li}_{x}\text{CoO}_2$ ". In: *Physical Review B* 70.17 (Nov. 2004), p. 174304. ISSN: 1098-0121. DOI: 10.1103/PhysRevB.70.174304. URL: <https://link.aps.org/doi/10.1103/PhysRevB.70.174304>.
- [245] Francesco Ricci et al. "An ab initio electronic transport database for inorganic materials". en. In: *Scientific Data* 4.1 (July 2017). Number: 1 Publisher: Nature Publishing Group, p. 170085. ISSN: 2052-4463. DOI: 10.1038/sdata.2017.85. URL: <https://www.nature.com/articles/sdata201785> (visited on 09/14/2023).
- [246] Lars Robben et al. "Symmetry reduction due to gallium substitution in the garnet $\text{Li}_{6.43(2)}\text{Ga}_{0.52(3)}\text{La}_{2.67(4)}\text{Zr}_2\text{O}_{12}$ ". In: *Acta Crystallographica Section E: Crystallographic Communications* 72 (2016). Publisher: International Union of Crystallography, pp. 287–289. ISSN: 20569890. DOI: 10.1107/S2056989016001924.
- [247] Fridolin Röder et al. "Simulating the Impact of Particle Size Distribution on the Performance of Graphite Electrodes in Lithium-Ion Batteries". In: *Energy Technology* 4.12 (Dec. 2016), pp. 1588–1597. ISSN: 21944288. DOI: 10.1002/ente.201600232. URL: <http://doi.wiley.com/10.1002/ente.201600232>.
- [248] Ahmad Nazrul Rosli et al. "The study of band structure of graphite intercalation compound containing sodium calculated using density functional theory". In: *Journal of Physics: Conference Series* 622.1 (2015). ISSN: 17426596. DOI: 10.1088/1742-6596/622/1/012049.
- [249] E. Peter Roth and Christopher J. Orendorff. "How electrolytes influence battery safety". In: *Electrochemical Society Interface* 21.2 (2012), pp. 45–49. ISSN: 19448783. DOI: 10.1149/2.F04122if.
- [250] Alvaro Ruiz-Serrano. "Computational methods for density functional theory calculations on insulators and metals based on localised orbitals.pdf". PhD thesis. University of Southampton, 2013.
- [251] Alvaro Ruiz-Serrano and Chris-Kriton Skylaris. "A variational method for density functional theory calculations on metallic systems with thousands of atoms". In: *The Journal of Chemical Physics* 139.5 (Aug. 2013), p. 054107. ISSN: 0021-9606. DOI: 10.1063/1.4817001. URL: <http://aip.scitation.org/doi/10.1063/1.4817001>.

- [252] Riccardo Sabatini, Tommaso Gorni, and Stefano de Gironcoli. "Nonlocal van der Waals density functional made simple and efficient". In: *Physical Review B* 87.4 (Jan. 2013), p. 041108. ISSN: 1098-0121. DOI: 10.1103/PhysRevB.87.041108. URL: <https://link.aps.org/doi/10.1103/PhysRevB.87.041108>.
- [253] S. A. Safran. "Stage Ordering in Intercalation Compounds". In: *Solid State Physics - Advances in Research and Applications* 40.C (1987), pp. 183–246. ISSN: 00811947. DOI: 10.1016/S0081-1947(08)60692-X.
- [254] Atsushi Sakuda, Akitoshi Hayashi, and Masahiro Tatsumisago. "Interfacial observation between LiCoO₂ electrode and Li₂S-P₂S₅ solid electrolytes of all-solid-state lithium secondary batteries using transmission electron microscopy". In: *Chemistry of Materials* 22.3 (2010), pp. 949–956. ISSN: 08974756. DOI: 10.1021/cm901819c.
- [255] Junwu Sang et al. "Theoretical formulation of Li₃: A + bNaXb(X = halogen) as a potential artificial solid electrolyte interphase (ASEI) to protect the Li anode". In: *Physical Chemistry Chemical Physics* 22.23 (2020), pp. 12918–12928. ISSN: 14639076. DOI: 10.1039/d0cp00151a.
- [256] David Santos-Carballal et al. "A DFT study of the structures, stabilities and redox behaviour of the major surfaces of magnetite Fe₃O₄". en. In: *Phys. Chem. Chem. Phys.* 16.39 (2014), pp. 21082–21097. ISSN: 1463-9076, 1463-9084. DOI: 10.1039/C4CP00529E. URL: <http://xlink.rsc.org/?DOI=C4CP00529E> (visited on 03/06/2024).
- [257] K. C. Santosh et al. "Point defects in garnet-type solid electrolyte (c-Li₇La₃Zr₂O₁₂) for Li-ion batteries". In: *Solid State Ionics* 261 (2014). Publisher: Elsevier, pp. 100–105. ISSN: 01672738. DOI: 10.1016/j.ssi.2014.04.021.
- [258] Biswajit Santra et al. "On the accuracy of density-functional theory exchange-correlation functionals for H bonds in small water clusters. II. The water hexamer and van der Waals interactions". In: *The Journal of Chemical Physics* 129.19 (Nov. 2008), p. 194111. ISSN: 0021-9606. DOI: 10.1063/1.3012573. URL: <https://doi.org/10.1063/1.3012573> (visited on 07/28/2023).
- [259] Amirreza Sazvar, Hossein Sarpoolaky, and Mohammad Golmohammad. "The effects of electric field on physical properties of LLZO made by flash sintering method". In: *Solid State Ionics* 386 (Nov. 2022). Publisher: Elsevier B.V. ISSN: 01672738. DOI: 10.1016/j.ssi.2022.116054.
- [260] A Schleede and Marianne Wellmann. "Über die struktur der Einwirkungsprodukte von Alkalimetallen auf Graphit". In: *Zeitschrift für Physikalische Chemie* 18.1 (1932), pp. 1–28. ISSN: 2196-7156.
- [261] Bruno Scrosati, ed. *Lithium batteries: advanced technologies and applications*. Hoboken, New Jersey: John Wiley & Sons, Inc, 2013. ISBN: 978-1-118-18365-6.
- [262] A. Senyshyn et al. "Lithium Intercalation into Graphitic Carbons Revisited: Experimental Evidence for Twisted Bilayer Behavior". In: *Journal of The Electrochemical Society* 160.5 (2013), A3198–A3205. ISSN: 0013-4651. DOI: 10.1149/2.031305jes.
- [263] David F. Shanno. "Conjugate Gradient Methods with Inexact Searches". In: *Mathematics of Operations Research* 3.3 (1978), pp. 244–256. ISSN: 0364-765X. DOI: 10.1287/moor.3.3.244.
- [264] Asma Sharafi et al. "Impact of air exposure and surface chemistry on Li-Li₇La₃Zr₂O₁₂ interfacial resistance". In: *Journal of Materials Chemistry A* 5.26 (2017). Publisher: Royal Society of Chemistry, pp. 13475–13487. ISSN: 20507496. DOI: 10.1039/c7ta03162a.
- [265] Asma Sharafi et al. "Surface Chemistry Mechanism of Ultra-Low Interfacial Resistance in the Solid-State Electrolyte Li₇La₃Zr₂O₁₂". In: *Chemistry of Materials* 29.18 (Sept. 2017). Publisher: American Chemical Society, pp. 7961–7968. ISSN: 15205002. DOI: 10.1021/acs.chemmater.7b03002.
- [266] Jimmy Xuan Shen, Matthew Horton, and Kristin A. Persson. "A charge-density-based general cation insertion algorithm for generating new Li-ion cathode materials". In: *npj Computational Materials* 6.1 (2020). Publisher: Springer US. ISSN: 20573960. DOI: 10.1038/s41524-020-00422-3. URL: <http://dx.doi.org/10.1038/s41524-020-00422-3>.
- [267] Yuta Shimonishi et al. "Synthesis of garnet-type Li₇-XLa₃Zr₂O₁₂-1/2x and its stability in aqueous solutions". In: *Solid State Ionics* 183.1 (Feb. 2011), pp. 48–53. ISSN: 01672738. DOI: 10.1016/j.ssi.2010.12.010.
- [268] Nicki C. Siersch et al. "Compressibility and high-pressure structural behavior of Mg₂Fe₂O₅". In: *American Mineralogist* 102.4 (Apr. 2017), pp. 845–850. ISSN: 0003-004X. DOI: 10.2138/am-2017-5837. URL: <https://www.degruyter.com/document/doi/10.2138/am-2017-5837/html>.
- [269] B. Simon et al. "On the choice of graphite for lithium ion batteries". In: *Journal of Power Sources* 81-82 (Sept. 1999), pp. 312–316. ISSN: 03787753. DOI: 10.1016/S0378-7753(99)00211-6. URL: <https://linkinghub.elsevier.com/retrieve/pii/S0378775399002116>.
- [270] Chris Kriton Skylaris and Peter D. Haynes. "Achieving plane wave accuracy in linear-scaling density functional theory applied to periodic systems: A case study on crystalline silicon". In: *Journal of Chemical Physics* 127.16 (2007), pp. 6–11. ISSN: 00219606. DOI: 10.1063/1.2796168.
- [271] Chris Kriton Skylaris et al. "Nonorthogonal generalized Wannier function pseudopotential plane-wave method". In: *Physical Review B - Condensed Matter and Materials Physics* 66.3 (2002), pp. 1–12. ISSN: 1550235X. DOI: 10.1103/PhysRevB.66.035119.
- [272] Chris-Kriton Skylaris et al. "Introducing <scp>ONETEP</scp> : Linear-scaling density functional simulations on parallel computers". In: *The Journal of Chemical Physics* 122.8 (Feb. 2005), p. 084119. ISSN: 0021-9606. DOI: 10.1063/1.1839852. URL: <http://aip.scitation.org/doi/10.1063/1.1839852>.

- [273] Daniel G. A. Smith et al. "Revised Damping Parameters for the D3 Dispersion Correction to Density Functional Theory". In: *The Journal of Physical Chemistry Letters* 7.12 (June 2016), pp. 2197–2203. ISSN: 1948-7185. DOI: 10.1021/acs.jpclett.6b00780. URL: <https://pubs.acs.org/doi/10.1021/acs.jpclett.6b00780>.
- [274] X. Y. Song, K. Kinoshita, and T. D. Tran. "Microstructural Characterization of Lithiated Graphite". In: *Journal of The Electrochemical Society* 143.6 (June 1996), pp. L120–L123. ISSN: 0013-4651. DOI: 10.1149/1.1836896. URL: <https://iopscience.iop.org/article/10.1149/1.1836896>.
- [275] Fernando A. Soto et al. "Formation and Growth Mechanisms of Solid-Electrolyte Interphase Layers in Rechargeable Batteries". In: *Chemistry of Materials* 27.23 (Dec. 2015). Publisher: American Chemical Society, pp. 7990–8000. ISSN: 0897-4756. DOI: 10.1021/acs.chemmater.5b03358. URL: <https://pubs.acs.org/doi/10.1021/acs.chemmater.5b03358>.
- [276] "Sparks fly: inside the strained Tesla-Panasonic relationship". In: *Financial Times* (May 2019). URL: <https://www.ft.com/content/bf33e6d0-6c99-11e9-80c7-60ee53e6681d> (visited on 05/30/2023).
- [277] Fernand Spiegelman et al. "Density-functional tight-binding: basic concepts and applications to molecules and clusters". In: *Advances in Physics: X* 5.1 (Jan. 2020). Publisher: Taylor & Francis _eprint: <https://doi.org/10.1080/23746149.2019.1710252>. ISSN: null. DOI: 10.1080/23746149.2019.1710252. URL: <https://doi.org/10.1080/23746149.2019.1710252> (visited on 09/11/2023).
- [278] Alexander G. Squires et al. "Low electronic conductivity of Li₇La₃Zr₂O₁₂ solid electrolytes from first principles". In: *Physical Review Materials* 6.8 (Aug. 2022). Publisher: American Physical Society, p. 085401. DOI: 10.1103/PhysRevMaterials.6.085401. URL: <https://link.aps.org/doi/10.1103/PhysRevMaterials.6.085401> (visited on 09/11/2023).
- [279] D. A. Stevens and J. R. Dahn. "The Mechanisms of Lithium and Sodium Insertion in Carbon Materials". In: *Journal of The Electrochemical Society* 148.8 (2001), A803. ISSN: 00134651. DOI: 10.1149/1.1379565.
- [280] R. Sudo et al. "Interface behavior between garnet-type lithium-conducting solid electrolyte and lithium metal". In: *Solid State Ionics* 262 (Sept. 2014). Publisher: Elsevier B.V., pp. 151–154. ISSN: 01672738. DOI: 10.1016/j.ssi.2013.09.024. URL: <https://linkinghub.elsevier.com/retrieve/pii/S0167273813004232>.
- [281] Chunwen Sun et al. "Recent advances in all-solid-state rechargeable lithium batteries". In: *Nano Energy* 33.January (2017). Publisher: Elsevier Ltd, pp. 363–386. ISSN: 22112855. DOI: 10.1016/j.nanoen.2017.01.028. URL: <http://dx.doi.org/10.1016/j.nanoen.2017.01.028>.
- [282] H. Sun. "COMPASS: An ab Initio Force-Field Optimized for Condensed-Phase ApplicationsOverview with Details on Alkane and Benzene Compounds". In: *The Journal of Physical Chemistry B* 102.38 (Sept. 1998). Publisher: American Chemical Society, pp. 7338–7364. ISSN: 1520-6106. DOI: 10.1021/jp980939v. URL: <https://doi.org/10.1021/jp980939v> (visited on 09/14/2023).
- [283] Huai Sun et al. "An ab Initio CFF93 All-Atom Force Field for Polycarbonates". In: *Journal of the American Chemical Society* 116.7 (Apr. 1994). Publisher: American Chemical Society, pp. 2978–2987. ISSN: 0002-7863. DOI: 10.1021/ja00086a030. URL: <https://doi.org/10.1021/ja00086a030> (visited on 09/14/2023).
- [284] Adrian Sutton and Robert W. Balluffi. *Interfaces in crystalline materials*. eng. Corr. ed. Monographs on the physics and chemistry of materials 51. Oxford Oxford New York: Clarendon Press Oxford university press, 1996. ISBN: 978-0-19-850061-2.
- [285] Michael W. Swift, James W. Swift, and Yue Qi. "Modeling the electrical double layer at solid-state electrochemical interfaces". In: *Nature Computational Science* 1.3 (Mar. 2021). Publisher: Springer US, pp. 212–220. ISSN: 2662-8457. DOI: 10.1038/s43588-021-00041-y. URL: <http://dx.doi.org/10.1038/s43588-021-00041-y>.
- [286] Attila Szabo and Neil S. Ostlund. *Modern quantum chemistry: introduction to advanced electronic structure theory*. Mineola, N.Y: Dover Publications, 1996. ISBN: 978-0-486-69186-2.
- [287] Kazunori Takada et al. "Interfacial modification for high-power solid-state lithium batteries". In: *Solid State Ionics* 179.27-32 (2008), pp. 1333–1337. ISSN: 01672738. DOI: 10.1016/j.ssi.2008.02.017.
- [288] Kenji Takahashi and Venkat Srinivasan. "Examination of Graphite Particle Cracking as a Failure Mode in Lithium-Ion Batteries: A Model-Experimental Study". In: *Journal of The Electrochemical Society* 162.4 (2015), A635–A645. ISSN: 0013-4651. DOI: 10.1149/2.0281504jes.
- [289] J. M. Tarascon and D. Guyomard. "The Li_{1+x}Mn₂O₄/C rocking-chair system: a review". In: *Electrochimica Acta* 38.9 (June 1993), pp. 1221–1231. ISSN: 0013-4686. DOI: 10.1016/0013-4686(93)80053-3. URL: <https://www.sciencedirect.com/science/article/pii/0013468693800533> (visited on 08/21/2023).
- [290] Yoshitaka Tateyama et al. "Theoretical picture of positive electrode–solid electrolyte interface in all-solid-state battery from electrochemistry and semiconductor physics viewpoints". In: *Current Opinion in Electrochemistry* 17.June (Oct. 2019). Publisher: Elsevier Ltd, pp. 149–157. ISSN: 24519103. DOI: 10.1016/j.coelec.2019.06.003. URL: <https://doi.org/10.1016/j.coelec.2019.06.003>.
- [291] Venkataraman Thangadurai and Werner Weppner. "Li₆Al₂Ta₂O₁₂ (A=Sr, Ba): Novel garnet-like oxides for fast lithium ion conduction". In: *Advanced Functional Materials* 15.1 (2005), pp. 107–112. ISSN: 1616301X. DOI: 10.1002/adfm.200400044.

- [292] Sascha Thinius et al. "Theoretical Study of Li Migration in Lithium–Graphite Intercalation Compounds with Dispersion-Corrected DFT Methods". In: *The Journal of Physical Chemistry C* 118.5 (Feb. 2014). Publisher: American Chemical Society, pp. 2273–2280. ISSN: 1932-7447. DOI: 10.1021/jp408945j. URL: <https://doi.org/10.1021/jp408945j> (visited on 09/13/2023).
- [293] K.E Thomas, John Newman, and R.M Darling. *Advances in Li ion Batteries*. 2002. ISBN: 0-306-47508-1.
- [294] Karen E. Thomas and John Newman. "Heats of mixing and of entropy in porous insertion electrodes". In: *Journal of Power Sources* 119-121 (2003), pp. 844–849. ISSN: 03787753. DOI: 10.1016/S0378-7753(03)00283-0.
- [295] Travis Thompson et al. "Electrochemical Window of the Li-Ion Solid Electrolyte Li₇La₃Zr₂O₁₂". In: *ACS Energy Letters* 2.2 (Feb. 2017), pp. 462–468. ISSN: 2380-8195. DOI: 10.1021/acsenergylett.6b00593. URL: <https://pubs.acs.org/doi/10.1021/acsenergylett.6b00593>.
- [296] Hong-Kang Tian, Bo Xu, and Yue Qi. "Computational study of lithium nucleation tendency in Li₇La₃Zr₂O₁₂ (LLZO) and rational design of interlayer materials to prevent lithium dendrites". In: *Journal of Power Sources* 392 (July 2018). Publisher: Elsevier B.V., pp. 79–86. ISSN: 03787753. DOI: 10.1016/j.jpowsour.2018.04.098. URL: <https://linkinghub.elsevier.com/retrieve/pii/S0378775318304476>.
- [297] Alexandre Tkatchenko and Matthias Scheffler. "Accurate molecular van der Waals interactions from ground-state electron density and free-atom reference data". In: *Physical Review Letters* 102.7 (2009), pp. 6–9. ISSN: 00319007. DOI: 10.1103/PhysRevLett.102.073005.
- [298] Atsushi Togo, Fumiya Oba, and Isao Tanaka. "First-principles calculations of the ferroelastic transition between rutile-type and CaCl₂-type SiO₂ at high pressures". In: *Physical Review B - Condensed Matter and Materials Physics* 78.13 (2008), pp. 1–9. ISSN: 10980121. DOI: 10.1103/PhysRevB.78.134106.
- [299] Atsushi Togo and Isao Tanaka. *\$|text{Spplib}|\$: a software library for crystal symmetry search*. arXiv:1808.01590 [cond-mat]. Aug. 2018. DOI: 10.48550/arXiv.1808.01590. URL: <http://arxiv.org/abs/1808.01590> (visited on 06/19/2023).
- [300] Tim S. Totton, Alston J. Misquitta, and Markus Kraft. "Assessing the polycyclic aromatic hydrocarbon anisotropic potential with application to the exfoliation energy of graphite". In: *Journal of Physical Chemistry A* 115.46 (Nov. 2011), pp. 13684–13693. ISSN: 10895639. DOI: 10.1021/jp208088s.
- [301] Richard Tran et al. "Surface energies of elemental crystals". en. In: *Scientific Data* 3.1 (Sept. 2016). Number: 1 Publisher: Nature Publishing Group, p. 160080. ISSN: 2052-4463. DOI: 10.1038/sdata.2016.80. URL: <https://www.nature.com/articles/sdata201680> (visited on 09/15/2023).
- [302] Mark E. Tuckerman and Michele Parrinello. "Integrating the Car–Parrinello equations. I. Basic integration techniques". In: *The Journal of Chemical Physics* 101.2 (July 1994), pp. 1302–1315. ISSN: 0021-9606. DOI: 10.1063/1.467823. URL: <http://aip.scitation.org/doi/10.1063/1.467823>.
- [303] A. Van der Ven et al. "First-principles investigation of phase stability in LixCoO₂". In: *Physical Review B* 58.6 (Aug. 1998), pp. 2975–2987. ISSN: 0163-1829. DOI: 10.1103/PhysRevB.58.2975. URL: <https://link.aps.org/doi/10.1103/PhysRevB.58.2975>.
- [304] A. Van der Ven et al. "First-Principles Statistical Mechanics of Multicomponent Crystals". In: *Annual Review of Materials Research* 48.1 (2018). _eprint: <https://doi.org/10.1146/annurev-matsci-070317-124443>, pp. 27–55. DOI: 10.1146/annurev-matsci-070317-124443. URL: <https://doi.org/10.1146/annurev-matsci-070317-124443> (visited on 09/14/2023).
- [305] Walter A. Van Schalkwijk and Bruno Scrosati, eds. *Advances in Lithium-Ion Batteries*. en. Boston, MA: Springer US, 2002. ISBN: 978-0-306-47356-2. DOI: 10.1007/b113788. URL: <http://link.springer.com/10.1007/b113788> (visited on 05/24/2023).
- [306] Jenel Vatamanu, Oleg Borodin, and Grant D. Smith. "Molecular dynamics simulation studies of the structure of a mixed carbonate/LiPF₆ electrolyte near graphite surface as a function of electrode potential". In: *Journal of Physical Chemistry C* 116.1 (Jan. 2012), pp. 1114–1121. ISSN: 19327447. DOI: 10.1021/jp2101539.
- [307] Chris Vavra. *Europe expected to be fastest-growing market for lithium-ion batteries*. en-US. July 2019. URL: <https://www.controleng.com/articles/europe-expected-to-be-fastest-growing-market-for-lithium-ion-batteries/> (visited on 05/30/2023).
- [308] Sundeep Vema et al. "Clarifying the Dopant Local Structure and Effect on Ionic Conductivity in Garnet Solid-State Electrolytes for Lithium-Ion Batteries". en. In: *Chemistry of Materials* 35.22 (Nov. 2023), pp. 9632–9646. ISSN: 0897-4756, 1520-5002. DOI: 10.1021/acs.chemmater.3c01831. URL: <https://pubs.acs.org/doi/10.1021/acs.chemmater.3c01831> (visited on 03/06/2024).
- [309] Juan C. Verduzco, Ernesto E. Marinero, and Alejandro Strachan. "Atomistic Mechanisms Underlying the Maximum in Diffusivity in Doped Li₇La₃Zr₂O₁₂". In: *The Journal of Physical Chemistry C* 127.22 (June 2023). Publisher: American Chemical Society, pp. 10806–10812. ISSN: 1932-7447. DOI: 10.1021/acs.jpcc.3c01604. URL: <https://doi.org/10.1021/acs.jpcc.3c01604> (visited on 06/12/2023).
- [310] Pallavi Verma, Pascal Maire, and Petr Novák. "A review of the features and analyses of the solid electrolyte interphase in Li-ion batteries". In: *Electrochimica Acta* 55.22 (Sept. 2010), pp. 6332–6341. ISSN: 00134686. DOI: 10.1016/j.electacta.2010.05.072. URL: <https://linkinghub.elsevier.com/retrieve/pii/S0013468610007747>.

- [311] J. Vetter et al. "Ageing mechanisms in lithium-ion batteries". In: *Journal of Power Sources* 147.1-2 (2005), pp. 269–281. ISSN: 03787753. DOI: 10.1016/j.jpowsour.2005.01.006.
- [312] S. H. Vosko, L. Wilk, and M. Nusair. "Accurate spin-dependent electron liquid correlation energies for local spin density calculations: a critical analysis". en. In: *Canadian Journal of Physics* 58.8 (Aug. 1980), pp. 1200–1211. ISSN: 0008-4204, 1208-6045. DOI: 10.1139/p80-159. URL: <http://www.nrcresearchpress.com/doi/10.1139/p80-159> (visited on 08/07/2023).
- [313] Oleg A. Vydrov and Troy Van Voorhis. "Nonlocal van der Waals density functional: The simpler the better". In: *Journal of Chemical Physics* 133.24 (2010). arXiv: 1009.1421. ISSN: 00219606. DOI: 10.1063/1.3521275.
- [314] Reinhard Wagner et al. "Crystal Structure of Garnet-Related Li-Ion Conductor Li_{7-3x}GaxLa₃Zr₂O₁₂: Fast Li-Ion Conduction Caused by a Different Cubic Modification?" In: *Chemistry of Materials* 28.6 (Mar. 2016). Publisher: American Chemical Society, pp. 1861–1871. ISSN: 15205002. DOI: 10.1021/acs.chemmater.6b00038.
- [315] A. van de Walle and G. Ceder. "Automating first-principles phase diagram calculations". In: *Journal of Phase Equilibria* 23.4 (2002). arXiv: cond-mat/0201511, pp. 348–359. ISSN: 10549714. DOI: 10.1361/105497102770331596.
- [316] Feng Wang et al. "Chemical distribution and bonding of lithium in intercalated graphite: Identification with optimized electron energy loss spectroscopy". In: *ACS Nano* 5.2 (2011), pp. 1190–1197. ISSN: 19360851. DOI: 10.1021/nn1028168.
- [317] Han Wang et al. "DeePMD-kit: A deep learning package for many-body potential energy representation and molecular dynamics". In: *Computer Physics Communications* 228 (July 2018), pp. 178–184. ISSN: 0010-4655. DOI: 10.1016/j.cpc.2018.03.016. URL: <https://www.sciencedirect.com/science/article/pii/S0010465518300882> (visited on 09/25/2023).
- [318] Lei Wang, Thomas Maxisch, and Gerbrand Ceder. "Oxidation energies of transition metal oxides within the {GGA} + {U} framework". In: *Physical Review B* 73.19 (May 2006), p. 195107. ISSN: 1098-0121, 1550-235X. DOI: 10.1103/PhysRevB.73.195107. URL: <https://link.aps.org/doi/10.1103/PhysRevB.73.195107> (visited on 12/19/2019).
- [319] Michael Wang and Jeff Sakamoto. "Correlating the interface resistance and surface adhesion of the Li metal-solid electrolyte interface". In: *Journal of Power Sources* 377.August 2017 (2018), pp. 7–11. ISSN: 03787753. DOI: 10.1016/j.jpowsour.2017.11.078.
- [320] Yanchao Wang et al. "CALYPSO: A method for crystal structure prediction". In: *Computer Physics Communications* 183.10 (Oct. 2012). Publisher: Elsevier B.V., pp. 2063–2070. ISSN: 00104655. DOI: 10.1016/j.cpc.2012.05.008. URL: <http://dx.doi.org/10.1016/j.cpc.2012.05.008>.
- [321] Christopher M. Wolverton. "Ground-state properties and phase stability of binary and ternary intermetallic alloys". Publication Title: Dissertation. PhD thesis. University of California Berkley, 1993. URL: <https://search.proquest.com/dissertations-theses/ground-state-properties-phase-stability-binary/docview/304048372/se-2?accountid=13963>.
- [322] K. C. Woo et al. "Effect of In-Plane Density on the Structural and Elastic Properties of Graphite Intercalation Compounds". In: *Physical Review Letters* 50.3 (Jan. 1983). Publisher: American Physical Society, pp. 182–185. DOI: 10.1103/PhysRevLett.50.182. URL: <https://link.aps.org/doi/10.1103/PhysRevLett.50.182> (visited on 08/22/2023).
- [323] K. C. Woo et al. "Experimental phase diagram of lithium-intercalated graphite". en. In: *Physical Review B* 27.12 (June 1983), pp. 7831–7834. ISSN: 0163-1829. DOI: 10.1103/PhysRevB.27.7831. URL: <https://link.aps.org/doi/10.1103/PhysRevB.27.7831> (visited on 09/14/2023).
- [324] Yihan Xiao et al. "Computational Screening of Cathode Coatings for Solid-State Batteries". In: *Joule* 3.5 (2019). Publisher: Elsevier Inc., pp. 1252–1275. ISSN: 25424351. DOI: 10.1016/j.joule.2019.02.006. URL: <https://doi.org/10.1016/j.joule.2019.02.006>.
- [325] Yihan Xiao et al. "Understanding interface stability in solid-state batteries". In: *Nature Reviews Materials* 5.2 (2020). Publisher: Springer US, pp. 105–126. ISSN: 20588437. DOI: 10.1038/s41578-019-0157-5. URL: <http://dx.doi.org/10.1038/s41578-019-0157-5>.
- [326] Hui Xie et al. "Lithium Distribution in Aluminum-Free Cubic Li₇La₃Zr₂O₁₂". In: *Chemistry of Materials* 23.16 (Aug. 2011), pp. 3587–3589. ISSN: 0897-4756. DOI: 10.1021/cm201671k. URL: <https://pubs.acs.org/doi/10.1021/cm201671k>.
- [327] Lin Xu et al. "Interfaces in Solid-State Lithium Batteries". In: *Joule* 2.10 (2018). Publisher: Elsevier Inc., pp. 1991–2015. ISSN: 25424351. DOI: 10.1016/j.joule.2018.07.009. URL: <https://doi.org/10.1016/j.joule.2018.07.009>.
- [328] Ming Xu et al. "Mechanisms of Li⁺ transport in garnet-type cubic Li_{3+x}La₃M₂O₁₂ (M = Te, Nb, Zr)". In: *Physical Review B* 85.5 (Feb. 2012), p. 052301. ISSN: 1098-0121. DOI: 10.1103/PhysRevB.85.052301. URL: <https://link.aps.org/doi/10.1103/PhysRevB.85.052301>.
- [329] Yuki Yamada et al. "Kinetics of lithium ion transfer at the interface between graphite and liquid electrolytes: effects of solvent and surface film". In: *Langmuir* 25.21 (Nov. 2009), pp. 12766–12770. ISSN: 07437463. DOI: 10.1021/la901829v.

- [330] Liu-Ming Yan et al. “Review of the first principles calculations and the design of cathode materials for Li-ion batteries”. en. In: *Advances in Manufacturing* 2.4 (Dec. 2014), pp. 358–368. ISSN: 2095-3127, 2195-3597. DOI: 10.1007/s40436-014-0086-x. URL: <http://link.springer.com/10.1007/s40436-014-0086-x> (visited on 03/05/2024).
- [331] R. Yazami and Ph Touzain. “A reversible graphite-lithium negative electrode for electrochemical generators”. In: *Journal of Power Sources* 9.3 (Jan. 1983), pp. 365–371. ISSN: 03787753. DOI: 10.1016/0378-7753(83)87040-2. URL: <https://linkinghub.elsevier.com/retrieve/pii/0378775383870402>.
- [332] H. Yoon et al. “Lithium electrochemistry and cycling behaviour of ionic liquids using cyano based anions”. en. In: *Energy & Environmental Science* 6.3 (2013), p. 979. ISSN: 1754-5692, 1754-5706. DOI: 10.1039/c3ee23753b. URL: <http://xlink.rsc.org/?DOI=c3ee23753b> (visited on 03/05/2024).
- [333] Akira Yoshino, Kenichi Sanechika, and Takayuki Nakajima. “Secondary battery”. US4668595A. May 1987. URL: <https://patents.google.com/patent/US4668595A/en> (visited on 05/30/2023).
- [334] Seungho Yu and Donald J. Siegel. “Grain Boundary Contributions to Li-Ion Transport in the Solid Electrolyte Li₇La₃Zr₂O₁₂ (LLZO)”. In: *Chemistry of Materials* 29.22 (Nov. 2017). Publisher: American Chemical Society, pp. 9639–9647. ISSN: 15205002. DOI: 10.1021/acs.chemmater.7b02805.
- [335] Seungho Yu et al. “Elastic Properties of the Solid Electrolyte Li₇La₃Zr₂O₁₂ (LLZO)”. In: *Chemistry of Materials* 28.1 (Jan. 2016). Publisher: American Chemical Society, pp. 197–206. ISSN: 0897-4756. DOI: 10.1021/acs.chemmater.5b03854. URL: <https://pubs.acs.org/doi/10.1021/acs.chemmater.5b03854>.
- [336] Seungho Yu et al. “Elastic Properties of the Solid Electrolyte Li₇La₃Zr₂O₁₂ (LLZO)”. In: *Chemistry of Materials* 28.1 (Jan. 2016). Publisher: American Chemical Society, pp. 197–206. ISSN: 0897-4756. DOI: 10.1021/acs.chemmater.5b03854. URL: <https://doi.org/10.1021/acs.chemmater.5b03854> (visited on 09/19/2023).
- [337] Yang-Xin Yu. “Can all nitrogen-doped defects improve the performance of graphene anode materials for lithium-ion batteries?” In: *Physical Chemistry Chemical Physics* 15.39 (Oct. 2013), p. 16819. ISSN: 1463-9076. DOI: 10.1039/c3cp51689j. URL: <http://xlink.rsc.org/?DOI=c3cp51689j>.
- [338] Yang-Xin Yu. “Graphylene: a promising anode material for lithium-ion batteries with high mobility and storage”. In: *Journal of Materials Chemistry A* 1.43 (Nov. 2013). Publisher: Royal Society of Chemistry, p. 13559. ISSN: 2050-7488. DOI: 10.1039/c3ta12639k. URL: <http://xlink.rsc.org/?DOI=c3ta12639k>.
- [339] Hartmut Zabel et al., eds. *Graphite Intercalation Compounds II*. Vol. 18. Springer Series in Materials Science. Berlin, Heidelberg: Springer Berlin Heidelberg, 1992. ISBN: 978-3-642-84481-2. DOI: 10.1007/978-3-642-84479-9. URL: <http://link.springer.com/10.1007/978-3-642-84479-9> (visited on 05/24/2023).
- [340] Renju Zacharia, Hendrik Ulbricht, and Tobias Hertel. “Interlayer cohesive energy of graphite from thermal desorption of polycyclic aromatic hydrocarbons”. In: *Physical Review B - Condensed Matter and Materials Physics* 69.15 (Apr. 2004). arXiv: cond-mat/0308451. ISSN: 01631829. DOI: 10.1103/PhysRevB.69.155406.
- [341] Jun Zhang et al. “NWPEsSe: An Adaptive-Learning Global Optimization Algorithm for Nanosized Cluster Systems”. en. In: *Journal of Chemical Theory and Computation* 16.6 (June 2020), pp. 3947–3958. ISSN: 1549-9618, 1549-9626. DOI: 10.1021/acs.jctc.9b01107. URL: <https://pubs.acs.org/doi/10.1021/acs.jctc.9b01107> (visited on 02/09/2024).
- [342] Ya-Qian Zhang et al. “Direct Visualization of the Interfacial Degradation of Cathode Coatings in Solid State Batteries: A Combined Experimental and Computational Study”. en. In: *Advanced Energy Materials* 10.27 (July 2020), p. 1903778. ISSN: 1614-6832, 1614-6840. DOI: 10.1002/aenm.201903778. URL: <https://onlinelibrary.wiley.com/doi/10.1002/aenm.201903778> (visited on 09/14/2023).
- [343] Xun Zhang, Wei Liu, and Yi Yu. “The effects of local strain on the cubic Li₇La₃Zr₂O₁₂(001)/Li(001) interface: A first-principles study”. In: *Solid State Ionics* 360 (Feb. 2021). Publisher: Elsevier B.V. ISSN: 01672738. DOI: 10.1016/j.ssi.2020.115546.
- [344] Zhenyu Zhang et al. “Operando Electrochemical Atomic Force Microscopy of Solid-Electrolyte Interphase Formation on Graphite Anodes: The Evolution of SEI Morphology and Mechanical Properties”. In: *ACS Applied Materials & Interfaces* 12.31 (Aug. 2020). Publisher: American Chemical Society, pp. 35132–35141. ISSN: 1944-8244. DOI: 10.1021/acsami.0c11190. URL: <https://doi.org/10.1021/acsami.0c11190> (visited on 09/13/2023).
- [345] Zhizhen Zhang et al. “New horizons for inorganic solid state ion conductors”. In: *Energy and Environmental Science* 11.8 (2018), pp. 1945–1976. ISSN: 17545706. DOI: 10.1039/c8ee01053f.
- [346] Yisi Zhu et al. “Dopant-Dependent Stability of Garnet Solid Electrolyte Interfaces with Lithium Metal”. In: *Advanced Energy Materials* 9.12 (2019), pp. 1–11. ISSN: 16146840. DOI: 10.1002/aenm.201803440.
- [347] Yizhou Zhu, Xingfeng He, and Yifei Mo. “First principles study on electrochemical and chemical stability of solid electrolyte-electrode interfaces in all-solid-state Li-ion batteries”. In: *Journal of Materials Chemistry A* 4.9 (2016). Publisher: Royal Society of Chemistry, pp. 3253–3266. ISSN: 20507496. DOI: 10.1039/c5TA08574H.
- [348] Yizhou Zhu, Xingfeng He, and Yifei Mo. “First principles study on electrochemical and chemical stability of solid electrolyte-electrode interfaces in all-solid-state Li-ion batteries”. en. In: *Journal of Materials Chemistry A* 4.9 (Feb. 2016). Publisher: The Royal Society of Chemistry, pp. 3253–3266. ISSN: 2050-7496. DOI: 10.1039/C5TA08574H. URL: <https://pubs.rsc.org/en/content/articlelanding/2016/ta/c5ta08574h> (visited on 09/18/2023).

- [349] Yizhou Zhu, Xingfeng He, and Yifei Mo. "Origin of Outstanding Stability in the Lithium Solid Electrolyte Materials: Insights from Thermodynamic Analyses Based on First-Principles Calculations". In: *ACS Applied Materials & Interfaces* 7.42 (Oct. 2015), pp. 23685–23693. ISSN: 1944-8244. DOI: 10.1021/acsami.5b07517. URL: <https://pubs.acs.org/doi/10.1021/acsami.5b07517>.
- [350] Guorong Zhuang, Yufeng Chen, and Philip N. Ross. "The Reaction of Lithium with Dimethyl Carbonate and Diethyl Carbonate in Ultrahigh Vacuum Studied by X-ray Photoemission Spectroscopy". In: *Langmuir* 15.4 (Feb. 1999). Publisher: American Chemical Society, pp. 1470–1479. ISSN: 0743-7463. DOI: 10.1021/la980454y. URL: <https://pubs.acs.org/doi/10.1021/la980454y>.